VORTEX SIMULATION OF THE REACTING SHEAR LAYER

by

Ghassem Heidarinejad

B.S., Mech. Eng., Tehran Polytechnic (1973)

M.S., Mech. Eng., Tehran Polytechnic (1975)

SUBMITTED TO THE DEPARTMENT OF
MECHANICAL ENGINEERING
IN PARTIAL FULFILLMENT OF THE REQUIREMENTS
FOR THE DEGREE OF

DOCTOR OF PHILOSOPHY

at the

MASSACHUSETTS INSTITUTE OF TECHNOLOGY
February 1989

Signature of Author .....
Department of Mechanical Engineering
February, 1989

Certified by .....
Ahmed F. Ghoniem
Associate Professor, Mechanical Engineering
Thesis Supervisor

Accepted by .....
Ain A. Sonin
Chairman, Departmental Graduate Committee

VORTEX SIMULATION OF THE REACTING SHEAR LAYER

by

GHASSEM HEIDARINEJAD

Submitted to the Department of Mechanical Engineering
in partial fulfillment of the
requirement for the Degree of Doctor of Philosophy
in Mechanical Engineering

ABSTRACT

Numerical simulation is used to study the reacting shear layer at high Reynolds numbers and moderate Damkohler numbers. The numerical schemes developed for this purpose are of the Lagrangian-kernel type, the vortex element method for the integration of the vorticity transport equation and the transport element method for the integration of the scalar transport equation. The unsteady equations are integrated by transporting the gradients of the gas dynamic variables along particle paths, while the intensification of the gradients due to the strain field is incorporated utilizing the relationship between the scalar field and the distortion of the flow map.

The growth rate of the perturbed temporal shear layer agrees well with the results of linear stability theory. The roll up of the vorticity extends the interface across which diffusion occurs and promotes entrainments currents into the convoluted structures leading to substantial enhancement of the mixing between the two streams. The structure of the forced spatial shear layer shows that, downstream the splitter plate the layer structure follows the forcing function. The velocity and mixing statistics agree well with experimental measurements obtained before mixing transition. Mixing asymmetry leads to the formation of a preferred mixture fraction within the eddies and is related to the dynamics of the vorticity field in the spatial layer.

The reacting shear layer reveals a strong similarity between instantaneous distributions of product concentration and vorticity irrespective of the chemical kinetic model or the Damkohler number. This is explained by the relationship between the product formation mechanism and the advection field generated by the strain associated with vorticity amalgamation into large eddies. Outside the eddies, the strain field reduces product concentration by thinning the layer, by reducing the time allowed for mixing, and by advective cooling. The structure of the reacting shear layer depends critically on the Damkohler numbers. The effect of the Damkohler number is strong around Da = 1 where the rate of product formation rises rapidly with the speed of the chemical reaction reaching an asymptotic value around Da = 20. At high Reynolds number, the rate of product formation is governed by the entrainment of reactants into the large eddies, which is weakly dependent on Re. The reactants ratio across the layer, coupled with mixing asymmetry, governs the chemical potential inside the eddies. Strong temperature-dependence produces an ignition delay at the early stages and an explosion within the eddy cores downstream.

Thesis committee : Prof. A.F. Ghoniem (Chairman)
Prof. J.C. Keck
Prof. A.A. Sonin
Prof. L.N. Trefethen

ACKNOWLEDGEMENTS

I would like to express my deepest thanks to professor Ahmed F. Ghoniem for his invaluable criticism, comments, and encouragement throughout this thesis research.

I also would like to thanks the members of my thesis committee, Prof. J. C. Keck, Prof. A. A. Sonin, and Prof. L. N. Trefethen for their valuable suggestions.

I wish to particularly acknowledge the government of Islamic Republic of Iran for their financial support throughout my study in MIT.

The work was supported by the National Science Foundation Grants CPE-840481 and CBT-8709465, the Department of Energy Contract DE-AC04-86AL16310 and Grant DE-FG04-87AL44875 and by the Air Force Office of Scientific Research Grant AFOSR 84-0356.

Lastly, I wish to express my deepest gratitude to my wife Shahnaz for her patience, understanding, and unwavering faith in me during my study in MIT.

TABLE OF CONTENTS

LIST OF SYMBOLS

SYMBOL	DESCRIPTION
A_f	Frequency factor
c	Species concentration
c_F	Fuel concentration
$c_{F\infty}$	Free stream fuel concentration
c_O	Oxidizer concentration
c_p	Specific heat at constant pressure
c_P	Products concentration
D	Molecular diffusion coefficient
D_a	First Damkohler number
E	Activation energy
erf	Error function
f	Core function
F	Fuel, derivative of the mapping function
g	Gradient of scalar
G	Green function
G.R.	Growth rate
h	Initial distance between two neighboring elements
H	Channel height
k	Heat conductivity
K	Kernel function
L	Length scale of the shear layer
L_e	Lewis Number
N	Number of computational elements
O	Oxidizer
P	Products
P_e	Peclet number
P_r	Prandlt number
Q	enthalpy of reaction
r	$\sqrt{x^2+ y^2}$
R_e	Reynolds number
s	Scalar

S_c	Schmit number
T	Absolute temperature
T_∞	Free stream temperature of the reactants
T_a	Normalized activation energy
T_f	Averaged temperature of the reacting zone
T_P	Product's temperature
u	Streamwise velocity
U_1	Fast-speed Free stream velocity
U_2	Slow-speed Free stream velocity
U_M	Mean velocity, $(U_1+U_2)/2$
ΔU	Velocity difference, U_1-U_2
v	Cross stream velocity
$\dot{W}$	Rate of products formation
x	Streamwise coordinate
X_{max}	Length of the computational domain
y	cross-stream coordinate
α	Thermal diffusivity
∇	Gradient operator
∇^2	Laplacian operator
Γ	Circulation
Ω	Initial vorticity distribution
ν	Kinematic viscosity
δ	Core radius
ρ	Density
ω	Vorticity
σ	Spread of the initial Gaussian
δ_p	Integral product thickness
δ_1	1% Product thickness
Ψ	Reactant ratio

Chapter 1

Introduction

1.1 BACKGROUND.

Non-premixed turbulent reacting flow has been the subject of extensive experimental, theoretical and numerical investigations (for review, see Bilger [1]). In most of the theoretical work, turbulence models are used to close a system of averaged transport equations that describe the statistical behavior of the aerothermodynamics variables. Much effort has gone into constructing accurate models and obtaining results that are in agreements with experimental measurements. Moment methods [2], eddy break-up and mixing controlled models [3], flame-sheet approximations [4], assumed probability-density functions (PDF) shape methods [5], and solutions based on modelled joint PDF of scalar [6,7], and based on modelled joint PDF of scalar and velocity [8] are examples of these models.

Numerous careful experimental investigations were conducted for the purpose of understanding the effect of turbulence on chemistry [9-12]. These studies have revealed, using flow visualization and point measurements, that reacting shear layer are dominated by large-scale structures and that the zone of product formation is confined to where these structure exist. It was also shown that the large-scale structures increase the rate of burning by enhancing the rate of entrainment of reactants into the reacting zone and thus improving the mixing of reactants. These results were utilized in the phenomenological models of reaction in shear layers [13,14].

Recent progress in numerical methods and availability of fast computer have had a major impact on turbulence research. With more accurate numerics and increased storage and computational speed, it has been possible to solve the time-dependent transport equations governing turbulent combustion over

some limited parameter range without the need for modeling. Such nearly model-free simulations have the advantage that the physics of the problem is not modelled a priori but is recovered directly from the solution. The results of the numerical simulation can be used to understand important mechanisms of turbulent transport and its influence on chemical reactions. Furthermore, since the instantaneous behavior of the variables is known at all points and at all times, accurate simulations offer a good method of probing the flow.

Numerical methods have been used in variety of forms for the simulation of turbulent flows in complex configurations (see, e.g., Refs. [15,16]). Finite-difference methods in which flow variables are defined on a grid and the transport equations are approximated by discretizing the derivatives on the grid nodes, were first to be used. Examples of this approach can be found in the work of Corcos and Sherman [17], who used a projection method to study the temporal evolution of a periodic shear layer, and in Grinstein et al. [18], who used a flux-corrected transport scheme to simulate the development of coherent structures in a two-dimensional, spatially-evolving shear layer and examined their effect on mixing.

Spectral methods, in which each variable is expanded in a series of harmonic functions that satisfy the differential equations on a number of collocation points, were applied by Riely et al. [19], to study a three-dimensional temporally-evolving reacting mixing layer assuming a temperature-independent reaction rate, constant density, and no heat release. McMurtry et al. [20], used a pseudo-spectral scheme to analyze the effect of chemical heat release on the dynamics of a two-dimensional mixing layer for a temperature-independent reaction rate. Givi et al. [21] employed a spectral simulation of a two-dimensional mixing layer with an Arrhenius rate expression and constant

density to study local flame extinction. Extension to spatially-growing layer was initiated by Givi and Jou [22]. In al cases, the Reynolds number was kept at order of (100), limited by the grid resolution and the number of harmonic modes.

Vortex methods, a particular class of Lagrangian particle methods, were also used to solve the Euler equation for a two-dimensional incompressible flow (Leonard [23], Beale and Majda [24], Hald [25], and Ghoniem and Ng [26]). These methods are based on the discretization of the vorticity into finite vortex elements which carry radially-symmetric, compact support of vorticity (Chorin [27]). By choosing the extent of the support, or the core radius of each element to be larger than the distance of separation between neighboring elements, the fields of individual elements overlap and high order discretization of the vorticity field can be achieved. Vortex elements move with the local flow velocity evaluated at their geometrical centers, which is computed as the summation over the contributions of all elements that exist in the field. The motion of a vortex element does not change its circulation and, in most applications, vortex elements possess invariable core shape and size.

The attraction of Lagrangian, grid-free, vortex method is that, by construction, computational vortex elements are expected to be, at all times, concentrated around zones of high velocity gradients. When properly exploited, this property endows the scheme with resolution necessary to study interesting phenomena that arise when molecular diffusion is small relative to convective transport. For instance, at high Reynolds numbers, vorticity exists on small patches of the fluid and its suffices to distribute computational elements within these patches and hence avoid wasting labor on zones of very small vorticity. That the elements move to capture large

velocity gradients is particularly important in unsteady and nonlinearly unstable flows where the evolution of the instability causes a substantial distortion of the vorticity distribution. Moreover, using a Lagrangian formulation of the equations of motion avoids the convective non-linearity and enables the construction of computational schemes which are explicit in time. The employment of moving Lagrangian grids (Fitts and Boris [28]), or grid-free schemes such as contour dynamics (Zabuski et al. [29]), are other successful ways of accomplishing the same goal.

1.2. BRIEF REVIEW.

The fact that vorticity is conserved along the particle path in a two-dimensional, uniform-density, inviscid flow make these method particularly simple for this class of problems. Convergence proofs of the inviscid vortex method shows that three factors govern their accuracy: (1) the scheme of discretization of the initial vorticity; (2) the form of the core function; and (3) the ratio of the core radius to the separation between vortex elements (Chorin et al. [30], Del-Prete and Hald [31], Hald [25,32] and Beale and Majda [24,33]). Results of these analysis have been supported by numerical tests (Nakamura et al. [34], Roberts [35], and Perlman [36]). In the following, all three factors are briefly discussed.

To initialize the strength of vortex elements, Del-Prete and Hald [31] and Hald [25] used average vorticity within an area element around the center of the element, while Beale and Majda [24] suggested using the vorticity at the center of the element. Nakamura et al. [34] minimized the global error between the continuous and the discrete vorticity distribution to evaluate the latter. Anderson and Greengard [37] proposed the use of a nonuniform mesh to discretize the vorticity field. Using the procedure in [24 or 31], one should

expect almost a second-order accuracy for short time if the core function is chosen to be a second-order Gaussian. A fourth-order Gaussian was shown to improve the accuracy. In both cases, a critical parameter is the ratio of the core radius to the distance of separation between the center of the elements, which must be chosen larger than unity to preserve the accuracy for long time.

As the elements move, their separation exceeds their initial value if a strong strain field arises. This, in effect, decreases the critical ratio of core radius/separation, leading to deterioration of the accuracy. The fact that large strain cause deterioration in the accuracy of vortex methods has been observed explicitly in analysis, e.g., Leonard [23]. Thus, for most inviscid vortex methods, which are based on using a fixed number of vortex elements with invariant cores, the evolution of large local strains can lead to large errors. For example, a circular patch of vorticity may deform into an elliptical shape with its major axis aligned with the principal direction of strain. If a small fixed number of computational elements is used, they may not be able to accommodate these severe changes. Anderson [38] and Krasny [39], when discretizing non-smooth vorticity, employed a very large core radius so that as vortex elements moved away from each other due to stretch, reasonable overlap could still be maintained to satisfy the requirements for accuracy. One may also be forced to consider schemes of redistributing the vorticity among a different set of elements under conditions of large strain. Similar schemes have been used in methods of contour dynamics to preserve the accuracy of the integration around the vorticity contours (Zabuski and Overman [40]). Krasny [41], in an independent effort, used a similar procedure in simulating the evolution of a vortex sheet by a desingularized Biot-Savart integral.

Vortex methods were extended to numerical simulation of the reacting flow in which the equations governing conservation of scalars were solved using other methods. The application of vortex methods in the calculation of premixed flame has been reported, among others, by Ghoniem et al. [42] and Sethian [43]. In diffusion flames, Ashurst and Barr [44] used the vortex method and an Eulerian flux-corrected transport algorithm to compute the transport of a conserved Shvab-Zeldivich scalar approximating the shape and convolution of the flame in the limit of infinitely fast chemical reactions. Lin and Pratt [45] used the vortex method and a Monte-Carlo method to calculate the time-dependent PDF of the scalar quantities for both gaseous and aqueous mixing layers. Ghoniem and Givi [46] used a vortex/transport element method to investigate the evolution of a spatially-growing constant density mixing layer using a low heat release chemical reaction with an Arrhenius rate expression.

In all the above approaches a fixed number of vortex elements were used for the velocity calculations with the same radially symmetric distribution for all times and the chemistry calculation were done in an Eulerian form. In order to accommodate the strong strain field developing at later times, we will show that other accuracy requirement may necessitate the application of more elaborate vorticity-updating scheme as vortex elements are moved along particle path. Also the fact that the scalar field should be treated in a Lagrangian form since the chemical reaction is truly a Lagrangian process, i.e., it occurs when the particles interact as they flow, motivates the implementation of a Lagrangian method for the simulation of high Reynolds number reacting flows.

Extension of Lagrangian element methods to integrate a scalar conservation equation has been applied to several problem in one dimension.

(Chorin [47], Ghoniem and Oppenhiem [48,49] and Ghoniem Sherman [50]). These schemes were based on using the scalar gradient, in analogy to vorticity, in the transport process. Anderson [38,51] constructed a scheme to solve for a two-dimensional thermal in the inviscid Boussinesq approximation by discretizing the density equation in its vortex form. This was done by casting the equation in gradient form and discretizing the density gradients among elements that could be transported. This scheme, while preserving the advantages of the vortex method, suffer from a major problem: A large strain field, while it may lead to the generation of large gradients, depletes the area of computational elements which are used to transport these gradients.

We have developed the transport element method, a generalized Lagrangian particle scheme which is constructed to compute solution of a convective-diffusive-reactive scalar transport equations. Ghoniem et al. [52] formulated the vortex element method in which the strain field is used to monitor the redistribution of the vorticity field at each time step to overcome the loss of resolution associated with the growth of the distance between neighboring vortex elements. The transport element method was formulated by Ghoniem et al. [53,54] to obtain solutions of the scalar conservation equations at high Reynolds number. This Lagrangian grid-free method is based on generalizing the concepts of the vortex element method to transport the scalar gradients. A conserved version of the transport element method was used to study scalar transport in a spatially-growing shear layer by Ghoniem et al. [53,54] and the results were validated by comparing the numerical solution with the experimental measurements [55]. The method was also used by Heidarinejad and Ghoniem [56] to study the effect of Reynolds and Damkohler number on the burning rate in a non-premixed spatially-growing shear layer, by Ghoniem and Krishnan [57] to study turbulence-combustion

interactions in a temporally-growing premixed shear layer with finite heat release, and by Krishnan and Ghoniem [58] to study the structure of heated jet in a cold environment. A three-dimensional version of the transport element method was developed and applied by Knio and Ghoniem [59] to study the entrainment augmentation due to the streamwise structure in a non-reacting shear layer.

1.3. ORGANIZATION.

In this thesis, we develop the vortex element and transport element methods, and apply them to a temporally-growing and spatially-developing two-dimensional turbulent shear layer. In the temporal shear layer we validate our numerical scheme and study the effect of turbulence on mixing. In the non-reacting spatial shear layer we use the transport of a passive scalar as a tool to validate our results with experimental measurement before mixing transition occurs. In the reacting shear layer we use a low-heat-release chemical reaction to investigate the effect of Reynolds and Damkohler numbers on the mixing rate. We focus our attention on chemical reactions with small heat release, and thus, the density is constant and the reaction rate is an Arrhenius expression.

This thesis is organized as follows. In Chapter 2, the problem is formulated and the governing equations are derived. In Chapter 3, the numerical schemes are derived in detail. In particular, Chapter 3 describes how the scalar gradients are related to the stretch in the flow map and how the initial and boundary conditions are implemented. In Chapter 4, the numerical results of the temporal shear layer are presented. The structure of the eddy under different forcing function is analyzed, and the rate of growth of the perturbation is compared with the results of the linear theory. The

different processes governing mixing, entrainment and diffusion are discussed for a range of Peclet numbers. In Chapter 5, the numerical results describing the structure of the non-reacting spatial shear layer at high Reynolds number are discussed in detail. In Chapter 6, the results describing the structure of the reacting layer and how it is affected by the Reynolds, Damkohler numbers, and other chemical parameters are discussed in detail. Finally, in Chapter 7, presents conclusions and a summary of the results.

Chapter 2

FORMULATION OF THE GOVERNING EQUATIONS

The conservation equations describing a turbulent reacting shear layer at low heat release are summarized in Table I (see Fig. 1 which represents shadowgraphs of a mixing layer selected from the experimental measurements of Brown and Roshko [60]). The chemistry is governed by a single step, second-order, irreversible reaction. The following assumptions are implicit in the model:

(1) The concentrations of the reactants are small;

(2) The heat release is low and does not affect the physical properties or the flow dynamics, so that one can decouple the momentum and energy equations;

(3) The reactants and products behave as perfect gases with equal molecular weights and equal densities;

(4) The transport properties are independent of the temperature and the state of the mixture;

(5) The chemical reaction rate can be expressed in terms of an Arrhenius rate expression; and,

(6) The Mach number is small.

TABLE I. THE GOVERNING EQUATIONS

Chemical reaction

$$F + O \longrightarrow P \qquad (1)$$

Continuity equation

$$\frac{\partial u}{\partial x} + \frac{\partial v}{\partial y} = 0 \qquad (2)$$

Momentum equation

$$\rho \frac{Du}{Dt} = \mu \nabla^2 u - \nabla p \qquad (3)$$

Energy equation

$$\rho c_p \frac{DT}{Dt} = k \nabla^2 T + Q \dot{W} \qquad (4)$$

Reactants conservation equation

$$\rho \frac{Dc_j}{Dt} = \rho D \nabla^2 c_j - \dot{W} \qquad (5)$$

Product conservation equation

$$\rho \frac{Dc_P}{Dt} = \rho D \nabla^2 c_P + \dot{W} \qquad (6)$$

Arrhenius rate expression

$$\dot{W} = A \rho^2 c_O c_F \exp(-\frac{E}{R_g T}) \qquad (7)$$

The definition of the symbols is as follows: t is time, $\mathbf{u}=(u,v)$ is velocity, $\mathbf{x}=(x,y)$ and x and y are the streamwise and the cross-stream directions, respectively, ρ is the density, p is pressure, T is temperature, c_j is the reactant concentration per unit mass with j=F for the "fuel", j=O for the "oxidizer" and c_p is for the products concentration, Q is the enthalpy

of reaction, E is activation energy, R_g is the gas constant, and ∇ and ∇^2 are the gradient and Laplacian operators, respectively. In our analysis the frequency factor A, which is in general a function of temperature, is assumed to be a constant.

In Table II, Eqs. (2)-(8) are rewritten in terms of non-dimensionalized variables represented by the symbol "~". All variables are non-dimensionalized with respect to the following scales or their combinations: the velocity difference of the free streams, $\Delta U=U_1-U_2$, the length scale of the shear layer, L, the free-stream concentration of fuel in the low-speed stream, $c_{F\infty}$, the free-stream temperature of the reactants at x=0, T_∞. The length scale of the shear layer, L, is equal to $\Delta/2$ in the temporal model, and Λ in the spatial model, where Δ is the initial thickness of the layer at time t=0, Λ is a typical eddy size. Note that $\Lambda=2\lambda^*$, and for an unforced layer $\lambda^*=6.6\Delta$, where λ^* is the wavelength of the most unstable perturbation.

TABLE II. THE GOVERNING EQUATIONS

(INTERMEDIATE STEP)

$$\frac{\partial \tilde{u}}{\partial x} + \frac{\partial \tilde{v}}{\partial y} = 0$$

$$\frac{D\tilde{u}}{Dt} = \frac{\nu}{L\ \Delta U} \nabla^2 \tilde{u} - \tilde{\nabla} \tilde{p}$$

$$\frac{D\tilde{T}}{Dt} = \frac{\alpha}{L\ \Delta U} \tilde{\nabla}^2 \tilde{T} + \tilde{W}\ \tilde{Q}$$

$$\frac{D\tilde{c}_j}{Dt} = \frac{D}{L\,\Delta U}\,\nabla^2 \tilde{c} - \dot{W}$$

$$\frac{D\tilde{c}_P}{Dt} = \frac{D}{L\,\Delta U}\,\nabla^2 \tilde{c} + \dot{W}$$

with

$$\dot{W} = A_f\,\tilde{c}_O\,\tilde{c}_F \exp\left(-\frac{T_a}{T}\right)$$

$$A_f = \frac{A\,\rho\,c_{F\infty}\,L}{\Delta U}$$

$$c_p(T_P - T_\infty) = c_{F\infty}\,Q$$

$$\tilde{Q} = \frac{T_P - T_\infty}{T_\infty}$$

$$T_a = \frac{E}{R_g\,T_\infty}$$

In what follows we drop the "~" and write in Table III the non-dimensionalized form of the governing equations in terms of the following dimensionless numbers: Reynolds number $R_e = \Delta U\ L/\nu$, Peclet number $P_e = \Delta U\ L/\alpha$, Lewis number $L_e = \alpha/D$, and Damkohler number $D_a = \tau_{flow}/\tau_{chem}$ with $\tau_{flow} = L/\Delta U$ and $\tau_{chem} = 1/[A\,\rho^2\,c_{F\infty} \exp(-T_a/T_f)]$, where T_f is an average temperature within the

reacting zone, the activation energy $T_a = E/R_g T_\infty$, the frequency factor $A_f = (A \rho c_{F\infty} L)/\Delta U$, and the effective heat release parameter, Q. We note that the Damkohler number can be changed by varying the free stream concentration of the reactant $c_{F\infty}$, the density ρ, or the value of the frequency factor A by employing a catalyst.

TABLE III. THE GOVERNING EQUATIONS

(NON-DIMENSIONALIZED)

$$\frac{\partial u}{\partial x} + \frac{\partial v}{\partial y} = 0 \tag{8}$$

$$\frac{\partial u}{\partial t} + u \cdot \nabla u = -\nabla p + \frac{1}{R_e} \nabla^2 u \tag{9}$$

$$\frac{\partial T}{\partial t} + u \cdot \nabla T = \frac{1}{P_e} \nabla^2 T + Q \dot{W} \tag{10}$$

$$\frac{\partial c_j}{\partial t} + u \cdot \nabla c_j = \frac{1}{P_e L_e} \nabla^2 c_j - \dot{W} \tag{11}$$

$$\frac{\partial c_P}{\partial t} + u \cdot \nabla c_P = \frac{1}{P_e L_e} \nabla^2 c_P + \dot{W} \tag{12}$$

$$\dot{W} = A_f c_O c_F \exp(-\frac{T_a}{T}) \tag{13}$$

Note that the enthalpy of reaction, Q, is non-dimensionalized with respect to $c_p T_\infty / c_{F\infty}$ rather than $c_p T_\infty$, where the former combination make the energy and species conservation equations insensitive to the concentration

of the reactants in a low heat release chemical reaction. In this regard, the non-dimensionalized value of the enthalpy of reaction, $\tilde{Q}$, and the predicted value of the temperature of the product, T_p, are related to the experimental parameters as follows:

$$\tilde{Q} = \frac{c_{F\infty}}{c_p T_\infty} Q$$

$$T_p = 1 + \tilde{Q}$$

Adding more steps to the chemical kinetics scheme will require integrating more species conservation equations to compute the evolution of the intermediate species. Using a chemical kinetics model to describe the reaction may be important in investigating some non-equilibrium phenomena such as ignition, extinction and the formation of tracer species. However, in this work for the sake of economy we will use a single step reaction to obtain a qualitative understanding of the mechanisms governing the intrinsic behavior of the shear layer, and leave the implementation of detailed chemistry to future extensions.

In Fig. 2, in the form of a flow chart, we show how a shear layer can be modelled. In the context of this work, a turbulent shear layer is an unstable shear layer in which pseudo-deterministic large-scale vortex structures, generated as "white" noise amplify within the vorticity layer due to its intrinsic broad-band instability, dominate the dynamics of the field. The results are thus limited to the combined effect of two-dimensional entrainment, molecular diffusion and chemical reaction, and hence the mixing transition is not allowed to affect the flow dynamics. We focus our attention

on chemical reactions with small heat release. Thus, the density is spatially and temporally constant, and the energy and momentum equations are decoupled. We only consider the effects of turbulence on chemistry.

At high heat release, the turbulence-chemistry interaction is expected to affect the flow dynamics through the velocity and vorticity fields generated by the density gradient. This is currently under investigation using the compressible vortex/transport element method (Ghoniem and Krishnan [57]). Moreover, the extra mixing, generated by the extra entrainment attained after transition and the generation of streamwise vorticity structures, is currently analyzed using the three-dimensional version of the transport element method (Knio and Ghoniem [59].

We summarize by noting that the simplest model of a reacting shear layer is governed by six non-dimensional parameters: the Reynolds number, the Prandtl number, the Lewis number, the energy release parameter, the frequency factor and the activation energy. In most cases of gas-phase reactions, one can take $Pr = Le = 1$, and reduce the dependence on the transport properties of the fluid to only the Reynolds number. In this case, the most important diffusion process is that of heat and/or mass and not that of momentum since while momentum diffusion plays a secondary role in the dynamics of the shear layer for values of the Reynolds number exceeding O(1000), diffusion is necessary for molecular mixing and can be the limiting mechanism in determining the mixing rate and thus the burning rate. This issue will be elaborated further in Chapters 4 and 5.

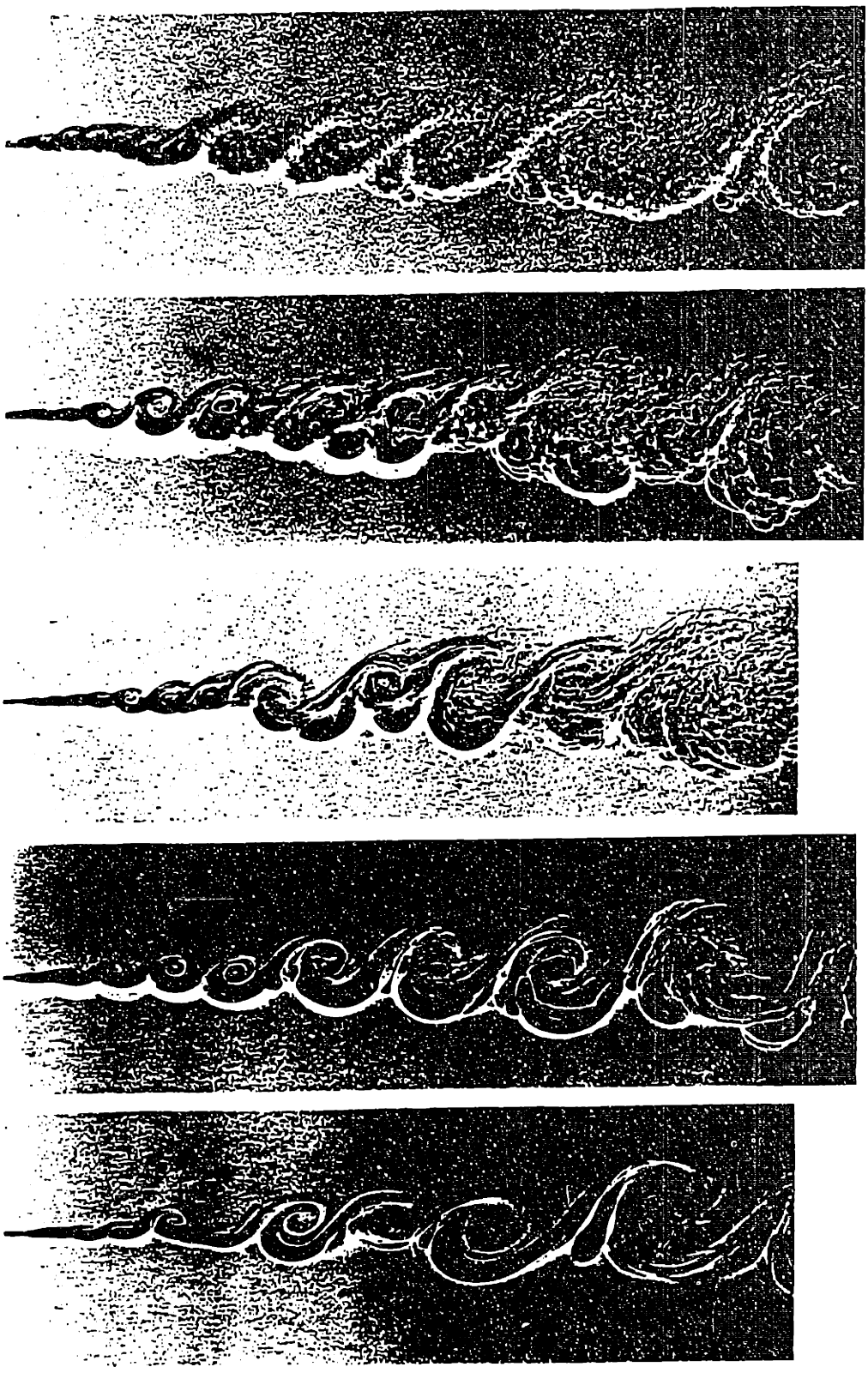

Fig. 1 Effects of Reynolds number. Mixing layers between helium (upper) and nitrogen (lower) with $\rho_2 U_2^2 = \rho_1 U_1^2$. (*a*) Reynolds number is proportional to 8×10 (pressure = 8 atm, $U_1 = 10\,\mathrm{m\,s^{-1}}$); (*b*) 8×5; (*c*) 4×10; (*d*) 4×5; (*e*) 2×10.

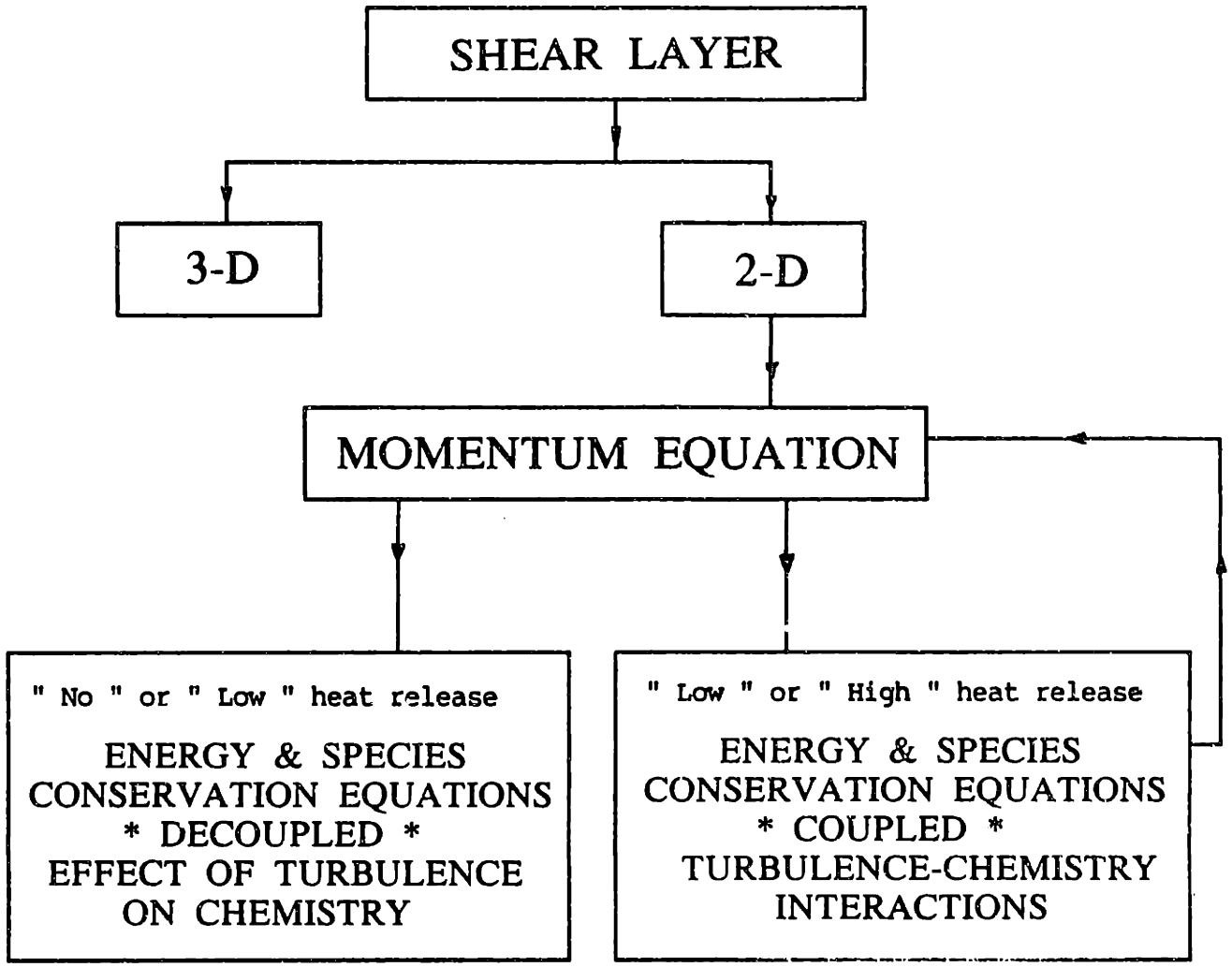

Fig. 2. Different models of a shear layer

Chapter 3

NUMERICAL SCHEMES

We will not solve the governing equations, Eqs. (8)-(12), as expressed in their Eulerian form in terms of the primary gas dynamic variables, the velocity, temperature and species concentrations. Instead, we rewrite Eqs. (8)-(12) in a Lagrangian form in terms of the vorticity, ω, and scalar gradients, g, as follows:

$$\frac{d\omega}{dt} = \frac{1}{R_e} \nabla^2\omega \tag{14}$$

$$\frac{dg}{dt} = - g.\nabla u - g \times \omega + \frac{1}{N_e} \nabla^2 g + \sum_{j=1}^{k+1} \frac{d\dot{W}}{ds_j} \; g_j \tag{15}$$

with

$$u(x) = \int K(x-x') \; \omega(x') \; dx' + u_p(x) \tag{16}$$

$$s(x) = \int \nabla G(x-x') \; . \; g(x') \; dx' + s_p(x) \tag{17}$$

Here, $N_e = P_e$ if s is temperature and $N_e = P_e L_e$ if s is concentration, k is the number of species, $g = \nabla s$, $K = (-\partial G/\partial y, \partial G/\partial x)$, $G(x) = -(1/2\pi) \ln r$ with $r = |x|$ is the Green function of the Poisson equation in an infinite domain, $r^2 = x^2 + y^2$, $dx = dx\,dy$, and $\omega = \omega e_z$ where e_z is the unit vector normal to the x-y plan, and $u_p(x)$ and $s_p(x)$ are components of the velocity and the scalar due to a potential field imposed to satisfy the boundary conditions, respectively. The generic scalar is s with $s=c_O$, c_F, c_P for species equations and $s = T/Q$ for the energy equation, d/dt is the Lagrangian derivative, and $d\dot{W}/ds_j$ is obtained from Eq. (13). Equations (14)-(17) are derived in more detail and are solved numerically using their discrete forms in Sections 3.1

and 3.2. The initial and boundary conditions relevant to the models of the shear layer are discussed in Sections 3.3 and 3.4. The effect of the distortion of the flow map due to the generation of a strong strain field at high Reynolds number, which may cause a deterioration in accuracy in the Lagrangian scheme, is discussed in Section 3.5. The solution we implemented to avoid the deterioration is also presented there.

3.1. THE VORTEX METHOD

Vortex methods are based on the discretization of the vorticity field by a finite number of computational vorticity elements. These element are displaced in a Lagrangian reference frame by the local velocity, $\mathbf{u}$, computed at their centers. The velocity field is decomposed into two components: a divergence-free component, $\mathbf{u}_\omega$, due to the vorticity field, and an irrotational component, $\mathbf{u}_p$, due to the potential field imposed to satisfy the boundary conditions, $\mathbf{u} = \mathbf{u}_\omega + \mathbf{u}_p$ (in accordance with the Hodge decomposition principles, see Batchelor [61] or Chorin and Marsden [62].) The velocity component due to the potential field, $\mathbf{u}_p$, may be incorporated into the calculation by using the image system of the vortex elements constructed to satisfy the no-flow condition due to the solid wall, and flow sources to satisfy the inlet condition upstream, as shown in Section 3.4. The velocity component due to the vorticity field, $\mathbf{u}_\omega$, is discussed in more detail below.

In a Lagrangian reference frame we will solve Eq. (14) in two fractional time steps: convection, which is governed by $d\omega/dt = 0$, and diffusion, which is described by $\partial\omega/\partial t = \nu \nabla^2\omega$. The first step is equivalent to transporting the vorticity elements along the particle path without changing their strength, while during the second step the convective effect is frozen and vorticity is spread due to momentum diffusion.

We start by approximating the initial vorticity field using a set of kernel functions of small support as follows:

$$\omega(\mathbf{x}, 0) = \sum_{j=1}^{N} \Gamma_j \, f_{\delta_j}(\mathbf{x} - \mathbf{X}_j)$$

where Γ is the strength of a vortex element, or its circulation, f_δ is the core function describing the shape of the vorticity distribution associated with an element, $\mathbf{X}$ is the initial location of the center of the vortex element, and δ is a measure of the spread of the vorticity field around its center known as the core radius. Details of how to select Γ, f_δ, and δ are discussed in Section 3.3. We consider an inviscid flow and solve for the first fractional step. Considering a vortex element with strength Γ located at the origin of the system of coordinates in a domain with no boundary, we first show how to compute its induced velocity field. We introduce the stream function, Ψ, to relate the velocity in its polar coordinate, $\mathbf{u}_\omega=(v_r,v_\theta)$, or Cartesian coordinate, $\mathbf{u}_\omega=(u,v)$, and the vorticity, ω, as follows:

$$u = \frac{\partial \Psi}{\partial y} \quad \text{and} \quad v = -\frac{\partial \Psi}{\partial x}$$

or (18a)

$$v_r = \frac{1}{r}\frac{\partial \Psi}{\partial \theta} \quad \text{and} \quad v_\theta = -\frac{\partial \Psi}{\partial r}$$

while

$$\omega = \frac{\partial v}{\partial x} - \frac{\partial u}{\partial y} = \frac{\partial v_\theta}{\partial r} \quad \frac{1}{r}\frac{\partial v_r}{\partial \theta} \qquad (18b)$$

Introducing Eqs. (18a) into (18b) and writing the results in polar coordinates, we get:

$$-\omega = \nabla^2\Psi = \frac{1}{r}\frac{\partial}{\partial r}\left(r\frac{\partial \Psi}{\partial r}\right) + \frac{1}{r^2}\frac{\partial^2 \Psi}{\partial \theta^2} \tag{19}$$

For the radially symmetric distribution of vorticity associated with a single element, $\partial/\partial\theta = 0$, and we can integrate Eq. (19) to obtain for v_θ:

$$v_\theta = \frac{1}{2\pi r}\int_0^r \omega\,(2\pi r)\,dr \tag{20}$$

Substituting for the vorticity field, ω, in terms of the strength of each element, Γ, and the core function, f_δ, that is $\omega = \Gamma f_\delta$, we get:

$$v_\theta = -\frac{\Gamma}{2\pi r}\,K_\delta(r) \tag{21}$$

with

$$K_\delta(r) = 2\pi \int_0^r r'\, f_\delta(r')\,dr'$$

or

$$u_\omega = (u,v) = -\frac{\Gamma}{2\pi}\,\frac{(-y,x)}{r^2}\,K_\delta(r) \tag{22}$$

with

$$r^2 = x^2 + y^2$$

The negative sign in the front of Eqs. (21) and (22) is due to the convention that counterclockwise circulation is positive. For a point vortex the core function is a delta function, that is $\kappa_\delta = 1$, and the velocity approaches infinity at the center of the vortex. This gives rise to numerical instability as two neighboring elements become very close to each other. To remove this instability and improve the accuracy of discretization of the vorticity field into finite elements, we use a second-order Gaussian core function described by:

$$f_\delta = \frac{1}{\pi \delta^2} \exp(-\frac{r^2}{\delta^2})$$

which gives a continuous and smooth distribution for the vorticity and velocity and their derivatives. Introducing the second-order Gaussian core into Eq. (22) we get:

$$u_\omega = (u,v)_\omega = -\frac{\Gamma}{2\pi} \frac{(-y,x)}{r^2} [1 - \exp(-\frac{r^2}{\delta^2})] \qquad (23)$$

In the second fractional step we include the momentum diffusion effect by freezing the motion and solving the equation $\partial\omega/\partial t = \nu \nabla^2\omega$ for a vorticity element defined by

$$\omega(r) = \frac{\Gamma}{\pi \delta^2} \exp(-\frac{r^2}{\delta^2})$$

and $\delta = \delta(t)$. The solution of this equation satisfies the equation $d(\delta^2)/dt = 4\nu$. Integrating and using the initial condition that $\delta(0) = \delta_0$, we get:

$$\delta^2 = \delta_0^2 + 4 \nu t.$$

Now we write the discretized form of the equations describing the vorticity and velocity fields in a two-dimensional incompressible flow as a summation of the contributions of all computational elements within the domain, as follows:

$$\omega(x,t) = \sum_{i=1}^{N} \Gamma_i \, f_\delta(x-\chi_i(t)) \tag{24}$$

$$u_\omega(x,t) = \sum_{i=1}^{N} \Gamma_i \, K_\delta(x-\chi_i(t)) \tag{25}$$

with

$$K_\delta(x) = -\frac{(y-y_i),-(x-x_i)}{r_i^2} \kappa_\delta(r_i)$$

$$r_i^2 = (x-x_i)^2 + (y-y_i)^2$$

where f_δ and κ_δ have been defined before and subscript "i" refers to the center of the ith element located at (x_i,y_i), (x,y) being an arbitrary point.

The second component of the velocity, u_p, which is added to satisfy the boundary conditions, will be discussed in Section 3.4.

Knowing the velocity at the center of the vortex element, u_j, we may update its location, χ_j, each time step, using $d\chi_j/dt = u_j(\chi_j,t)$ as follows:

$$X_j(X_j,\ t+\Delta t) = X_j(X_j,t) + \Sigma_2 u_j(X_{j2})\ \Delta t$$

where Σ_2 is a second-order time-integration scheme, $X_j(X_j\ 0)=X_j$, X_j being the location of the element at time t=0.

3.2. THE TRANSPORT ELEMENT METHOD

In most shear flows, scalar gradients occupy a much smaller portion of the flow field that occupied by the scalar itself. Therefore, it ought to be more efficient to use the gradient of the scalar as the main variable in the computational scheme. Moreover, to avoid the non-linearity of the convective terms as in the vortex method, and to be compatible with the Lagrangian nature of a chemical reaction in flowing system, the basic concepts of the vortex element method are expected to obtain solutions for the energy and species conservation equations. For a given scalar distribution, s(x,t), at time t=0 there is a corresponding scalar gradient distribution $g(x,0) = \nabla s$. In the initialization procedure which is discussed in the next section, the initial scalar gradient distribution is used to calculate the initial strength of the transport element, $\Delta g_i = g(X_i,0)\ \delta A_i$ where δA_i is the area of the material element associated with this element (Δg in scalar transport is equivalent to Γ in vorticity transport). The strength of each transport element, Δg, together with its core function, f_δ, and the core radius, δ, describe the scalar gradient field as follows:

$$g(x,0) = \nabla s(x,0) = \sum_{j=1}^{N} \Delta g_j(0)\ f_\delta(x - X_j) \qquad (26)$$

where f_δ and δ are defined previously and are in general different than those used for the vortex elements. In what follows, we drive the equations governing conservation of scalar, s, in terms of its gradient, $g = \nabla s$, and solve the scalar transport equation, Eq. (15), numerically in three fractional steps, namely convection, diffusion, and reaction. We start with a non-diffusive, non-reactive flow in which the governing equation for the scalar, s, is as follows:

$$\frac{ds}{dt} = \frac{\partial s}{\partial t} + u \cdot \nabla s = 0 \qquad (27)$$

We take the gradient of Eq. (27), and drive the equations relating the scalar, s, to its gradient, $g = \nabla s$, at later time. This is done by taking the gradient of Eq. (27),

$$\frac{dg}{dt} = - g \times \nabla u - g \times \omega \qquad (28)$$

using the identity $\nabla \times g = 0$. In the early stages of this research we wrote Eq. (28) in terms of its components:

$$\frac{dp}{dt} = - \frac{\partial u}{\partial x} p - \frac{\partial v}{\partial x} q \qquad (29a)$$

$$\frac{dq}{dt} = - \frac{\partial u}{\partial y} p - \frac{\partial v}{\partial y} q \qquad (29b)$$

where g=(p,q) and p and q are the x and y components of the gradients, and integrated these equations along particle paths to find the evolution of the gradients at later time. For this purpose, we used the following initial conditions: $p(x,0) = ds(x,0)/dx$ and $q(x,0) = ds(x,0)/dy$, which were known from

Eq. (26), and the derivatives of the velocity field, which were obtained by analytically differentiating the velocity field (these expressions are presented in Table IV in Section 3.4.1).

The scalar concentration can be recovered from the scalar gradients as follows. Since $g = \nabla s$, by taking the divergence we get:

$$\nabla^2 s = \nabla \cdot g$$

The solution of this equation in an infinite domain can be written as:

$$s(x) = - \int \nabla.g \; G(x - x') \, dx'$$

Integrating by parts, we get:

$$s(x) = \int g(x) \cdot \nabla G(x - x') \, dx' \qquad (30a)$$

Extending the concept of the Hodge decomposition of a velocity field to the scalar computation, an extra component, s_p, can be imposed to satisfy the boundary condition as follows:

$$s(x) = \int g(x) \cdot \nabla G(x - x') \, dx' + s_p(x) \qquad (30b)$$

The evaluation of s_p for a confined flow is presented in Section 3.4. Introducing the scalar gradient distribution, $g(x)$, from Eq. (26) into the Eq. (30), and using a second order Gaussian core to smooth the distribution of g around the center of the element, we calculate the value of the scalar as follows:

$$s(x,t) = \sum_{j=1}^{N} \left(p_j \frac{\partial G_j}{\partial x} + q_j \frac{\partial G_j}{\partial y} \right) \left[1-\exp\left(-\frac{r_j^2}{\delta_j^2}\right)\right] + s_p(x) \quad (31)$$

where

$$\frac{\partial G_j}{\partial x} = \frac{1}{2\pi} \frac{\Delta x_j}{r_j^2} \quad , \quad \frac{\partial G_j}{\partial y} = \frac{1}{2\pi} \frac{\Delta y_j}{r_j^2}$$

$$r_j^2 = (\Delta x_j)^2 + (\Delta y_j)^2$$

However the numerical results showed that this initial version of the transport element method suffers from the following problems:

(1) It is computationally expensive since the gradients of the velocity vector must be computed at each time step;

(2) The strong strain field which develops at later times negatively affects the estimation of the velocity gradient ∇u. As we will show in Section 3.5, a vortex method which uses a fixed number of vortex elements loses resolution at the later stages of the flow;

(3) Eqs. (29) or (28) are stiff and there is an error associated with the integration method.

The above sources of error lead to a slight deviation of the calculated scalars from their free stream values the later times, and, to a lesser extent, within the convoluted eddy. Hence it was concluded that the method did not conserve the thermal energy within the domain and could not be used to compute the evolution of a conserved scalar accurately.

Later we developed and applied a conservative version of the transport element method by relating the scalar gradients to the flow map. In this version, the material line that lies on the surface of constant s at time t = 0, δl, is related to the gradient of scalar at the same point, g, as follows. Let $g = |g|\, n$ where $n = g / |g|$ is the unit vector in the direction of gradient. We have:

$$\frac{d\,(\,|g|^2)}{dt} = 2\,|g|\,\frac{d(|g|)}{dt} = \frac{d}{dt}\,(\,g\,.\,g\,) = 2\,g\,.\,\frac{dg}{dt}$$

which implies that

$$\frac{d\,(|g|)}{dt} = n\,.\,\frac{dg}{dt} \qquad (32)$$

Expanding dg/dt, we get:

$$\frac{dg}{dt} = \frac{d}{dt}(\,|g|\,n\,) = |g|\,\frac{dn}{dt} + n\,\frac{d(\,|g|\,)}{dt} \qquad (33)$$

Now, combining Eqs. (28), (32) and (33), we obtain:

$$|g|\,\frac{dn}{dt} + (n.(\,-g.\nabla u - g \times \omega))n = -g.\nabla u - g \times \omega \qquad (34)$$

and by dividing by $|g|$ and noting that $n.(g \times \omega) = 0$ we get:

$$\frac{dn}{dt} = -\,n.\nabla u - n \times \omega + (\,n\,.\,(\,n.\nabla u\,))\,n \qquad (35)$$

substituting the expression for dn/dt from (35) into (33) we get:

$$\frac{d|g|}{dt} = -\,(\,n\,.(\,-n.\nabla u\,))\,|g| \qquad (36)$$

Equation (36) states that although the value of the scalar itself is invariant along the material path, the magnitude of its gradient changes according to the change of its direction and the stretch of the flow map. In what follows we relate $d|g|/dt$ to the stretching of a material element, δl, initially lying in the direction normal to the scalar gradient, g. The variation of δl is governed by the equation:

$$\frac{d(\delta l)}{dt} = \delta l \,.\, \nabla u \qquad (37)$$

If δl is chosen to lie on a surface of constant s at time $t=0$, then the equation $ds/dt = 0$ implies that it will always remain on this surface. If n' denotes the unit vector in the direction of δl, then $n.n' = 0$ at any time. We may write $\delta l = |\delta l|\ n'$, and follow a similar procedure to derive a differential equation for the change of δl with time. After some algebra we get:

$$\frac{d|\,\delta l\,|}{dt} = (\,n'.(\,n'.\nabla u\,))\,|\,\delta l\,| \qquad (38)$$

Comparing Eqs. (36) and (38) and noting that $n.(n.\nabla u) = -\,n'.(n'.\nabla u)$, we arrive at the following important conclusion which relates the stretch of the iso-scalar lines to the scalar gradient:

$$\frac{g}{\delta l} = \text{constant} \qquad (39)$$

See Fig. 3 for a physical interpretation of this expression.

If the initial jump of the scalar value across an element is $\delta s_i = s_2 - s_1$, we may calculate the strength of each transport elements as follows:

$$\Delta g_i(t) = \left[\frac{\partial s}{\partial n} \delta l \, \delta n(t) \right]_i = \delta s_i \, \delta l_i \, n_i(t) \qquad (40)$$

where $\delta l_i = |\delta l_i|$, $(\partial s/\partial n)_i \sim (\delta s_i/\delta n_i)$, and δl_i and $n_i(t)$ are measured along the mesh sides. See Fig. 4 for a physical interpretation of the expression. Combining Eqs. (26), (40) and (30), we can calculate the scalar field in a two-dimensional incompressible flow as a summation of the contributions of all the computational elements in a domain without boundaries as

$$s(x,t) = \sum_{i=1}^{N} \Delta g_i(t) \cdot \frac{(x-x_i),(y-y_i)}{r_i^2} \, K_\delta(r_i) \qquad (41)$$

where r_i and K_δ are defined as before.

To obtain a solution for the convective-diffusive-reactive equation, Eq. (15), we follow the same procedure used for vorticity, ω. Equation (15) is solved in three fractional steps: convection by transporting the elements along particle path and changing their strength according to Eq. (40), diffusion, and reaction. The effect of scalar diffusion is implemented by expanding the core radius according to:

$$\delta^2 = \delta_0^2 + 4\alpha t \qquad (42)$$

The third fractional step in solving Eq. (15) involves the chemical source terms. We start by considering the effect of the source term in the

scalar conservation equation, $ds/dt = \dot{W}$, while the convection and diffusion effects are frozen, and take the variation of both sides:

$$\delta \left\{ \frac{ds_i}{dt} = \dot{W}_i(s_j) \right\} \quad j = 1,k+1 \quad \text{for } i = 1,N$$

which yields

$$\frac{d(\delta s_i)}{dt} = \sum_{j=1}^{k+1} \frac{\partial \dot{W}}{\partial s_j} \quad (\delta s_j)_i \qquad (43)$$

where k is the number of reactants.

The application of the transport element method to the low heat release reacting shear layer proceeds according to the following steps:

(1) Calculate the velocity at the center of each transport element and move the elements to new locations using the equations presented in Section 2-4;

(2) Calculate the new strength of the element using Eq. (40);

(3) Include the effect of diffusion by expanding the core radius of each element using Eq. (42);

(4) Calculate the scalar value at the center of each transport element using Eq. (41);

(5) Update the scalar variation, δs, associated with each transport element using Eq. (43).

3.3. INITIAL CONDITIONS

The free shear layer is shown in Fig. 5. The initial vorticity distribution across a free shear layer with free stream velocities U_1 and U_2 can be represented by a second-order Gaussian:

$$\Omega(y)=\left(\frac{\Delta U}{\sigma\sqrt{2\pi}}\right)\exp\left(-\frac{Y^2}{2\sigma^2}\right) \qquad (44)$$

where σ is the standard deviation of the Gaussian distribution and $\Delta U=U_1-U_2$. Note that the initial shear layer vorticity thickness is $\Delta=2\sqrt{2}\sigma$. The corresponding velocity distribution is:

$$U(y) = U_M+ \left(\frac{\Delta U}{2}\right)\operatorname{erf}\left(\frac{Y}{\sigma}\right) \qquad (45)$$

where U(y) is the streamwise velocity, $U_M=0.5(U_1+U_2)$, and

$$\operatorname{erf}(x) = \frac{2}{\sqrt{\pi}}\int_0^x \exp(-t^2)dt$$

is the error function.

To start the computation, the initial vorticity is discretized among computational elements located on N_y layers stacked in the y-direction within the zone where $|\Omega|>0$, and separated by a distance h in the x-direction (see Fig. 6). These elements are used in the transport process as described in Sections 3.1 and 3.2. Each element is characterized by a core radius, δ, a core function, f_δ, and its strength, Γ. The strength Γ_j, for each element can be defined by either of the following two expressions:

$$\Gamma_j = \int_{\delta A_j} \omega \, dA$$

or

$$\Gamma_j = \omega(X_j)\ \delta A_j$$

where X_j is the center of the original mesh, and δA_j is the material area surrounding it. In order to determine the initial locations of the centers of the elements, y_i, and their strengths, Γ_i, $i=1,N_y$, we define an error index, E_Ω, as follows:

$$E_\Omega = \int_{-\infty}^{+\infty} |\Omega(y)-\omega(y)|dy \qquad \text{for any } x$$

where $\Omega(y)$ and $\omega(y)$ are the exact and discretized vorticity distributions. The following initialization procedures were tried:

(1) Fix the locations of the center of elements, y_i, and use a least-squares method to minimize the quantity H, defined as:

$$H = \int_{-\infty}^{+\infty} [\ \Omega(y) - \sum_{j=1}^{N_y} \Gamma_j\ f_\delta]^2\ dy\ + a\ [\ \sum_{j=1}^{N_y} \Gamma_j - \int_{-\infty}^{+\infty} \Omega(y)\ dy\ ]$$

where a is a Lagrange multiplier and N_y is the number of layers. Minimizing H with respect to Γ_j and a yields simultaneous equations for Γ_j and a. After solving the equations for Γ_j, we calculate the error index E_Ω to check the accuracy of the results;

(2) Fix the strength of the elements, Γ_i, and minimize the quantity H with respect to y_j and a, and after solving the resulting equations for y_j, check the error index E_Ω; and

(3) Fix the location of the centers, y_i, and calculate the strengths of elements, Γ_i, by solving the following system of equations;

$$\Omega(y_j) = \sum_{i=1}^{N} \Gamma_i \, f_\delta(y_i - y_j) \quad \text{where} \quad j=1,N \tag{46}$$

The values of y_i should be chosen to minimize E_Ω.

The first and second approaches are consistent with the definitions of Γ used by Del-Prete and Hald [31]. The third approach is consistent with the definition of Γ used by Beale and Majda [24]. The numerical experiments by Perlman [36] show that the initialization based on the second definition of Γ can provide higher order accuracy. Among the approaches just mentioned, we have found that the third one, which amounts to a collocation technique, to be the most accurate.

For an accurate initialization, strong overlap between the neighboring vortex elements must be allowed, i.e., δ must be larger than h. Moreover, h must be varied until the error index, E_Ω, falls below the accuracy of the machine, say 10^{-6}, which is the maximum permissible error in our initialization procedure. Numerical experiments show that if strong overlap is not imposed the error index increases rapidly as δ/h decreases below 1. Thus, the overlap between neighboring elements is necessary for accurate discretization of the initial vorticity field. This is consistent with the convergence theory of vortex methods [24-25,30-33] It also rules out point vortices as an accurate means of representing a vorticity field.

To measure the effect of the accuracy of the initial discretization of vorticity among vortex elements on the flow field for short time, we used the numerical simulation to calculate the rate of growth of a perturbation in a temporal shear layer. This values was then compared with the growth rate based on the eigensolution of the linearized form of the governing equation within the initial stages, the Rayleigh equation. Details of the linear

theory, calculations of the growth rate and comparisons are presented in Chapter 3.

In the calculation of a spatial shear layer, we use the same vorticity distribution as that of an unperturbed shear layer for the newly introduced elements at the tip of the splitter plate. We then apply Eq. (46) to discretize the incoming vorticity among new vortex elements. First, we fix the minimum number of layers to meet our initialization accuracy requirement. Then, by discretizing the incoming vorticity field on the square mesh we calculate the side of mesh in the streamwise direction. During a time step, Δt, each layer has moved away from the inlet section, and a gap is created between the end of the layer and inlet section which should be filled with the new elements. Based on this gap and the side of each element, we introduce the necessary number of elements to satisfy the conservation of vorticity.

For calculation of the scalar, $U(y)$ and $\Omega(y)$ are replaced with the scalar, s, and its gradient, $g=\nabla s$, respectively. In the temporal model, we compute the evolution of a thermally stratified shear layer in which temperature is passively transported. In the non-reacting spatial shear layer, the scalar is the concentration of a species diluted in an inert base flow and introduced in the slow stream. In the reacting shear layer we introduce the reactants on the opposite sides of the splitter plate in the high-speed and low-speed streams, as shown in Fig. 7, with a normalized error function distribution:

$$\frac{C_F}{C_{F\infty}} = 0.5\ [1+\mathrm{erf}(\frac{Y-0.5}{\sigma}) \quad , \quad \frac{C_O}{C_{F\infty}} = Y\ \frac{C_F}{C_{F\infty}}$$

where $Y=c_{O\infty}/c_{F\infty}$ is the reactants ratio and $c_{O\infty}$ and $c_{F\infty}$ are the free stream values of the reactants. The same elements, or particles, are used to transport the vorticity and scalar gradients.

In the simulations, the shear layer is discretized among eleven or thirteen layers of computational elements in the temporal model, and five or seven layers for the non-reacting and reacting spatial models respectively. The top and bottom layers are added to capture the extra gradients which develop downstream as the shear layer grows in the cross stream direction. The total number of elements is kept at an affordable level, usually below 5000.

3.4. BOUNDARY CONDITIONS

A turbulent shear layer represents a smoothing of a discontinuity formed between two parallel, semi-infinite streams having different properties when brought together. The two streams are initially separated by a splitter plate, which generates two boundary layers as a result of no-slip condition on both side of the plate. By the "mixing layer" we refer to the region after which the wake resulting from the merging of the two boundary layers has developed a monotonic velocity distribution. The highly unstable nature of the shear layer (due to the Kelvin-Helmholtz instability mechanism) provides a mechanism for the growth of small perturbations and formation of large scale structures. These structures, in general, move downstream with the mean velocity of the flow, U_M. By the mechanism of the subharmonic instability, each two, or occasionally three, neighboring structures undergo pairing, forming larger structures and maintaining the periodicity of the flow.

In the spatial shear layer, the computational domain is attached to the laboratory reference frame and is confined by the solid walls on the top and

bottom. The inlet conditions on the left-hand side are well-defined. The exit conditions on the right-hand side are, however, not so well defined. In most cases, they are time-dependent since the flow requires a long distance downstream to reach a fully developed state where a well defined, steady boundary condition can be imposed. Practically, in order to limit the computational effort, one is forced to delete the computational elements at a specified section, X_{max}, without including the effect of the deleted field explicitly in the form of a boundary condition [15]. As we shall see later, we employ a conformal transformation and solve for the potential component in a free space without requiring an explicit boundary condition at the exit section.

In our temporal shear layer model, the length of the computational domain is limited to the size of one or few large scale structures. In this case, we deal with a moving computational domain related to the stationary reference frame via a Galilean transformation involving the mean velocity U_M, and the boundary conditions are periodic on both sides of the domain.

The two solutions based on the temporal and spatial shear layer are equivalent if the following conditions are met:

(1) The mean velocity, $U_M = (U_1+U_2)$, is constant; and

(2) The velocities of the two streams are close to each other, that is $(u_1-U2)/(U_1+U_2)<<1$. The latter restriction, known as the Taylor hypothesis, states that there is an auto-correlation between the two solutions if:

$$\frac{\partial}{\partial t} = - U_M \frac{\partial}{\partial x}$$

Otherwise, there are some qualitative differences between the two solutions since the governing equations are parabolic in time and elliptic in space. In

a spatial shear layer, an event which occurs downstream of the splitter plate induces a change in velocity everywhere in the flow, including upstream, whereas for the temporal shear layer an event is clearly unable to affect the previous development of the flow. In addition, unlike the temporal shear layer, in the spatial shear layer the amounts of fluid entrained from each stream are different because of the asymmetry of the inlet boundary condition. More on this issue, the asymmetric entrainment, will be presented in Chapters 5 and 6.

The temporal shear layer is mathematically well defined when periodic boundary conditions are used. However, due to the limitation of the Taylor hypothesis, which is another manifestation of the periodic boundary condition, the velocity difference does not play any role in the dynamics. In principle, this model should only give qualitative insight into the physics of the governing processes rather than quantitative information which can be compared with experimental measurements. We found that the temporal shear layer is more accurate than expected, and as we will show later, its results strongly resemble the experiment measurements.

3.4.1. THE TEMPORAL SHEAR LAYER

The temporal shear layer is shown in Fig. 5. In this work, this model is used as a test problem to validate the numerical scheme in the early stages of development and to study the dynamics in the non-linear range. To derive an expression for u_p in this case, we start with a single vortex element located at (x_k,y_k) within the computational domain and apply Eq. (23) to calculate the total velocity, (u,v), induced by the element and its infinite number of periodic images (not a mirror image) in both sides of the domain, at an arbitrary point, x(x,y), as follows:

$$u(x,y) = -\frac{\Gamma}{2\pi} \sum_{-\infty}^{+\infty} \{ [\frac{(y-y_k),\ -[x-(x_k+k\lambda)]}{r_k^2}] [1 - \exp(-\frac{r_k^2}{\delta_k^2})] \}$$

where

$$r_k^2 = (y - y_k)^2 + [x - (x_k + k\lambda)]^2$$

The expression for velocity can be decomposed into two parts:

$$u(x,y) = \frac{\Gamma}{2\pi} \{ - \sum_{-\infty}^{+\infty} \frac{(y-y_k),\ -[x-(x_k+k\lambda)]}{r_k^2} +$$

$$\sum_{-\infty}^{+\infty} \frac{(y-y_k),\ -[x-(x_k+k\lambda)]}{r_k^2} \exp(-\frac{r_k^2}{\delta_k^2}) \}$$

There is a closed form for the first summation, and because we deal with a fast decaying function in the second case, and since $\delta << \lambda$, the effect of the cores is included only for the nearest sister vortices (k=-1,0,1). Therefore:

$$u(x,y) = \frac{\Gamma}{2\pi} \{ \frac{\pi}{\lambda} \frac{-\sinh(\frac{2\pi\ \Delta y}{\lambda}),\sin(\frac{2\pi\ \Delta x}{\lambda})}{\cosh(\frac{2\pi\ \Delta y}{\lambda})-\cos(\frac{2\pi\ \Delta x}{\lambda})} + \sum_{k=0}^{\pm 1} \exp(-\frac{r_k^2}{\delta_k^2}) \}$$

$$\sum_{k=0}^{\pm 1} \frac{(y-y_k),\ -[x-(x-(x_k+k\lambda)]}{r_k^2} \exp(-\frac{r_k^2}{\delta_k^2}) \} \qquad (47)$$

Now we consider N elements within the computational domain, and apply Eq. (47) to calculate the total velocity induced at an arbitrary point (x,y). Thus, we obtain:

$$u(x,y) = \sum_{j=1}^{N} \frac{\Gamma_j}{2\pi} \left\{ \frac{\pi}{\lambda} \frac{-\sinh\left(\frac{2\pi\,\Delta y_j}{\lambda}\right),\ \sin\left(\frac{2\pi\,\Delta x_j}{\lambda}\right)}{\cosh\left(\frac{2\pi\,\Delta y_j}{\lambda}\right) - \cos\left(\frac{2\pi\,\Delta x_j}{\lambda}\right)} + \sum_{k=0}^{\pm 1} \frac{\Delta y_j,\ -(\Delta x_j)_k}{(r_j^2)_k} \exp\left(-\frac{(r_j^2)_k}{(\delta_j^2)}\right) \right\} \qquad (48)$$

with

$$\Delta x_j = x - x_j$$

$$\Delta y_j = y - y_j$$

$$(\Delta x_j)_k = x - (x_j + k\lambda)$$

$$(r_j^2)_k = (\Delta x_j^2)_k + \Delta y_j^2$$

In what follows we use Eq. (48) to drive the derivatives of the velocity expression for a temporal model. These derivatives, which are needed in calculation of the scalar value using Eq. (29), are presented in Table IV.

Table IV.

Derivatives of the velocity expressions

for a temporal shear layer

$$\frac{\partial u(x,y)}{\partial x} = \sum_{j=1}^{N} \left\{ \frac{\Gamma_j \pi}{\lambda^2} \frac{\sin\left(\frac{2\pi \Delta x_j}{\lambda}\right) \sinh\left(\frac{2\pi \Delta y_j}{\lambda}\right)}{\left[\cosh\left(\frac{2\pi \Delta y_j}{\lambda}\right) - \cos\left(\frac{2\pi \Delta x_j}{\lambda}\right)\right]^2} + \right.$$

$$\left. \left[\frac{\Gamma_j}{\pi} \sum_{k=0}^{\pm 1} \frac{-(\Delta y_j)(\Delta x_j)_k}{(r_j)_k^2} \left(\frac{1}{(r_j)_k^2} - \frac{1}{(\delta_j)^2} \right) \right] \exp\left(-\frac{(r_j)_k^2}{(\delta_j)^2}\right) \right] \right\}$$

$$\frac{\partial u(x,y)}{\partial y} = \sum_{j=1}^{N} \left\{ \frac{-\Gamma_j \pi}{\lambda^2} \frac{1 - \cos\left(\frac{2\pi \Delta x}{\lambda}\right) \cosh\left(\frac{2\pi \Delta y}{\lambda}\right)}{\left[\cosh\left(\frac{2\pi \Delta y_j}{\lambda}\right) - \cos\left(\frac{2\pi \Delta x_j}{\lambda}\right)\right]^2} + \right.$$

$$\left. \left[\frac{\Gamma_j}{2\pi} \sum_{k=0}^{\pm 1} \frac{1}{(r_j)_k^2} \left(\frac{(\Delta x_j)_k^2 - (\Delta y)_j^2}{(r_j)_k^2} - 2 \frac{(\Delta y_j)^2}{(\delta_j)^2} \right) \exp\left(-\frac{(r_j)_k^2}{(\delta_j)^2}\right) \right] \right\}$$

$$\frac{\partial v(x,y)}{\partial x} = \sum_{j=1}^{N} \left\{ \frac{+\Gamma_j \pi}{\lambda^2} \frac{\cos\left(\frac{2\pi \Delta x_j}{\lambda}\right) \cosh\left(\frac{2\pi \Delta y_j}{\lambda}\right) - 1}{\left[\cosh\left(\frac{2\pi \Delta y_j}{\lambda}\right) - \cos\left(\frac{2\pi \Delta x_j}{\lambda}\right)\right]^2} + \right.$$

$$\left. \left[\frac{-\Gamma_j}{2\pi} \sum_{k=0}^{\pm 1} \frac{1}{(r_j)_k^2} \left(\frac{(\Delta y_j)^2 - (\Delta x_j)_k^2}{(r_j)_k^2} - 2 \frac{(\Delta x_j)_k^2}{(\delta_j)^2} \right) \exp\left(-\frac{(r_j)_k^2}{(\delta_j)^2}\right) \right] \right\}$$

$$\frac{\partial v(x,y)}{\partial y} = \sum_{j=1}^{N} \left\{ \frac{-\Gamma_j \pi}{\lambda^2} \frac{\sin\left(\frac{2\pi \Delta x_j}{\lambda}\right) \sinh\left(\frac{2\pi \Delta y_j}{\lambda}\right)}{\left[\cosh\left(\frac{2\pi \Delta y_j}{\lambda}\right) - \cos\left(\frac{2\pi \Delta x_j}{\lambda}\right)\right]^2} + \right.$$

$$\left. \frac{\Gamma_j}{\pi} \sum_{k=0}^{\pm 1} \frac{(\Delta x_j)_k (\Delta x_j)}{(r_j)_k^2} \left(\frac{1}{(r_j)_k^2} + \frac{1}{(\delta_j)^2} \right) \right] \exp\left(-\frac{(r_j)_k^2}{(\delta_j)^2}\right) \Bigg] \Bigg\}$$

The same procedure used for the velocity calculation can be employed to drive the corresponding expression for the scalar s:

$$s(x,y) = \sum_{j=1}^{N} \left\{ \frac{\pi}{\lambda} \frac{\frac{p_j}{2\pi} \sin\left(\frac{2\pi \Delta x_j}{\lambda}\right) + \frac{q_j}{2\pi} \sinh\left(\frac{2\pi \Delta y_j}{\lambda}\right)}{\cosh\left(\frac{2\pi \Delta y_j}{\lambda}\right) - \cos\left(\frac{2\pi \Delta x_j}{\lambda}\right)} + \right.$$

$$\left. \sum_{k=0}^{\pm 1} \frac{p_j (\Delta x_j)_k, \; q_j \Delta y_j}{(r_j^2)_k} \exp\left(-\frac{(r_j^2)_k}{(\delta_j)^2}\right) \right] \Bigg\} \qquad (49)$$

where $p = ds/dx$ and $q = ds/dy$ are the scalar gradients in x and y direction, and Δx_j, Δx_j, $(\Delta y_j)_k$, and $(r_j^2)_k$ are defined as before. The strengths of the transport elements (p,q) can be updated using either Eq. (29) or Eq. (40).

3.4.2. THE SPATIAL SHEAR LAYER

A spatial, confined shear layer is shown in Fig. 7. Since in our calculations the vorticity layer initially coincides with the layer of finite

scalar gradients, the same set of elements is used to transport the vorticity and the scalar gradients. Since the Reynolds number is high, the growth of the boundary layers on the confining walls is neglected. The computational elements are deleted at the exit plane. This introduces a perturbation upstream and ensures that the roll up and at least the first pairing will take place within the domain. Since this perturbation is not applied in an organized manner, the resulting shear layer will be considered as an unforced layer.

As already mentioned, in order to avoid addressing the issue of the exit boundary condition explicitly, and to obtain the potential components u_p and s_p in closed form, we invoke a Schwarz-Christoffel transform [63] to map the two-dimensional physical plane $z = x + i\ y$, onto the upper half of the computational plane, $\zeta = \xi + i\ \eta$, using:

$$F(\zeta) = \pi\left(\zeta - \frac{1}{\zeta}\right) \tag{50}$$

$$\zeta = \pm \sqrt{\exp(2\pi z)+1} \tag{51}$$

where z is normalized with respect to the length scale Λ; "+" is used for $y<0.5$ and "-" is used for $y>0.5$ and $F(\zeta)=d\zeta/dz$ (see Figs. 7). Implementation of the other boundary conditions is facilitated by the following facts:

(1) The two incoming streams are represented by two line sources with the strength of $S_1 = 0.5U_1/\pi$ and $S_2 = 0.5U_2/\pi$ located at $\zeta_{s1}=(-1,0)$ and $\zeta_{s2}=(+1,0)$, respectively. Note that 0.5 in the expression of the strength comes from the fact that these sources cover only the upper half of the computational plane;

(2) The no-flow boundary condition across the solid walls is satisfied by

using the mirror images of the computational elements with respect to the real axis, $\zeta=\xi+i0$. These images have the same strength as the original elements but with a negative sign. The total complex velocity, $w=u-iv$, at the center of jth element, $z(\zeta_j)$, is given by:

$$w(z_j)= \{ \frac{S_1}{\zeta_j-\zeta_{s1}} + \frac{S_2}{\zeta_j-\zeta_{s2}} + \sum_{j=1}^{N} \frac{i\,\Gamma_i}{2\,\pi\,\delta_i} [- \frac{|\Delta\zeta|_{ij}}{\Delta\zeta_{ij}} + \frac{|\Delta\tilde{\zeta}|_{ij}}{\Delta\tilde{\zeta}_{ij}}] \} F(\zeta_j)$$

$$- \frac{i\Gamma_j}{4\pi} \left(\frac{dF}{d\zeta} \right)_j \qquad (52)$$

where the last term is the self-induced velocity which arises due the transformation between the physical and computational domains, and

$$\Delta\zeta_{ij} = \zeta_j - \zeta_i \text{ , and } \Delta\tilde{\zeta}_{ij} = \zeta_j - \tilde{\zeta}_i$$

where $\tilde{\zeta}$ is the complex conjugate. The scaling factor used to transform the length from the z-plane to the ζ-plane at point $z(\zeta)$ is $F(\zeta)$ and vice versa; i.e., $\delta|_\zeta=\delta|_z F(\zeta)$. It is important to remember that we made no approximation in driving Eq. (52), and that the resolution of the numerical scheme is not restricted by a mesh size.

In what follows, we employ the same procedure used to evaluate the velocity field to derive the corresponding expression required to calculate the value of the scalar at an arbitrary point $\zeta=\xi+i\eta$. The total contribution to the scalar concentration at a point (ξ,η) is due to the following:

(1) Two line sources with logarithmic distributions located at $\zeta_{s1}=(-1,0)$, and $\zeta_{s2}=(1,0)$, serving the upper half the computational plane, and representing the effect of the incoming streams. For a source located at

ξ_s, we derive the expression representing the scalar distribution at an arbitrary point, ξ, as follows. We write the scalar flux through a semi-circle with center located at the source, and passing through the desired point,

$$\text{Flux} = \pi\ (\xi - \xi_s)\ \frac{ds}{d\xi} = \text{Constant}$$

and integrate to find the variation of s with ξ as

$$s(\xi) = C\ \text{Log}(\xi - \xi_s) + T$$

Because there are two sources, the contribution of the incoming flow to the scalar concentration is

$$s(\xi) = C_0 + C_1\ \text{Log}(\xi - \xi_{s1}) + C_2\ \text{Log}(\xi - \xi_{s2}).$$

(2) The transport elements in the upper half of the ζ-plane representing the distribution of the scalar gradients inside the computational domain;

(3) The mirror images of the transport element in the lower half of the ζ plane which are used to satisfy the no-flux wall condition. These images have the same strength as the original elements but with negative signs to cancel the flux induced at the boundary. The total scalar distribution is given by:

$$s(\zeta) = s(z) =$$

$$C_0 + C_1\ \log(\zeta - \zeta_{s1}) + C_2\ \log(\zeta - \zeta_{s2}) +$$

$$\sum_{j=1}^{N} \{ \frac{p_j}{2\pi} \frac{\Delta\xi}{r^2} [1-\exp(-\frac{r^2}{\delta_j^2})] + \frac{q_j}{2\pi} \frac{\Delta\eta}{r^2} [1-\exp(\frac{r^2}{\delta_j^2})] +$$

$$\frac{p_j}{2\pi} \frac{\Delta\xi}{r_i^2} [1-\exp(-\frac{r_i^2}{\delta_j^2})] + \frac{q_j}{2\pi} \frac{\Delta\eta_i}{r_i^2} [1-\exp(-\frac{r_i^2}{\delta_j^2})] \} \qquad (53)$$

with $\Delta\xi=\xi-\xi_j$, $\Delta\eta=\eta-\eta_j$, $r^2=\Delta\xi^2+\Delta\eta^2$, $\Delta\eta_i=\eta+\eta_i$,

$r_i^2=\Delta\xi^2+\Delta\eta_i^2$, $(q_j)_z=(p_j)_z- i\,(q_j)_z$, and $(q_j)_\zeta=(p_j)_\zeta- i\,(q_j)_\zeta$;

$$(p_j)_z = \frac{ds}{dx}, \quad (q_j)_z = \frac{ds}{dy}, \quad (p_j)_\zeta = \frac{ds}{d\xi}, \quad (q_j)_\zeta = \frac{ds}{d\eta}$$

$$q_\zeta = q_z \frac{|F(\zeta)|^2}{F(\zeta)}$$

Note that the walls are assumed to be adiabatic and impermeable. We may implement other boundary conditions by defining the appropriate image system for the gradient elements in the domain.

In order to find the values of the constants C_0, C_1, and C_2, it is important to use a combination of the boundary points at the inlet and exit planes of the domain and ensure that the effect of the sources decays with the distance downstream. We use Eq. (53) twice for the following sets of the boundary conditions:

(1) $s(0.0,0.0,t)=s_{\infty 2}$, $s(0.0,1.0,t)=s_{\infty 1}$, and $s(X_e,0.0,t)=s_{\infty 2}$ at $x_{Exit}=4.0$;

(2) $s(0.0,0.0,t)=s_{\infty 2}$, $s(0.0,1.0,t)=s_{\infty 1}$, and $s(X_e,1.0,t)=s_{\infty 1}$ at $x_{Exit}=4.0$.

Each time step, two sets of C_0, C_1, and C_2, are calculated by applying the above two conditions. The average of the two sets of constants is used for the rest of the calculations.

We remark that this method of implementing the effects of the boundary condition in the solution of the scalar transport equation is similar to the method of sources and sinks in classical heat conduction analysis (Carslon and Jaeger).

3.5. EFFECT OF STRETCH

At time t=0, the initial vorticity distribution is represented by a finite number of vortex elements. These elements are located at equal distances from each other, and carry radially symmetric vorticity distributions. The shape of the distribution is defined by the core function and its spread, known as the core radius. At later times, since different elements move at different velocities depending on their location, the distances between the neighboring elements may increase much beyond their initial values. If this distance exceeds the core radius, the accuracy of the discretization of the vorticity field deteriorates and the computation of the velocity field becomes inaccurate.

This loss of accuracy, associated with the development of strong stretch, illustrates one of the fundamental problems of Lagrangian methods. Vortex elements, which start as cores with radial symmetry, may not properly represent the vorticity field after it has developed strong local strains. As the effective distance between neighboring elements, $\Delta\chi$, increases, the ratio $\delta/\Delta\chi$ (equivalent to δ/h) reaches levels where the vorticity discretization becomes inaccurate. Several remedies may be suggested:

(1) Utilizing deformable cores;

(2) Employing large cores; or

(3) Using more elements as the distance between the original elements increases.

The first scheme, utilizing deformable cores, is based on the observation that an initial core with the radial field will become elliptical as stretch develops, with its major axis aligned with the local principal direction of strain. However, there is an obvious limitation on maintaining one ellipse as a single element as the ratio between the axis exceeds a reasonable value. The scheme can also be tedious computationally since the formulas describing the velocity field of an elliptical vorticity structure are complicated [64].

The second scheme, in which one uses a large core radius, does not yield accurate predictions for the growth rate within the linear range since it does not allow for accurate discretization of the initial vorticity field. Moreover, it will fail at the point where $\delta/\Delta\chi<<1$ due to stretch. It does, however, delay the loss of accuracy since it maintains a reasonable overlap between the neighboring elements for longer times [38].

The third option, redistributing the vorticity and the scalar gradients fields among an increasing number of elements arranged along the direction of the principal direction of strain, is employed here. We monitor the distance between neighboring elements in the direction of maximum positive stretch $\Delta\chi$. If $\Delta\chi>\Delta\chi_{max}$, an extra element is placed halfway between the original elements and the vorticity and the scalar gradients are redistributed to compute the share of the new element.

A more economical scheme is based on interpolating the strength of the two original elements equally among the three elements, i.e., assuming uniform stretch between the two original elements. This amounts to splitting the original vortex pair formed of two neighboring vortex discs into three discs when the distance between the centers of the two discs exceeds a threshold, as shown in Fig. 8. We also monitor the minimum distance between the two

neighboring elements, and if $\Delta\chi<\Delta\chi_{min}$, we replace them with a new element conserving the related properties such as the total strengths. In the spatial model, in order to keep the number of the computational elements at an affordable level, we use a variable $\Delta\chi_{max}$ and $\Delta\chi_{min}$, that is $\Delta\chi_{max} = a + b\,x$ and $\Delta\chi_{min} = c + d\,x$, where a, b, c and d are positive constants and x is the streamwise coordinate. Choosing a proper set of a, b, c and d in fact involves a trade-off between the computational effort and the accuracy of the scalar calculation. In our computations we use a=1.5, b=c=d=0, for the temporal model, and a=1.5, b=2.5, c=0.5, d=1.5, for the spatial model.

3.6. CONCLUSIONS

We have developed the vortex element method by accurately discretizing the vorticity field among finite vortex elements with strongly overlapping cores and by using the strain which develops at later times to redistribute the vorticity among more elements arranged in the principal direction of strain between the original elements. This enables the method to remain robust for long time calculations and after severe distortions of the flow map have been encountered. High-order spatial discretization can be achieved by using more elaborate core functions, such as fourth-order Gaussian cores [24]. However, we did not find that to be necessary in actual applications. Temporal accuracy is governed by the order of the scheme used in the integration of the particle transport equation. In most applications here, we found the second-order Runge-Kutta method to be sufficient.

The vortex method, being Lagrangian, naturally avoids the non-linearity of the convective terms in the original equations. Moreover, since the velocity calculations are elliptic, there is no inherent stability limit on the time step, it is controlled only by accuracy. Without discretizing the

convective derivatives, the method minimizes the numerical diffusion in the solution and thus it is most suitable for simulating flows at high Reynolds number, O(1000-100000). This is important in turbulent flow applications since, as will be shown in Chapters 4 and 5, the rates of mixing and burning can change substantially if the Reynolds number drops below O(1000), and the level of turbulent scalar fluctuations can depend critically on the Reynolds number for values O(1000-10000).

The transport element method, which was formulated to obtain solutions for the scalar transport equation, retains all the properties of the vortex method by extending its essential concepts to the transport of scalar gradients in a Lagrangian form. The method is made conservative by utilizing the relationship between the distortion of the flow lines and the evolution of the scalar gradients. In a reacting flow, the method provides a natural way of tracking the development of the chemical reaction between neighboring fluid elements as they flow. We remark that the overhead involved in computing the transport of a passive scalar is minimized by the fact that all the functions required to compute the local values of scalar concentration are also used in the computations of the vortex method. In the reacting flow case, however, an extra restriction is imposed on the time step when the chemical time scales are small compared with the flow time scales and when the chemical reaction is stiff.

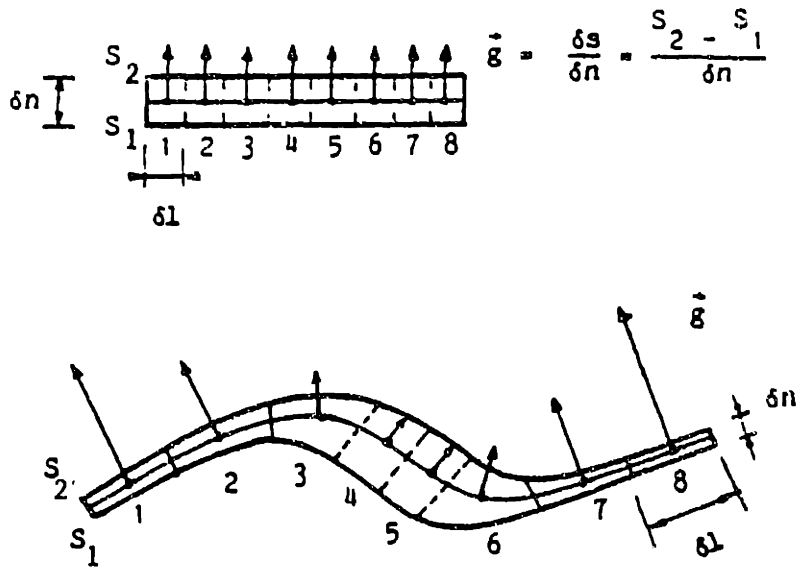

Fig. 3. Schematic sketch showing the evolution of a material layer separating two values of the conserved scalar, s, and the associated scalar gradient, g, under the effect of stretch.

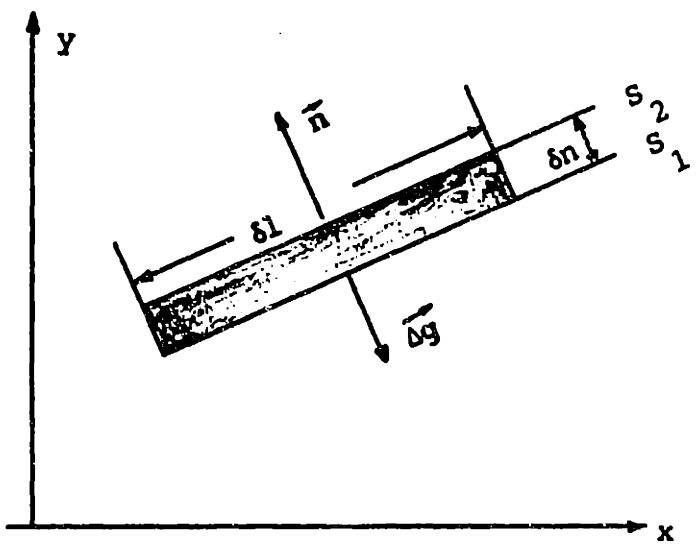

Fig. 4. Schematic sketch showing one transport element and the associated scalar gradient.

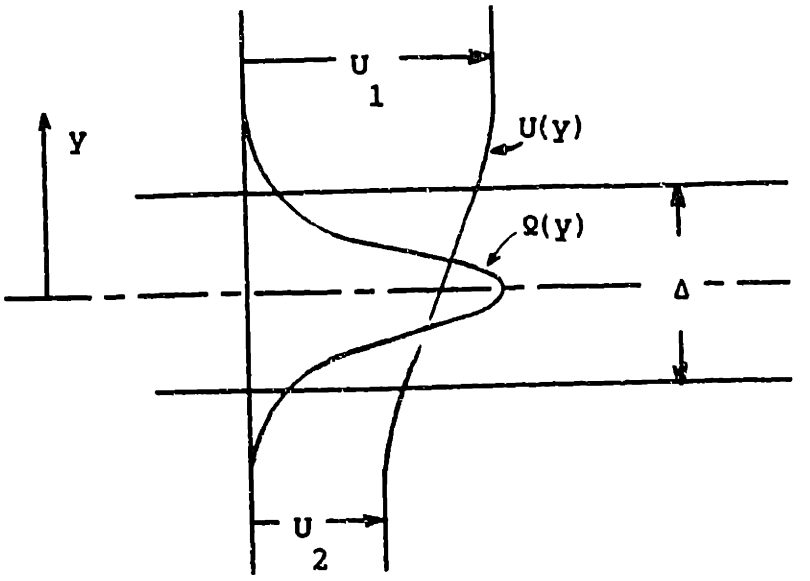

Fig. 5. Schematic diagram of a free shear layer.

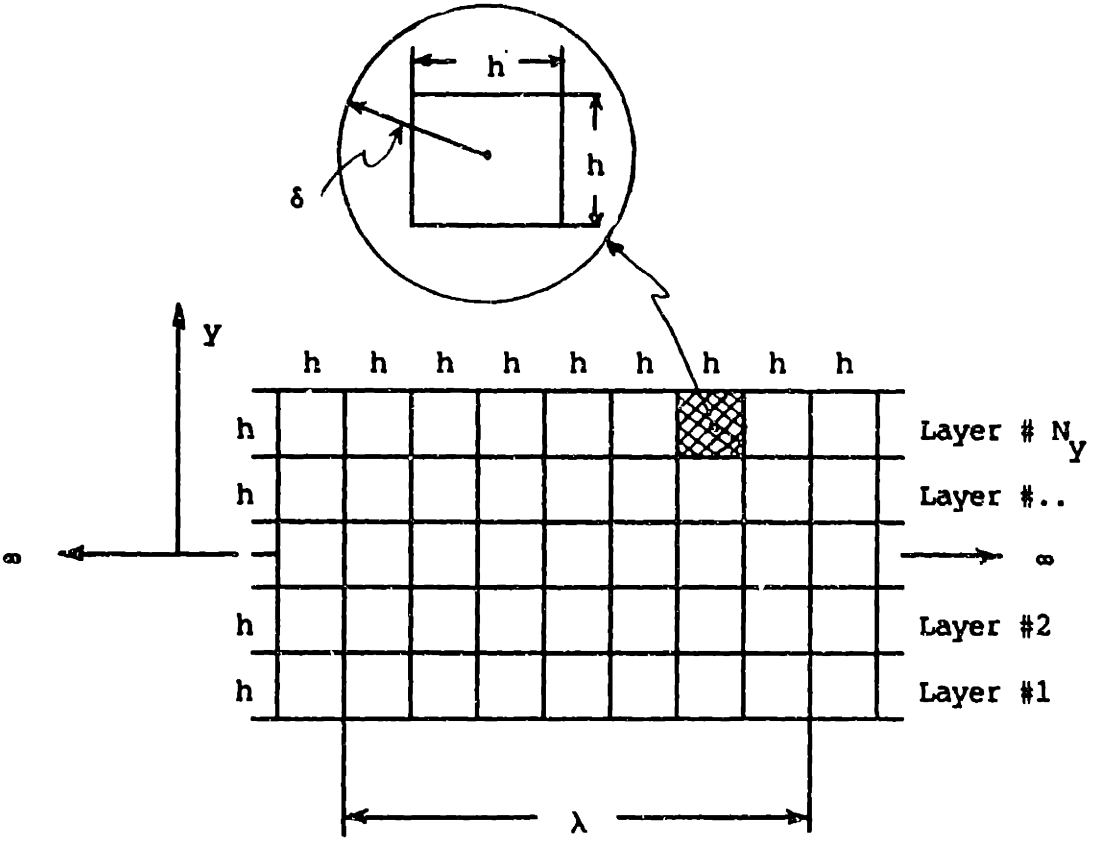

Fig. 6. The initial mesh used to descritize the vorticity and the scalar gradients at time t=0.

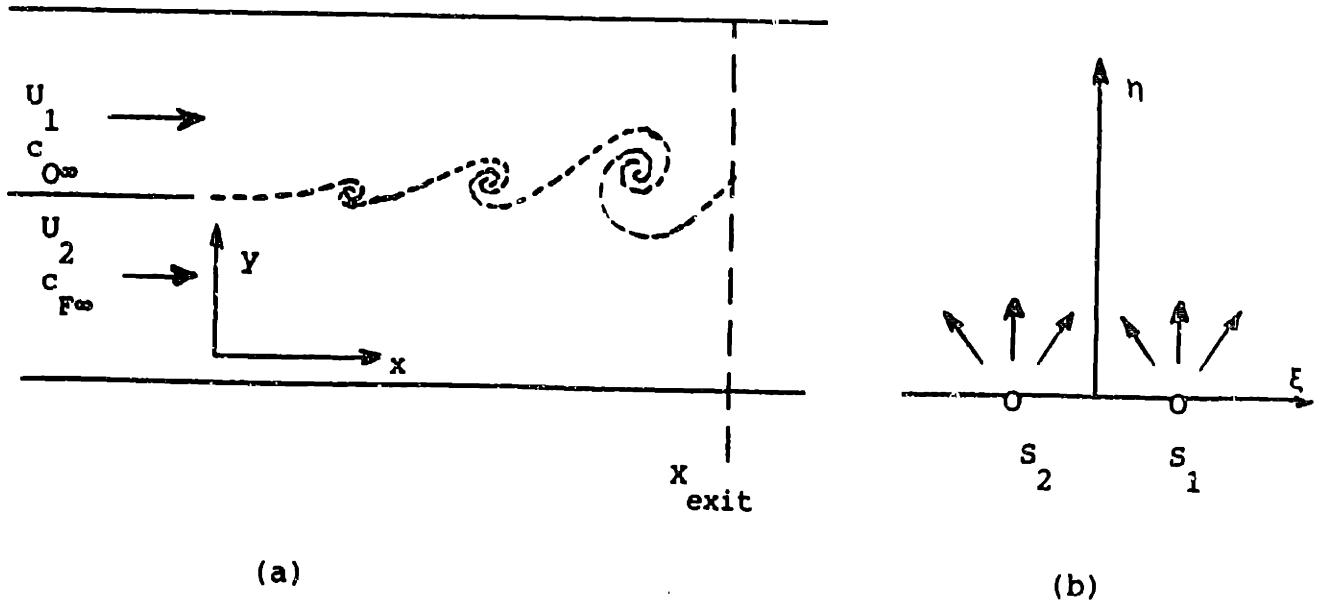

(a) (b)

Fig. 7. Schematic diagram of a spatial shear layer (a) physical plane, (z plane), (b) computational plane (ζ plane).

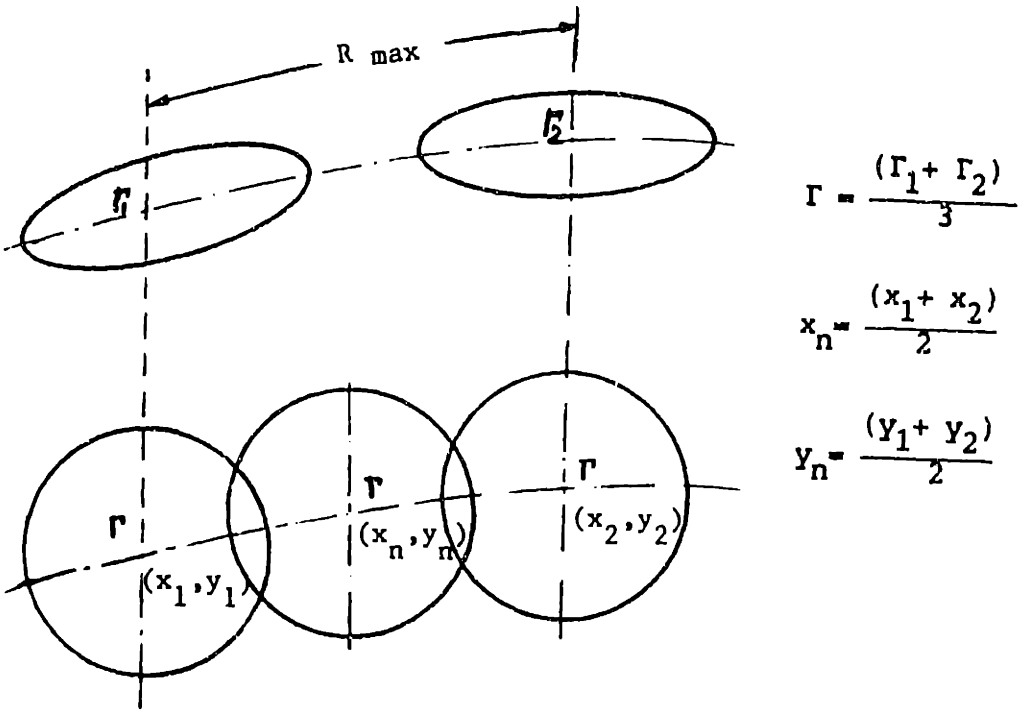

Fig. 8. Insertion-and-interpolation process.

Chapter 4

THE TEMPORAL SHEAR LAYER

The temporal shear layer model describes the evolution of a single eddy or a small number of eddies in a frame of reference that moves with the mean velocity of the flow. Mathematically, it is a well-defined problem in which periodic boundary conditions are imposed on the sides of domain. In the temporal shear layer, the length of the computational domain is limited to the perturbation wavelength in a forced layer, λ, and one can afford to use more elements within the domain to improve the resolution. The highly unstable nature of a free shear layer, via Kelvin-Helmholtz instability, provides a mechanism for the growth of small perturbations and formation of large scale structures.

The velocities of the streams must, however, be close to each other, and the velocity difference does not play a role in determining the layer's response to perturbations. This restricts the application of the results of the temporal model and in theory the temporal model should only give qualitative insight into the physics of the governing processes rather than a quantitative measure for the shear layer behavior. In practice, we found that the temporal shear layer is more powerful than expected, and as we will see later the numerical results agree well with the experiment under the conditions listed in Chapter 3.

We use the temporal model of the shear layer to validate our numerical scheme and learn more about the physics and behavior of one or two eddies. Later in Chapters 5 and 6 we will consider a spatial model which is closer to the physical reality. The length and velocity scales here are half the vorticity thickness of the shear layer $\Delta/2 = \sigma\sqrt{2}$ where σ is the standard

deviation of the Gaussian distributing the vorticity distribution, and the velocity difference between the two streams is $\Delta U = U_1 - U_2$.

4.1. GROWTH RATE AND THE LINEAR THEORY

To measure the effect of the accuracy of the initial discretization of vorticity among vortex elements on the flow field for short time, we used our numerical results to calculate the rate of growth of the perturbation, G.R., and compared it with the growth rate based on the eigensolution of the linearized form of the governing equation, known as the Rayleigh equation. Based on the linear theory analysis, if a shear layer which is defined by its thickness, Δ, and the shape of the laminar base flow, U(y), is perturbed by small disturbances, the total streamwise and cross-stream velocities, u and v, are given by:

$$u(x,y,t) = U(y) + \hat{u}(x,y,t)$$

$$v(x,y,t) = \hat{v}(x,y,t)$$

where $\hat{u}$ and $\hat{v}$ are the velocity fluctuations computed from

$$\hat{u}(x,y,t) = \text{Real} \{ \tilde{u}(y) \exp[i\alpha (x - c\, t)] \}$$

$$\hat{v}(x,y,t) = \text{Real} \{ \tilde{v}(y) \exp[i\alpha (x - c\, t)] \}$$

$$\tilde{u}(y) = \tilde{u}_r(y) + i\, \tilde{u}_i(y)$$

$$\tilde{v}(y) = \tilde{v}_r(y) + i\, \tilde{v}_i(y)$$

$$c = c_r + i\, c_i$$

$\alpha = 2\pi/\lambda$

the subscripts "r" and "i" refer to the real and imaginary parts of the corresponding variables, c is the wave speed, and α is the wave number based on the wavelength, λ. In a uniform-density, temporally-growing shear layer, $c_r=0$ and the growth rate, is defined as G.R. = α c, where c is the eigenvalue of the Rayleigh equation:

$$\tilde{v}''(y) = \left(\frac{U''(y)}{U(y) - c} + \alpha^2 \right) \tilde{v}(y) \qquad (54)$$

and " is the second derivative with respect to y. The boundary conditions of Eq. (54) in an unbounded domain are:

$$\tilde{v}(\pm \infty) = 0 \quad \text{and} \quad \frac{d\tilde{v}}{dy} (\pm \infty) = 0$$

Equation (54), the Rayleigh equation, is obtained by linearizing the original inviscid flow equations around the base flow and expressing the solution in terms of temporally growing waves [65]. We have numerically solved the Rayleigh equation using a Runge-Kutta shooting method to satisfy the boundary conditions, and plotted the growth rate, αc, versus the perturbing wave number, α, for three base flow velocity profiles, namely, linear, tanh, and error function shown in Fig. 9.

Analysis of Fig. 9 reveals that for a shear layer with a fixed base flow, there is a most unstable wavelength, λ^*, which gives the highest growth of small disturbances with a very small amplitude ε. For the other wavelengths, the growth rate is less [34,66]. Moreover, results show that the instability of a finite thickness shear layer is a broad-band instability,

i.e., the shear layer will respond to a perturbation with any wavenumber between 0 and n_{max}, corresponding to wavelength $\lambda = \infty - 2\pi/n_{max}$. As the layer becomes thinner, it responds to shorter and shorter perturbation wavelengths. An infinitely thin shear layer, a vortex sheet, is absolutely unstable, while a finite thickness shear layer is capable of suppressing the growth of short-wavelength perturbations. These results can also be used to conclude that if the layer is disturbed with white noise, most of the eddy that forms due to the growth of some selected perturbations will have wavelength λ^*. However eddies with size different than λ^* may also form but with lower probability.

In order to calculate the growth rate based on the numerical results, we defined the index I as follows:

$$I(t) = \text{Log} \left\{ \int_0^{\lambda} \int_{-\infty}^{+\infty} | \hat{u}(x,y,t) | \, dx \, dy \right. \tag{55}$$

and calculated the growth rate as

$$\text{G.R.} = \frac{dI(t)}{dt} \tag{56}$$

which is compatible with the definition of the growth rate in the linear theory. In section 4.2 we will check the accuracy of the numerical results for the growth of the layer in its linear range by comparing the growth rate based on our numerical simulation and the growth rate based on the results of the linear theory.

4.2. DYNAMICS

First, we study the evolution of a shear layer perturbed by the most unstable wavelength, λ^*, with different amplitudes. In Fig. 10, we plot the growth of the perturbation defined by Eq. (55) for $\varepsilon=0.001\lambda^*$, $\varepsilon=0.01\lambda^*$ and $\varepsilon=0.1\lambda^*$. The growth can be divided into two ranges: (1) linear, (2) nonlinear. In the linear range, the slope of the curve is constant and is equal to the growth rate of the shear layer defined by Eq. (55). From Fig. 10 and for $\varepsilon=0.001\lambda^*$ and $\varepsilon=0.01\lambda^*$, the growth rate is G.R.=0.215, which agrees well with the result of the linear theory. For $\varepsilon=0.1\lambda^*$, the perturbation leads directly to the nonlinear range.

The development of the eddy structures is depicted in Figs. 11, 12, and 13 in terms of the vortex elements and their velocity vectors at different time steps. In Figs. 14 and 15 we have plotted the kinetic energy based on the velocity fluctuation, $u'.u'/2$, where $u'=u(x,t)-u(x,0)$; and the amount of stretch experienced by the flow, L/L_0.

The evolution of the shear layer depicted in Figs. 11-13 can be divided into four stages: (1) linear growth; (2) rise to a maximum amplitude; (3) decay to a constant amplitude; and, (4) very slow decrease of amplitude. The flow of kinetic energy from the main stream into the eddy during the first two stages, and the reversal of that process during the last two stages, shown in Fig. 14, is the main reason for formation and decay of these structures.

The extent of the first stage, where the perturbation amplitude is small, is easily identified from the plots of the shear layer structure, Fig. 11, which remains flat and experiences almost no stretch as seen in Fig. 15. It can also be seen from the plot of the growth rates, Fig. 10, which remains constant, or in the kinetic energy based on the velocity fluctuation, Fig. 14, which remains almost zero. It is interesting to note that during the "linear" range, the perturbation is very small, grows exponentially!

The most important feature of the second stage is formation of a core at the center of the eddy with braids extending between the two neighboring eddies. This is accompanied by a sharp rise in the kinetic energy based on the velocity fluctuation, reaching its maximum value at the end of this stage. During this stage, the layer experiences the highest rate of stretch and the core maintains almost a circular configuration. The stretch is concentrated within the braids.

During the third stage, the eddy deforms into an elliptical structure, and the cross-stream axis of the ellipse decreases from its maximum value. This is accompanied by reversal of flow of the kinetic energy, based on the velocity fluctuation, from the eddy into the main flow. More stretch along the braids and within the core is observed. A slowdown of the eddy rotation is also seen during this stage. By the end of the third stage, the thickness of the braids at the saddle points has become extremely small.

At the final stage, the envelope of the core reaches a dynamic equilibrium, i.e., it does not rotate any more, while its boundaries keep stretching as the fluid within the eddy starts to move in the main direction of the stream. In reality, a single eddy cannot exist forever. As soon as the forcing effect of the fundamental frequency, ceases, other disturbances can energize different mechanisms like the pairing mechanism, and two neighboring eddies merge to form a larger structure.

The final structure of the most unstable shear layer is almost independent of the amplitude of perturbation. This conclusion agrees with the plot of the kinetic energy based on the velocity fluctuation, Fig. 14, which suggests that the eddy can absorb the same amount of kinetic energy independent of the initial perturbation amplitude. Thus, we expect to get almost the same peak value for the growth of perturbation in Fig. 10. It

should be noted that in Fig. 10, we plot the logarithm of the amplitude of the perturbations, which means that we are dealing with even smaller values as the amplitude of the initial perturbation decreases. For the sake of a better representation, we normalize the values in such a way that all curves pass through the origin, and hence the curves are shifted up in the favor of the smaller amplitudes.

The total kinetic energy in the flow within the computational domain, u.u/2, is plotted in Fig. 16, and as we expect it is conserved since the flow is inviscid. Note that the numerical diffusion, which could have dissipated some of this energy, is small.

Figure 17 shows a qualitative comparison between the experimental results of Roberts et al. [67] and our computational results. Here we use an inverse Galilean transformation to compare the experimental results of spatially-developing layer at equal space intervals with the computational results of the temporal model at equal time intervals.

Next, we perturb the shear layer by the fundamental wavelength, λ^*, and the subharmonic wavelength, $2\lambda^*$, simultaneously with $\varepsilon=0.1\lambda^*$ for both waves. The pairing process, which results from the growth of the subharmonic instability, is depicted in Fig. 18. The results show that when the amplitudes of the two perturbations are equal, pairing starts at the end of the second stage of the fundamental mode and before any further substantial elongation of the eddies. The growth of the subharmonic perturbation closely resembles that of the fundamental, as shown in the latest stage. The eddies continue to deform while they pair until the "vortex fluid" contained within each structure starts to rotate around a common center and their original boundaries become indistinguishable. It is interesting to see the

filamentation of the newly formed structure and the formation of a new generation of braids.

Finally we perturbed the shear layer by a single wavelength, different from the most unstable one, with various amplitudes. Figure 19 shows the vorticity field for $\lambda=10.5$ and $\varepsilon/\lambda=0.01$. The computed growth rate is 0.214 while the analytical value is 0.208. Because the wavelength of the perturbation is different than that of the most unstable mode, the growth rate is smaller. More vorticity remains in the braids since the eddy is not strong enough to accomplish the same stretch as in the case of λ^*. The braids are thicker and the outer edge of the eddy is less organized.

Figures 20 and 21 show results for $\lambda=2\lambda^*$ with $\varepsilon=0.01\lambda$ and 0.1λ, respectively. The computed growth rate for the first case is 0.18 while the analytical value is 0.173. The core is smaller and weaker than for the case of λ^* and hence the braids are thicker and maintain more of the original vorticity. Comparing Figs. 20 and 21, we see that contrary to the most unstable case, the effect of the initial perturbation is more pronounced here in terms of the size and shape of the eddy and the braids. The higher amplitude of the initial perturbation is equivalent to a larger physical perturbation which leads to a stronger instability and tends to form a larger core with thinner braids. The ratio between the major and minor axes of the elliptical core increases with ε and secondary waves start to grow along the braids.

Figures 22 and 23 show results for $\lambda=3\lambda^*$ with $\varepsilon=0.01\lambda$ and $\varepsilon=0.1\lambda$, respectively. The effect of the amplitude is emphasized further since at large ε, the core splits into two eddies. This bifurcation phenomenon was observed before by Pozrikidis and Higdon [68]. The braid instability is

manifested here by the long waves that grow between the cores at the later stages of development of the layer.

4.3. TRANSPORT OF PASSIVE SCALAR

In order to study the mixing process which results from the combined effects of convection and diffusion, we simulate the evolution of a thermally stratified shear layer in which the top stream has a higher temperature than the bottom stream, $(T_\infty)_{Top} > (T_\infty)_{Bottom}$. The dynamic effects of temperature stratification are neglected in this model and hence the structure of the thermally stratified layer is the same as that of the cold layer. In the temporal model of the shear layer, we normalize the temperature distribution as follows:

$$\tilde{T}(x,y,t) = \frac{T(x,y,t) - (T_\infty)_{Bottom}}{(T_\infty)_{Top} - (T_\infty)_{Bottom}}$$

In what follows we drop the " ~ " and refer to the normalized temperature as $T(x,y,t)$.

We choose first to address the transport of a passive scalar into the layer, or the entrainment of the free-stream fluid into the structure that forms due to the roll up of the vorticity layer. As mentioned earlier, the numerical scheme enables us to isolate the effects of individual processes. That is, we ignore the diffusion and let convection bring material particles of different temperature close to each other. At time t=0, the temperature distribution of an unperturbed layer is described by an error function, with $T(x,y,0)=0.5[1+\mathrm{erf}(y)]$. This choice is motivated by the fact that this is the fundamental solution of the diffusion equation. Therefore, an initial

discontinuity in temperature would develop into an error function before the perturbation grows to the point whence convection effects become important. In the computations, we used the same particles to transport the vorticity elements and elements of the temperature gradient. This represents a substantial saving in the computation since the kernel functions appearing in the expressions of the velocity and the temperature can be computed only once. All the computations in this chapter were performed using the original formulation of the transport element method, i.e., Eqs. (29), (31) and Table IV.

Results obtained for the temperature distribution in the totally inviscid shear layer of Figs. 11, 12, and 13 are shown in Figs. 24, 25 and 26, respectively. To quantify the overall entrainment, we define a quantity γ, similar to the growth rate (see Eq. (55)), as:

$$\gamma(t) = \int_0^{\lambda} \int_{-\infty}^{+\infty} | T(x,t) - T(x,0) | \, dx \qquad (57)$$

where $T(x,t)$ and $T(x,0)$ are the instantaneous and initial temperature distributions respectively. In Fig. 27, the natural logarithm of $\gamma(t)$ is plotted for three cases shown in Figs. 24-26.

Within the linear range, the temperature distribution remains almost the same, except for getting shifted up or down depending on the local sign of the perturbation. Thus, the distribution of the scalar inside the layer has not changed due to the linear growth of the perturbation. During the second stage, and with roll up of the interface and the establishment of a spiral center at the midpoint of the wavelength, a complex temperature gradient

develops as a result of the motion of the cold fluid upward and the hot fluid downward around the spiral center.

In the second stage, if the number of transport elements remained the same, i.e., stretch were not accommodated by introducing elements where the local strain is large, the temperature distribution would collapse very quickly. In the problem of a periodic shear layer, this collapse leads to values of $T(x,+\infty,t)<1$ and $T(x,-\infty,t)>0$. The reason of the loss of accuracy is clear from Eq. (15). When the elements move apart, the accuracy of computing the velocity gradient ∇u deteriorates, and hence the new value of g_j accumulates large errors. Thus, while the calculation of the velocity field at the early stages of strong stretch using a fixed number of vortex elements may be acceptable for a short period of time, the calculation of the velocity gradient and evolution of a passive scalar will show unacceptable errors. To continue beyond the linear stage, the distance between the neighboring elements in the principal direction of strain, ΔX, must be monitored. If $\Delta X>\Delta X_{max}$, one extra element is added between the two original elements and the total value of g_j is redistributed equally between the three elements. In the temporal calculation, we used $\Delta X_{max}=1.5h$.

The effect of the shear layer roll up on the temperature distribution is seen in Figs. 24-26. Immediately after the interface reaches a vertical position, an S-shaped temperature profile starts to form, indicating that cold fluid has been transported from the lower stream into the upper stream and vice versa. This phenomenon, known as engulfment or entrainment, relies solely on convective transport and is observed most clearly when molecular diffusion, which acts to dissipate the sharp gradients, is small. Fast entrainment, with small diffusion, leads to "unmixedness" of hot and cold fluid within the eddy core. With more fluid being transported to the opposite

stream, the S-shape grows, reaching a maximum amplitude when the interface becomes horizontal at the spiral center. At this moment, fluid with the maximum and the minimum temperatures has been entrained into the core, i.e., entrainment has reached all the way to the free stream to bring fluid into the core of the eddy. This is the stage of maximum entrainment when the core size reaches its largest size and can not accommodate any more fluid. In the case of $\varepsilon=0.1\lambda$, it corresponds to t=9.0, which is the end of the second stage of development. To make the correspondence between the temperature profiles and the evolution of the interface with T = 0.5 clear, we plot the latter in Fig. 28 which shows the actual elements that were used in the computation of this interface. At t ~ 8, the interface has rotated 180° around the spiral center. This is the first step in the process of homogenization of the core.

As the core rotates further into the third stage, the inner part of the interface develops a secondary instability that rolls up in a very similar manner to the primary instability. This secondary instability is in phase with the primary instability and can be envisioned by zooming in on the intersection between the interface and the horizontal centerline of the layer. Due to the elongation of the outside envelope of the core, the wavelength of the secondary instability grows with time, as seen from Fig. 28. However, the amount of fluid within the elliptical envelope remains constant, or decreases slowly as seen from Fig. 27. The growth of the secondary instability provides a mechanism of internal stirring within the core. During the growth of the secondary instability, an inverted S-shape, or a Z-shape, forms in the middle of the temperature profile, Figs. 24-26. The convection field associated with this instability turns the fluid in a clockwise fashion making the inside of the core more uniform. This is seen from the decay of the peaks in the temperature profile as this Z-shape grows.

The onset and subsequent growth of successively shorter wavelength instabilities continues, leading to more changes in temperature distribution within the eddy core. An asymptotic limit of this process can be foreseen: it is the formation of a temperature profile with the following shape: $T=T_{+\infty}$ at $y>\Delta'/2$; $T=T_{-\infty}$ at $y<-\Delta'/2$, and $T=(T_{+\infty}+T_{-\infty})/2$ in between, where Δ' is the minor axis of the elliptical envelope at $x=\lambda/2$. This shape has been measured experimentally by Konrad [69], for mixing layer flow at high Reynolds numbers (see also Broadwell and Breidenthal [13]).

By the end of the third stage, the layer cannot absorb any more energy and a relaxation process occurs during which some of the kinetic and thermal energy are fed back into the main flow streams. This reverse action is accompanied by the fluid leaving the core and moving back into the main streams at a very slow rate.

4.4. DIFFUSION AND MIXING

The generation of large temperature gradients within the core as successive instabilities evolve gives rise to large molecular diffusion fluxes which act to smooth out some of these gradients. While for most cases of interest the diffusion transport is very small relative to the convective transport, i.e., the Reynolds number is high, diffusion plays an important role since mixing at molecular scales can only be accomplished via molecular diffusion. Thus, the combined action of convective entrainment and molecular diffusion leads to the homogenization of the temperature within the eddy core. As mentioned earlier, to simulate the effect of diffusion for small diffusivities in our current shear layer model, we expand the core radius of transport elements using Eq. (42), with the following modification: the number of transport elements which discretize the gradient field increases with time

to accommodate for the distortion of the flow map. Utilizing an increasing number of elements to perform the convective transport is essential since it is important to determine the gradient field in terms of location and strength of the elements accurately before the diffusion effects can be added. In essence, adding transport elements at area of high strain allows the computational elements to capture all the vorticity and temperature gradient at all times, even after the vorticity has been fragmented by the action of the strain field. Without this step, strain will create areas which are void of elements, and thus, diffusion can not be represented.

The results in Fig. 29 show the temperature profile at time t=20 for the case of λ^* and $\varepsilon=0.1\lambda^*$, evaluated for α =0.0, 0.00001, 0.0001, 0.001, 0.01 and 0.1. Note that the temperature profiles of the first two cases are almost identical, indicating that the effective diffusivity of the inviscid calculation is on the order of 10^{-5}. In the last case, the temperature profile is similar to the case of pure diffusion, indicating that diffusion proceeds at a rate faster than the instability. It is also noticeable that for moderate values of α, $0.0001<\alpha<0.01$, diffusion only affects the core of the eddies, making them achieve a homogeneous state faster.

To define a quantitative measure of mixing in a single phase fluid with thermal stratification, we observe first that mixing is only achieved by molecular diffusion. Large entrainment fluxes bring the unmixed fluid layers in contact along a larger interface; however, molecular diffusion across this interface is what accomplishes the actual mixing. A measure of mixing can be defined as:

$$M(t,\alpha,\varepsilon) = \int_0^{\lambda} \int_{-\infty}^{+\infty} | T(x,t,\alpha,\varepsilon) - T(x,t,0,\varepsilon) | \, dx \qquad (58)$$

Note that $M(t,0,\varepsilon) = 0$, while $M(t,\alpha,0)$ is due to diffusion only. In Fig. 30 $M(t,\alpha,0.1)$ is plotted for λ^* and various values of α. It represents mixing due to the combined action of entrainment and diffusion. At very small values of α, mixing is limited by the amount of diffusion across the fluid layer which has been entrained into the eddy core. Since for these values of α the convective transport is faster than the diffusive transport, mixing increases approximately as $\sqrt{\alpha}$. However, as α increases, and at later times, mixing proceeds at slower rate since it becomes bounded by entrainment of unmixed fluid into the eddy core, which almost ceases by the end of the second stage of roll up.

4.5. CONCLUSION

In this part of the work, the vortex element method has been used to compute both the early and late stages of development of an inviscid temporal mixing layer.

1. We find that using a scheme which depends on equating the vorticity at the centers of the elements with the accumulated value induced by all elements is necessary to obtain accurate results for the initial vorticity discretization. We also find that to ensure the accuracy of the solution for short times, the ratio of the core radius/to separation should be larger than one. Very large cores induce a strong perturbation in the vorticity field, while smaller core cause a fast deterioration of accuracy. Using fourth-order Gaussian cores results in better accuracy than using second-order Gaussian cores. However, we feel that the improvement in accuracy does not warrant the added cost.

2. As time proceeds, the distance between neighboring elements exceeds its initial value due to the generation of strong strain. This leads to the computation of inaccurate velocities, which is manifested by irregular motion of the vortex elements. To overcome this problem, the vorticity is constantly redistributed among elements inserted along the principal direction of strain to capture the local deformation of the vorticity field and to improve the resolution of the calculations. This is achieved by an insertion-and-interpolation process which is applied where the distance between the neighboring centers along the principal direction of strain exceeds a threshold value. We have shown, using the solution for a shear layer perturbed at different wavelengths and amplitudes, that this process yields accurate solutions for the vorticity distribution at long times and after a strong strain field has caused a severe distortion of the streamlines. This scheme enables one to accurately compute the local velocity gradient which, while not required in connection with vorticity convection, is necessary for the accurate evolution of the convection of a passive scalar.

3. The temperature gradients, distributed over transport elements which resemble vortex elements in their structures, are used to compute the temperature distribution as the roll up evolves. Contrary to vorticity, scalar gradients are not conserved along particle paths, and thus, the strength of these transport elements is changed according to the straining and rotation of the material elements.

4. The scheme is capable of capturing very sharp gradients that develop within the core since the elements migrate toward these zone by convection. The multiplication of these elements via stretch, which inadvertently mimics the physical process by which large scalar gradients are generated, provides a naturally adaptive grid to compute these gradients. By expanding the cores of

the transport elements, the effect of small diffusivities can be simulated as a small perturbation to the convection field. Diffusion, even at high Peclet number, is responsible for generating areas of uniform temperature inside the eddy since it acts to smooth out the sharp gradients created by convection.

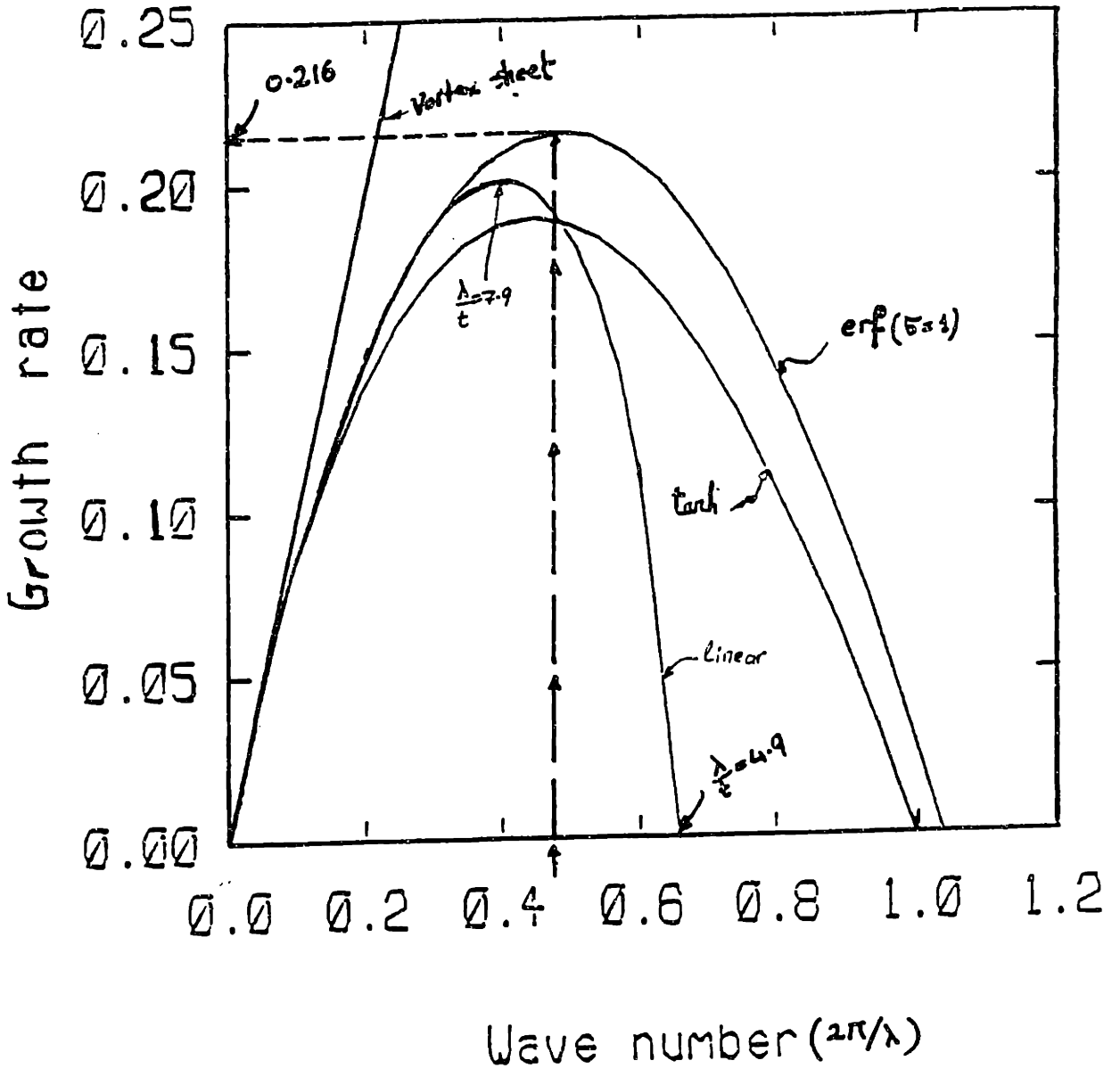

Fig. 9. The growth rate of a temporal shear layer, αc, versus wave number for various base flow.

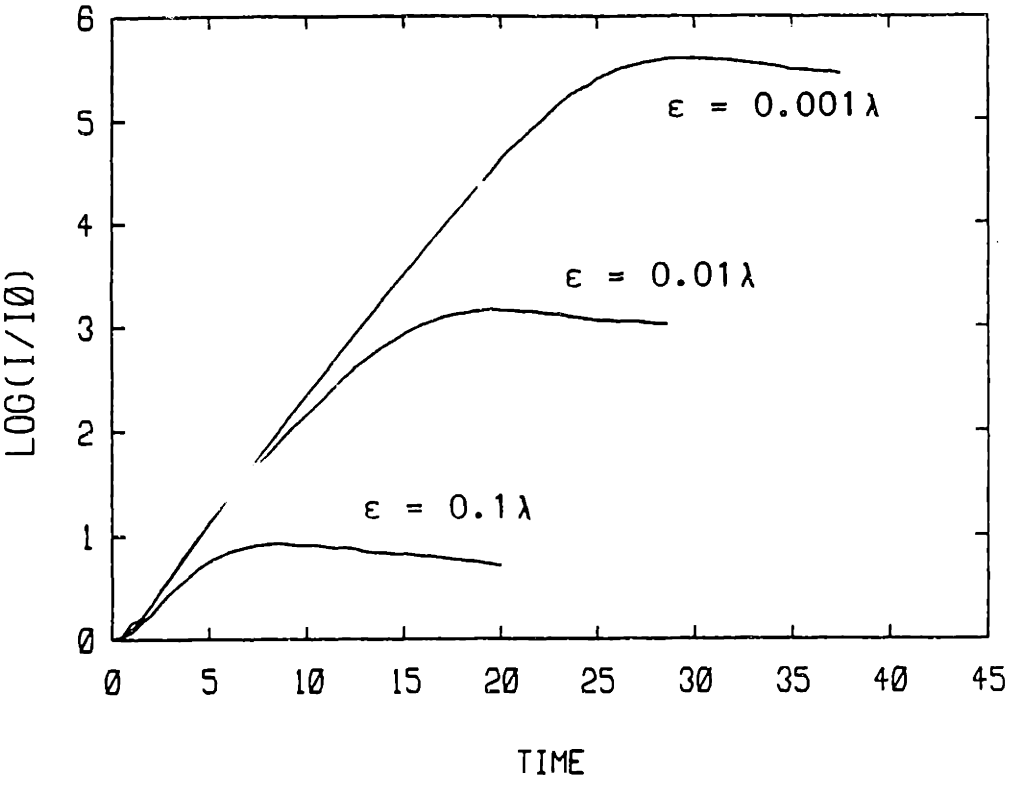

Fig. 10. The growth of the perturbation with time for the most unstable case for three values of the initial perturbation, $\varepsilon/\lambda^* = 0.001$, 0.01 and 0.1. Each curve is normalized with respect to the corresponding value at t=0.

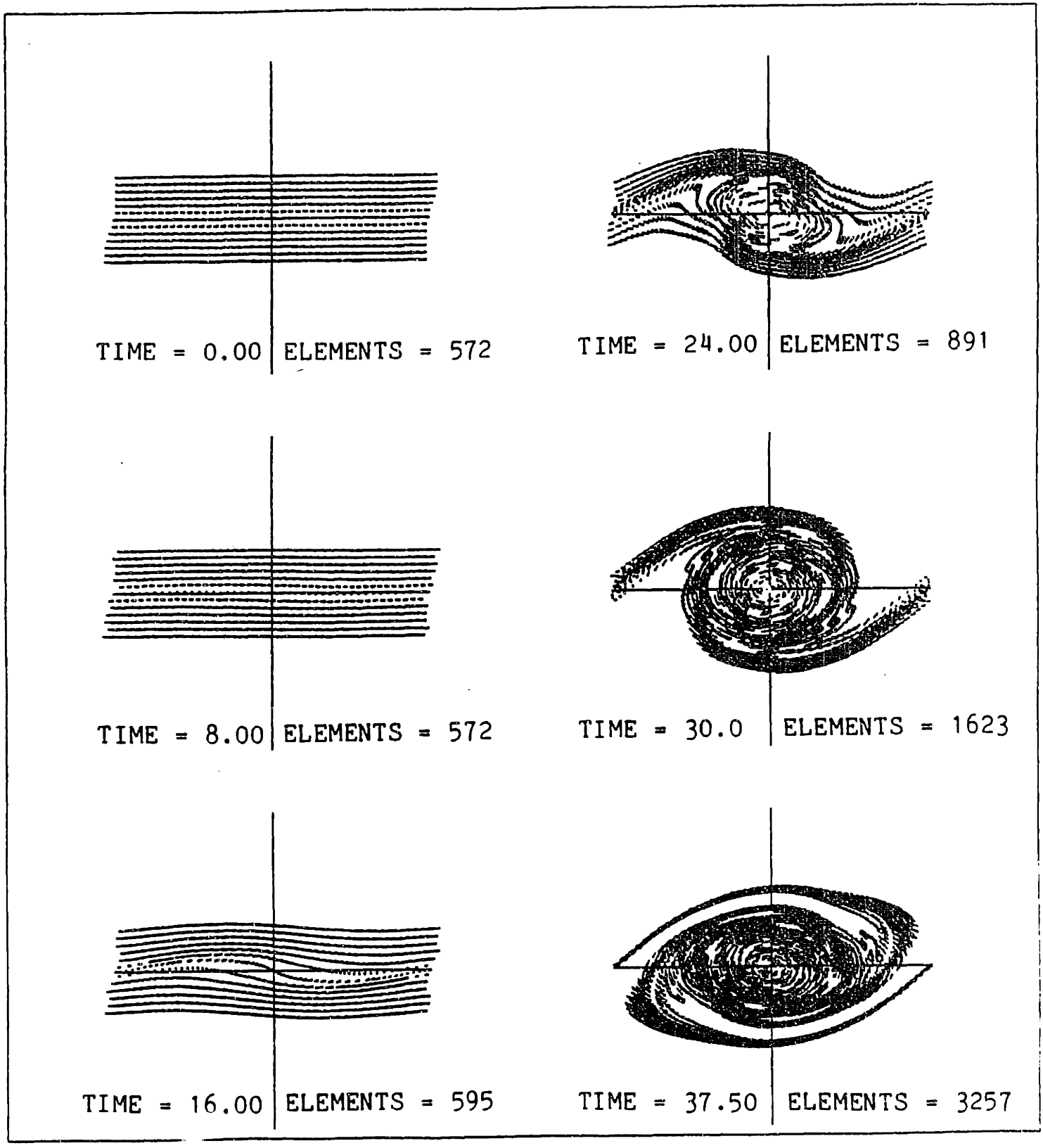

Fig. 11. The location and velocity of the vortex elements during the roll-up of a temporal shear layer.

$\lambda=\lambda^*$, with $\varepsilon/\lambda=0.001$.

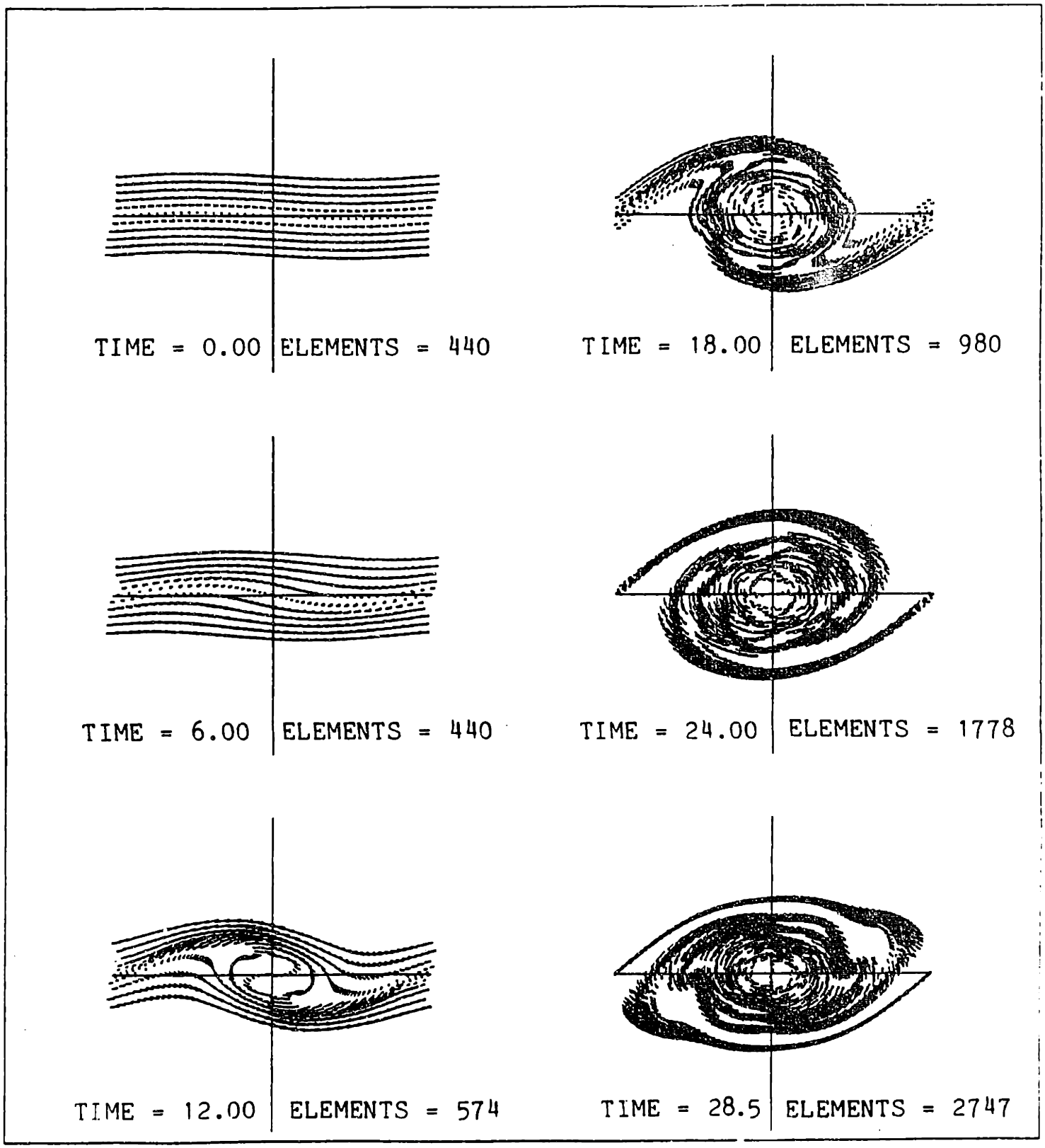

Fig. 12. The location and velocity of the vortex elements. $\lambda=\lambda^*$, with $\varepsilon/\lambda=0.01$.

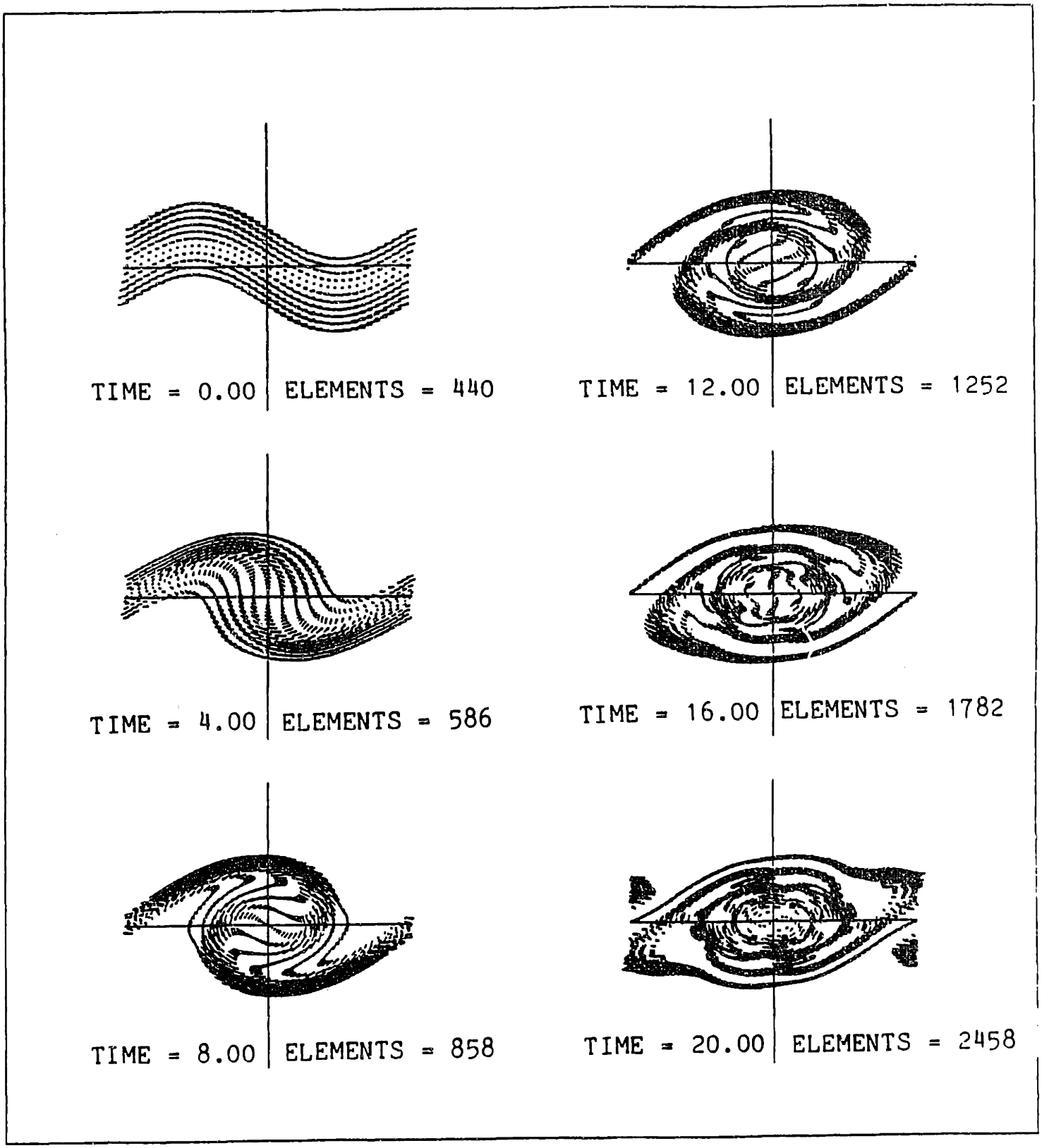

Fig. 13. The location and velocity of the vortex elements. $\lambda=\lambda^*$, with $\varepsilon/\lambda=0.1$.

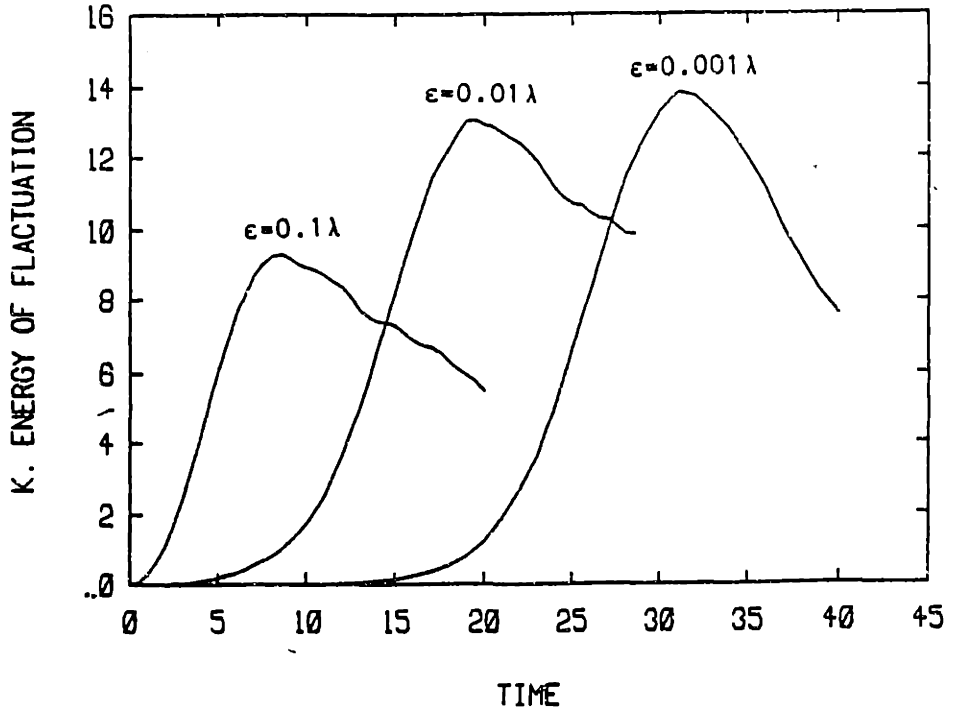

Fig. 14. The total kinetic energy of the perturbation based on the perturbation velocity.

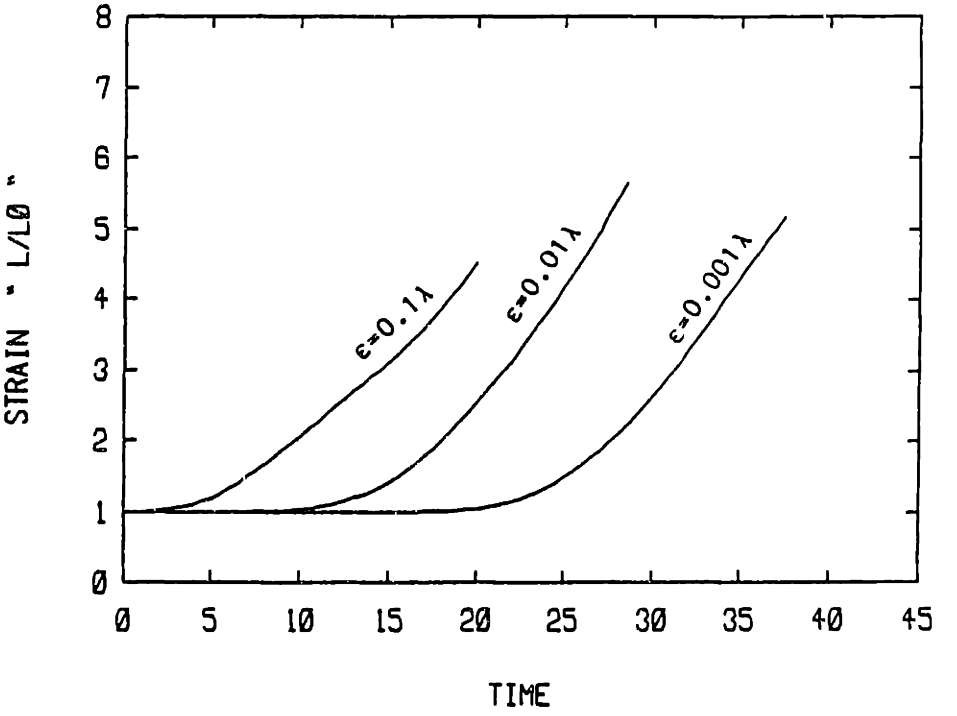

Fig. 15. The total length of the interface, originally at y=0, with time for the cases presented in Figs. 11, 12, and 13, normalized with respect to its length at time t=0.

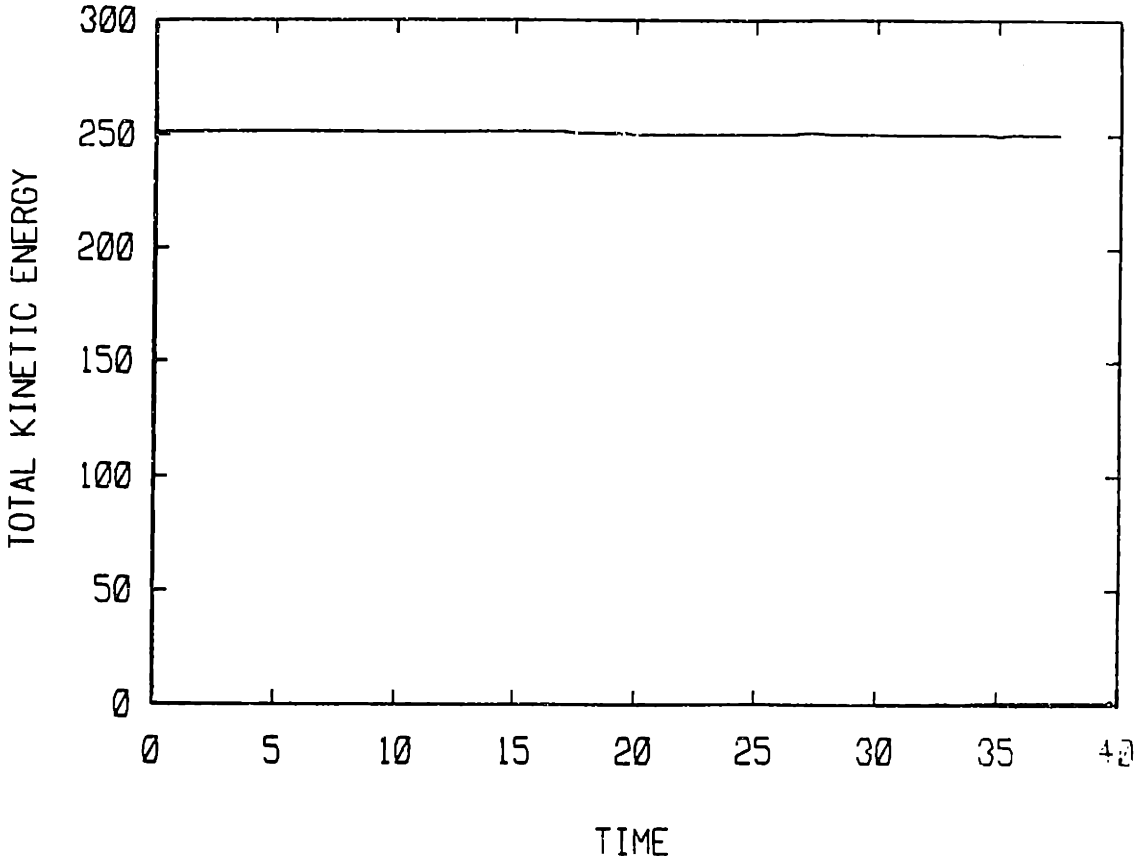

Fig. 16. The total kinetic energy of the flow, u^2 for ε/λ=0.001, 0.01, and 0.1.

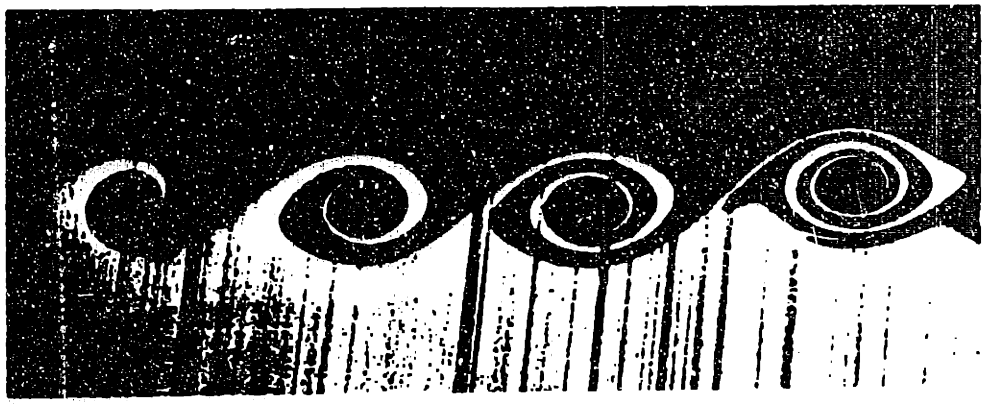

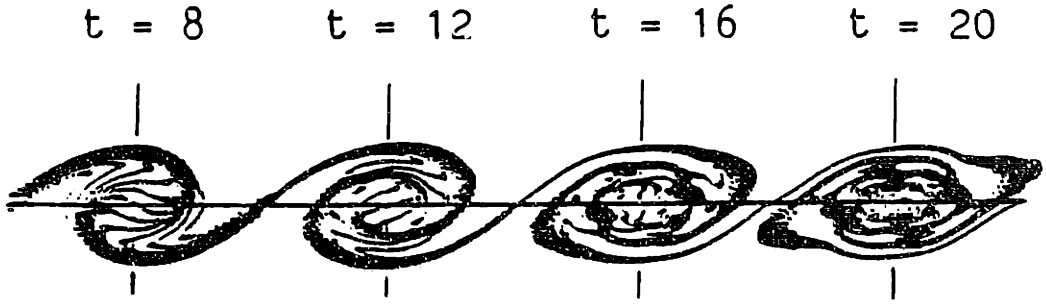

Fig. 17. The evolution of the vorticity field with time, compared with the experimental results of Roberts et al. [23] for spatial development of a small perturbation of a shear layer.

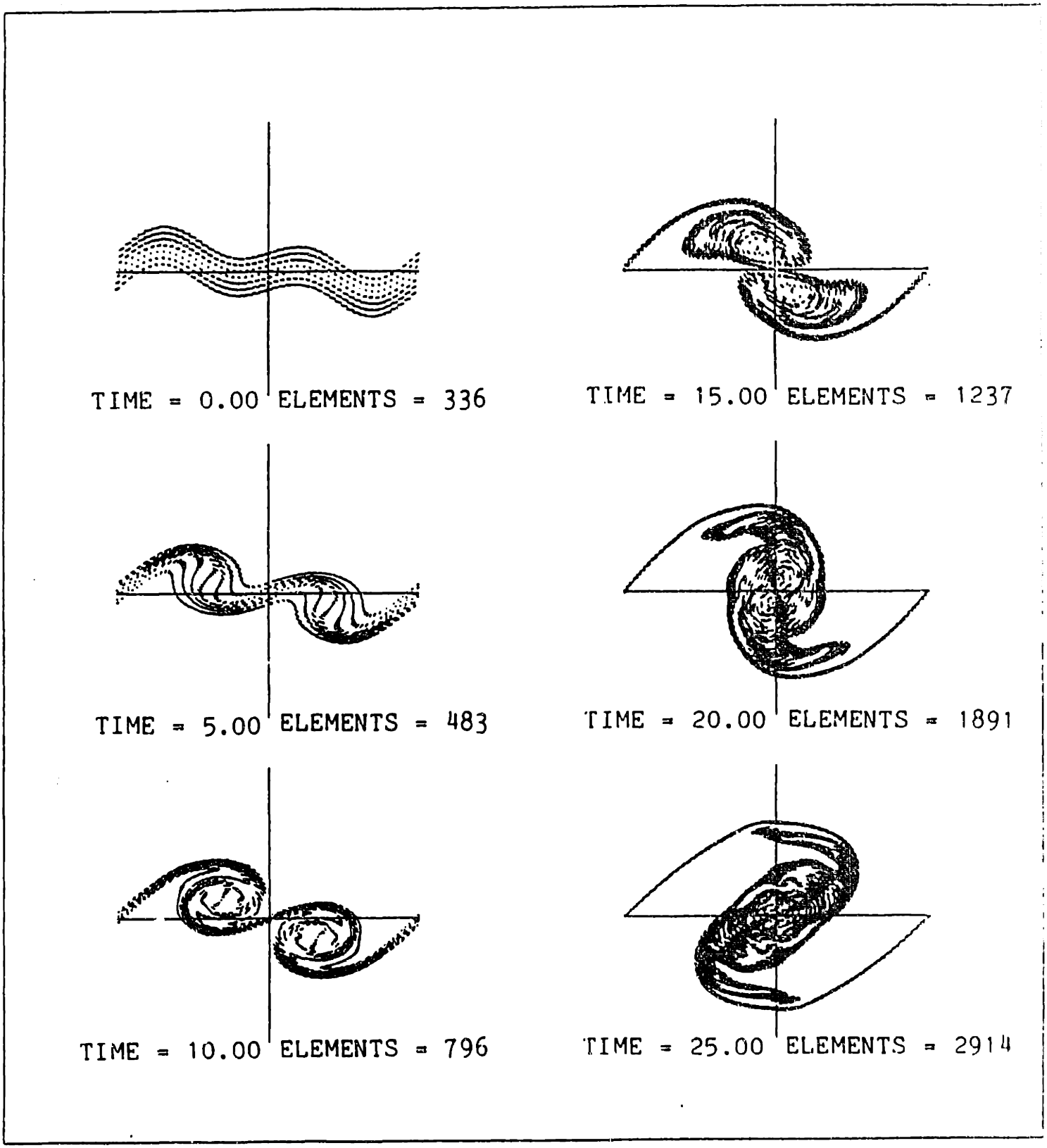

Fig. 18. The location and velocity of the vortex elements for two perturbations, $\lambda_F=\lambda^*$ and $\lambda_S=2\lambda^*$, with $\varepsilon_F=\varepsilon_S=0.1\lambda^*$.

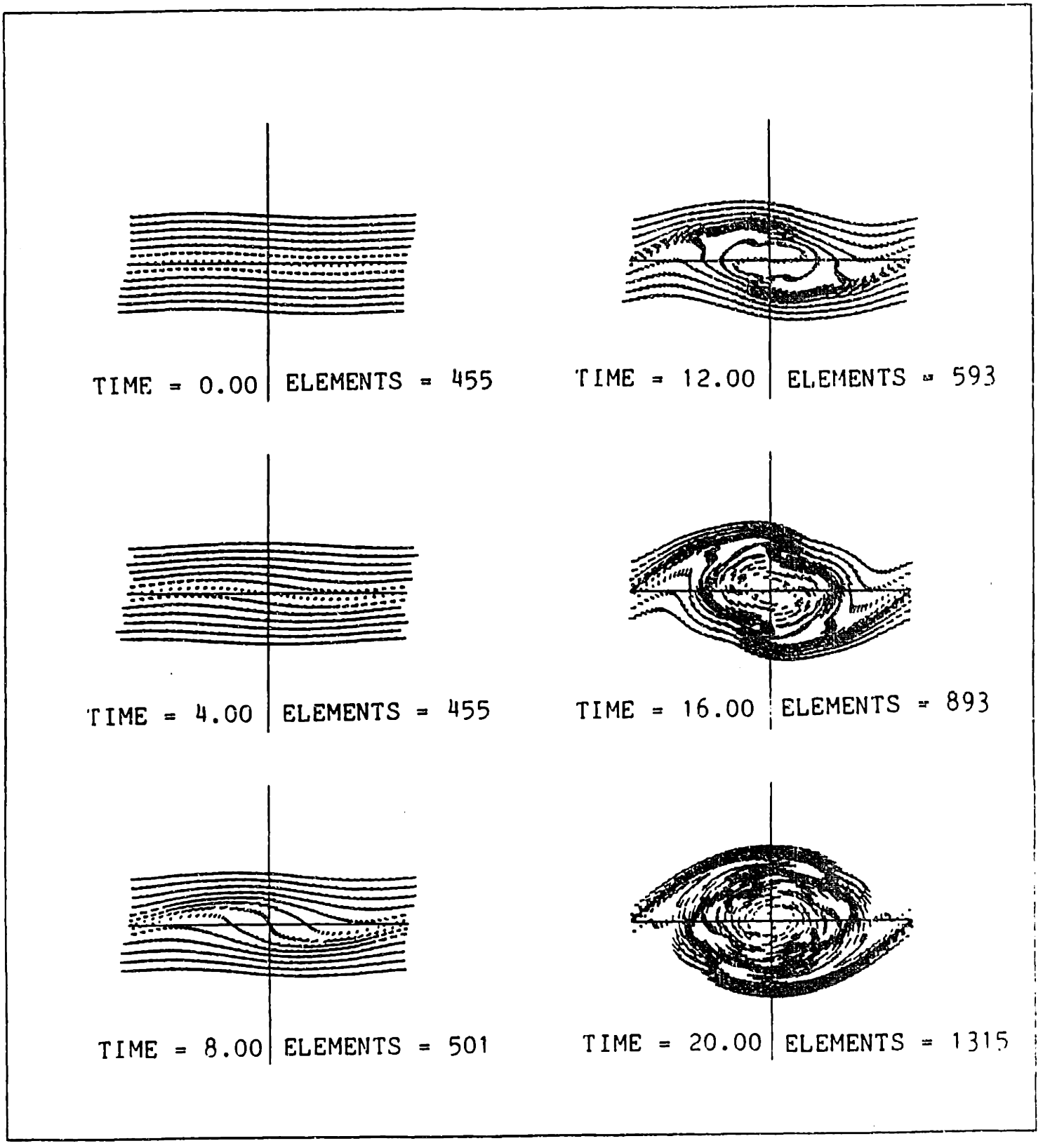

Fig. 19. The location and velocity of the vortex elements for λ=10.5, and ε/λ=0.01.

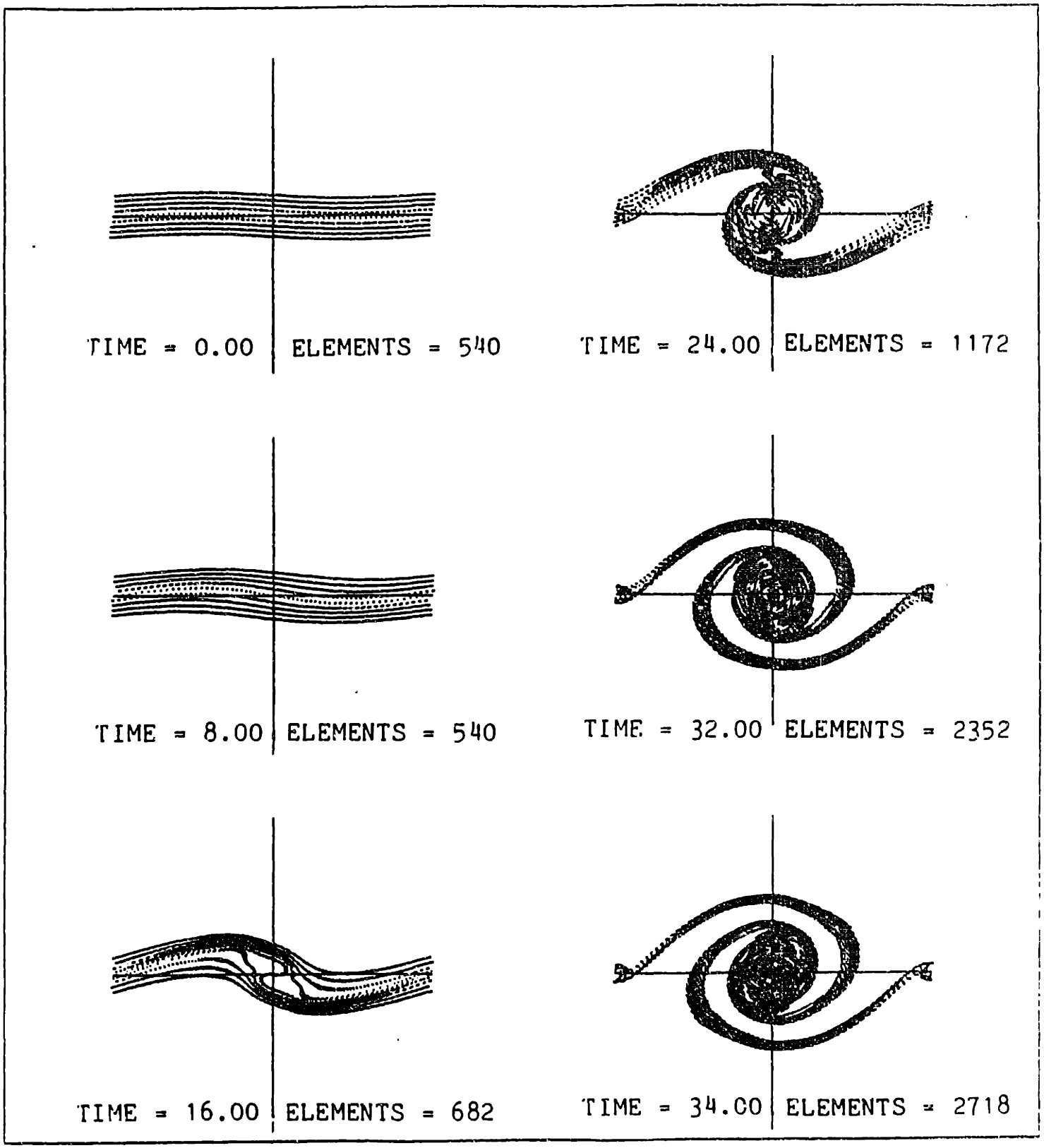

Fig. 20. The location and the velocity of the vortex elements for $\lambda=2\lambda^*$, $\varepsilon/\lambda=0.01$.

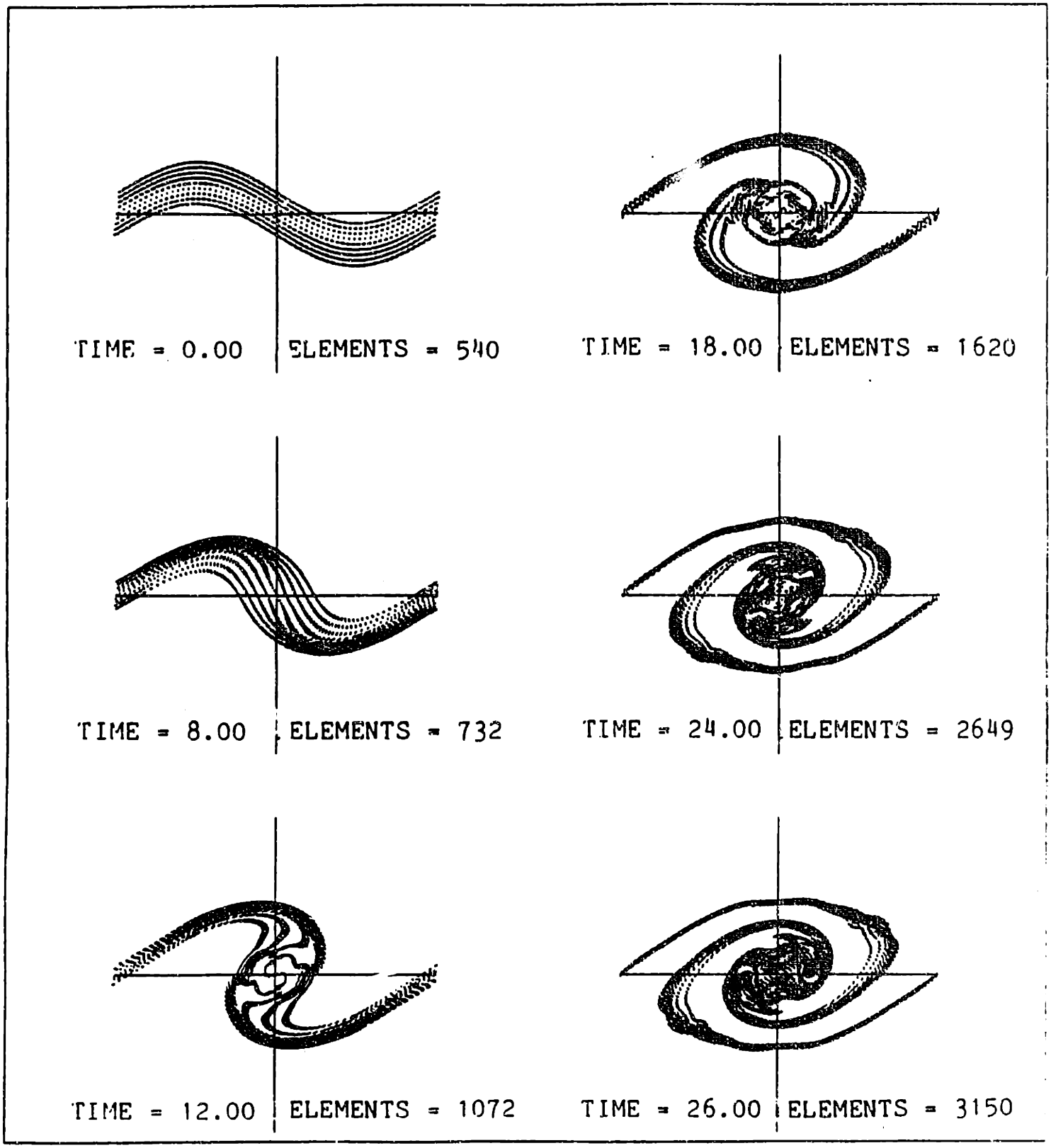

Fig. 21. The location and the velocity of the vortex elements for $\lambda=2\lambda^*$, $\varepsilon/\lambda=0.1$.

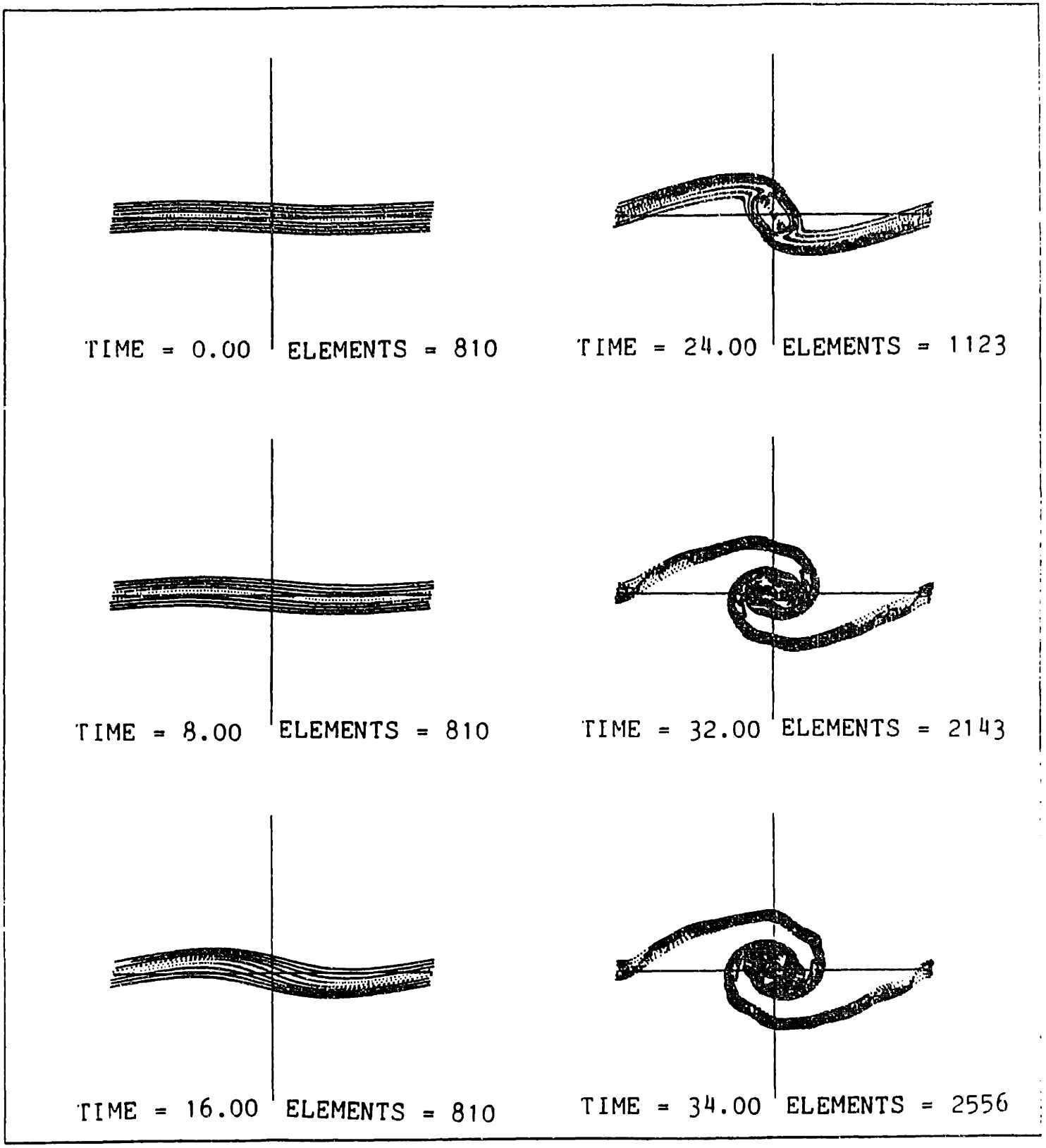

Fig. 22. The location and the velocity of the vortex elements for $\lambda=3\lambda^*$, $\varepsilon/\lambda=0.01$.

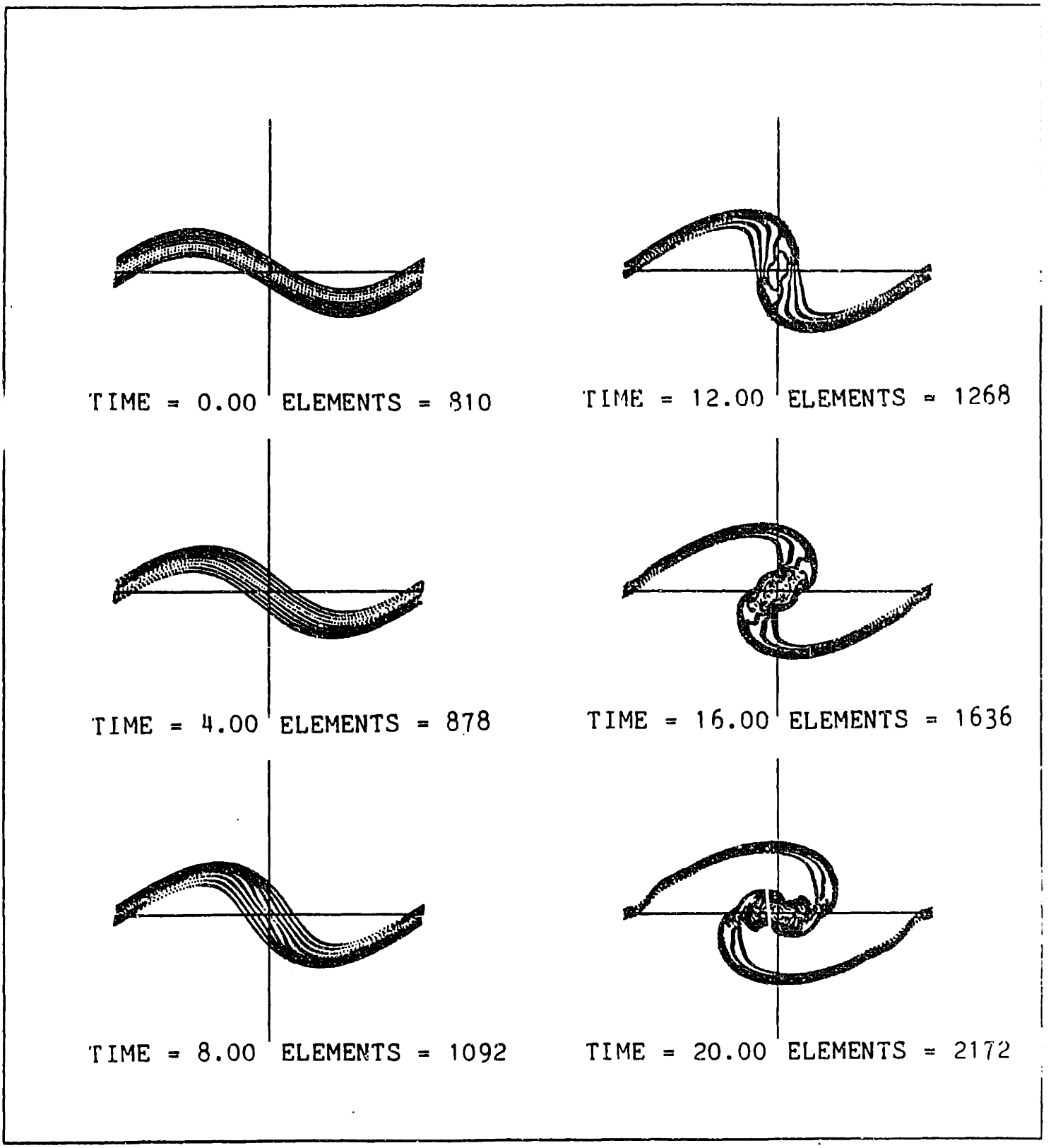

Fig. 23. The location and the velocity of the vortex elements for $\lambda=3\lambda^*$, $\varepsilon/\lambda=0.1$.

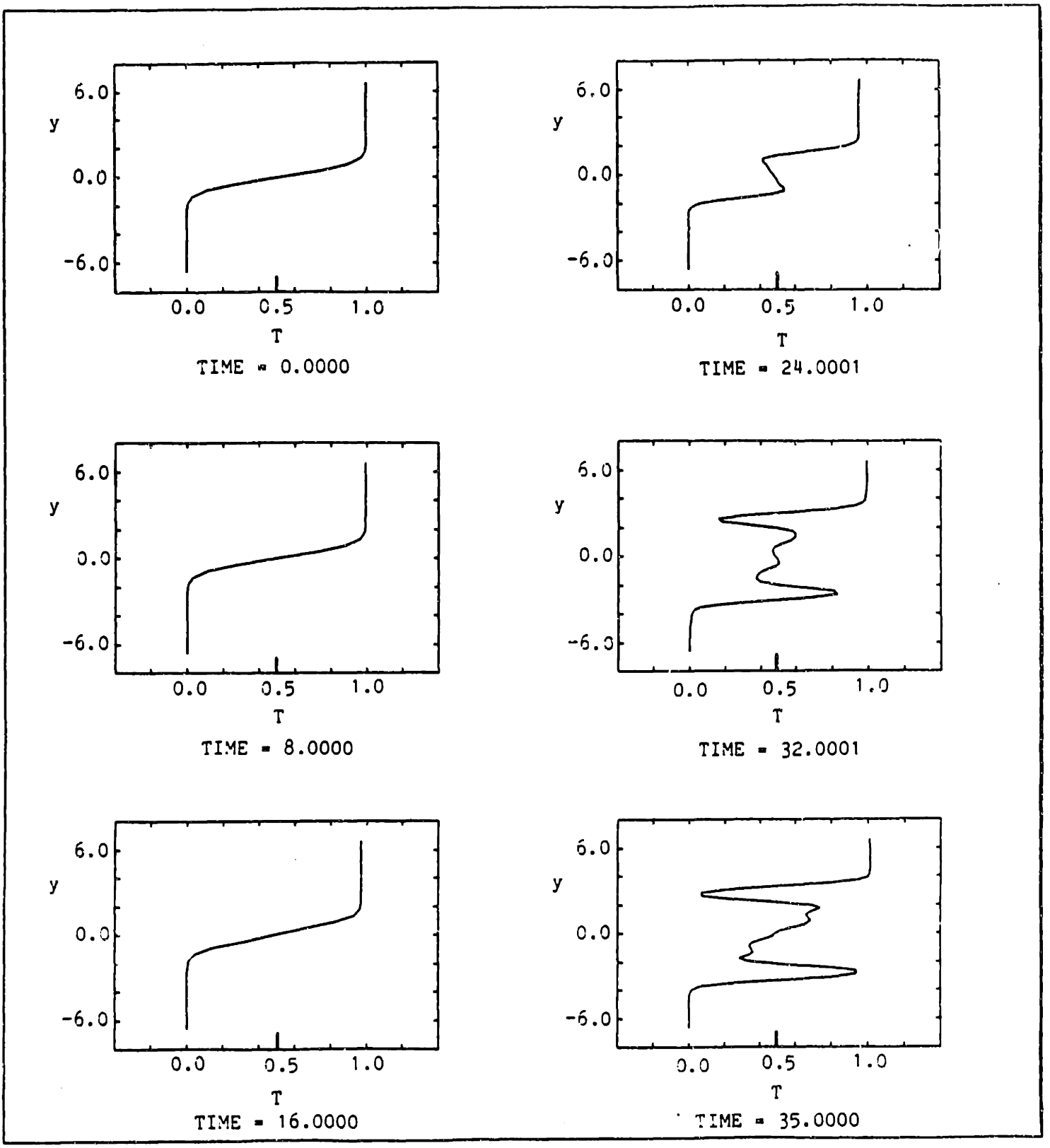

Fig. 24. The temperature distribution across the layer at the center of the core, for λ^* and $\varepsilon/\lambda=0.001$.

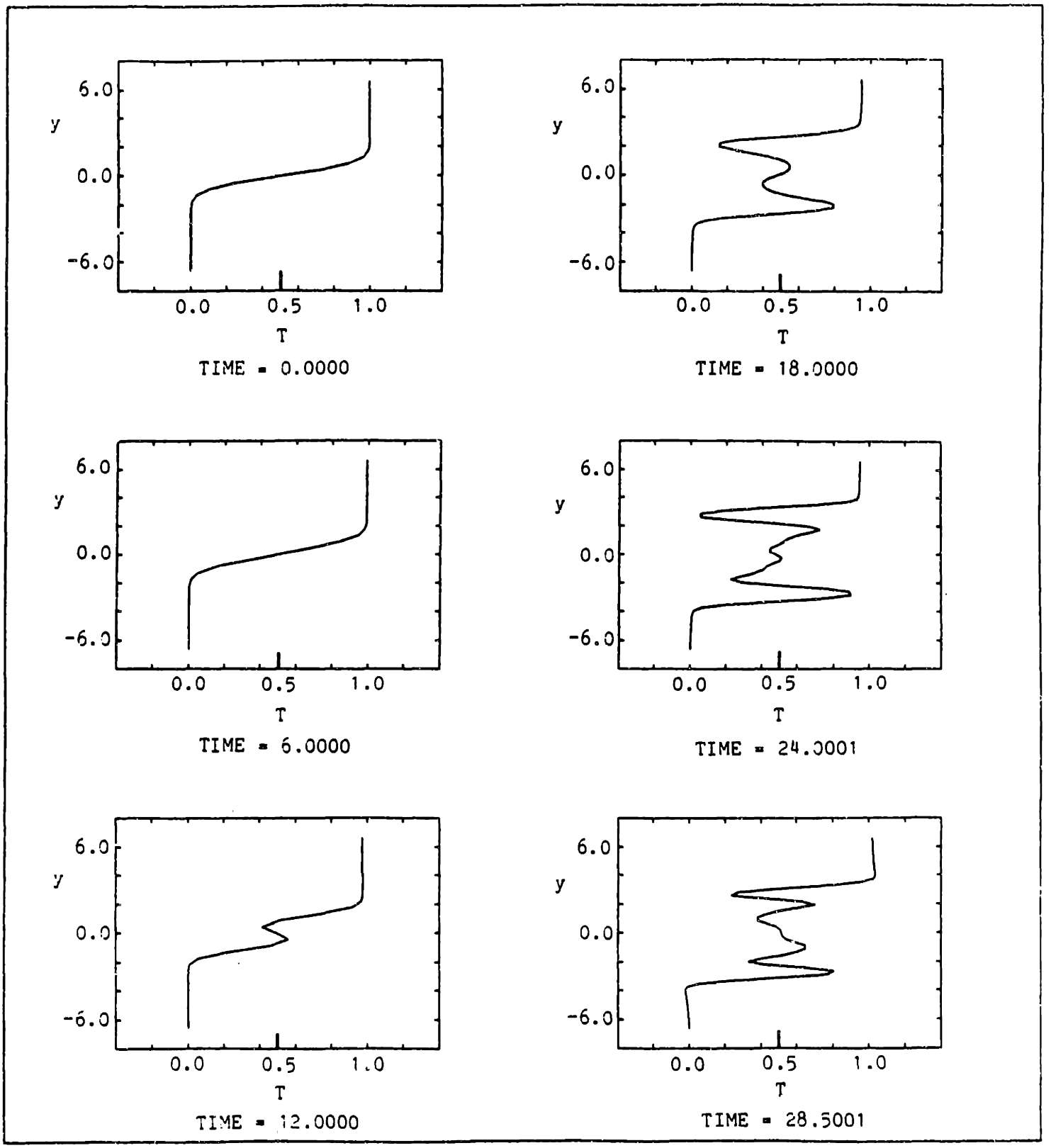

Fig. 25. The temperature distribution across the layer at the center of the core, for λ^* and ε/λ=0.01.

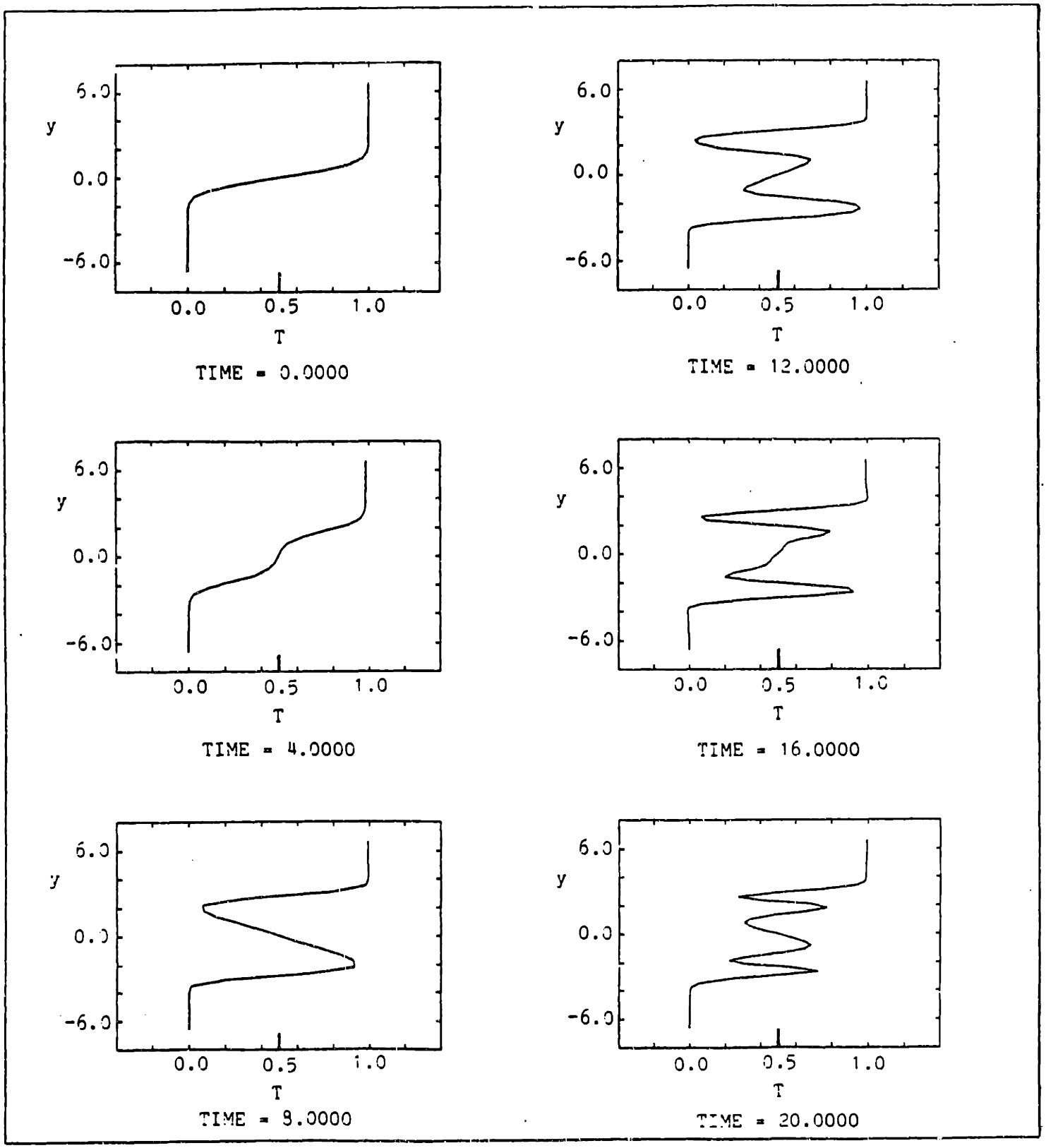

Fig. 26. The temperature distribution across the layer at the center of the core, for λ^* and ε/λ=0.1.

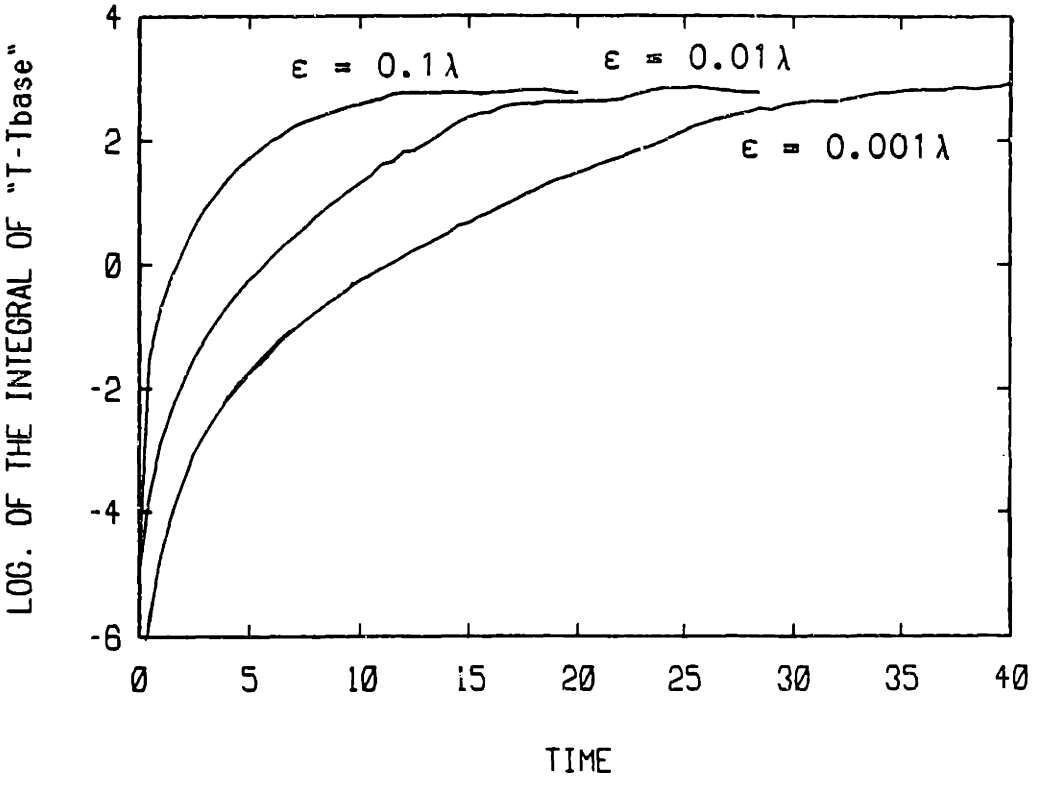

Fig. 27. The variation of the logarithm of the temperature thickness γ with time for the cases in Figs. 10, 11, and 12.

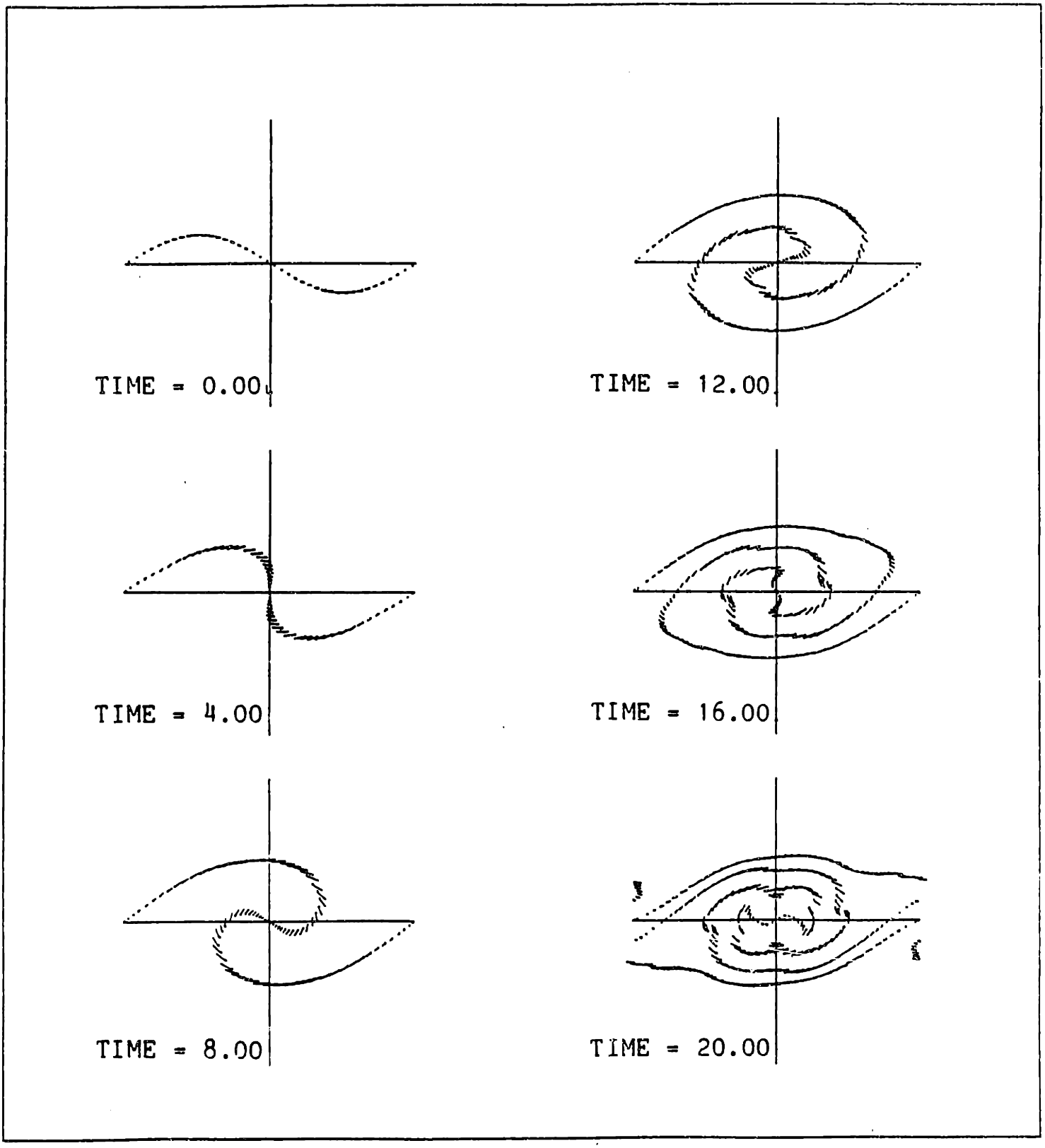

Fig. 28. The roll-up of the interface, defined by the layer which coincide with y=0 at t=0 for the case shown in Fig. 12.

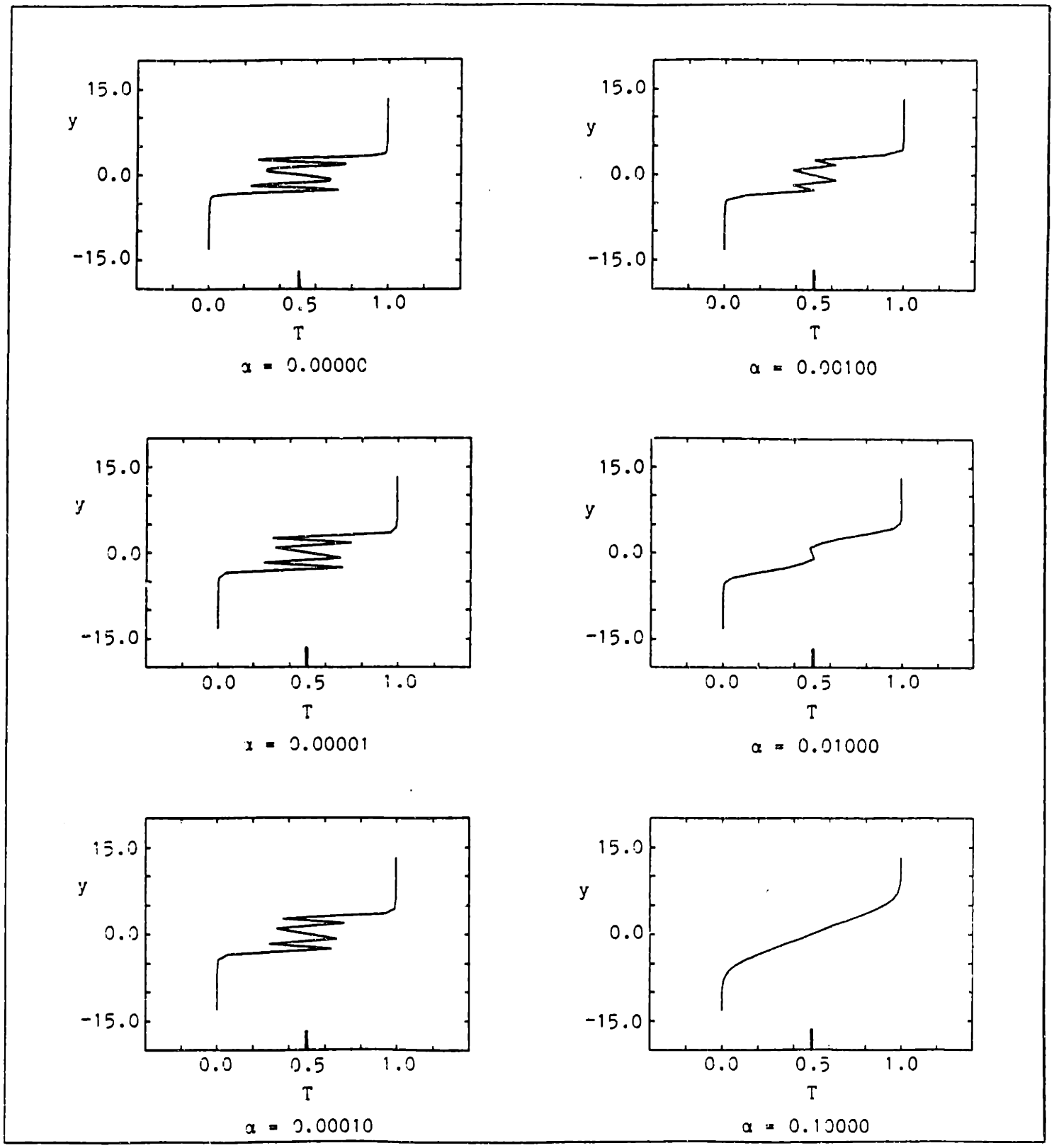

Fig. 29. The effect of thermal diffusion on the temperature distribution across the layer. Temperature is at t=20 for the case shown in Fig. 12.

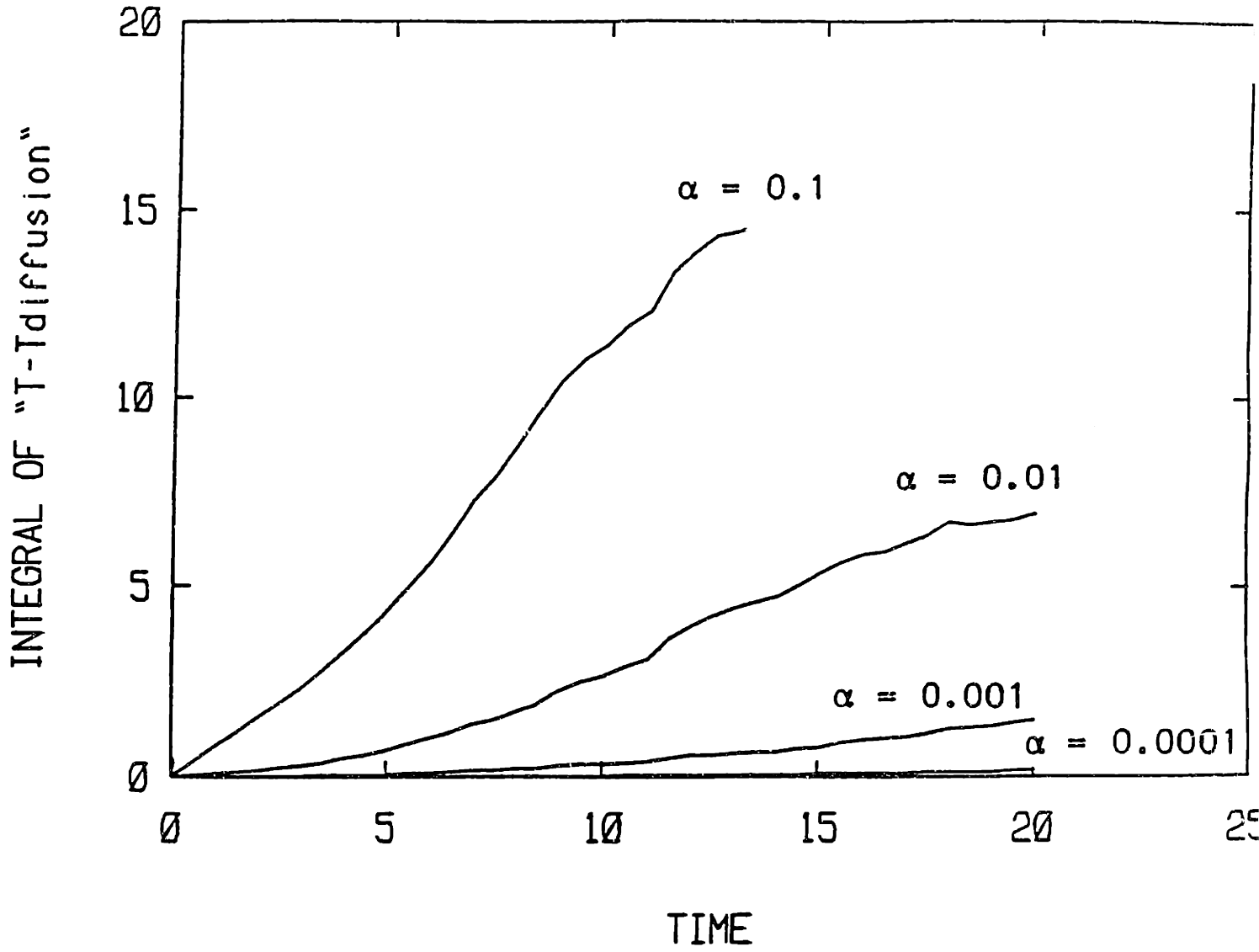

Fig. 30. Total mixing M(t,α,0.1) due to the combined action of enetrainment and diffusion, evaluated for different value of α.

Chapter 5

NON-REACTING SPATIAL SHEAR LAYER

In the spatial model of the shear layer, two streams having the same density but different velocities are brought together downstream of a splitter plate. In this case, the velocity difference, ΔU, which was absent in the temporal model is an important parameter. Larger ΔU means larger shear between the two stream, and hence stronger strain field, stronger entrainment and probably higher rates of mixing.

In the computations, the vorticity is generated at an average rate of $d\Gamma/dt = \Delta U\, U_M$ at the tip of the splitter plate, where U_M is the mean velocity of the two streams. The vorticity generated during each time step, Δt, is discretized among a finite number of overlapping elements of radially symmetric cores which are positioned in the form of columns and layers downstream from the tip. As time elapses and the newly introduced elements move downstream, the distance between the neighboring elements exceeds its initial values due to development of a strong stretch. Large scalar gradients are generated and the flow map is strongly distorted, and therefore the initially overlapping elements can not be maintained. The maximum distance between the neighboring elements which is defined as a multiple of the original spacing, is used as a measure of stretch, and the vorticity and scalar fields are continuously redistributed. We found that at least 5 layers in the cross stream direction are necessary to recover the velocity and scalar values with reasonable accuracy.

5.1. RESULTS OF THE LINEAR THEORY

The development of mixing layers downstream of a splitter plate is initially dominated by a linear instability mechanism. The initial vorticity

distribution is inviscidly unstable to small perturbations via the Kelvin-Helmholtz instability mechanism. Thus, two-dimensional waves grow with downstream distance and are observed to roll up into vortices. The spatial growth rate, $-\alpha_i$, is the eigensolution of Rayleigh equation, Eq. (54), in terms of spatially growing waves with $c_i=0$ and $c_r>0$.

The nondimensional spatial growth rate, $-\alpha_i\theta/R$, vary with Strouhal number, $S_t=f\theta/U_M$, in the fashion displayed in Fig. 31. These data are collected by Ho and Huerre [70], and $R=\Delta U/2U_M$ is known as the velocity ratio and θ is the momentum thickness of the shear layer. The Strouhal number $(S_t)_n=0.032$ for the most unstable wave corresponds to the natural frequency f_n of the shear layer: it changes by only 5% for $0<R<1$. In the limit of small shear, $R<<1$, the nondimensional spatial and temporal growth rates are almost equal.

5.2. DYNAMICS

In Fig. 32(a), we plot the instantaneous location and velocity vectors of all vortex elements for the unperturbed shear layer with $U_1=1$, $U_1/U_2=2$ and length of the computational domain $X_{exit}=6$. The velocity vectors are plotted relative to the mean velocity of the two streams. In Fig. 32(b), the same is plotted for an unperturbed layer with $U_1=1$, $U_1/U_2=3$ and $X_{exit}=5$. The plots exhibit a very clear and accurate portrait of the roll up and pairing processes of the vorticity layer. Evidently the growth of the layer can be divided into two ranges: a linear range in which the random perturbations grow selectively and lead to the organization of the vorticity into semi-round structures, and a non-linear range in which the vorticity field is formed of large eddies that move downstream and interact by pairing. During the roll up, the vorticity within the shear layer is attracted toward the center of a

large eddy, entraining fluid from both sides and forming what appears, in a reference frame moving with the large eddy, to be a moving focal point of a spiral. Between neighboring large eddies, a zone of strong strain is developing where the vorticity is depleted and scalar gradients are growing.

This "braids" zone can be described as a moving saddle point where locally, and in a frame of reference which moves with the large eddy, the fluid flow experiences a separation into two stream; one moving to the left and the other moving to the right with respect to the saddle point (the saddle point is a stagnation point in a frame of reference moving with the large eddy). Downstream, the process of roll up continues until a stronger perturbation forces two neighboring eddies to interact in a pairing process. Since the layer is perturbed by the elliptic effect which results from deleting the vortex elements at the exit plane, and because this perturbation is not applied in a regular manner, the structure of the layer is less organized.

In both cases, three generations of eddies are seen within the computational window: eddies which form due to the roll up of the vorticity layer, eddies which form due to the pairing of two of these eddies, and eddies which form due to the pairing of two of the paired eddies. We call these three types of eddies by the type of instability that promotes their formation: "fundamental" eddies, "first subharmonic" eddies, and "second subharmoinc" eddies. We note that as the velocity ratio across the layer is increased, the number of computational elements used to discretize the vorticity and the scalar gradient fields increases substantially. This is due to the stronger shear, vorticity and strain fields that develop at higher velocity ratios. The computations automatically capture these changes without degrading the resolution, but at the expense of increasing the time.

The frequency of shedding the fundamental eddies in both cases can be computed as follows. The wavelength of the large eddies is $\lambda \sim 0.5$ in both cases. The corresponding Strouhal number based on the momentum thickness, θ, is $S_t = f\ \theta/U_M = \theta/\lambda = 0.033$, where f is the shedding frequency. The computation of the momentum thickness will be shown in the next section. This Strouhal number is very close to the Strouhal number for the most unstable mode of a spatially growing shear layer calculated from the linear stability theory. It is important to note that not all eddies are shed at this frequency. As shown in in Section 5.1, this is a broad band instability which can support a wide range of frequencies. However, we found that most of the eddies are shed at, or very close to this most unstable frequency. This can be explained by the fact that the gain curve, shown in Fig. 31, is flat around its maximum.

Similar remarks could be made about the pairing process. Most of the time, as soon as two eddies are shed they pair into one larger structure. However, once every few cycles, an eddy escapes pairing and flows as a single eddy to the exit of the domain. We also found that three eddies can "pair" simultaneously, forming a structure with a wavelength equal to 3λ.

In order to examine the effect of forcing on the structure of the shear layer, we perturb the layer at frequencies close to the most unstable mode and its first subharmonic by oscillating the incoming vorticity layer according to $\Delta y=\varepsilon_F \sin(2\pi U_M t/\lambda^*)+\varepsilon_S \sin(4\pi U_M t/\lambda^*)$. Here Δy is displacement of the center of the vortex element due to the forcing, t is time, and ε_F and ε_S are the amplitudes of the fundamental and subharmonic respectively. This is similar to the forcing produced by mounting a loadspeaker on the top wall directly above the tip of the splitter plate and using this speaker to send acoustic waves at the amplitude and frequency defined by this relation. Under the

forcing condition, the evolution of the layer is expected to be more organized.

In Fig. 33, we plot the structure of the layer for $\varepsilon_F=0.01\lambda^*$, $\varepsilon_S=0$ with $\lambda^*=0.5$. The amplitude of the perturbation is kept small to distinguish between the linear range and the non-linear range of growth. It is clear that after the linear range of growth of the perturbations, large eddies are shed at the forcing frequency. Contrary to the unforced case, pairing is delayed further downstream. Thus, while this small amplitude forcing is incapable of increasing the rate of amplitude of the perturbation, it organizes the shedding process and delays the growth of the subharmonic perturbations. Pairing is resumed after the effect of forcing decays.

In order to study the structure of the layer under higher amplitude perturbations, we plot the structure of the layer for $\varepsilon_F = 0.05\lambda^*$, $\varepsilon_S=0$, $\lambda^*=0.5$ along with $U_1/U_2=3$ in Fig. 34. The structure of the layer is different than that in the previous cases in the following ways: (1) there is no linear range since the higher physical perturbation suppresses any other randomly generated perturbations, and the layer responds immediately by closely following the forcing frequency; (2) the larger the amplitude, the more pairing is delayed and the layer is organized.

In Fig. 35 we plot the structure of the layer perturbed by the fundamental and subharmonic frequencies, $\varepsilon_F=\varepsilon_S=0.01\lambda^*$. The plot shows that there is a linear range of the growth of the fundamental perturbation but it is shorter than that of the unforced layer. The presence of the subharmonic perturbation simulates and speeds up the pairing interaction in an organized manner. For more on the forced layer, see Ghoniem and Ng [26].

5.3. TRANSPORT OF PASSIVE SCALAR

We have used the transport element method to investigate the mixing process by passively transporting a scalar throughout the domain under the combined effect of entrainment and diffusion. The distribution of the concentration of a scalar diluted in an inert base flow immediately downstream of the splitter plate is described by an error function, $c(0,y-0.5)=0.5\{1-\mathrm{erf}[(y-0.5)/0.5\Delta]\}$, where Δ is the thickness of the layer at time t=0. The corresponding scalar gradient is a Gaussian, similar to the vorticity distribution. Computations were performed for different values of the Peclet number to show the effect of molecular diffusion on the mixing dynamics at high Reynolds numbers.

Figure 36 shows the instantaneous profiles of the scalar, c, at different sections downstream the channel superimposed on the instantaneous distribution of the vortex, or transport elements for purely inviscid calculation, $P_e=\infty$ (see Fig. 32(a) at time=51). The sections are chosen at the centers of the vortex eddies in Fig. 36(a), and across the braids in Fig. 36(b). The distributions show that even at sections far downstream of the splitter plate, zones of completely unmixed fluid still exists within the layer (unmixedness). These zones correspond to the gulfs, or "tongues", of pure fluid brought into the layer from either side by the inviscid mechanism of entrainment, i.e., the convective transport of fluid across the centerline of the layer by the roll up of the vorticity field.

Instantaneous concentration profiles show clear signs of asymmetric entrainment within the large structures. Mixing asymmetry, which arises due to the asymmetric growth of the eddies during the initial stages of roll up, is indicated by the fact that the profiles are not symmetric around the line c=0.5. Comparing Fig. 36(a) with the results of the temporal model in which the boundary conditions are periodic, one sees that the concentration profiles

in Figs. 24-26 are perfectly symmetric around the line c=0.5 at all times. Thus, asymmetric entrainment is due to the asymmetric flow field generated by unequal free stream velocities on the two sides of the layer and by the downstream growth of the vorticity concentration in the cross-stream direction in the spatially-growing layer.

We also learn from Fig. 36(a) that the average concentration of the scalar in the fluid within the eddy is less than the mean average of the concentration on the two streams. The fluid trapped within the eddy is defined by concentration $0 < c < 1$, but not equal to either 0 or 1. The average value of the concentration within the eddy is known as the preferred mixture fraction, c_p. Since $c_p < 0.5$, as indicated by Fig. 36(a), the eddy entrains more fluid from the high-speed stream where $0 < c < 0.5$ than from the low-speed stream where $0.5 < c < 1.0$. The value of c_p depends weakly on the x-location but strongly on the velocity ratio.

Asymmetric entrainment indicates that the structure may not have started to move at exactly the mean velocity of the two stream since it first appeared within the layer. This is evident from the history of the velocity component imposed by the incoming streams on the flow downstream of the splitter plate. This component decays from values close to that of the velocity of the high-speed stream near the tip of the plate to values equal to average of the two streams some distance downstream.

To show the asymmetry of entrainment associated with the formation of the large scale structures, we plot the scalar contours for a single eddy located at $x \sim 4.0$ at time $t = 40.65$ in Fig. 37. In Fig 37(a), the flow is totally inviscid, $P_e = \infty$, and the entrainment from both streams into the large structure is shown in the form of extended "tongues" that reach into the core of the eddy. Clearly, the tongue of the high-speed stream is larger and

reaches deeper into the eddy than that of the low-speed stream. In order to show the asymmetric mixing associated with the asymmetric entrainment, the same eddy is represented in Fig. 37(b) for the flow when there is a finite diffusion effect, $P_e = 2500$. The figure shows that the scalar gradients are smoother and that the island of the fluid with $c < 0.5$ is larger than that with $c > 0$.

5.4. STATISTICS OF THE NUMERICAL RESULTS

In order to validate our scheme, we compare the numerical results with the experimental measurements of Masutani and Bowman [55]. This experiment was selected for comparison because the two-dimensionality of the flow was carefully maintained and verified, and hence it provides experimental measurements of mixing statistics before mixing transition occurs. Mixing transition occurs further downstream due to the growth of three dimensional structures around the two-dimensional structures.

Figure 38 shows the mean momentum thickness of the layer, θ. The growth of the layer can be divided into the "linear" and "non-linear" ranges. What we called the linear range (following the definitions of the linear theory of stability) exhibits a plateau, followed by a small but exponential rise in θ. In the nonlinear range, the value of θ increases linearly with $d\theta/dx=0.0165$. The computed value of $d\theta/dx$, while smaller than the value measured by Masutani and Bowman [55], falls in the middle of the scatter of the experimental data documented by Ho and Huerre [70]. It should be noted that Masutani and Bowman [55] remarked that the growth rate of their layer is about 15-20% larger than the value measured by the majority of other experiments. The effect of difference in the growth rate will appear in all

the comparisons: the experimental profiles spread out into the free streams faster than the predicted profiles.

The average streamwise velocity and root-mean-square of its fluctuations are shown in Figs. 39 and 40(a). The plots show that the averaged streamwise velocity reaches a self-similar distribution early downstream, which also resembles the initial error function velocity distribution of the vorticity layer. On the other hand, velocity fluctuation statistics reach a self-similar state some distance further downstream. The transition region for the development of the velocity fluctuation is most likely within the region of growth of the initial perturbation and before a "mature" eddy has formed. As shown in Figs 39 and 40(a), the numerical results agree well with the measurement of Masutani and Bowman [55] in a two-dimensional shear layer. The agreement will improve substantially if $(y-y_0)$ is normalized with respect to the local momentum thickness $\theta(x)$ instead $(x-x_0)$ since this will absorb the difference between the spread rates of the two layers. The average cross-stream velocity fluctuation is shown in Fig. 40(b), while the Reynolds shear stress is shown in Fig. 40(c). While Masutani and Bowman [55] did not report experimental data on either quantity, both curves strongly resemble measurements reported by other investigators.

It is important to emphasize that the velocity fluctuations are due to flow unsteadiness imposed by the formation and interactions of the large eddies. The unsteadiness arises due to flow instability, regardless of the boundary conditions, which are steady, and leads to the augmentation of interaction between the two streams via the fluctuation fluxes. The order of magnitude of these fluctuations, in each direction, is about 20% of the velocity jump across the layer.

In Fig. 41 we plot the variation of scalar concentration with time. The peak low values of the scalar concentration corresponds to the time when the cores of the large structures pass over the point. In Figs. 41(a) and 41(c), since the flow is completely inviscid, the fluctuations are higher, the gradients are sharper, and the state of the scalar is almost unmixed, i.e., there is a strong drop between 0 and 1. In Figs. 41(b) and 41(d), the distribution of the scalar is more homogenized and the mean value can be better guessed. However, in both figures, and at the extension of the splitter plate, y=0.5, the average value of the scalar is not the same as the average of the scalar concentration in the two streams, 0.5. This is because of the asymmetry of the entrainment in the favor of the high speed stream, and the shift of the center of the eddies toward the low speed side. In fact the average scalar concentration, $c = 0.5$, is achieved at $y \sim 0.42$ rather than $y = 0.5$.

In Fig. 42 we plot the the averaged concentration profiles (a) for different values of the Peclet number at the same streamwise locations, x=5, and (b) at different streamwise location for the same Peclet number, both compared with the data of Masutani and Bowman [55]. The mean concentration profiles differ substantially from the initial error function profile, and develop downstream to form a zone of almost constant value, between two inflection points, around the midsection of the shear layer and toward the high-speed side. This constant value is close to the preferred-mean concentration within the cores. Diffusion, which generates strong fluxes around areas of sharp gradients, tends to make the profiles smoother. However, as shown by Fig. 42, the effect of diffusion on the mean concentration is minor.

A comparison between the mean concentration profiles and the mean velocity profile indicates that the former penetrates further into the free stream than the latter. This supports the hypothesis that, in these shear flows, mixing is entrainment-dominated and the entrainment, while it is a consequence of the vorticity-induced field, acts on the vorticity-free part of the flow by the Biot-Savart effect. Mixing enhancement by the roll up of the shear layer, due to its intrinsic instability, is thus not limited to the neighborhood of the area where $|\omega| \neq 0$. Instead, the mixing zone extends further into the free streams as we move downstream.

The root-mean-squared concentration fluctuations are shown in Fig. 43 for: (a) different values of the Peclet number at the same streamwise location; and, (b) at different streamwise locations for the same Peclet number, both with the experimental measurements of Masutani and Bowman [55]. As expected, at zero molecular diffusion the maximum value of c' approaches 0.5, the unmixed state, indicating that the concentration in the fluid passing by the measurement point is alternating between the two extreme states. With increasing levels of molecular diffusion, the maximum value of c' decreases, and the whole profile attains smaller values showing that the limits between which the values of c is oscillating decrease. The peak and the wide plateau which are observed in this distribution correspond roughly to the transition between the slow stream in which $c=1$ and the mixing core of the eddy.

Figure 43(a) shows that molecular diffusion has a pronounced effect on the concentration fluctuations, emphasizing the influence of diffusion on the instantaneous profiles and on the outcome of time-dependent processes which may take place within the shear layer, such as chemical reactions. Figure 43(b) shows that the concentration fluctuations reach self-similarity downstream of the station at which the mean profiles reach self-similarity,

similar to the velocity profiles. This is not surprising since the controlling transport mechanism here is convection. The figure also shows that the penetration of the transported spices cannot be measured by its mean values only.

Some deviations between the numerical results and the experimental measurements, which may have resulted in different growth rates, may be attributed to the relative amplitude of noise in the numerical and experimental studies, and the expected scatter in experimental results.

The probability-density function of the concentration across the cross section x=5 is shown in Fig. 44 for two values of Peclet number: $P_e=\infty$ and $P_e=2500$. The bimodal shape, characteristic of non-diffusive entrainment, is clearly exhibited by the plot, and is indicative of the absence of numerical diffusion even at such distance downstream. At $P_e=2500$, concentrations at intermediate values of c appear, with higher probability, close to the high-speed side where c~0. Evidence for the existence of a preferred concentration within the core is given in Fig. 44(b). Intermediate values of c appear between the two peaks at c=0 and c=1, with higher probability for $0<c<0.5$ than for $0.5<c<1$.

5.5. CONCLUSIONS

Numerical simulation of a non-reacting, uniform density, spatially-growing, confined two-dimensional shear layer has been performed using a transport element method.

1. The results show that the basic dynamical processes that govern the development of a shear layer are the roll up of the initial vorticity layer into large scale eddies after an initial delay during which perturbations are selectively amplified, and the pairing of these eddies downstream. The most

probable shedding frequency is close to the frequency of the most unstable mode as predicted by the linear stability theory, with small variation around this frequency. Pairing can be described as the roll up of two neighboring eddies, a subharmonic instability. In most cases, pairing occurs between two eddies, but less frequently it occurs among three eddies and at times it does not occur. Pairing is repeated downstream.

2. Forcing the layer by cross-stream oscillations at relatively small amplitudes enables the layer to skip the initial linear growth phase and shed eddies at the forcing frequency immediately downstream of the splitter plate. This is in agreement with the fact that the layer is a linearly unstable flow that responds to very small perturbations within a frequency range. However, if the forcing function is monochromatic and close to the most unstable frequency, forcing delays pairing, i.e., it hampers the growth of the layer downstream. For better organization and continued faster growth, the layer should be forced by a combination of the fundamental and the subharmonic frequencies simultaneously. Thus, growth of mixing layers can be actively controlled in the direction of enhancing or suppressing their growth.

3. The most important difference between the temporal and the spatial models of the shear layer is the explicit dependence of the latter on the velocity difference across the layer. We found that this parameter, for values not equal to unity, leads to mixing asymmetry within the large structure since the layer is forced to entrain more high-speed fluid than low-speed fluid. These unequal entrainment fluxes are induced by an unsymmetric large vortex eddy which forms under the influence of conditions imposed by a non-uniform field governed by the boundary conditions. This asymmetry offers a passive means of controlling the mixing within the layer by exchanging the scalars between the two streams.

4. The statistics of the numerical results show good agreement with the experimental measurements within the non-linear range. These statistics are generated solely by intrinsic instability of the shear layer, which leads to the generation of flow unsteadiness downstream of steady boundary conditions. The statistics of the passive scalar emphasize the important role of molecular diffusion in the mixing process and indicate that a mean preferred mixture fraction, which is different from the average mean of the two streams, exits within the eddies.

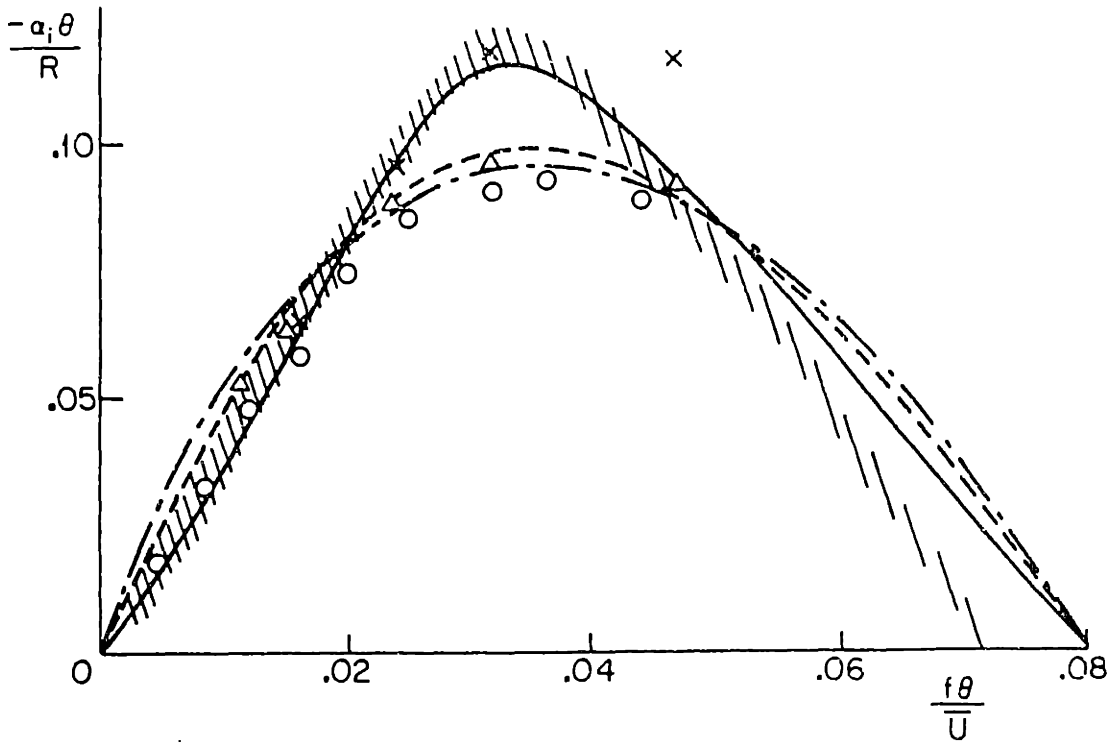

Fig 31. Variations of (a) normalized amplification rate with Strouhal number $f\theta/\bar{U}$. Linear stability theory (from Monkewitz & Huerre 1982): — $R = 1$; —·— $R = 0.5$; — — — $R \ll 1$ Experiments: □ $R = 1$ (Sato 1960); ○ $R = 1$ (Freymuth 1966); × $R = 0.72$ (Miksad 1972); \\\ $R = 1$ (Fiedler et al. 1981); △ $R = 0.31$ (Ho & Huang 1982); ■ $R = 1$ (Drubka 1981).

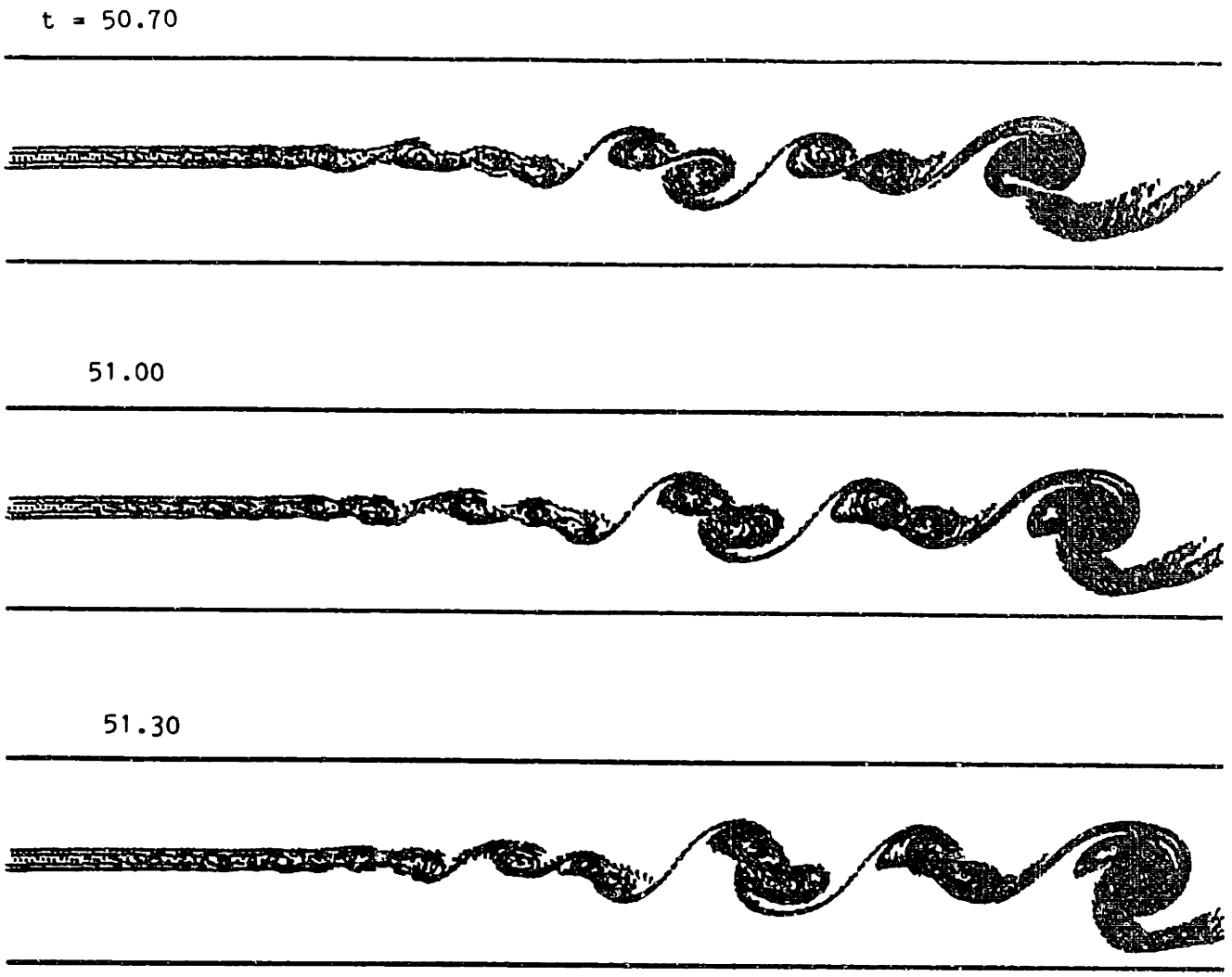

Fig. 32(a). The location and velocity of the vortex elements during the roll-up of a spatial shear layer for $U_1/U_2=2$, $\varepsilon=0$, and $X_{exit}=6$ at different time.

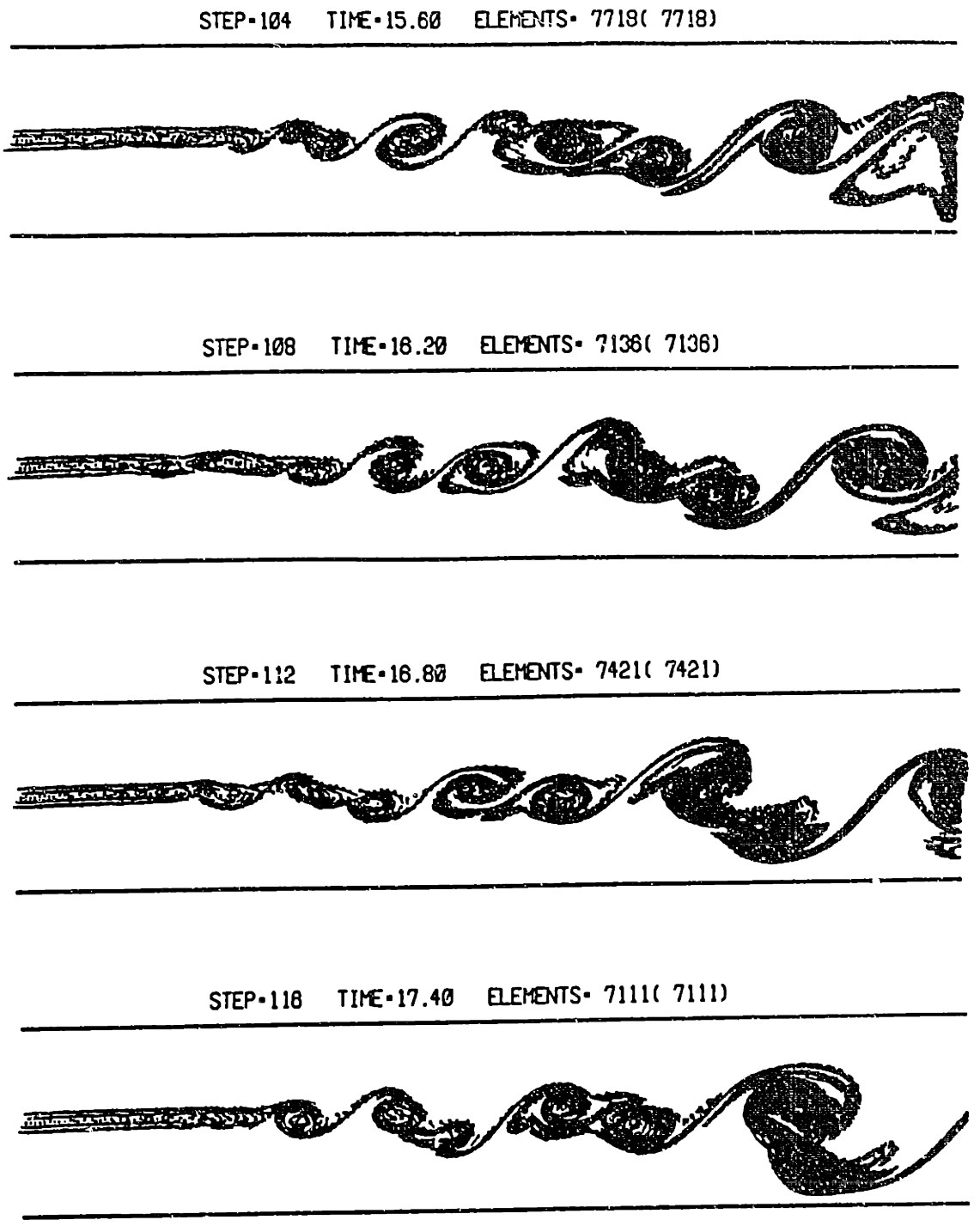

Fig. 32(b). The location and velocity of the vortex elements during the roll-up of a spatial shear layer for $U_1/U_2=3$, $\varepsilon=0$, and $X_{exit}=5$ at different time.

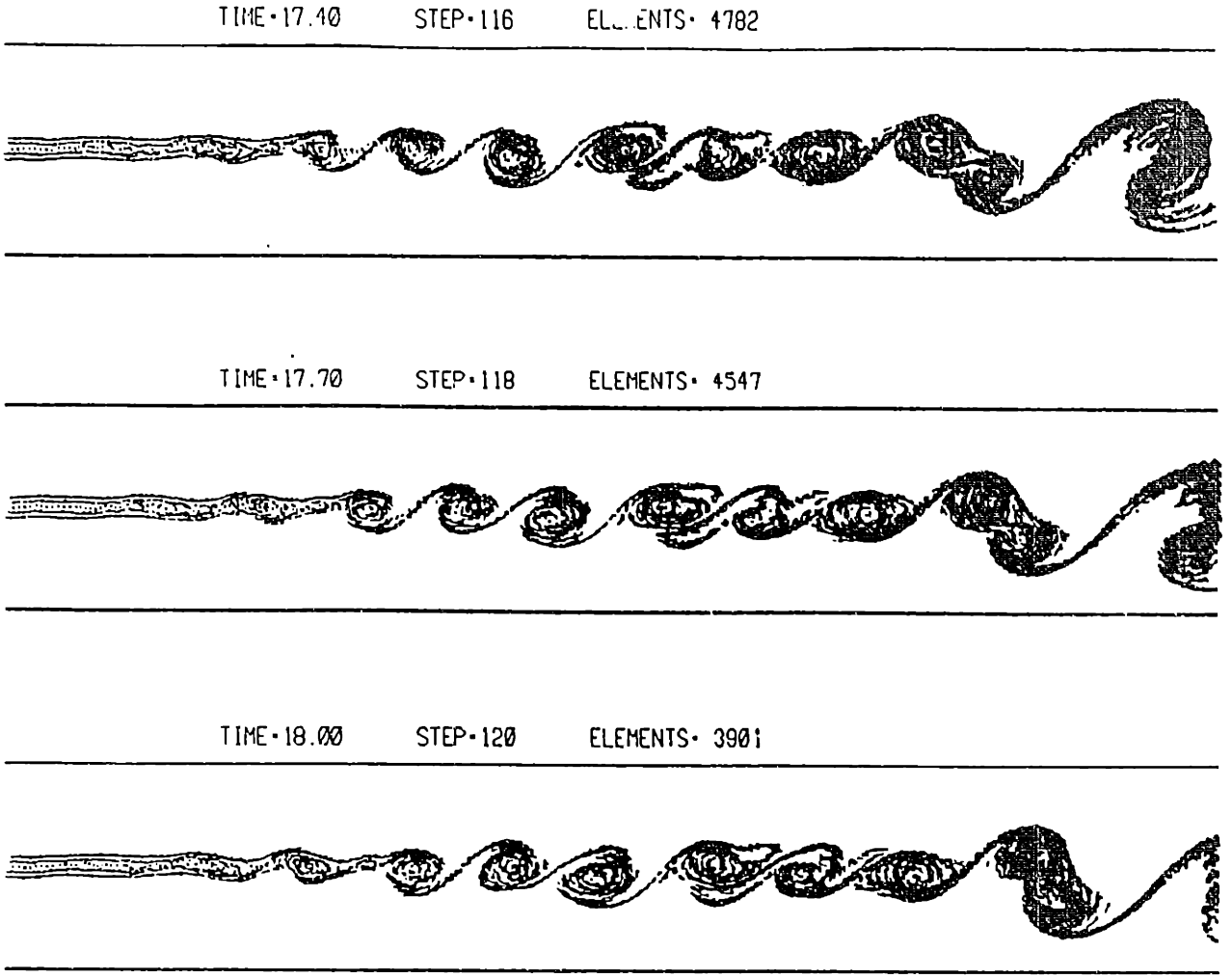

Fig. 33. The location and velocity of the vortex elements during the roll-up of a spatial shear layer for $U_1/U_2=2$, $\lambda=\lambda^*$, $\varepsilon/\lambda=0.01$, and $X_{exit}=6$ at different time.

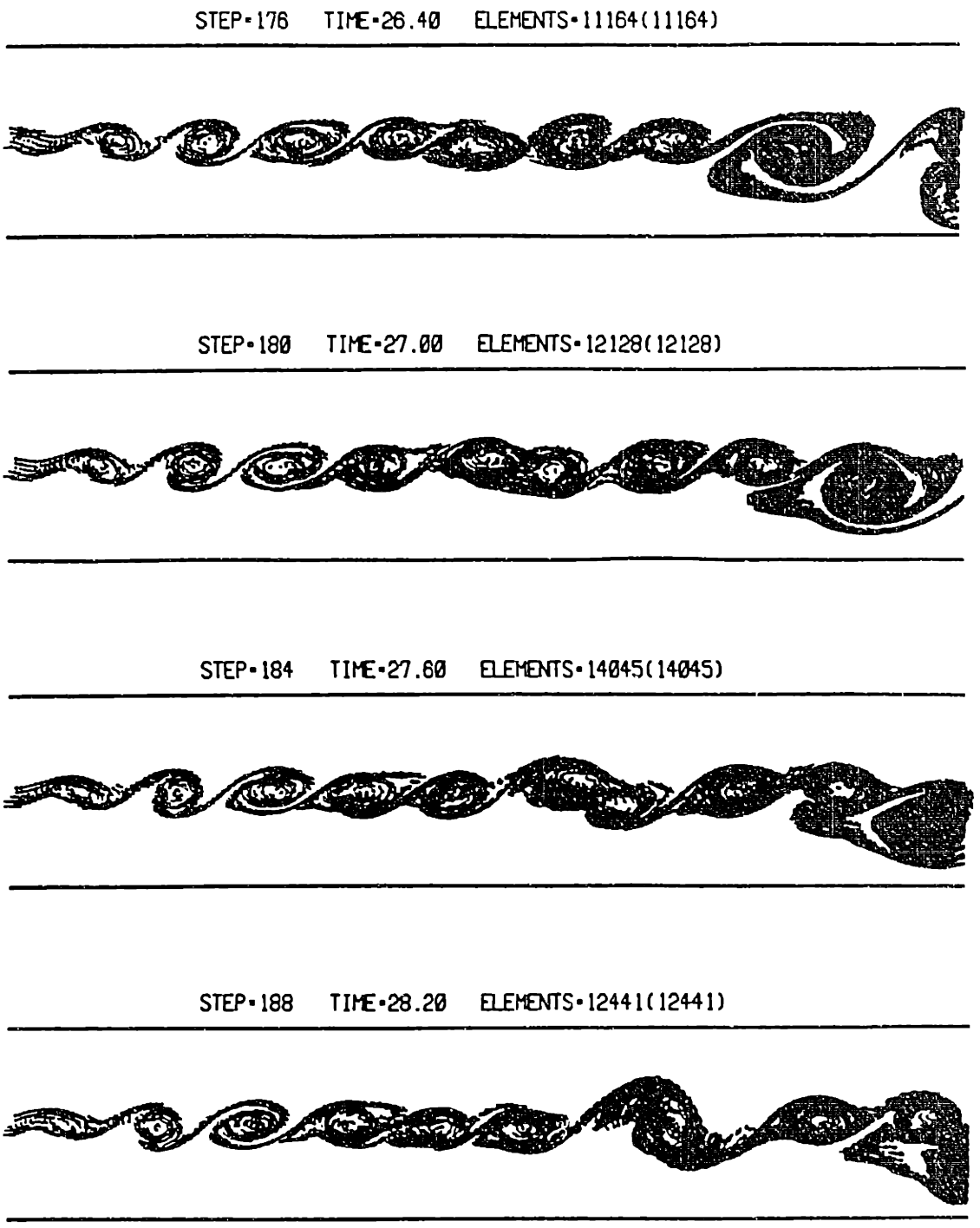

Fig. 34. The location and velocity of the vortex elements during the roll-up of a spatial shear layer for $U_1/U_2=3$, $\lambda=\lambda^*$, $\varepsilon_F=0.05\lambda^*$, $\varepsilon_S=0$ and $X_{exit}=5$ at different time.

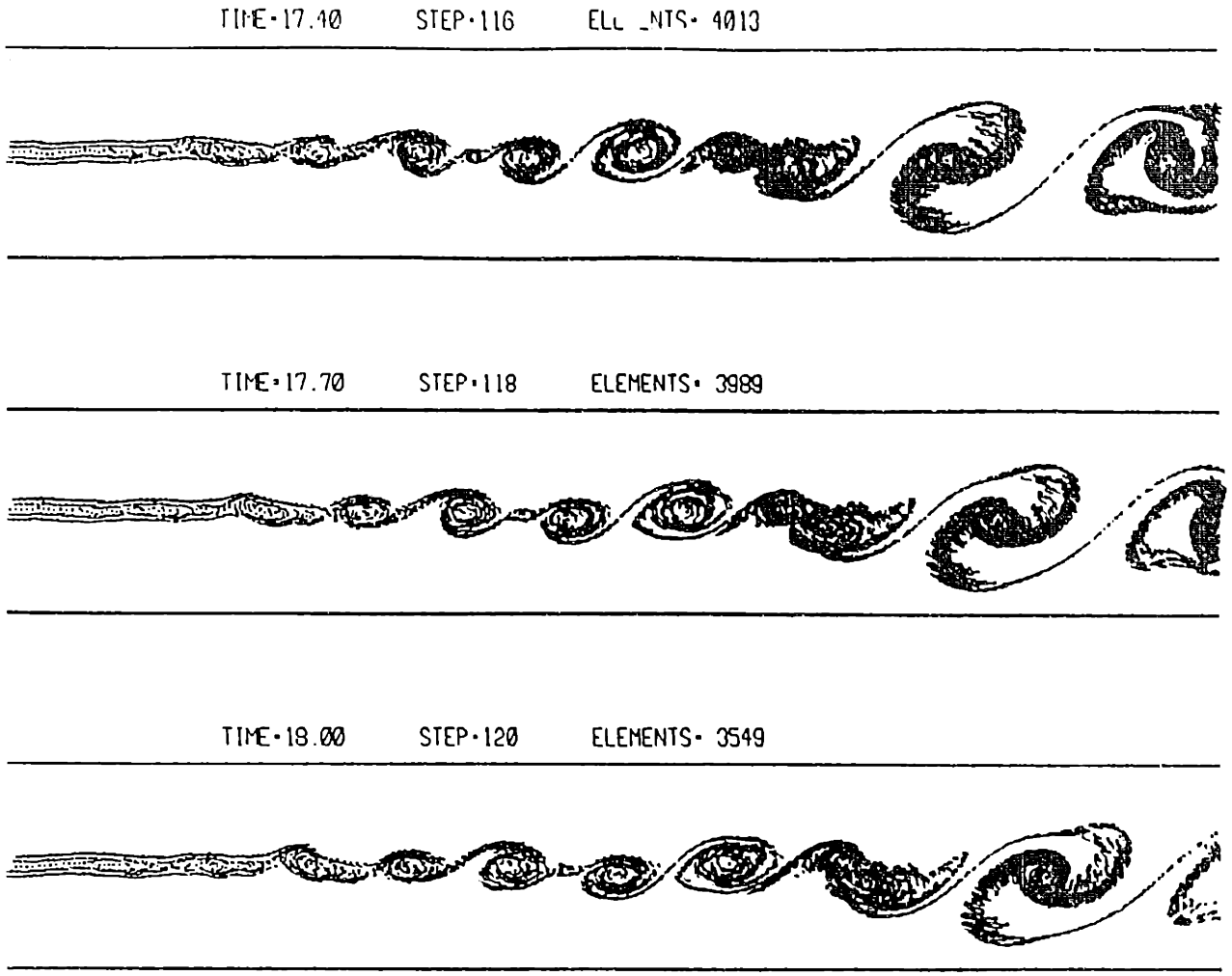

Fig. 35. The location and velocity of the vortex elements during the roll-up of a spatial shear layer for $U_1/U_2=2$, $\lambda_F=\lambda^*$, $\lambda_S=2\lambda^*$, $\varepsilon_F=\varepsilon_S=0.01\lambda$, and $X_{exit}=6$ at different time.

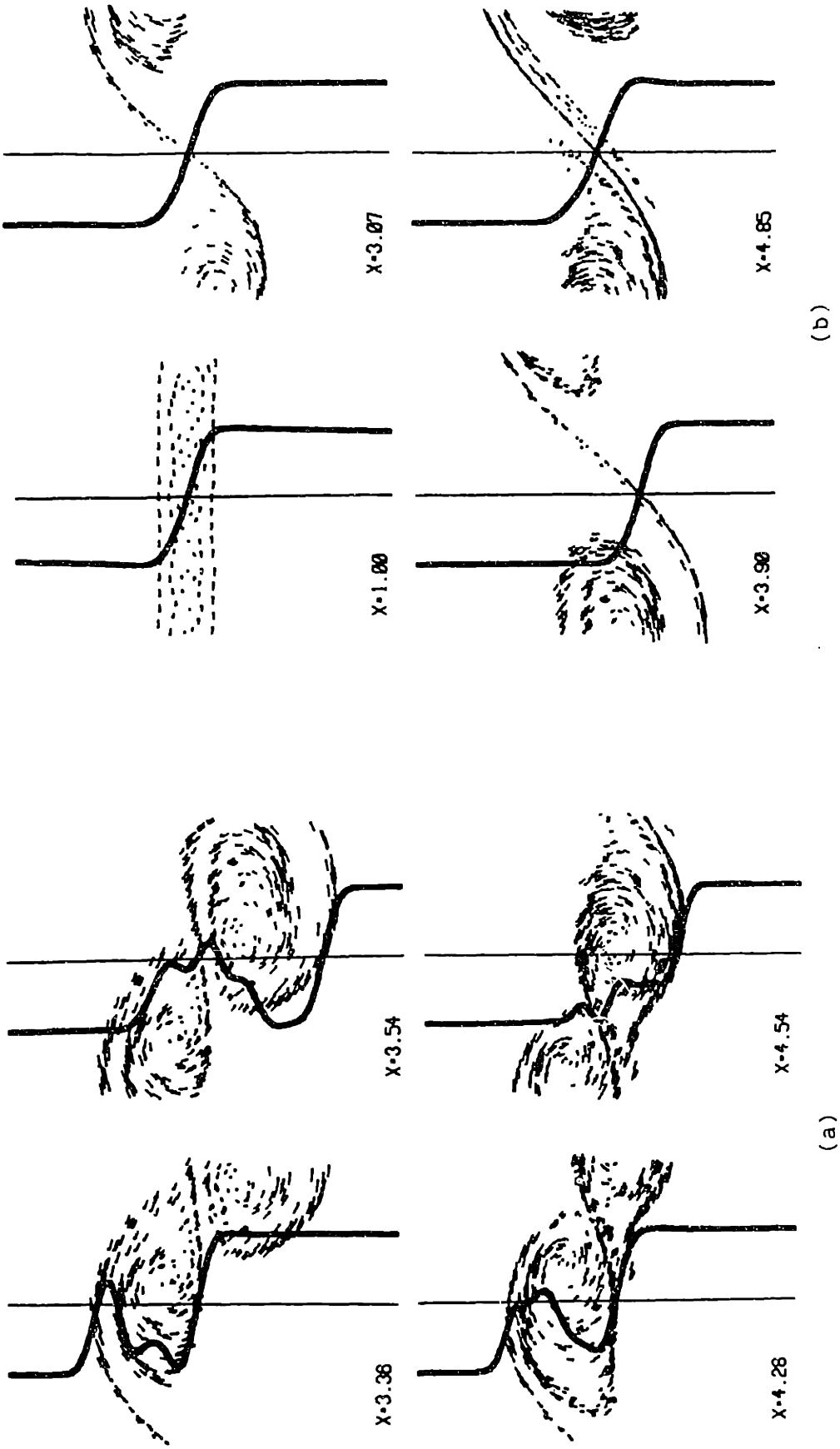

Fig. 36. Instantaneous concentration profiles superimposed on the vortex elements: (a) across the mid-section of the eddies; and (b) across the braids.

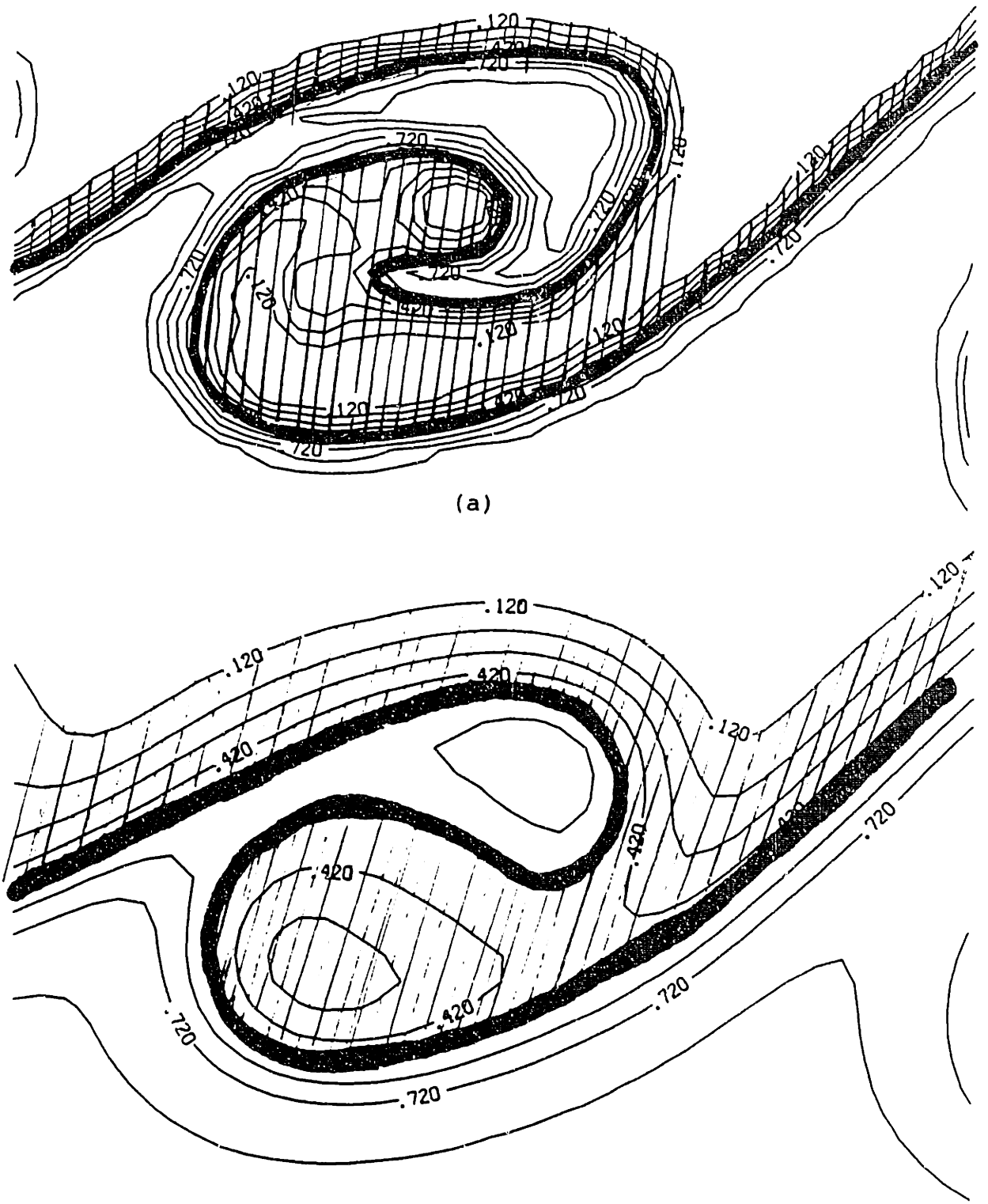

Fig. 37. Instantaneous scalar contours for a single eddy within the spatial shear layer at time t=40.65, x=4 for: (a) $P_e=\infty$; (b) $P_e=2500$.

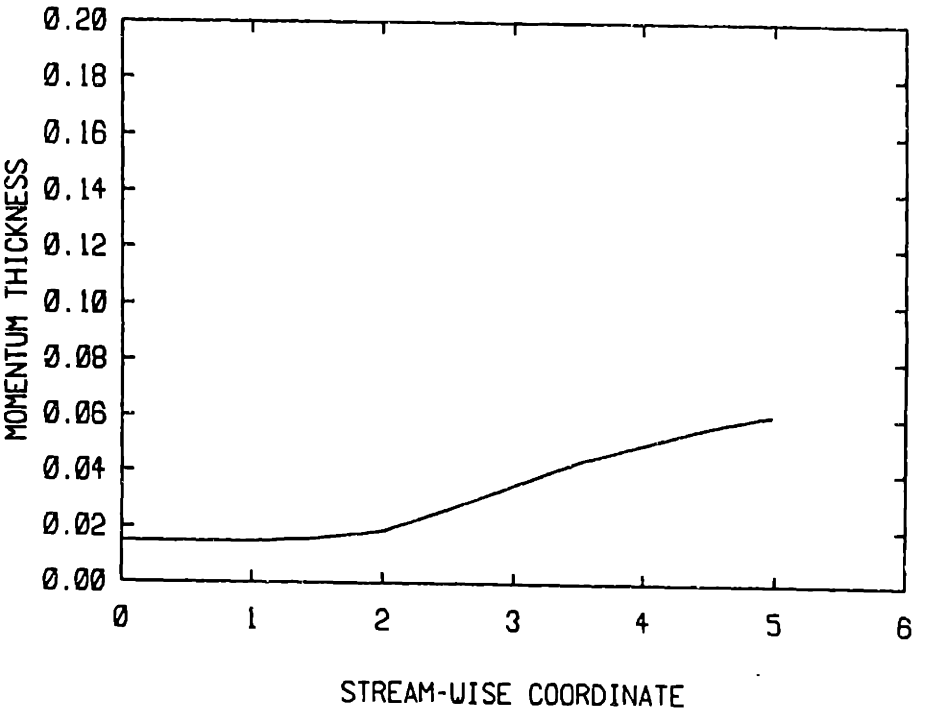

Fig. 38. Average momentum thickness for the spatial shear layer.

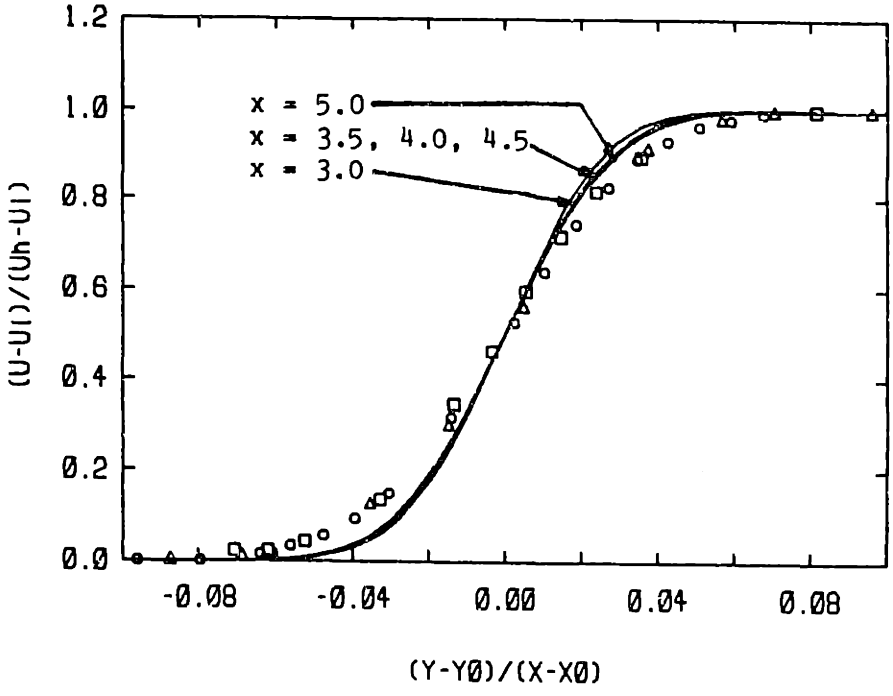

Fig. 39. The time-average streamwise velocity profiles at x=3.0, 3.5, 4.0, 4.5, and 5. The experimental results of Masutani and Bowman [55] are shown by symbols.

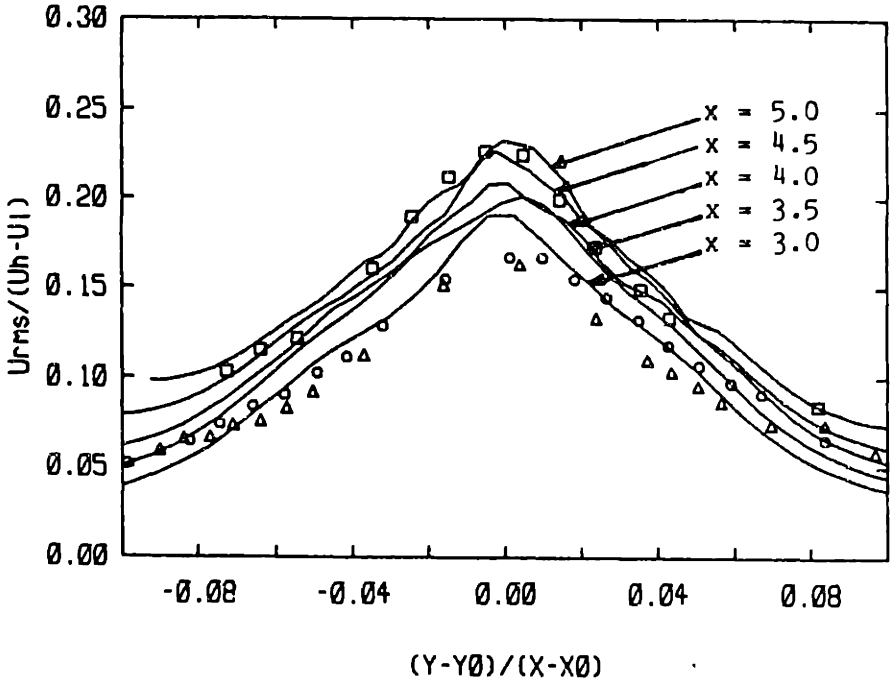

Fig. 40(a) The time-average streamwise velocity fluctuations at x=3.0, 3.5, 4.0, 4.5, and 5. The experimental results of Masutani and Bowman [55] are shown by symbols.

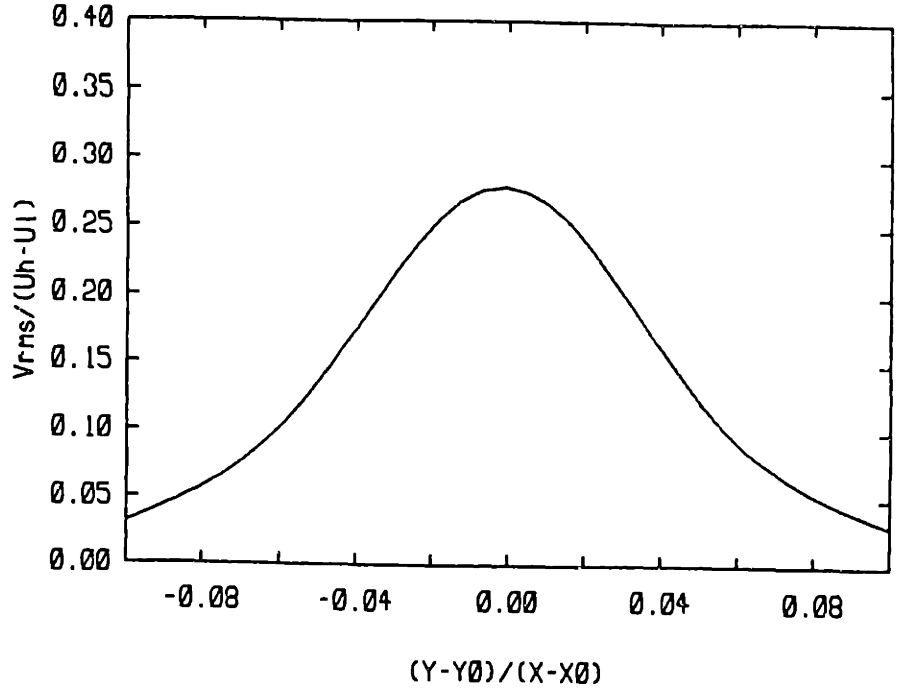

Fig. 40(b) The time-average crossmw-stream velocity fluctuations at x=3.5. The experimental results of Masutani and Bowman [55] are shown by symbols.

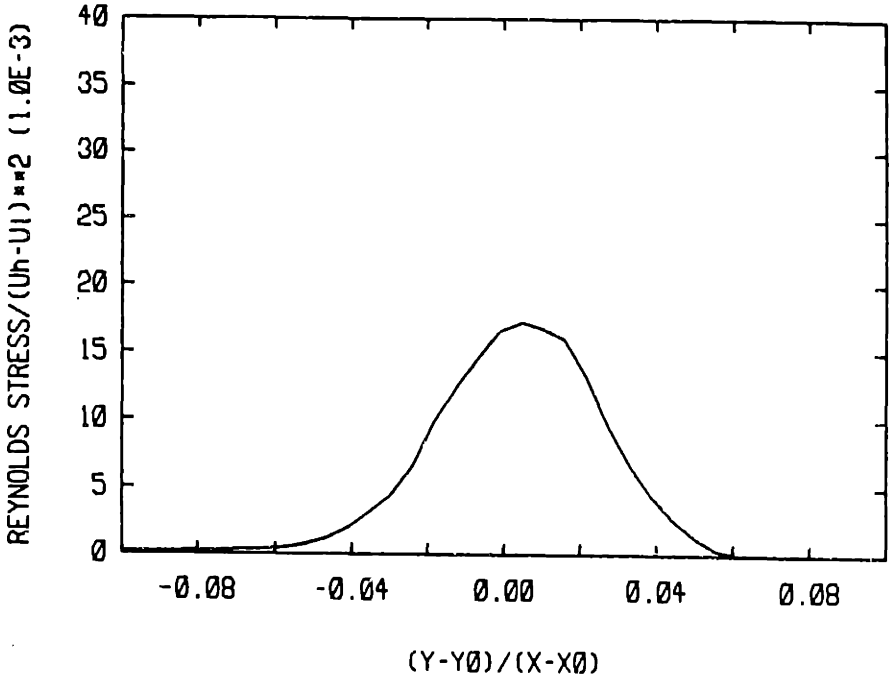

Fig. 40(c) The time-average Reynolds shear stress x=3.5. The experimental results of Masutani and Bowman [55] are shown by symbols.

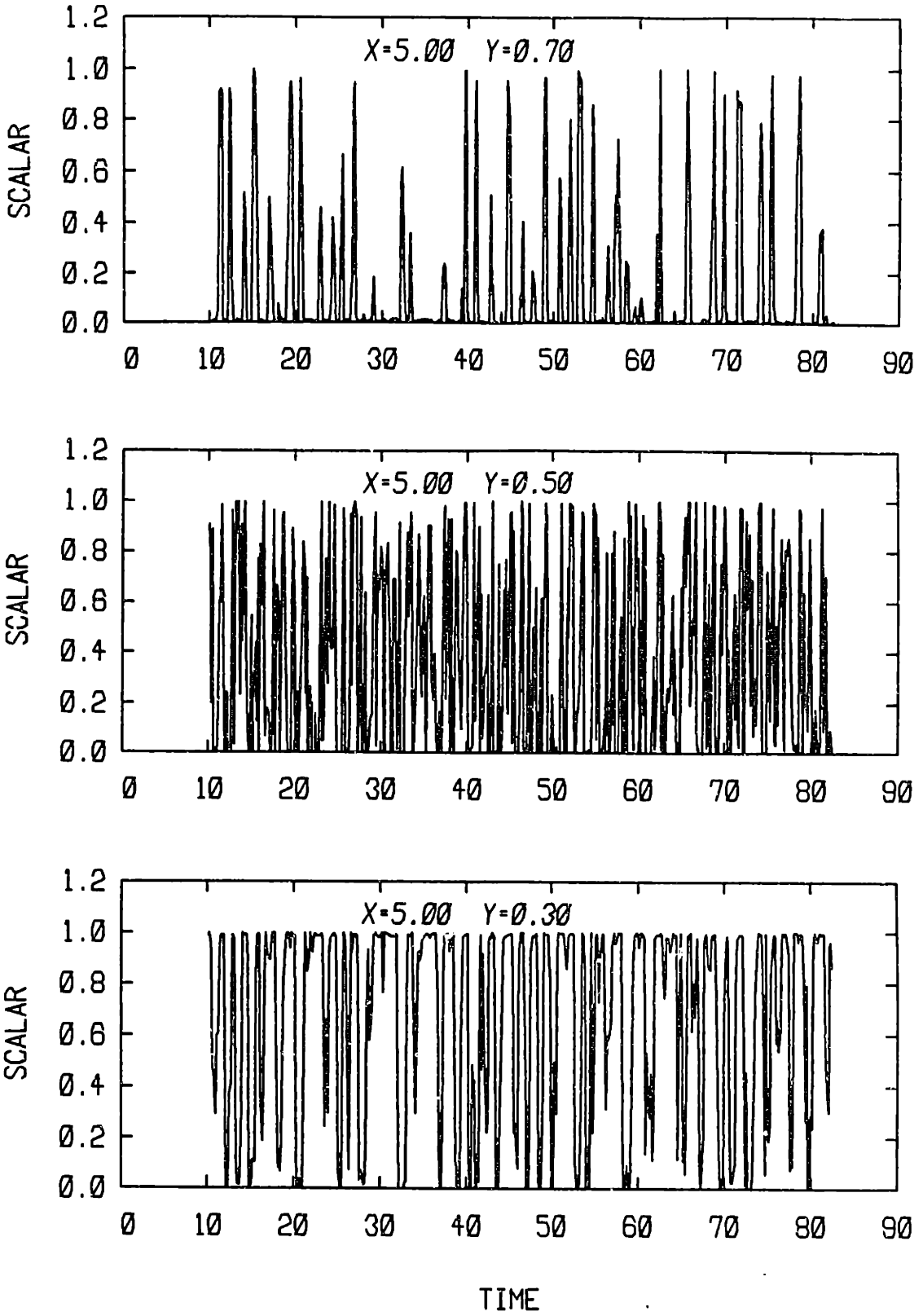

Fig. 41(a) Instantaneous values of concentration with time at x=5.0 for y=0.3, 0.5, and 0.7 with $P_e=\infty$.

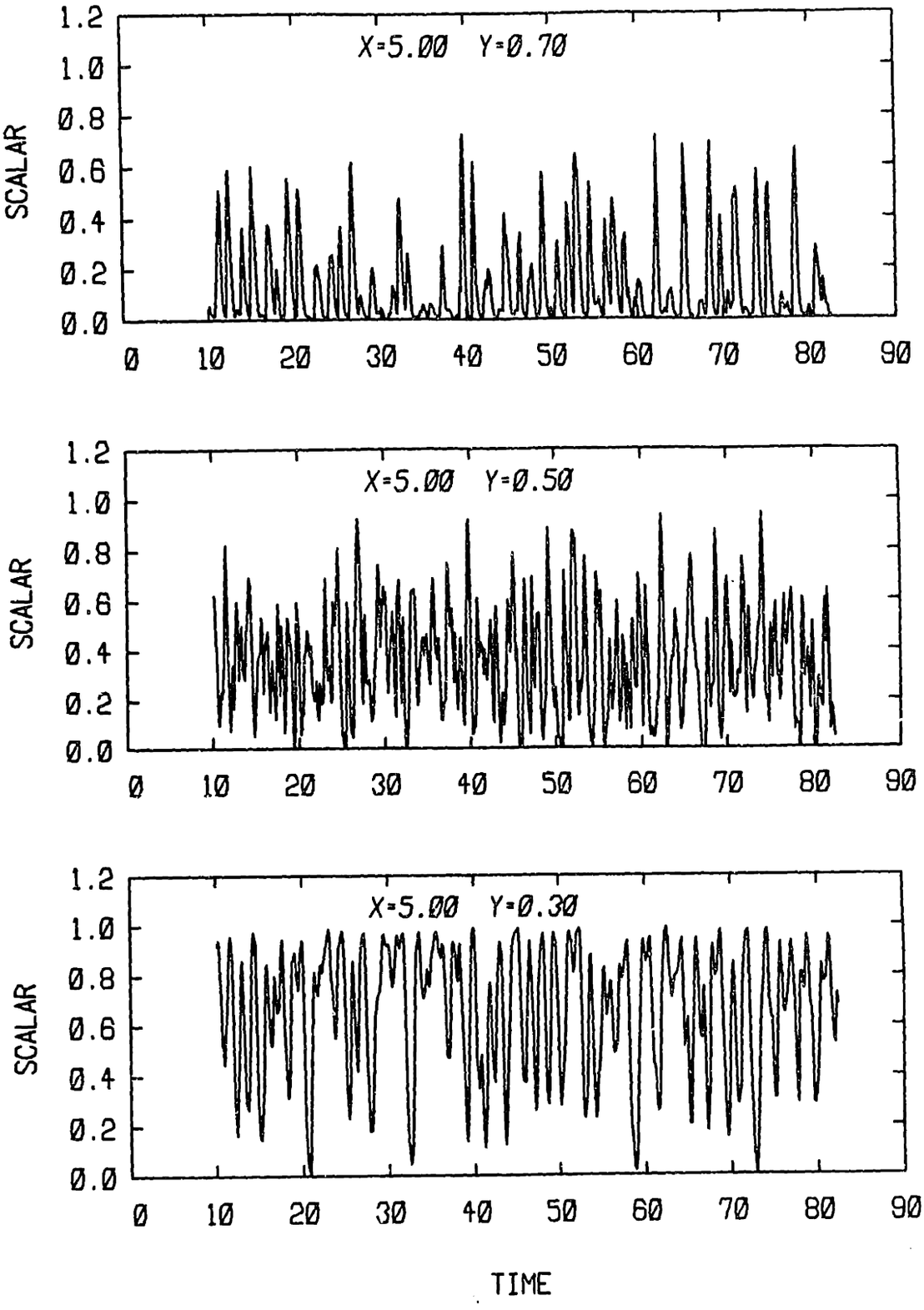

Fig. 41(b) Instantaneous values of concentration with time at x=5.0 for y=0.3, 0.5, and 0.7 with P_e=2500.

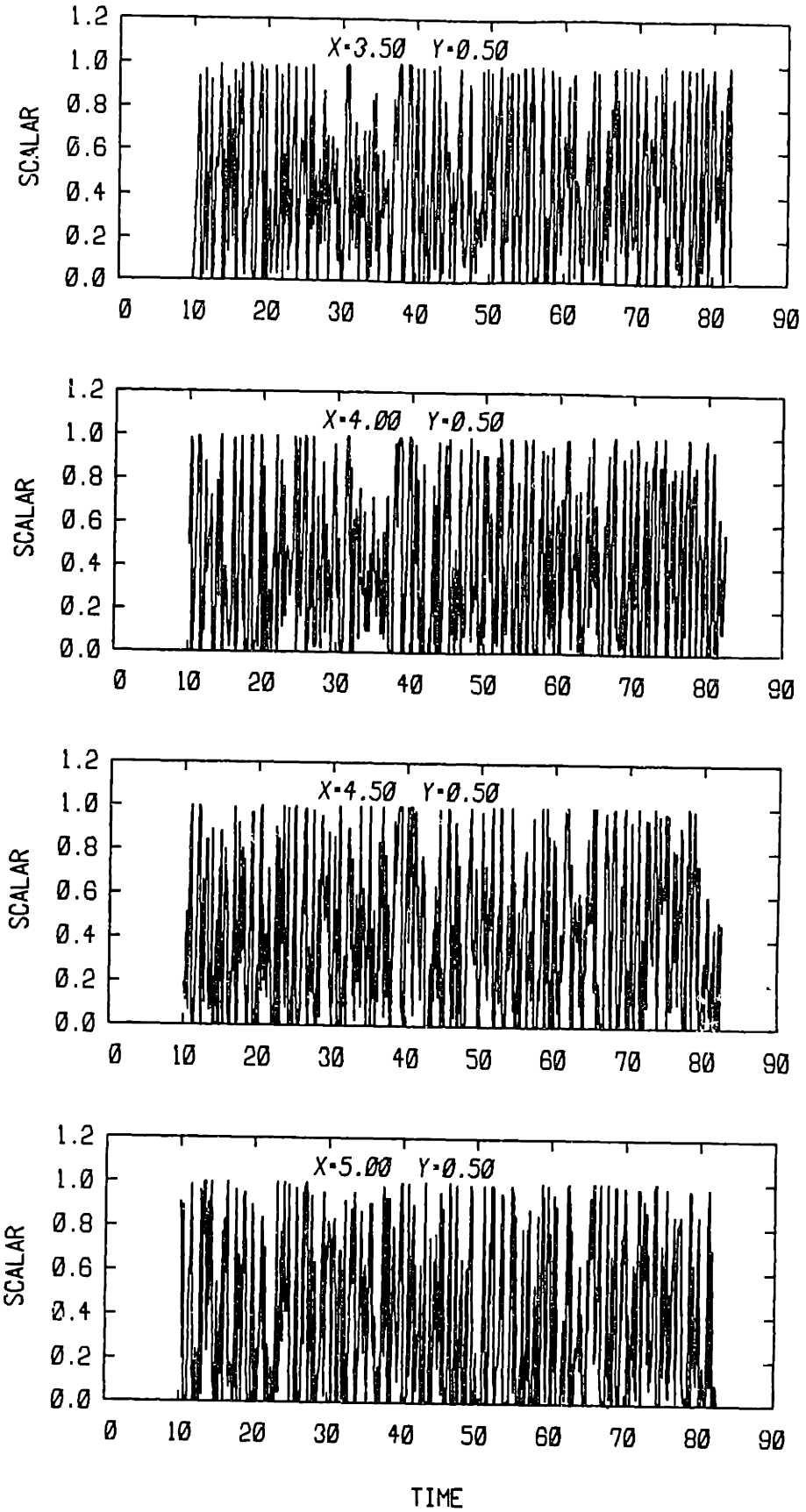

Fig. 41(c) Instantaneous values of concentration with time at y=0.5 for x=3.5, 4.0, 4.5 and 5.0 with $P_e=\infty$.

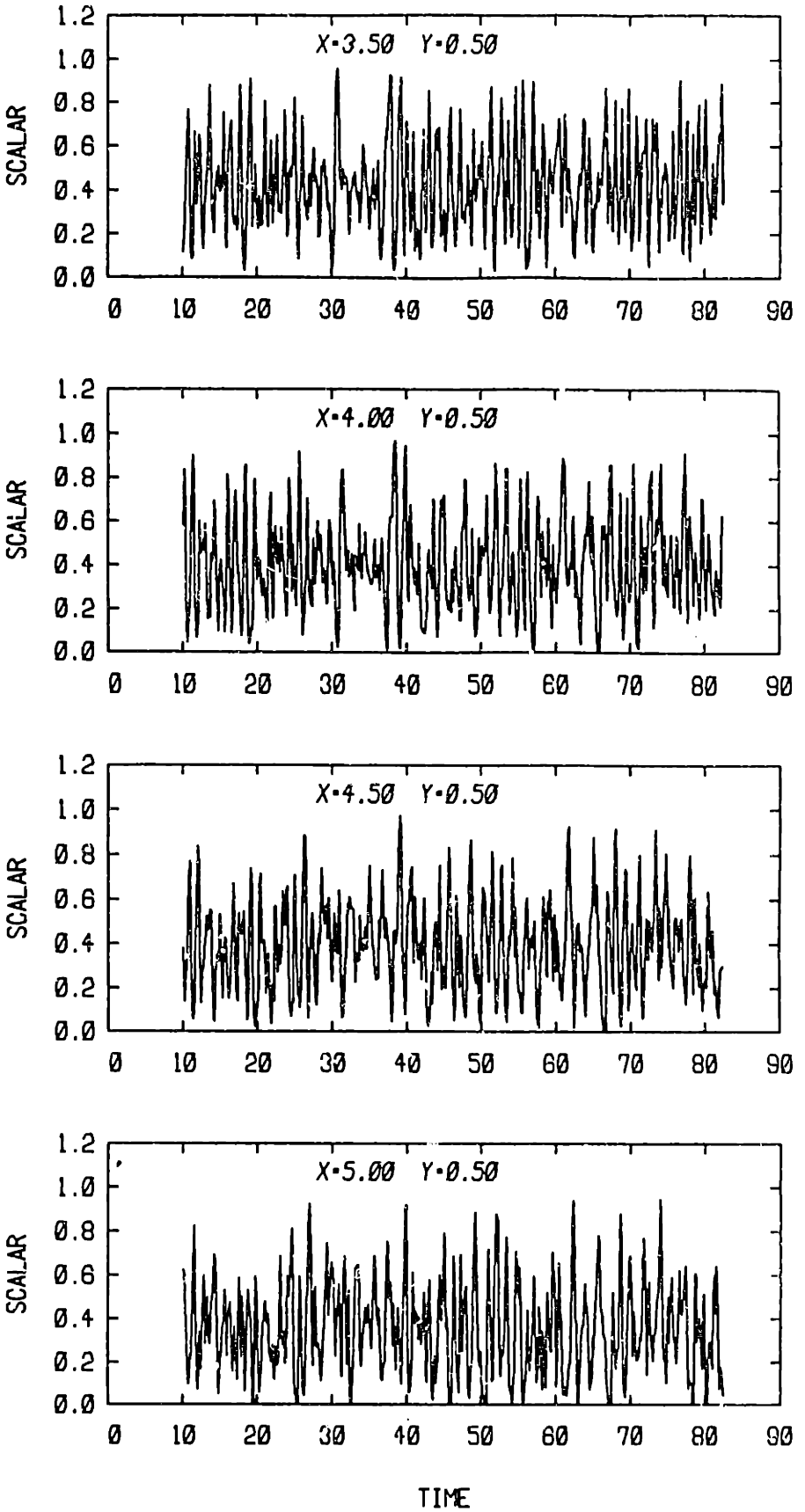

Fig. 41(d) Instantaneous values of concentration with time at y=0.5 for x=3.5, 4.0, 4.5 and 5.0 with P_e=2500.

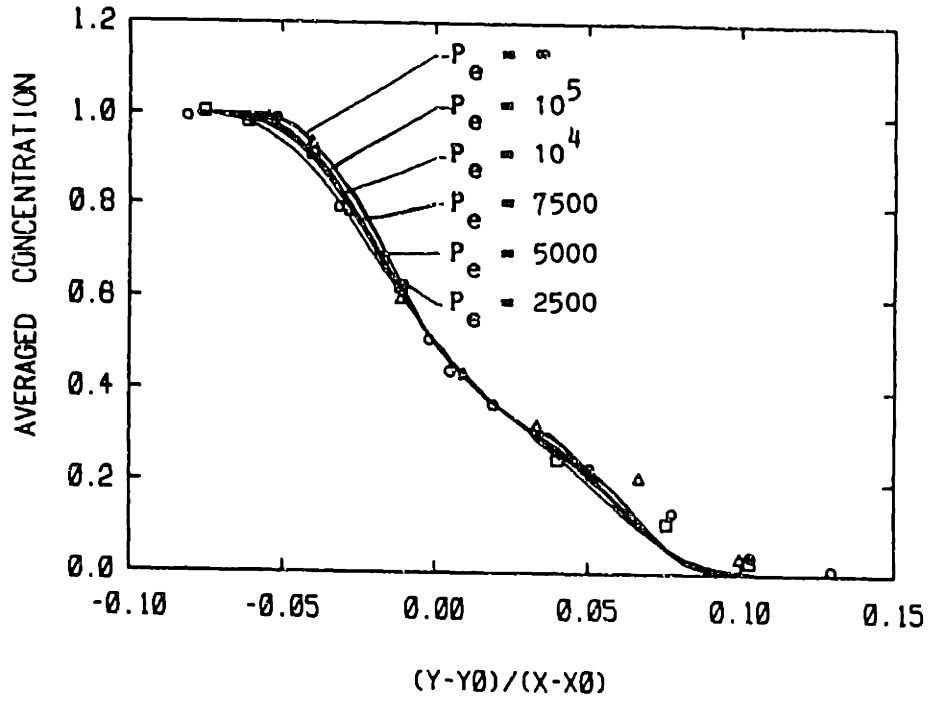

(a)

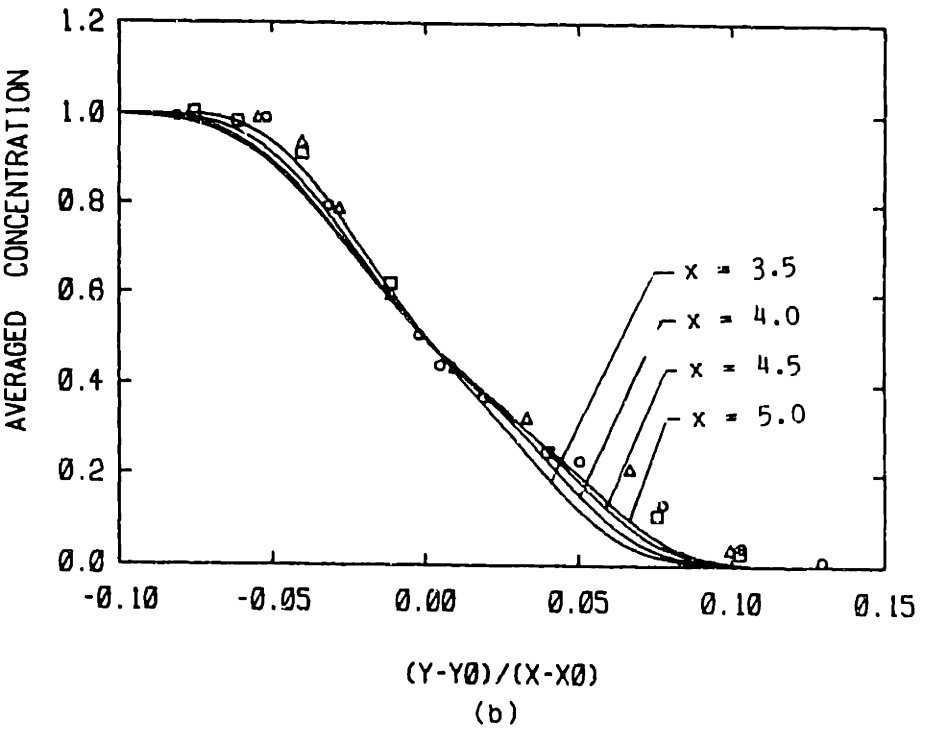

(b)

Fig. 42. Time-average concentration profiles: (a) at x=5.0 for $P_e=\infty$, 10^5, 10^4, 7500, 5000, and 2500; and (b) at x=3.5, 4.0, 4.5, and 5.0 for P_e=2500. Symbols correspond to the experimental data [55].

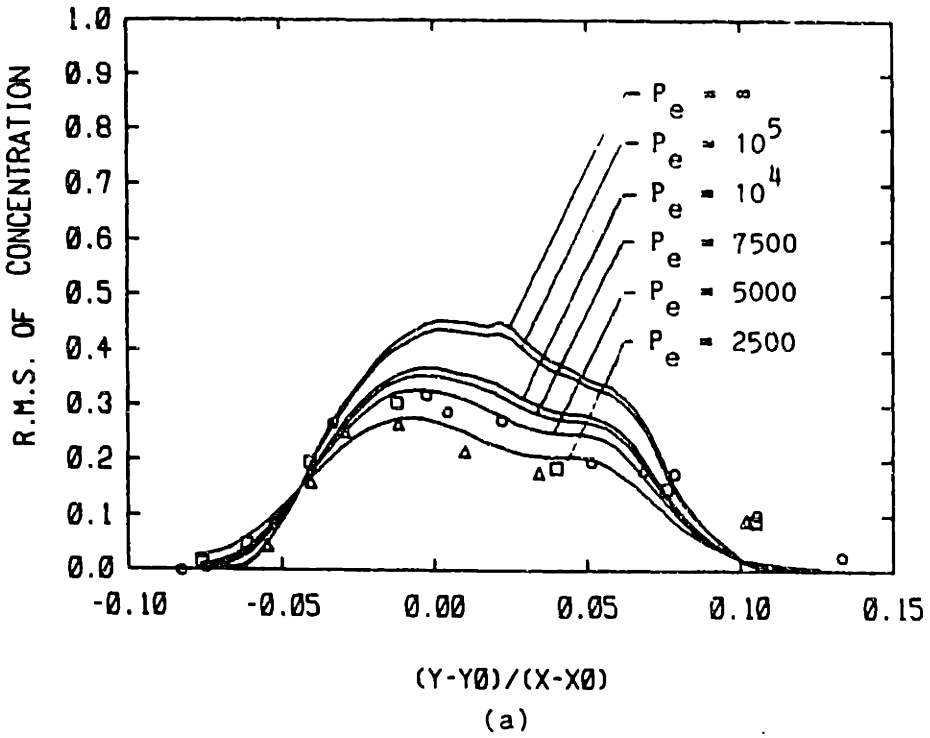

(a)

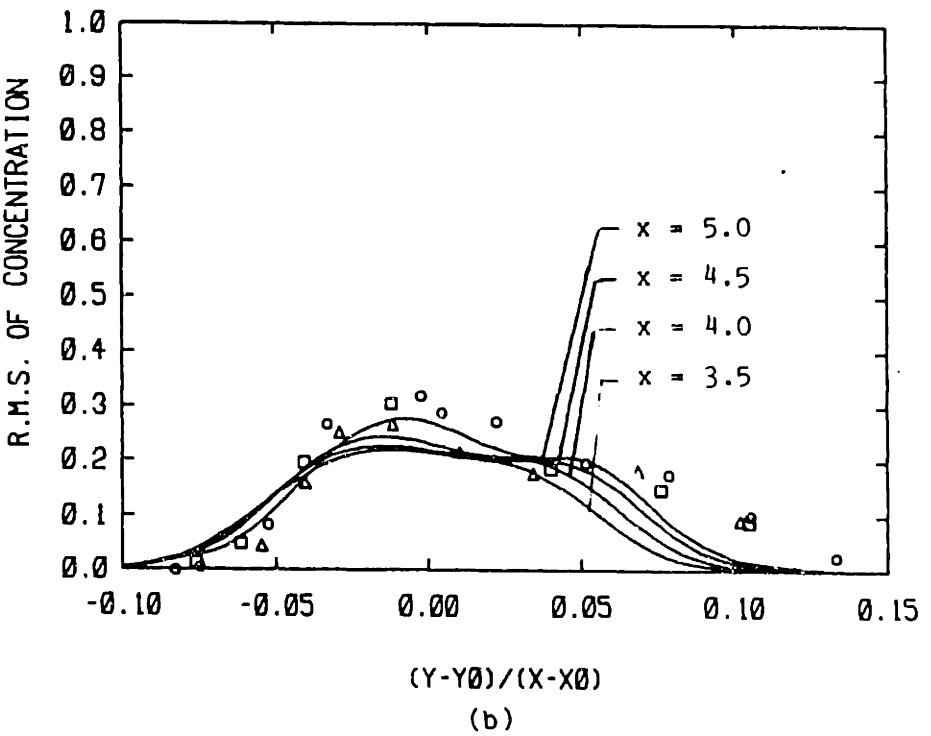

(b)

Fig. 43. Time-average concentration fluctuations: (a) at x=5.0 for $P_e=\infty$, 10^5, 10^4, 7500, 5000, and 2500; and (b) at x=3.5, 4.0, 4.5, and 5.0 for $P_e=2500$. Symbols correspond to the experimental data [55].

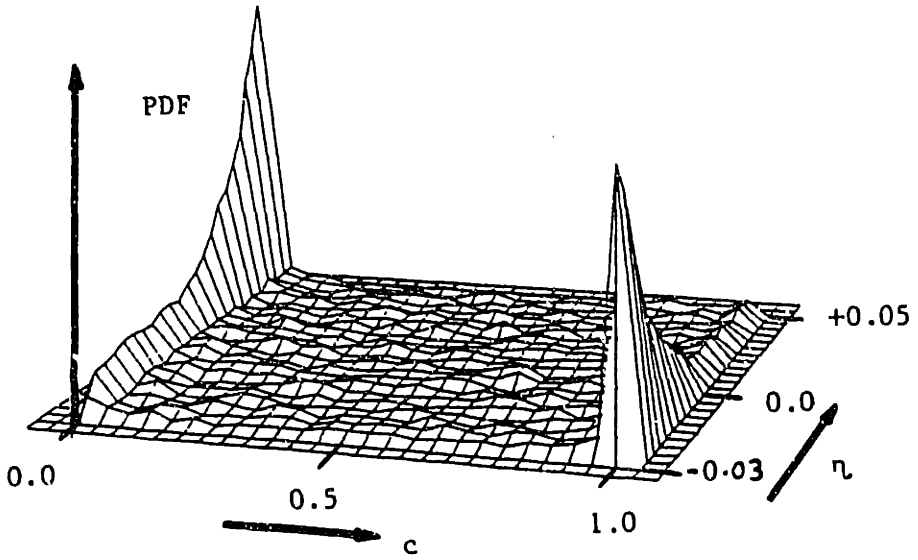

(a)

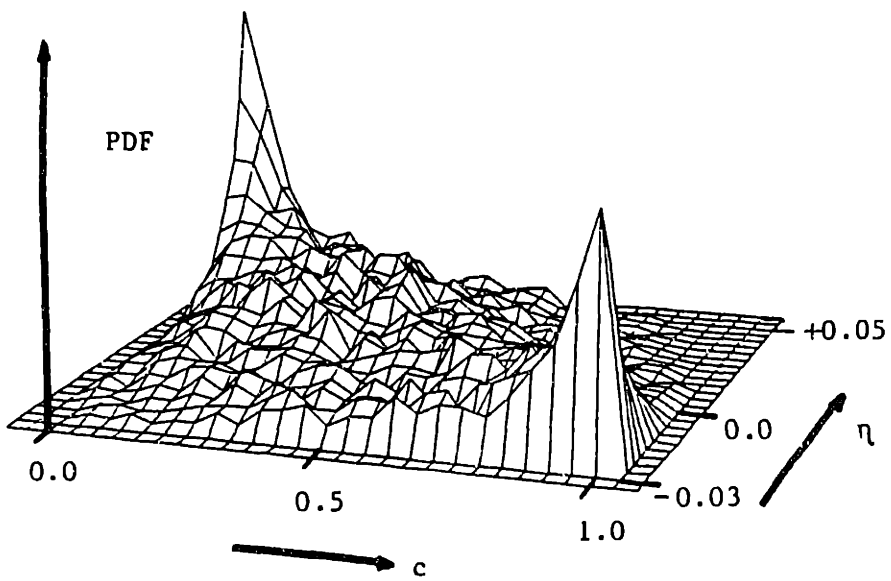

(b)

Fig. 44. Probability-density function of scalar concentration at x=5.0 for: (a) $P_e=\infty$; and (b) $P_e=2500$. $\eta = (y-y_0)/(x-x_0)$.

Chapter 6

THE REACTING SHEAR LAYER

In this chapter we apply the transport element method to a non-premixed, spatially-developing reacting shear layer. Fuel and oxidizer, both diluted in an inert gas, are introduced on opposite side of the splitter plate. The chemistry is governed by a single-step, second-order reaction and the amount of heat release is low. In a low heat release reaction, the thermodynamics and transport properties of the layer are not significantly different from the non-reacting case. The effect of heat release on the flow dynamics is removed by ignoring the spatial and temporal variations of density. This way, one can decouple the momentum and energy equations. The same result can be obtained if the mixture is highly diluted with an inert gas. In the experimental measurements of a shear layer using a low heat release reaction, Masutani and Bowman [55], Wallace [11] and Mungal and Dimotakis [12] used a dilute concentration of reactants with a maximum mean-temperature rise of less than 6 K, 100 K and 97 K above ambient, respectively, to achieve the same conditions.

The small temperature rise of the products suggest that: (i) the dynamics of the layer is not affected by any significant density variation; and, (ii) a temperature-independent reaction rate may be a natural approximation for the source term of the chemical reaction, since temperature variation is small. In this case, the exponential term in the Arrhenius expression of the reaction rate can be written as $\dot{W}=D_a c_F c_O$ with $D_a = A_f \exp(-T_a/T_f)$ where T_f is an average temperature in the reacting zone. In this case, the non-dimensional parameters of the problem are limited to R_e, D_a, and Ψ. It should be noted that this condition is satisfied if $(T_a/T_p)(\Delta T/T_p)<<$, where ΔT is the temperature rise and T_a is the non-dimensionalized activation

energy. On the other hand, the constant-density flow assumption depends on $\Delta\rho/\rho<<1$, where $\Delta\rho$ is the difference between the reactants and products density and ρ is the reactants density. Assuming that both reactants and products are perfect gases with the same molecular weight and that the pressure is constant, $\Delta\rho/\rho = \Delta T/T_p$. In this work, we assume that the density is constant and that the dynamics are independent of the chemical energy release. Thus, an isothermal reaction model is used only in the first part of this chapter. In the second part, we consider the effect of the temperature on the reaction rate. In the following analysis, we assume that both the Prandtl number and the Lewis number are equal to 1.

To investigate the effects of turbulence on chemistry, we use the turbulent reacting shear layer code to obtain solutions for a laminar reacting shear layer, i.e., when roll up is not allowed, and use these results as a base for comparison. Under the low heat release assumption, there is a semi-analytical expression for the velocity field of the laminar reacting shear layer. In our solution for the laminar layer, this expression is used to obtain the position of the elements at each time step. Once the locations of the vortex and transport elements are known from this semi-analytical solution, the chemical source term is integrated in a similar way as in the turbulent case. The distribution of both reactants within the layer at t=0, and at x=0 for any value of t, is shown in Fig. 45.

6.1. THE TURBULENT SHEAR LAYER

The total amount of burning within the shear layer is measured by the time-averaged integral product thickness, $\delta_p(x)$, defined as:

$$\delta_p(x) = \int_0^{+1} \bar{c}_p(x,y)\, dy \qquad (59)$$

where $\bar{c}_p(x,y)$ is the time-averaged value of $c_p(x,y,t)$. To obtain the following results, we ran the calculations until a stationary state was reached. We then collected a sample of 200 time steps for averaging. During the sampling time, we estimate that 30 large eddies had passed through the computational domain (see Fig. 49). The dynamics of the layer, including the frequency of shedding, the growth rate and the velocity statistics, have been analyzed before in the previous chapters. Thus, we will proceed directly to the analysis of the burning process.

In Fig. 46, we plot δ_p versus the streamwise coordinate at R_e=5000, D_a=10.0 and γ=1.0 for the laminar and turbulent layers. The figure shows that product formation starts immediately downstream of the splitter plate and grows rapidly. This is expected since the chemical reaction is temperature-independent, i.e., there is no ignition delay, and the two reactants are assumed to be partially diffused into each other. In the case of the laminar layer, δ_p reaches an asymptotic value around x~1.0. In the case of the turbulent layer, the value of δ_p is almost the same as that of the laminar layer up to the point where the latter reaches a constant value.

Existence of a constant value for the product thickness in the laminar shear layer can be predicted from the analogy between this problem and the Emmons problem in which there is a reaction zone between a flat plate of fuel and a parallel gaseous oxidizing stream. The main conclusion of the analysis of the Emmons problem [71], which can approximately be extended to the present case, is that there is an asymptotic value for the integral product thickness. This agrees with our results of the numerical simulation. The slight decrease

in δ_p of the turbulent layer with respect to the laminar layer is due to the strain produced by the growth of the perturbation and the formation of the first large eddy at x~1.5. This effect will be discussed in more detail later.

Downstream, the product thickness of the turbulent layer continues to rise beyond its asymptotic value of the laminar layer. To rationalize this behavior, we plot, in Fig. 47, the shape of the interface as it deforms due to the instability of the vorticity layer in terms of: (a) the location and velocity of the vortex elements initially located along the midsection of the vorticity layer, y=0.5, where initially $c_F=c_O=1/2$; (b) the continuous line interface which coincides initially with $c_F=c_O=1/2$; and, (c) the total length of the same line interface in the turbulent case divided by the total length of the interface in the laminar case, L/x. These plots show that the increase in the total product thickness in the turbulent case is due to the enlargement of the interface between the reacting streams within the large vortex eddies which form due to the roll up of the vorticity layer. Across this enlarged interface, molecular diffusion, thus mixing, leads to the enhancement of the rate of burning. The same effect can be expressed in terms of the entrainment of reactants into the structures that evolve due to the roll up of the vorticity layer. This entrainment, which results from the engulfment of fluid from both sides of the interface as it stretches, provides the first step of mixing within the large structures. The second step is the diffusion across the interface between the fuel and air streams.

It is noted that while the length of the interface, L, increases many fold as the vorticity rolls up, the increase in the product thickness is approximately limited by L/x (see Figs. 46 and 47(b)). This can be explained by the fact that a large part of the interface disappears within the burnt

core. In other words, a large portion of this interface becomes inactive, or non-reacting, as soon as the reactants are depleted within the core, i.e., the core becomes practically homogeneous. To clarify this issue, we focus our attention on analyzing the dynamics and the chemical reaction within a single eddy downstream of the shear layer.

Figure 48 depicts the following instantaneous information for one single eddy: (a) the vorticity contours, (b) the product concentration contours, (c) the high-speed stream reactant contours, and (d) the line which corresponds initially to y=0.5. These plots show that:

(1) There is a strong similarity between the vorticity contours and the product concentration contours, indicating the dominant role which the convective field, or the entrainment, plays in the burning process;

(2) While some traces of vorticity remain in the braids between neighboring eddies, most of the vorticity is entrained and concentrated within the eddy cores;

(3) The product concentration, on the other hand, is highly concentrated within the cores, with almost no product appearing within the braids;

(4) The reactants concentration is distributed almost evenly around the outer edge of the eddy, i.e., the reactant from the high speed side has penetrated the low speed stream, reaching the eddy core and vice versa;

(5) The original interface between the air and fuel streams is strongly convoluted within the eddy core which consists mostly of products;

(6) The center of the eddy, measured by the highest vorticity or product concentration, is in the low velocity stream indicating a definite asymmetry in the structure; and

(7) This asymmetry is emphasized by the presence of more high velocity fluid

than low velocity fluid within the eddy and the unequal convolution of the different branches of the core.

These observations show that, at this value of the Damkohler number, the reacting eddy can be best described as a core of products surrounded by a convoluted interface between the fuel and air streams. This interface, which remains on the outer edges of the vorticity core, is about three times the length of the original unconvoluted interface since it forms a Z-shape where an eddy exists. Most of the product formation takes place across this interface, as will be shown in detail in the next section. However, due to the convective field that exists within the eddy, these products are entrained into the core. Product concentration within the braids is very small due to two reasons:

(1) The relative velocity between the two streams is high within the braids, hence, very little mixing occurs there; and,

(2) Whatever products are formed are immediately entrained towards the eddy center. Thus, the stretch within the braids affects the product concentration by lowering the time available for mixing of reactants before the chemical reaction.

The temporal behavior of the layer is depicted in Fig. 49 where the variation of the product concentration with time within the mixing zone is shown at: (a) $y = 0.5$ and $x = 2.0$, 3.0 and 4.0; and (b) $x = 4.0$ and $y = 0.3$, 0.4, 0.6 and 0.7. The figure shows that the frequency of fluctuation of the local value of the product concentration decreases while its amplitude increases as we move downstream. The drop in the frequency is due to the pairing of the first generation of eddies, the fundamental eddies, which form as a result of the roll up of the vorticity layer, as well as that of the second generation of eddies, the subharmonic eddies, which form due to the

pairing of the first generation. There is approximately 43, 30 and 17 waves at x = 2.0, 3.0 and 4.0, respectively, within the time window shown in the figure. These correspond to the number of eddies passed through these sections within the same time window (the eddies were seen in plots of the vorticity field similar to those shown in Fig. 32. Since the flow was not forced in any organized way, pairing was found to occur among two, and at times three eddies at once. Moreover, eddies escaped pairing every few cycles. Similar observations could be made for the pairing among the second generation eddies.

The increase in the fluctuation amplitude of product concentration is due to mixing enhancement by the strong entrainment currents into the large vortex eddies. It is important to point out that strong entrainment currents are generated during pairing as well as during roll up, as was shown in Chapter 4. These results emphasize the role which the subharmonic instabilities play in the evolution of the mixing layer. Pairing, as mentioned before, involves the roll up of the neighboring eddies around a common center. Thus, a similar stretch of the common interface, accompanied by strong entrainment currents of both reactants into the new layer structure, is generated. These results indicate that an active way of promoting mixing and faster burning is to force the layer at its natural subharmonic frequency.

Figure 49(b) shows that the product concentration is not symmetric around y = 0.5. This is due to the asymmetric entrainment of reactants into the large eddies. As we showed in Chapter 5, the fluid from the top stream penetrates further into the eddy than that from the bottom stream, leading to the generation of higher product concentration in the lower half of the eddy than in the upper half. We also note that while the mean value increases as we move downstream and, at any particular section, close to y = 0.5, the value

of c_p fluctuates between the two extremes, even at the center of the eddy. This is because of the depletion of products within the braids between the eddies, as shown in the contour plots.

The effect of various physical parameters on the rate of product formation in the turbulent shear layer is now analyzed and related to the dynamics which has just been elaborated.

6.2. EFFECT OF DAMKOHLER NUMBER

As mentioned in Chapter 2, the Damkohler number is defined as the ratio between the convective time scale and the chemical reaction time scale. It is expected that as D_a increases, the total product formation should increase. The time-average product distribution across the section x=4.0 is shown in Fig. 50 for different values of the Damkohler number. The curves indicate that the cross-stream extent of the reacting layer is independent of the Damkohler number. The maxima of all these curves lie at the same point $y < 0.5$, and the product distributions are asymmetric around their maximum values. This is a result of the asymmetric entrainment which has been observed before in non-reacting layers. The curves also indicate that at low D_a, the eddy is formed of almost a uniform core of products at low concentration, i.e., products are uniformly generated inside the large eddy. At high D_a, there are sharp gradients of products between the eddy core and the free streams indicating that products are generated primarily on the outer edges of the eddies.

Figure 50 shows that the time-average value of c_p at the center of the eddy, defined by the maximum of the curve, is 0.25. On the other hand, Fig. 49(b) indicates that at the same period, the instantaneous value of product concentration fluctuate between 0.0 and 0.8. These fluctuations are

associated with the passage of the large scale eddies over the measuring point, which raises the value of the concentration to its maximum value and then causes it to drop to its minimum value as the braids pass over the same point.

In Fig. 51, the integral product thickness, δ_p, is plotted against the streamwise coordinate, x, for R_e=5000, D_a=0.2-15 and Ψ=1.0. At low D_a, δ_p increases slowly with x. Under these conditions, the effect of mixing enhancement due to roll up on the rate of product formation is weak since chemistry is slow, i.e., the chemical rates do not match the mixing rates. As D_a increases, the distinction between the two stages of the reacting shear layer, before and after roll up, becomes more pronounced. In particular, after roll up the rate of increase of δ_p, i.e., $d\delta_p/dx$, increases with D_a. Thus, while before roll up the strain field negatively affects the rate of burning by thinning the layer, after roll up the strain field enhances the rate of reaction within the large eddies by promoting entrainment into the large structures.

The plot also shows that for a fixed x, the change in δ_p with D_a is not linear. To illustrate this non-linearity, we select the section at x=4.0 and plot the local value of δ_p versus D_a for two values of the Reynolds number, R_e=5000 and 10000, in Fig. 52 (Ψ=1.0). At low Damkohler number, the rate of product formation and δ_p are strongly affected by D_a since they are limited by the speed of the chemical reaction. The product integral thickness reaches an asymptotic value as D_a is increased since now it is limited by mixing. The figure also shows that at high Reynolds numbers δ_p is weakly dependent on the Reynolds number since by doubling the diffusivity the product integral thickness hardly changes (here, the Reynolds number was changed without changing the Damkohler number). This can be explained by the fact that at

high Damkohler number the rate of mixing is limited by entrainment of reactants into the eddy core and not by diffusion. This issue will be addressed in more detail in the next section.

The effect of the Damkohler number on the structure of the shear layer is investigated further by comparing the instantaneous values of the product concentration, c_p, the oxidizer concentration, c_o, and the potential for the chemical reaction, $\dot{W}/D_a = c_F c_O$, for $D_a = 0.2$ and 10 in Fig. 53. In the fast chemistry case, the potential of the chemical reaction, $\dot{W}/D_a$, is highest on the outer edges of the large eddy and reaches very small values at the center where the product concentration is highest. Thus, at high Damkohler numbers, the reaction takes place at the interface between the fuel and the oxidizer. It is also noticed that under these conditions, the penetration of either reactants streams into the eddy is limited due to the fast consumption of reactants by the chemical reaction. On the other hand, in the slow chemistry case, the speed of the chemical reaction is highest at the center of the eddy where the product concentration is highest. Thus, at low Damkohler numbers, the reaction takes place at the center of the eddy where the fuel and oxidizer have been mixed. Under these conditions, the penetration of the reactants streams into the large eddy is deep.

In Fig. 54, the numerical results are compared with the experimental measurements of Mungal and Frieler [72]. In order to do a one-to-one comparison: (1) the product integral thickness, δ_p, is normalized with respect to the 1% thickness of the layer at the same location, δ_1 (the distance between points at which the mean product concentration is 1% of its maximum value); and (2) the Damkohler number is recomputed according to the definitions used by these authors, D_{ax}, which is based on the mean velocity, U_M, and the value of x at which δ_p and δ_1 are measured. As expected, the

numerical results are below the experimental measurements since the numerical solution is limited to two-dimensional physics and thus mixing transition is not allowed to affect the flow dynamics. The extra mixing, generated by the extra entrainment attained after transition and the generation of streamwise structure, should account for the difference between the numerical and the experimental results (see Knio and Ghoniem [59]).

In order to illustrate, by parametric modeling, the effect of the mixing transition on product formation and to show how the enhancement of diffusion by the streamwise vortex structures can affect the burning process, we increase the molecular diffusion by decreasing the Reynolds number to 2500 and 500. The results, depicted in Fig. 54 at $D_{ax} = 27$, show that the value obtained at $R_e = 500$ falls within the scatter of the experimental measurements. This agreement is not based on a fundamental simulation of the three-dimensional flow but on the choice of the Reynolds number to compensate for the extra mixing due to three-dimensional effects. Thus, we will not pursue the matter any further.

The fast chemistry, mixing-limited regime is reached when $D_a > 1$. Based on the length scale of the large eddies, the chemical reaction can be considered fast for $D_a > 20$ as indicated by Fig. 51. Beyond this value of D_a, the rate of burning will not benefit from increasing the speed of the chemical reaction and only mixing enhancement can promote the formation of more products within the layer. This is an important conclusion since this limit has been considered as $D_a \sim \infty$. Our computations indicate, however, that mixing-controlled combustion occurs as soon as the chemical time scale becomes an order of magnitude larger than the convective time scales. Using Damkohler number based on the x-location, D_{ax}, the fast-chemistry limit is reached at $D_{ax} \sim 50$.

6.3. EFFECT OF REYNOLDS NUMBER

Figure 55 shows the time-averaged product concentration profiles at x = 4.0 for D_a = 10 and R_e = 500, 5000 and 50000. In this case, we fix both the convective and chemical time scales and change the diffusion time scale. The plots show that the shear layer thickness depends on the Reynolds number through molecular diffusion, however it is a weak dependence at high Reynolds numbers. This is consistent with the results presented in Figs. 49 and 51, which indicated that at high Reynolds number the rate of product formation measured by the integral product thickness is a weak function of the Reynolds number (since all the computations were performed at Schmidt number, S_c=1, the Peclet number of mass diffusion is the same as the Reynolds number). Both figures show that doubling the Reynolds number, i.e., reducing the molecular diffusion by a factor of two, has a negligible effect on the product formation rate.

Figure 55 confirms mixing asymmetry at all values of Reynolds numbers. As previously seen in Fig. 50, the distribution of the product is asymmetric around its maximum value, reaching deeper into the low-velocity stream than the high-speed stream. This is due to the fact that entrainment into the large eddies favors the high-speed stream. This asymmetry is emphasized by the fact that as the effect of molecular diffusion increases, the product thickness grows more into the low-velocity stream than into the high-velocity stream. The asymmetric entrainment has been observed in non-reacting flow simulations and in experimental studies of shear layers. It is due to the asymmetric vorticity distribution inside the eddies that form between two streams of unequal velocities.

The normalized product thickness, δ_p/δ_1, is depicted in Fig. 56 as a function of the Reynolds number. The plot shows that increasing R_e by one order of magnitude lowers the normalized product thickness by 10%. As indicated by the contour plots in Figs. 48 and 53, at high Reynolds number diffusion occurs across a thin layer between the fuel and the air on the outer edges of the large eddies. Since the layer is thin, the rate of diffusion across the interface is faster than the convection of the reactants towards the eddy. Therefore, the burning process is governed by the slower mechanism, convection or entrainment, and the effect of the Reynolds number is not strongly felt.

The importance of these results lies in the fact that one can not enhance the rate of burning by promoting molecular diffusion, or very small scale mixing, beyond a certain level. The fact that mixing at high Reynolds numbers is governed by the entrainment into the large structure and not by diffusion either within these structures or outside their cross-stream extent is strongly emphasized.

6.4. EFFECT OF THE STRAIN FIELD

In Fig. 57, we plot the instantaneous product distribution and the corresponding vorticity field for different parts of the computational domain for R_e=5000 and D_a=10. Clearly, the product concentration can be linked to the dynamics of the layer or the vorticity field. Both fields show one moving saddle point within the braids which connect each two neighboring eddies, and one moving center point at the middle of each eddy. Due to the strong rotational field within the core of each eddy, the braids in both sides of the saddle points are stretched and the products generated within the braids are drawn into and inhaled by the eddy. The concentration of the products is thus

lower around the braids with a minimum at the saddle point, while it is much higher inside the core of the eddies with a maximum at the center point. The critical point which appears at the center of the eddy acts as focus point for the product concentration.

Invoking the above reasoning, we may answer the question of why, in the initial stages of the turbulent reacting layer, is there a slight drop in the product thickness compared with the corresponding laminar reacting layer? This was first pointed out in Fig. 46. In Fig. 58 we plot the ratio of the averaged product thickness of the turbulent to the laminar shear layer. Note that δ_p is the integral product thickness, $\int c_p \, dy$, while δ_1 is the "displacement" product thickness and is the distance between c_p=0.01 and c_p=0.99. Thus, δ_p indicates the total amount of products within the shear layer while δ_1 marks the physical extent of the products within the layer in the cross-stream direction. Initially, this ratio is close to unity because the layer behaves as a laminar layer. Moving downstream both ratios drop below 1. This is the region close to the formation of the first mature eddy (see Fig. 57(a)). The formation of an eddy exerts a finite strain on the initial part of the shear layer, causing it to become thinner than the laminar layer. Since the vorticity layer and the reaction zone overlap, the reacting zone also becomes thinner and the product thickness decreases. The effect of the large eddy is not strong enough to deplete all the products; only part of the product is inhaled into the right side of the zone.

6.5. EFFECT OF REACTANTS RATIO Y

For the chemical reaction described by Eq. (1), the reactants ratio Y is defined as the ratio of the free-stream concentrations of the high-speed stream, $c_{O\infty}$, to the low-speed stream, $c_{F\infty}$:

$$\Upsilon = \frac{c_{O\infty}}{c_{F\infty}} \qquad (60)$$

For the reaction symbolized by Eq. (1), a unit volume of one species is required to completely "oxidize" a unit volume of the other species, i.e., $\Upsilon=1$ corresponds to complete combustion. In the context of the shear layer there is no need to distinguish which species acting as the fuel or oxidizer. The important concern is the ratio of the high-speed to low-speed reactant concentrations since the mixing layer entrains fluid from both sides at different rates.

In Fig. 59 we plot the total amount of products in the layer for $0<x<4$, that is:

$$\text{Total amount of products} = \int_0^4 \int_0^1 \bar{c}_p(x,y)\, dx\, dy$$

against the reactants ratio when the low-speed free-stream concentration is fixed, $c_{F\infty}= 1.0$, and the high-speed free-stream concentration is changed, $c_{O\infty}=$ 0.0 - 8.0. For small values of Υ, the amount of products increases as the high-speed reactant is burned out by an excess of low-speed reactant. With further increase in Υ, an asymptotic limit is reached, corresponding to $\Upsilon=5$, where the low-speed reactant within the large eddies is now burned out by an excess of high-speed reactant.

Although for the chemical reaction with $\Upsilon>1$ there is a higher concentration of the reactants and hence a higher diffusion flux within the eddies, the product formation, as mentioned before, is a weak function of the Reynolds number and thus of diffusion. The increase in the product thickness

is due to the presence of higher species concentration and thus larger potential for the chemical reaction. In other words, the chemical reaction with $\Upsilon>1$ is equivalent to a faster reaction with lower reactants concentration but with a higher Damkohler number. Based on the above argument, we can explain the strong similarity between Figs. 52 and 59.

Mixing asymmetry can affect the rate of burning and the total amount of product formed within the domain when $\Upsilon \neq 1$. To show this, we computed the total amount of product with $\Upsilon = c_O/c_F = 2/1$ and $\Upsilon = c_O/c_F = 1/2$ without interchanging the two reactants between the two streams. Without mixing asymmetry, the ratio between the total products in both cases should have been one. However, we found that the ratio of the total product in the two cases was 1.08. The increase in the total product formation is due to the previously observed fact that the large eddies entrain more from the high-velocity stream than from the low-velocity stream (for experimental verification, see Koochesfahani and Dimotakis [73].) Thus, with higher concentration in the low velocity stream, there is a stronger chemical potential and more products form within the large eddies.

6.6. EFFECT OF CHEMICAL PARAMETERS

Now we investigate the effect of the temperature-dependent exponential term in the reaction rate expression, Eq. (13). In this case, and according to the global energy equation, complete combustion of reactants at temperature T_∞ will raise the temperature by $\Delta T=Q$ and the product temperature will be $T_P = 1 + Q$. Thus, between the reactant's state and the product's state, the Arrhenius term in the rate of reaction expression will increase by a factor of approximately 150 for a typical value of $T_a = 10$. It should be mentioned that between the two states, the factor $c_F c_O$ is greatly reduced and the increase in

the total rate of reaction is not as high as shown by the temperature-dependent terms alone. However, it is expected that temperature dependence will have a strong effect on the burning process in the shear layer.

Contrary to the case of temperature-independent kinetics, here we have two independent parameters that govern the rate of reaction: the pre-exponential factor, A_f, and the activation energy, T_a. These can be changed independently by varying the flow conditions, ρ, ΔU or $c_{F\infty}$, to affect the pre-exponential factor, or by using a catalyst to affect the effective activation energy. In the following, we will analyze results obtained for $A_f = 8000$, $T_a = 10$ and $Q = 1$. The average Damkohler number in this case is about 10, based on average temperature and concentration. We note that the dynamic field remains the same since the density changes are ignored.

The plot in Fig 60 shows a comparison between the product thickness for the laminar and turbulent shear layer in this case. The slow rise in δ_p in the initial stages is due to the low temperature of the reactants which reduces the rate of product formation until the slow heat release increases the temperature of the fluid element to values close to the "ignition temperature". Thus, the layer experiences an ignition delay in the streamwise direction equivalent to that observed in time in a homogeneous combustion bomb (this delay can be substantially reduced by preheating the reactants). The temperature increase along the streamwise direction is shown in Fig 61 in the form of instantaneous and time-average values along the line y=0.5, i.e., along the extension of the splitter plate. After roll up, the average temperature is smaller than the instantaneous temperature due to the local cyclical changes associated with passage of large hot eddies, as will be shown in Fig. 62(c). We also note that where the instantaneous temperature decreases below the average value there is a braid between two eddies.

The rate of product formation increases after roll up at a much higher rate for the turbulent layer than for the laminar layer, similar to what was observed in the temperature-independent kinetics. In both cases, however, the rise in δ_p is more than that recorded in the temperature-independent kinetics case and is associated with the effect of the Arrhenius term, as mentioned before. Thus, the layer experiences an explosion within the eddies. This explosion, which occurs in the downstream direction analogous to what is known to occur in time in a homogeneous combustion bomb. The burning process in the early stages of the shear layer is therefore controlled by the kinetic rate and not by the mixing. This lasts until the local temperature reaches values close to the ignition temperature. We remark that within the initial stages, the product thickness of the turbulent layer is smaller than that of the laminar layer. This, as mentioned before, is due to the stretch associated with the formation of the large eddies on the right-hand side of the initial stages, which leads to a slight thinning of the reacting zone thickness.

The structure of the scalar field within the shear layer is shown in Fig. 62 in terms of the instantaneous concentration of the oxidizer and the product and temperature contours. The reactants contours exhibit the result of the roll up of the vorticity layer and the entrainment of both streams into the large structures in the form of extended "tongues" that reach into the core of the eddy. When compared with the temperature-independent kinetics, high Damkohler number case, shown in Fig. 53(b), the penetration of the reactants into the eddy is more pronounced here. This is due to the fact that cool reactants can coexist in this case, contrary to the T-independent kinetics case, and that fast burning can only occur after enough temperature rise. The contours show another manifestation of asymmetric entrainment within both of the structures that appear within the plotting window. Note

the presence of two small eddies in the beginning of a pairing process on the left side of the window.

The product and temperature contours exhibit strong similarity, indicating that it is the temperature that controls the kinetic rate in this case. There is a high concentration of products and high temperature within the eddy cores, while in the braids zones the product concentration is zero and the temperature is that of the reactants. We also observe that the concentration gradients of products within the eddies are higher in this case than in the temperature-independent kinetic case. Concomitantly, there is stronger depletion of products within the braids due to the cooling associated with the entrainment of hot products into the eddy cores. The center of the eddy, as defined by the point of maximum concentration, is in the bottom, low velocity stream and the edges of the eddy, as defined by the contour $c_P = 0.02$, penetrate further into the bottom stream than the top stream. Both are further proofs of the mixing asymmetry in these flows.

To analyze the chemical potential in the field and to show how it is related to the flow dynamics, we plot the contours of $c_F c_O$ and $\dot{W}$, and the vorticity contours in Fig. 63. These plots were constructed at the same time step and for the same window as in Fig. 62. The strong similarity between the product concentration distribution and the vorticity distribution persists in this case and emphasizes the dominant role of the convection field in these flows. More revealing are the contours of $c_F c_O$, which exhibit some similarity to those in Fig 53 for temperature-independent kinetics. The zone of finite $c_F c_O$ in the current case exits on the outer edges of the large eddies and within the braids, and is thicker than that of the temperature-independent kinetic case. However, $c_F c_O$ does not constitute the chemical potential in the current case. The latter, as indicated by $\dot{W}$, show that finite chemical

potential exist only within smaller zones around the outer edges of the eddies. The low temperature in the braids zone, brought about by the fast entrainment of products into the eddy cores, extinguishes the chemical reaction there. It is in this sense, the heating and cooling of mixed reactants, that mixing by strong entraiment currents is still the dominant mechanism in reacting shear layers when the kinetics are strong functions of the temperature.

The instantaneous temperature contours in Fig. 62 explain the variation of the temperature as one moves downstream from the shear layer shown in Fig. 61. It is also clear why the average local temperature is lower than the instantaneous values attained within the eddies. The relationship between the two values is governed by the eddy passage frequencies and the rate of burning within each eddy.

6.7. CONCLUSION

Numerical simulations of a two-dimensional, two-stream, non-premixed, spatially-growing reacting shear layer have been carried out using the vortex method and the transport element method. Fuel and oxidizer, both diluted in an inert gas, react downstream of a splitter plate, forming products according to a low heat release, single step chemical reaction. Results were analyzed to study the effect of turbulence on the rate of burning at high Reynolds number and within a range of the Damkohler numbers.

1. Instantaneous distributions of the product concentration and vorticity exhibit a strong similarity, indicating the dominant role of convection in determining the local concentrations and the rate of mixing.

2. At low Damkohler numbers, products form at the center of the large eddies after reactants have been drawn in and well mixed. At high Damkohler

numbers, products form both at the center or on the outer edges of the eddies and are then drawn towards their centers. In both cases, products are not found within the braids since the large relative velocity between the streams does not allow enough time for mixing and since large eddies are continuously inhaling products that form on their boundaries.

3. In the temperature-dependent kinetics, the temperature and the concentration fields are strongly similar, indicating that temperature controls the kinetic rate in this case. The gradients of the product concentration are higher inside the core of the eddy, and the products concentration in the braids is lower than in temperature-independent case. The reactants can penetrate more into the eddy because they are not burnt until their temperature reaches the ignition point, beyond which they react.

4. At high Reynolds number, product formation is a weak function of the Reynolds number, indicating that while mixing is enhanced by entrainment, it is also limited by it. Diffusion occurs within the thin convoluted layers too fast to affect the mixing process. While strong diffusion, corresponding to very low Reynolds numbers O(100), was shown to compensate for the lack of mixing transition in the two-dimensional simulations, three dimensional simulations are necessary to properly account for this mechanism, which is essentially convective (Knio and Ghoniem [59]).

5. The results confirm the phenomenon of mixing asymmetry due to the finite velocity difference between the two streams by showing that the average product concentration on the lower side of the layer is higher than on the upper side.

6. Another manifestation of this phenomenon is the dependence of the product thickness on the value of Υ when $\Upsilon \neq 1$. In this later case, we found that for the same arrangement of the reactants in the two streams, more

products form for $\Psi < 1$ than for $\Psi > 1$ due the higher entrainment from the high-speed stream than from the low-speed stream.

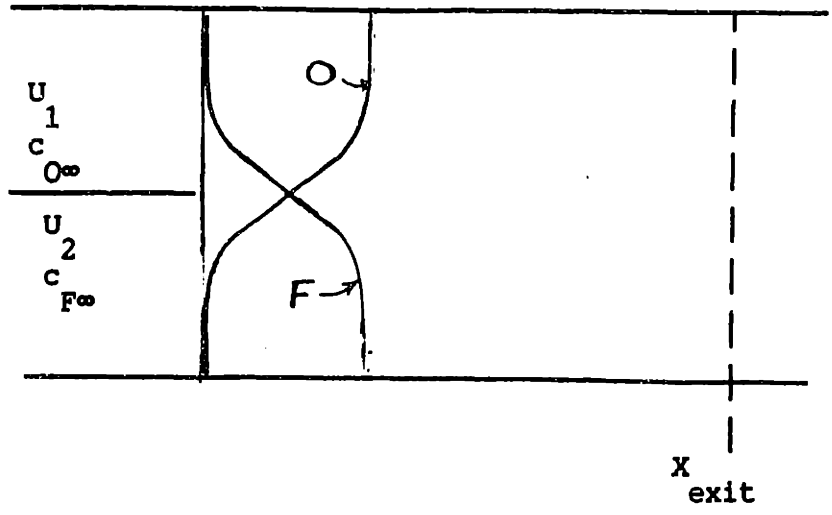

Fig. 45. Reactants distribution for an unperturbed layer and x=0 at all times.

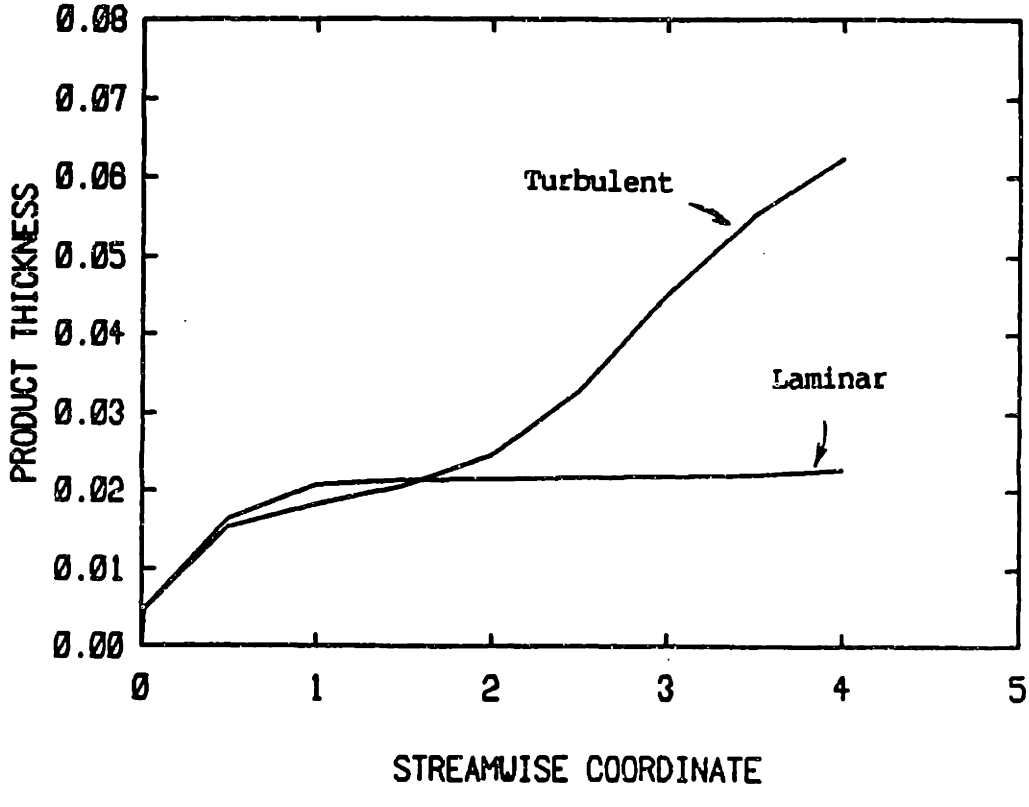

Fig. 46. Averaged δ_P vs. x for laminar and turbulent shear layer at R_e=5000, D_a=10, and Ψ=1.

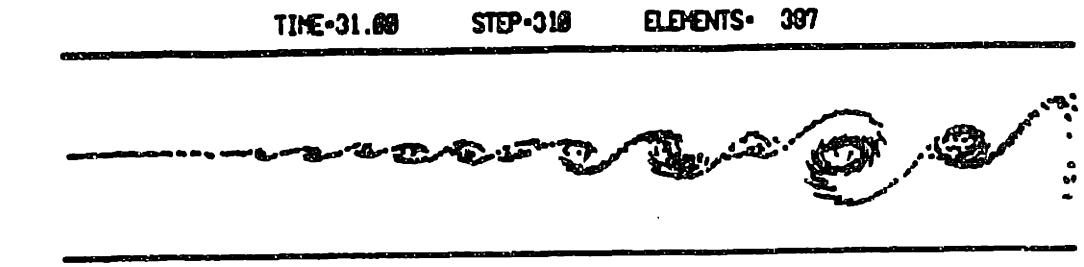

(a)

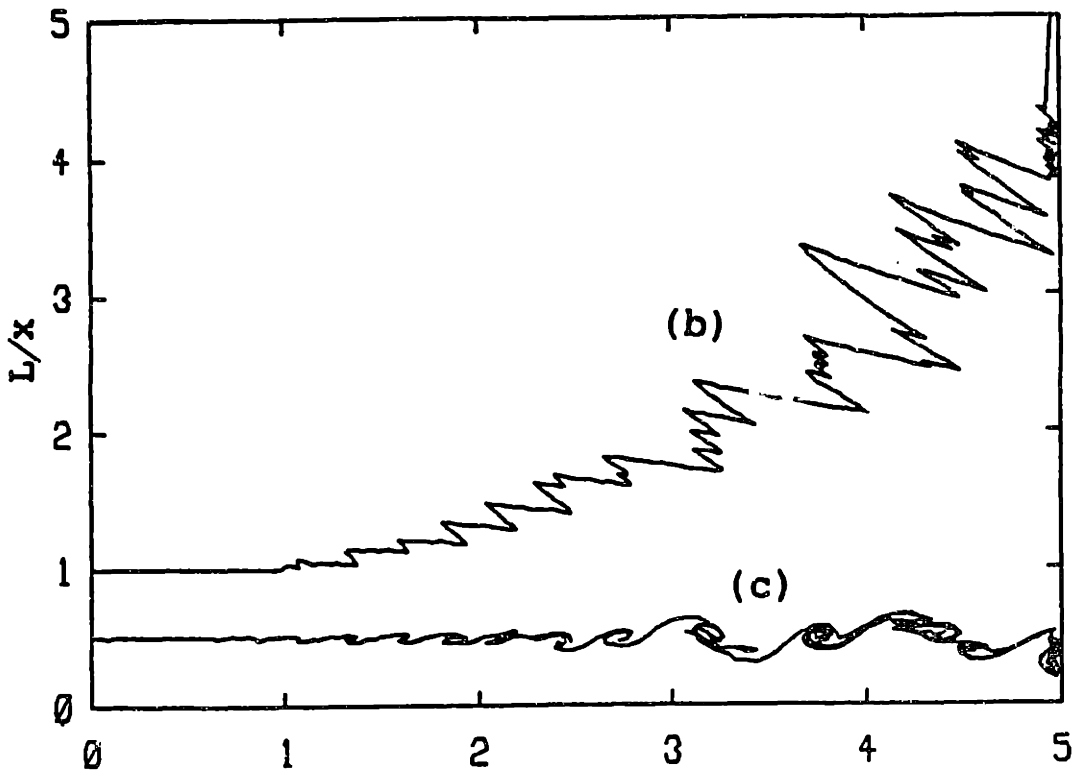

Fig. 47. Instantaneous interface of layer at later time in terms of: (a) vortex elements and velocity vector, (b) L/x; and (c) interface (line of y=0.5 at time t=0.

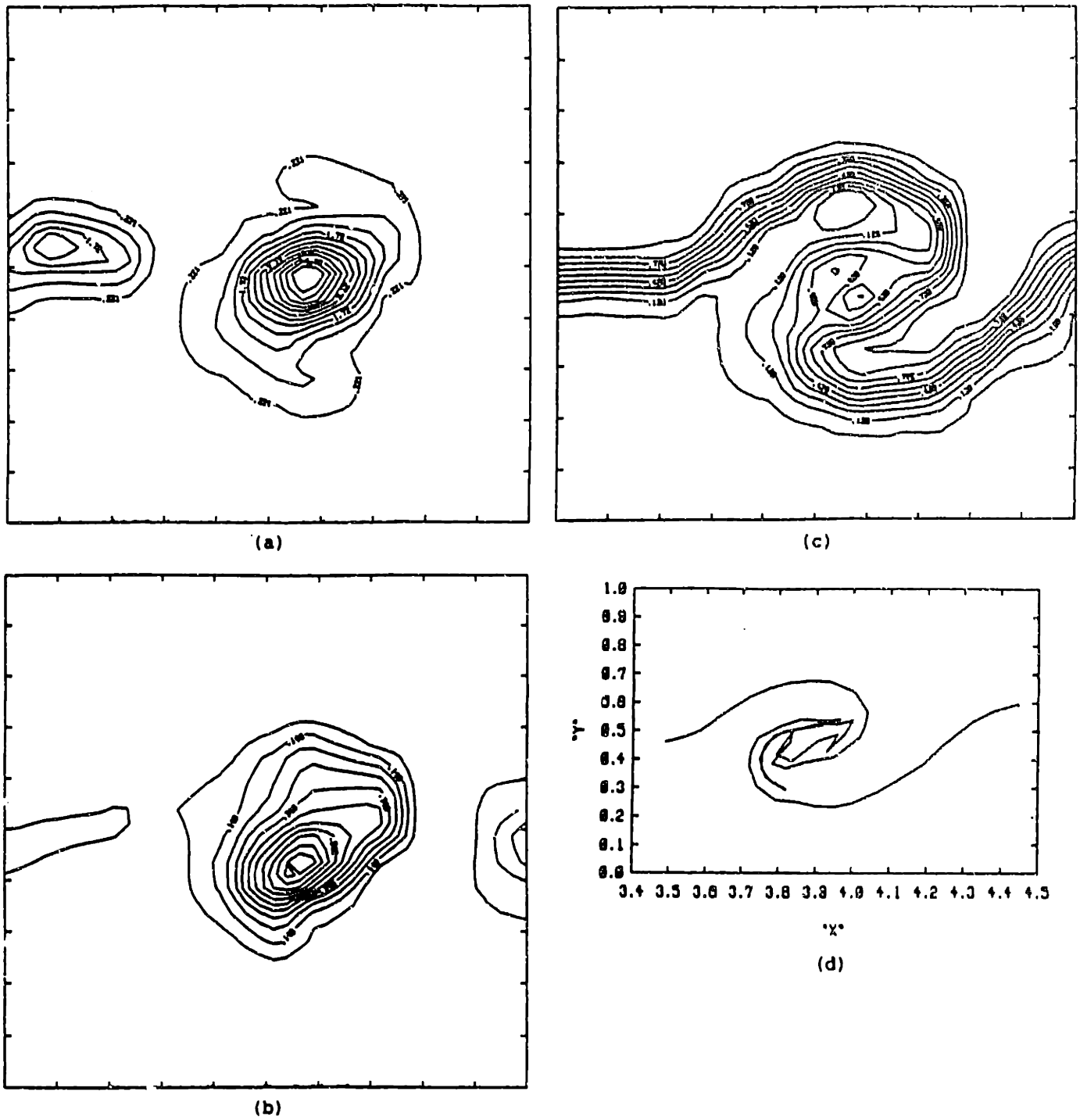

Fig. 48. Instantaneous distribution within an eddy in terms of: (a) vorticity contours, (b) products contours, (c) Oxidizer contours; and (d) interface (y=0.5 at time t=0).

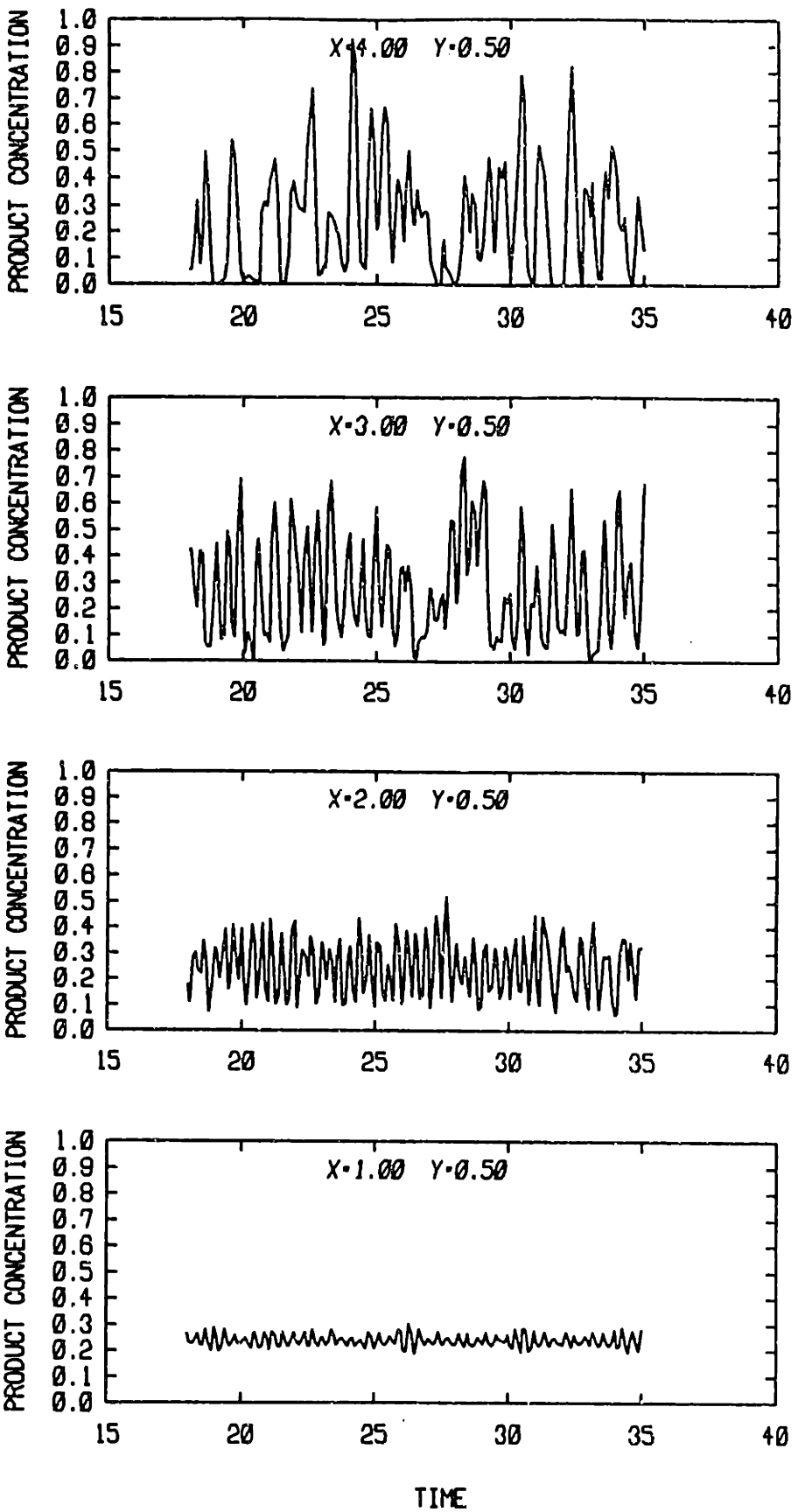

Fig. 49(a) Instantaneous values of product concentration with time at R_e=5000, D_a=10, Y=1 for y=0.5 and x=1, 2, 3, and 4.

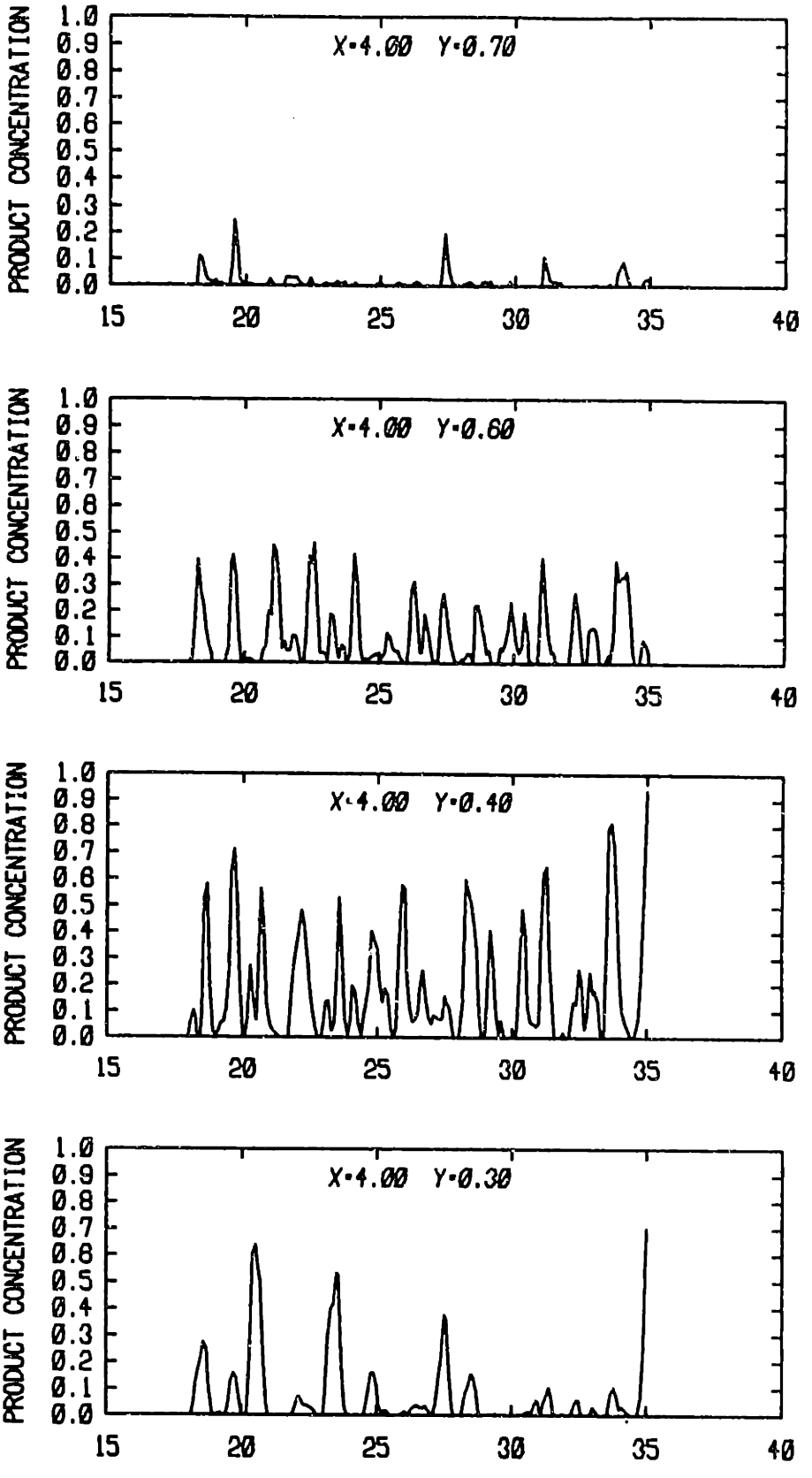

Fig. 49(b) Instantaneous values of product concentration with time at R_e=5000, D_a=10, Y=1 for x=4.0 and y=0.3, 0.4, 0.6, and 0.7.

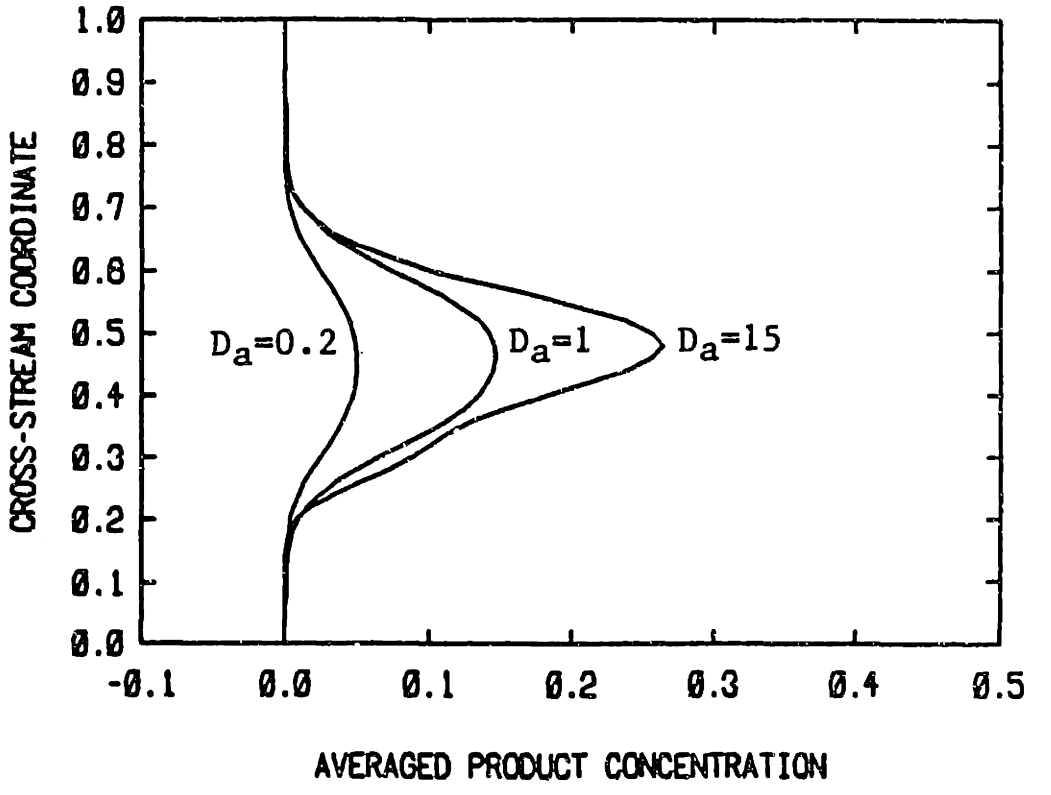

Fig. 50. Time-average product distribution, $c_p(y)$, for Da=0.2, 1, and 15 at Re=5000, $\bar{Y}$=1 at x=4.

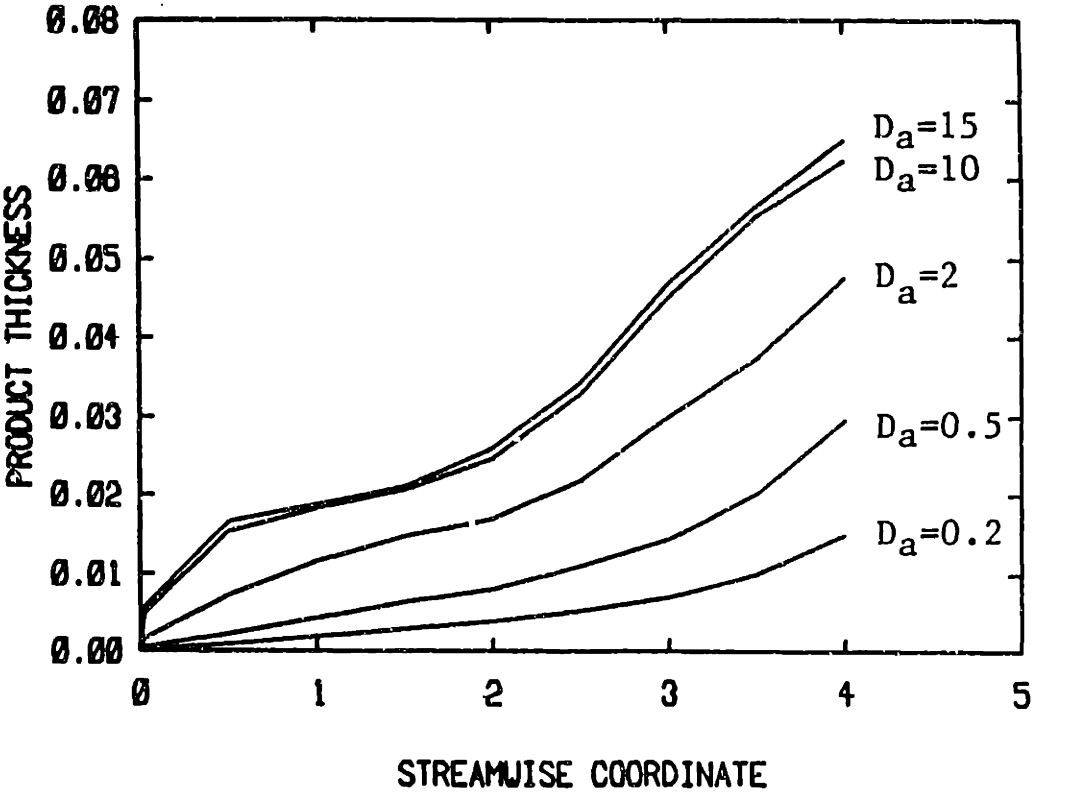

Fig. 51. Time-average δ_p vs. x for D_a=0.2-15, R_e=5000 and $\bar{Y}$=1.

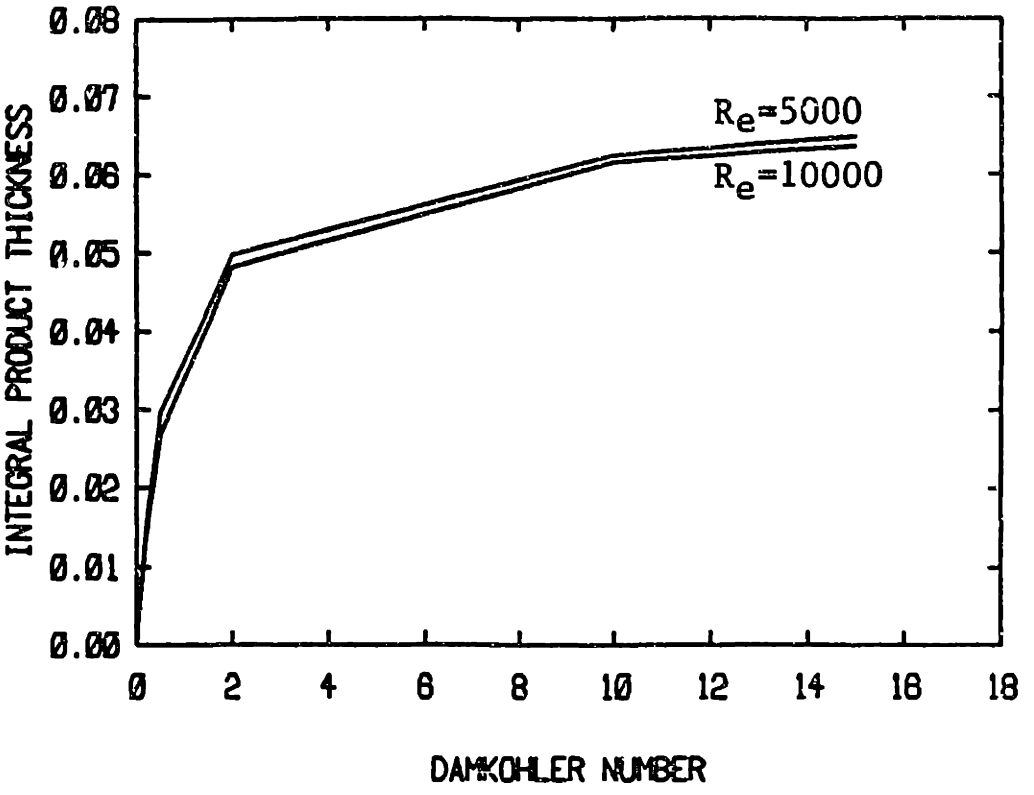

Fig. 52. Time-average δ_p vs. D_a for R_e=5000, 10000 and γ=1.

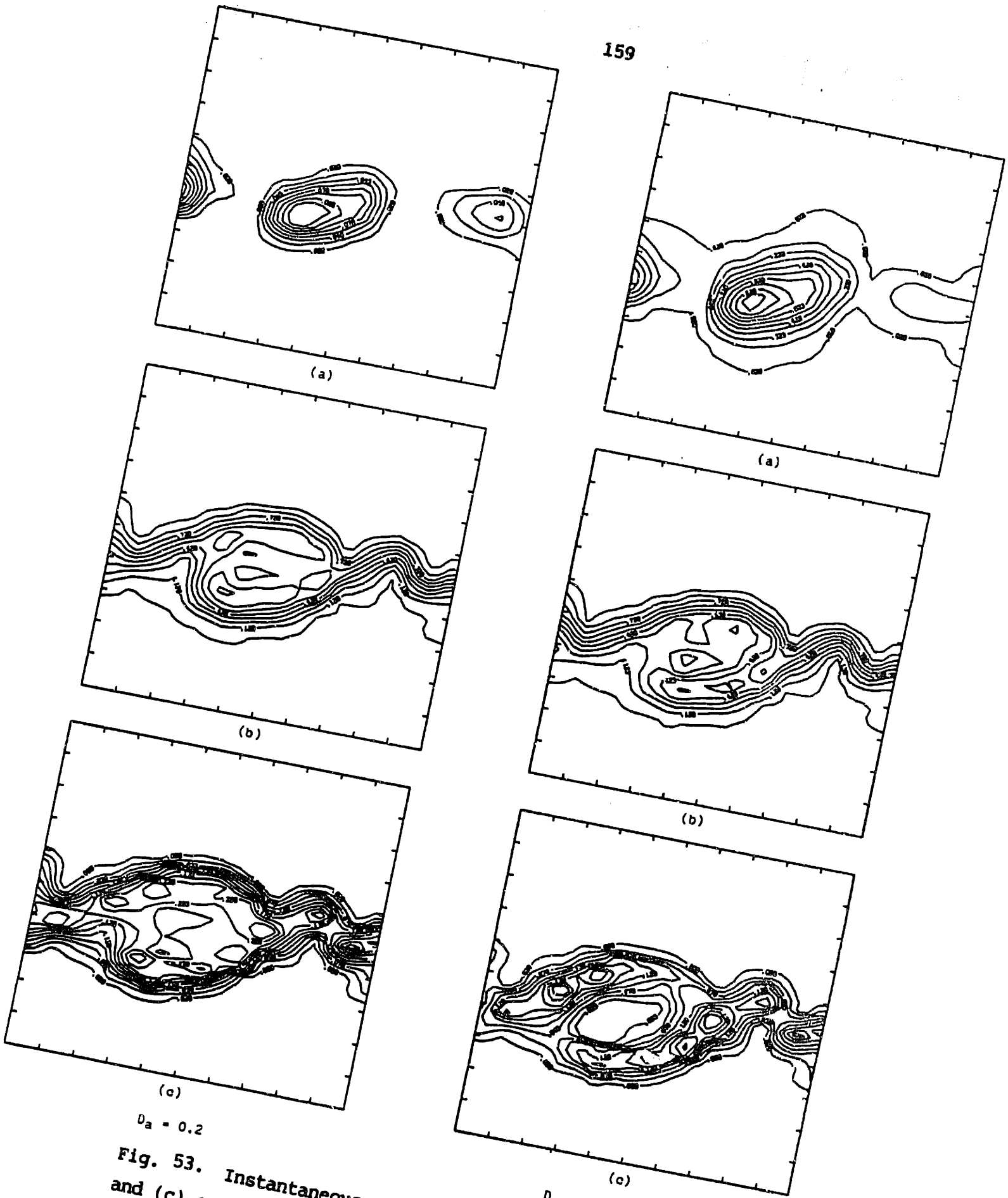

Fig. 53. Instantaneous contours of: (a) C_P, (b) C_O, and (c) $C_O C_F$ for D_a=0.2 and 10 at R_e=5000 and γ=1

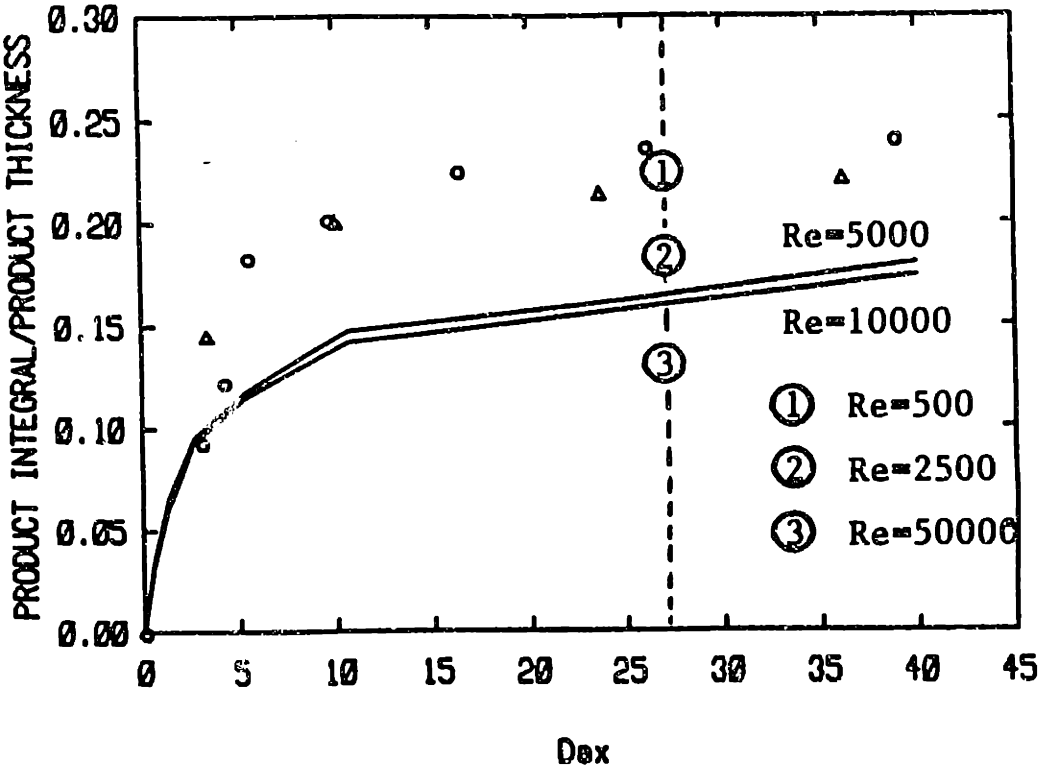

Fig. 54. Average normalized product thickness, δ_p/δ_1, vs. D_{ax} for R_e=5000 and γ=1

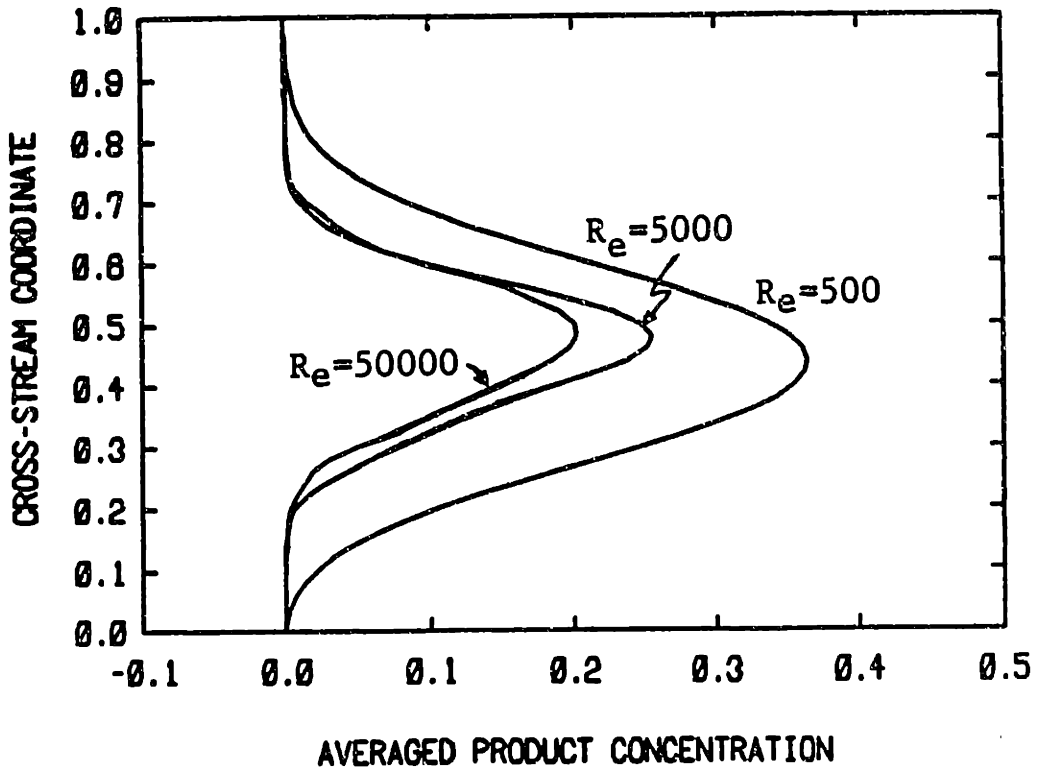

Fig. 55. Time-average product distribution, $c_p(y)$ for R_e=500-5000 with D_a=10, γ=1 at x=4.

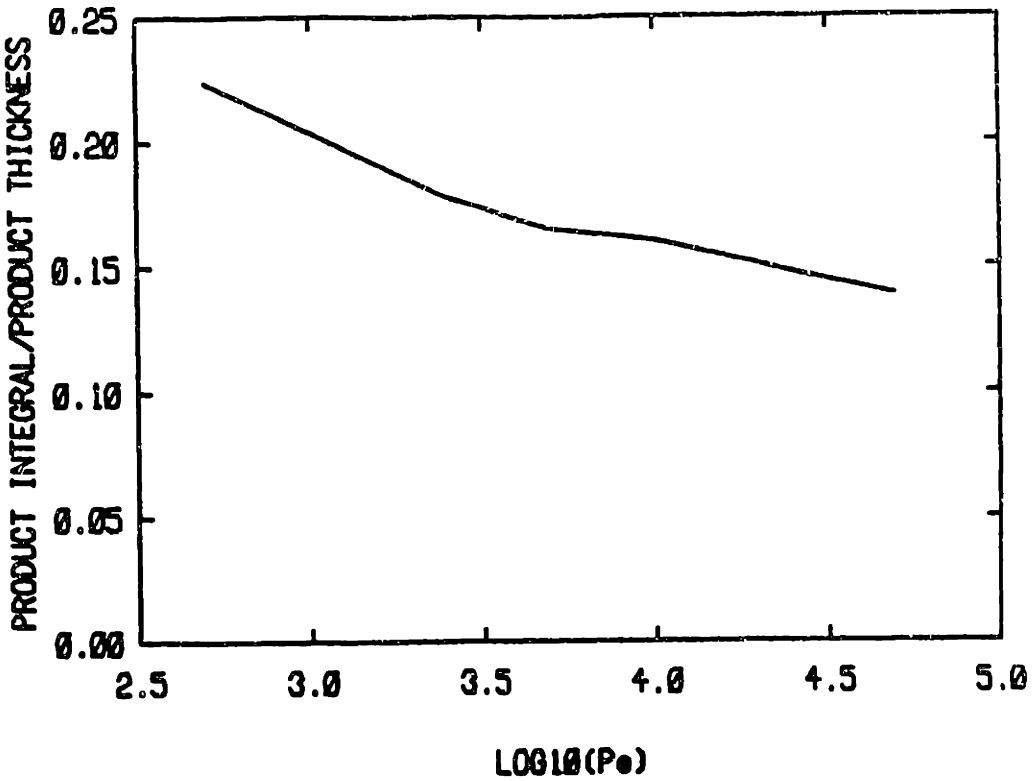

Fig. 56. Average normalized product thickness δ_p/δ_1 vs. R_e for D_a=10 and γ=1.

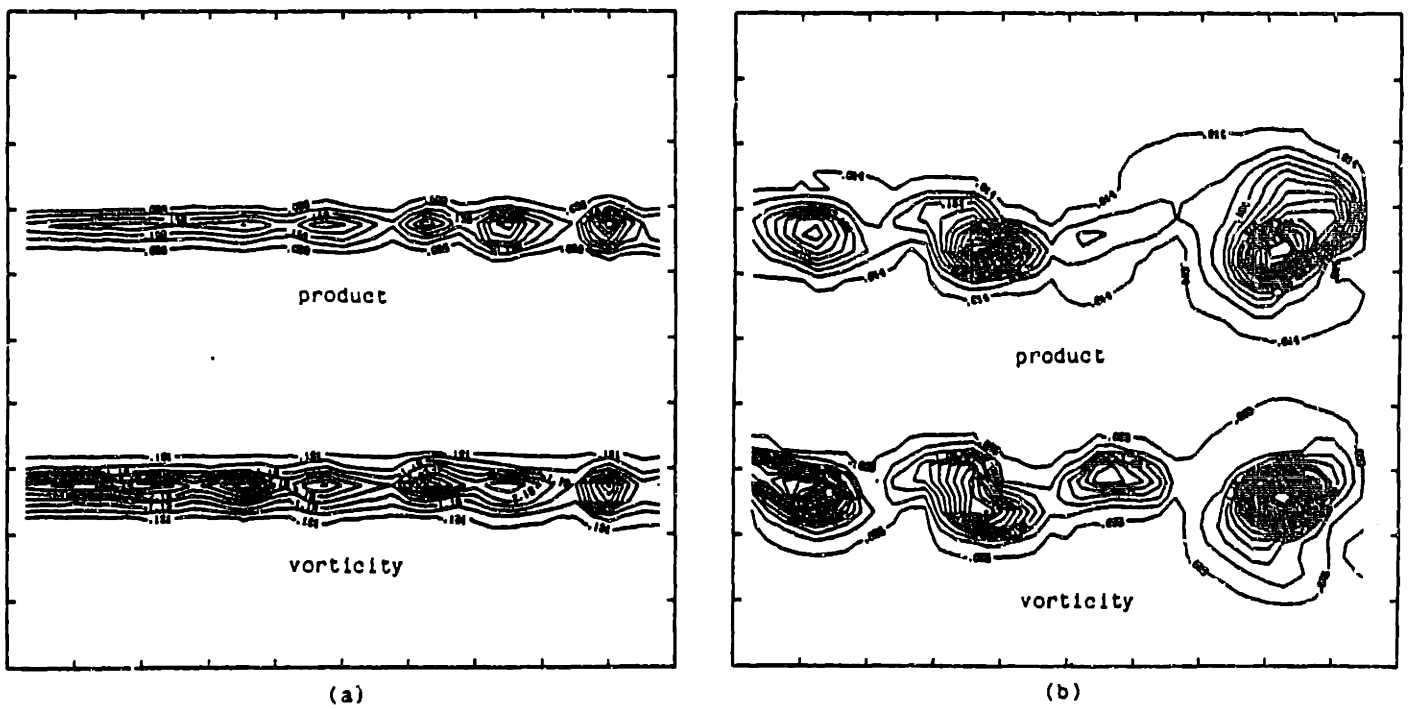

Fig. 57. Instantaneous Product and vorticity contours: (a) x=0.35-2.2; (b) x=2.35-4.2.

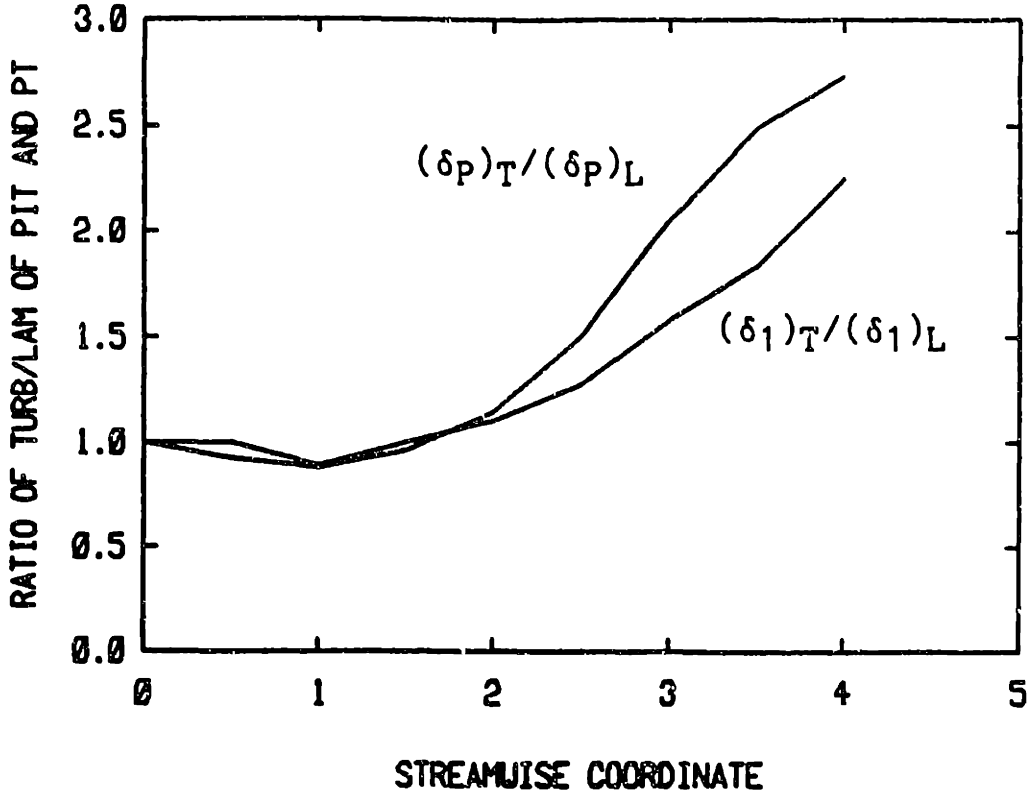

Fig. 58. Ratio of (turbulent to the laminar) the integral product thickness, δ_p, and the product thickness, δ_1, vs. x for D_a=10, R_e=5000, and Ψ=1.

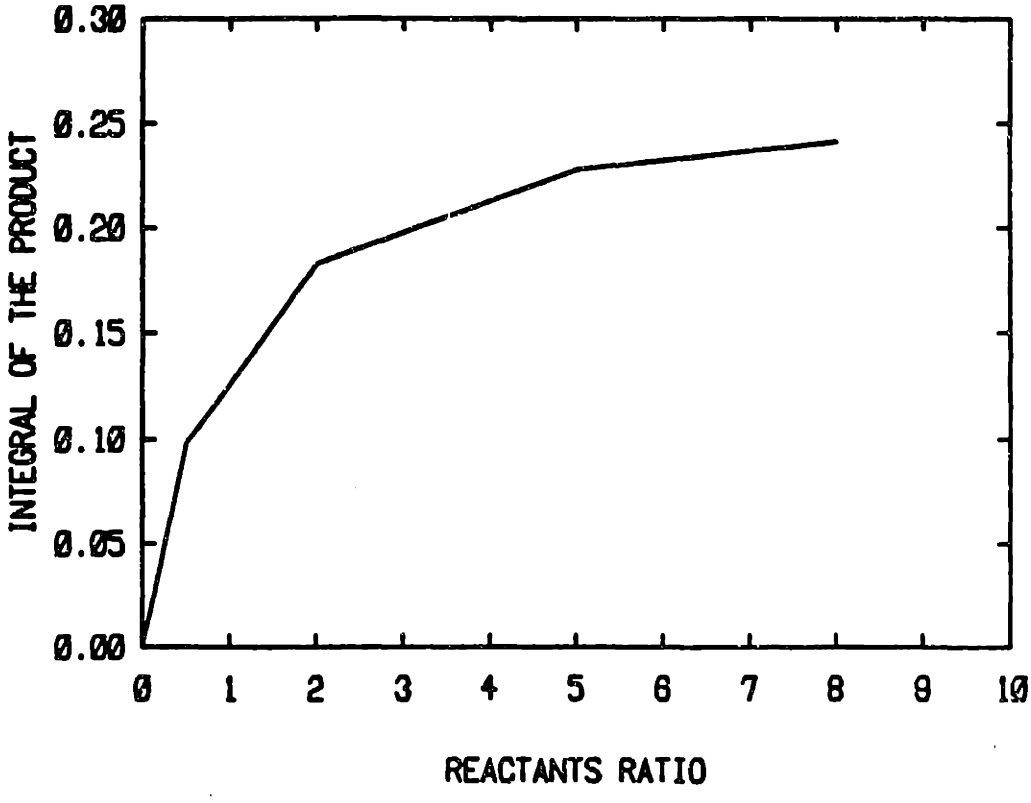

Fig. 59. $\int c_p(x,y)\,dx\,dy$ vs. Ψ for R_e=5000 and D_a=10.

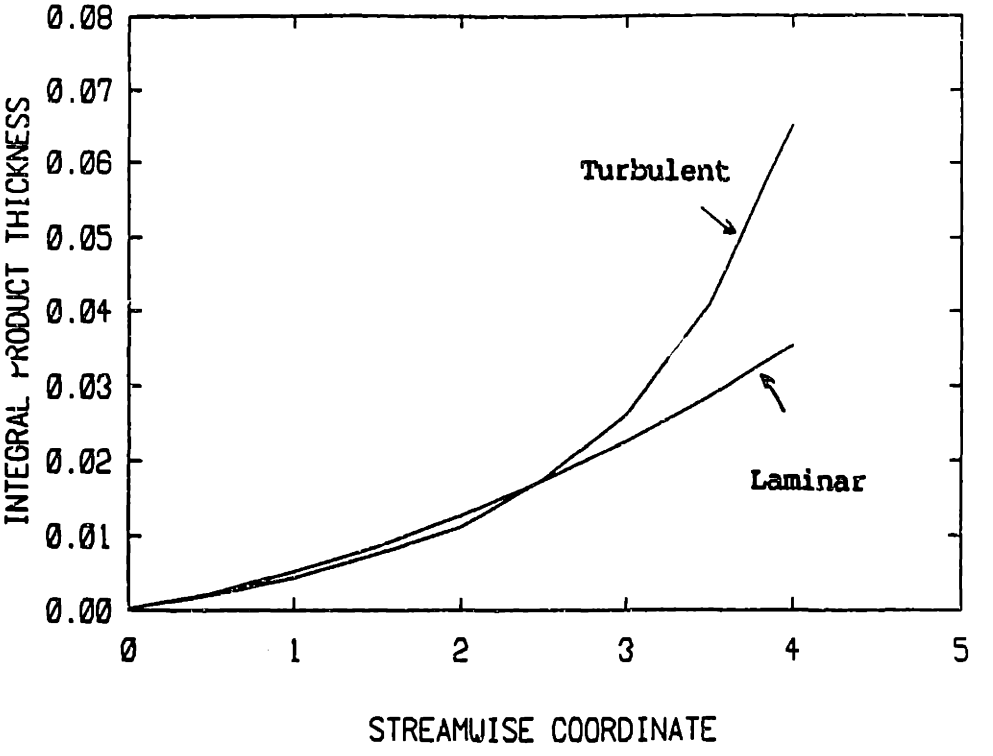

Fig. 60. Time-average δ_p vs. x for laminar and turbulent shear layer at R_e=5000, A_f=8000, T_a=10, Q=1, and $\bar{Y}$=1.

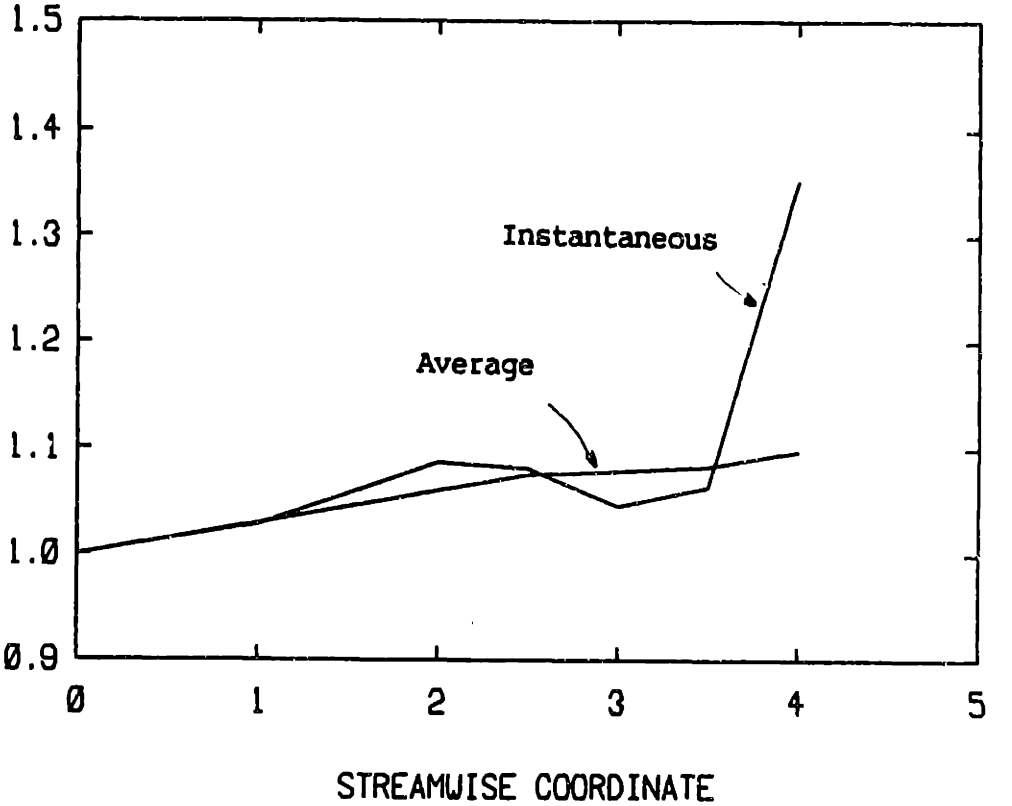

Fig. 61. Instantaneous (at time t=17.0), and time-average Temperature along y=0.5 vs. x.

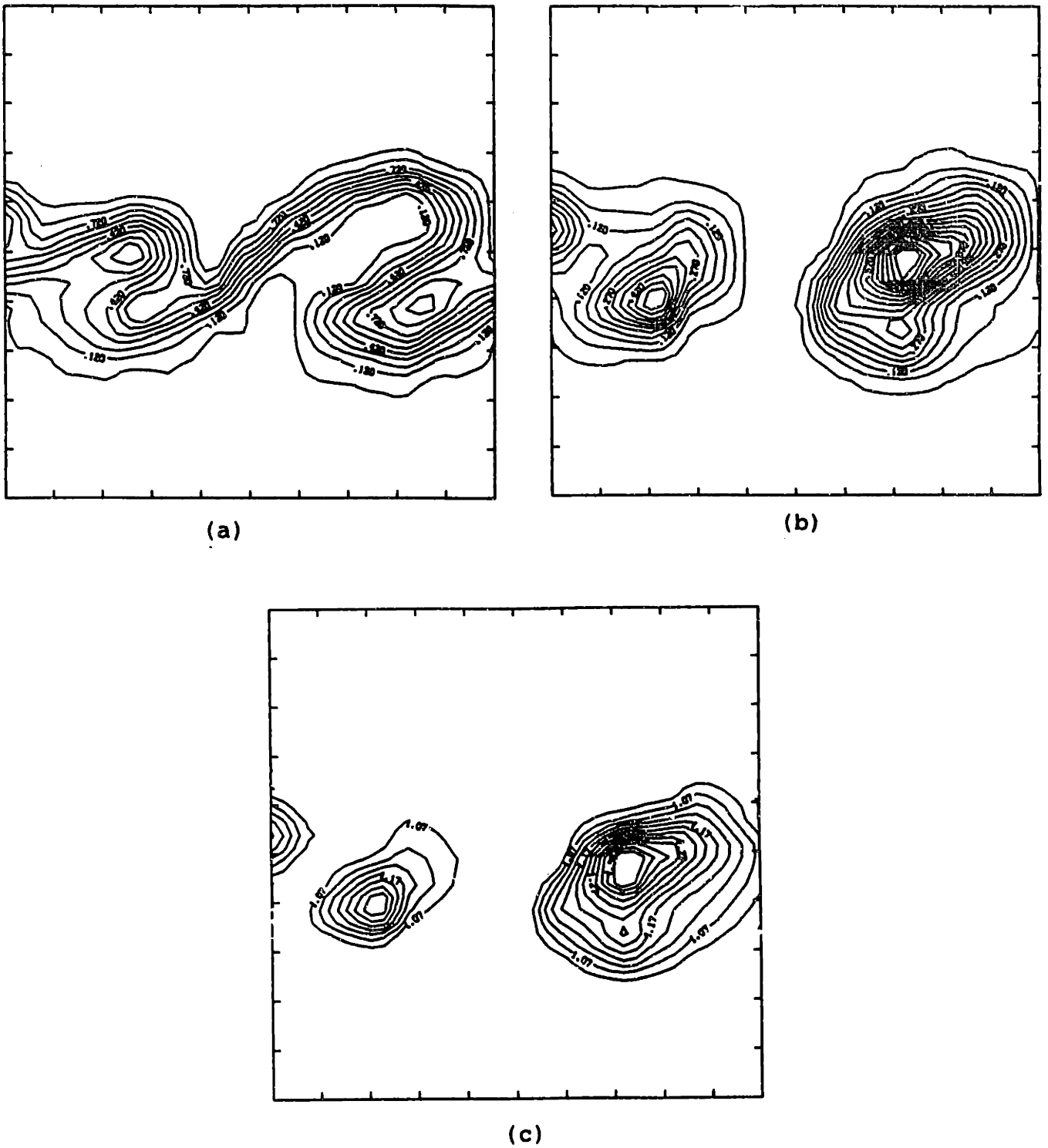

Fig. 62. Instantaneous contours of: (a) oxidizer concentration, (b) product concentration; and (c) temperature. Chemical parameters same as Fig. 60.

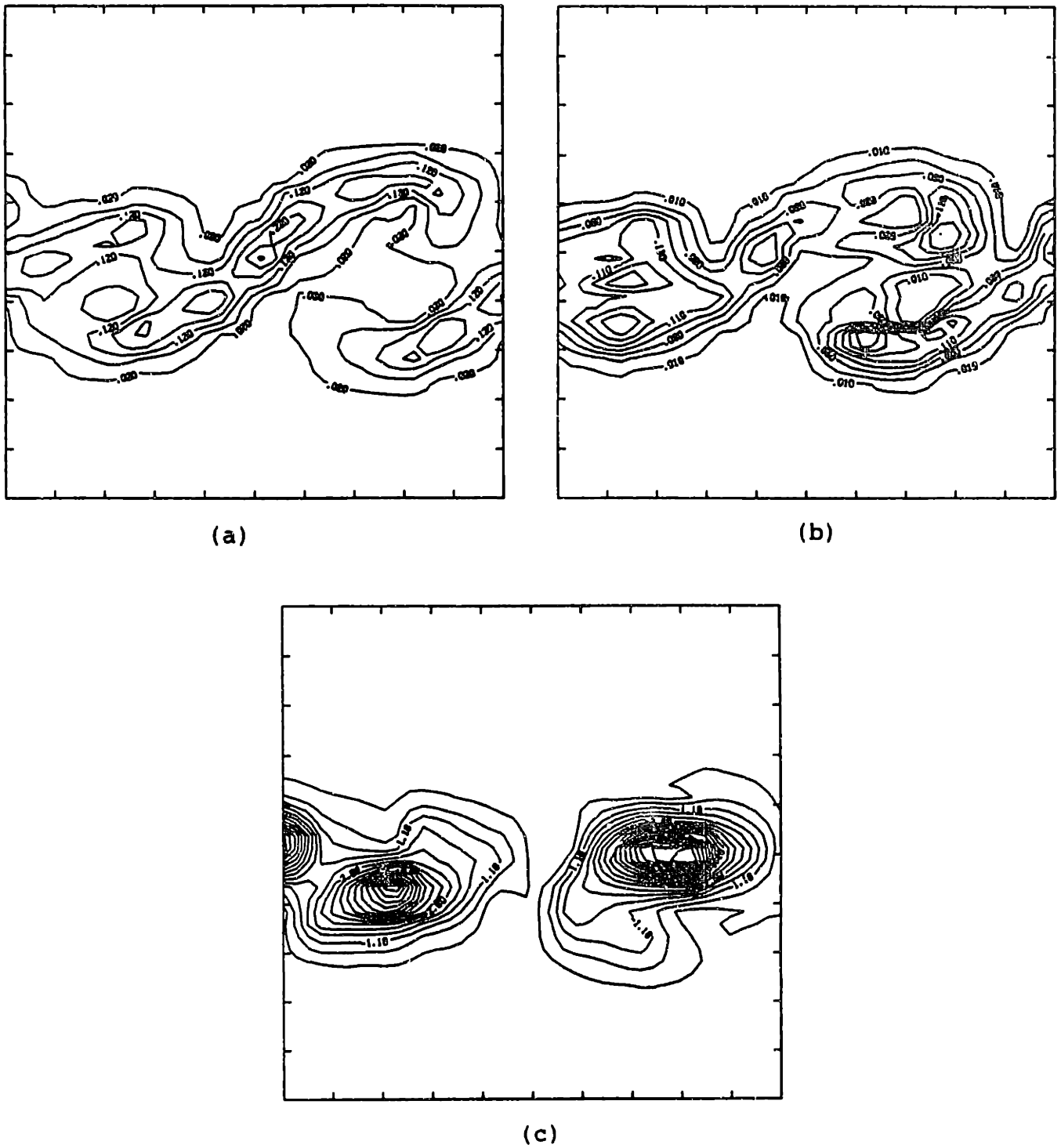

Fig. 63. Instantaneous contours of: (a) $c_O c_F$, (b) $c_O c_F \exp(-T_a/T)$; and (c) vorticity. All other parameters same as Fig. 60.

Chapter 7

Conclusions

The vortex/transport element method has been developed to study two-dimensional, two-stream, constant-density, non-premixed, reacting shear layer in which heat, mass and momentum are transported at large Reynolds numbers. The numerical scheme is Lagrangian, naturally compatible with the Lagrangian nature of the chemistry, and the computational elements are placed where there exist the gradient of the primitive variables and/or there is strong stretch. The numerical scheme is applied to the reacting as well as non-reacting turbulent mixing layers. Particular attention is given to understanding the effect of turbulence on chemistry, flame stability under condition of strong stretch, and different flow parameters. The conclusions are as follows:

1. The vortex/scalar transport element method is developed in which the vorticity and scalar gradients are accurately discretized among strongly overlapping computational elements. The method is Lagrangian and avoid the non-linearity of the convective terms in the original equations. The method is rendered conservative by utilizing the relationship between the distortion of the flow lines and the evolution of the scalar gradients.

2. It is found that a second order Gaussian core function is sufficient to give a continuous and smooth distribution for the vorticity, velocity, and their derivatives. A second order time-integration scheme is also found adequate to integrate the time-dependent equations along the particle path. In the reacting flow case, however, an extra restriction is imposed on the time step when the chemical time scales are small compared with the flow time scales and when the chemical reaction is stiff.

3. Results of the numerical simulation of the non-reacting shear layer show that the basic dynamical processes that governs the development of the

layer are the roll up of the initial vorticity layer into large scale eddies and the pairing of these eddies downstream.

4. Due to the different velocity distribution at the inlet and exit of the computational domain there exists a small but nonzero streamwise velocity gradient which in turn leads to its corresponding cross stream velocity. The highest value of the cross stream velocity occurs around the tip of the splitter plate where the asymmetry of the inlet velocity distribution is the highest, and diminishes downstream where the flow approaches a more uniform distribution. This phenomena leads to the asymmetry of the entrainment of fluids from both stream into the layer and shift of the center of the eddies toward the low-speed side. This is in fact the most important difference between the temporal and the spatial models of the shear layer, and it depends explicitly on the velocity difference across the layer.

5. Another manifestation of the mixing asymmetry is the dependence of the product formation on the value of Y when $Y \neq 1$. In this later case, we found that for the same arrangement of the reactants in the two streams, more products form for $Y < 1$ than for $Y > 1$ due the higher entrainment from the high-speed stream than from the low-speed stream.

6. In the reacting shear layer the instantaneous distributions of the product concentration and vorticity exhibit a strong similarity, indicating the dominant role of convection in determining the local concentrations and the rate of mixing. This similarity can be expressed mathematically in the form of $c_p(x,y,t) = f(R_e,D_a)\ \omega(x,y,t)$ where f is a weak function of R_e and a strong function of D_a.

7. At low Damkohler numbers, products form at the center of the large eddies which are the reacting eddies while at high Damkohler numbers, the chemical reaction is strong around the outer edges of the eddies, however, the

formed products are then drawn towards the centers of the eddies. In both cases, products are not found within the braids since the large relative velocity between the streams does not allow enough time for mixing and since large eddies are continuously inhaling products that form on their boundaries.

8. In order to compensate for the lack of mixing transition in the two-dimensional simulations, three dimensional simulations are necessary to properly account for this mechanism which is essentially a convective mechanism.

REFERENCES

1. Bilger, R.W., "Turbulent flow with non-premixed reactants," Turbulent reacting flows, Spring-Verlag, Berlin, 1980, pp. 65-113.

2. Donaldson, C. duP. and Varma, A.K., "Remarks on the constructions of a second-order closure description of turbulent reacting flows," Combustion Sience and Technology, Vol. 13, 1976, pp. 55-78.

3. Givi, P., Ramos, J.I., and Sirigano, W.A., "Turbulent reacting concentric jets: Comparison between PDF and moment calculations," Progress on Astronautics and Aeronautics, Vol. 95, AIAA, New York, 1984, pp. 384-448.

4. Bilger, R.W., "Turbulent jet diffusion flames," Progress in Energy and Combustion Science, Vol. 1, 1976, pp. 87-109.

5. Lockwood, F.C. and Naguib, A.S., "The prediction of the fluctuations in the properties of free, round jet, turbulent, diffusion flames," Combustion Flame, Vol. 24, 1975, pp. 109-124.

6. Givi, P., Sirignano, W.A., and Pope, S.B., "Probability calculations for turbulent jet flows with mixing and reaction of NO and O_3," Combustion and Sience Technology, Vol. 37, 1984, pp. 599-674.

7. Nguyen, T.V. and Pope, S.B., "Monte-Carlo calculations of turbulent diffusion flames," Combustion Science and Technology, Vol. 42, 1984, pp. 13-45.

8. Pope, S.B. and Correa, S.M., "Joint PDF calculations of non-equilibrium turbulent diffusion flame," Proceeding of the 21st Symposium (International) on Combustion, the Combustion Institute, Pitsburgh, PA, 1988, pp. 1341-1348.

9. Batt, R.G., "Turbulent mixing of passive and chemically reacting species in a low-speed shear layer," J. Fluid Mech., Vol. 82, 1977, pp. 53-95.

10. Breidenthal. R.E., "Structure in turbulent mixing layers and wakes using a chemical reaction," J. Fluid Mech., Vol. 109, 1981, pp. 1-24.

11. Wallace, A.K., "Experimental investigation of the effects of chemical heat release in the reacting turbulent plane shear layer," Ph.D. Thesis, University of Adelaide, 1981; also AFOSR Report AFOSR-TR-84-0650.

12. Mungal, M.G., and Dimotakis, P.E., "Mixing and combustion with low heat release in a turbulent shear layer," J. Fluid Mech., Vol. 148, 1984, pp. 349-382.

13. Broadwell, J.E. and Breidenthal, R.E., "A simple model of mixing and chemical reaction in a turbulent shear layer," J. Fluid Mech., Vol. 125, 1982, pp. 397-410.

14. Broadwell, J.E. and Mungal, M.G., GALCIT Report FM86-01, Caltech, 1986.

15. Ghoniem, A.F., "Computational methods in turbulent reacting flows," Lectures in Applied Mathematics, Vol. 24, American Mathematical Society, Providence, RI, 1986, pp. 199-265.

16. Oran, E.S. and Boris, J.P., Numerical simulation of reactive flows, Elsevier Science Publishing Co., New York, 1987.

17. Corcos, G.M. and Sherman, F.S., "The mixing layer: Deterministic models of a turbulent flow; Part 1: Introduction and the two-dimensional flow," J. Fluid Mech., Vol. 139, 1984, pp. 29-65.

18. Grinstein, F.F, Oran, E.S, and Boris, J.P., "Numerical simulations of asymmetric mixing in planar shear flows." J. Fluid Mech., Vol. 165, 1986, pp. 201-220.

19. Riley, J.J., Metcalfe, R.W., and Orszag, S.A., "Direct numerical simulations of chemically reacting turbulent mixing layers," Physics of Fluids, Vol. 29, 1986, pp. 406-422.

20. McMurtry, P.A., Jou, W.H., Riley, J.J., and Metcalfe, R.W., "Direct numerical simulations of a reacting mixing layer with chemical heat release," AIAA Journal, Vol. 24, No. 6, 1986, pp. 962-970.

21. Givi, P., Jou, W.H., and Metcalfe, R.W., "Flame extinction in a temporally evolving mixing layer," Proceeding of the 21st Symposium (International) on combustion, The Combustion Institute, Pitsburgh, PA, 1988, pp. 1251-1262.

22. Givi, P., and Jou, W.H., "Mixing and chemical reaction in a spatially developing mixing layer," Journal of Nonequilibrium Thermodynamics, (to be published).

23. Leonard, A., "Vortex methods for flow simulation," J. Comput. Phys., Vol. 37, 1980, pp. 289-335.

24. Beale, J.T. and Majda, A., "Higher order accurate vortex methods with explicit velocity kernel," J. Comput. Phys., Vol. 58, No. 2, 1985, pp. 188-209.

25. Hald, O.H., "The convergence of vortex methods, II.," SIAM J. Num. Anal., Vol. 16, 1979, pp. 726-755.

26. Ghoniem, A.F. and Ng, K.K., "Numerical study of the dynamics of a forced shear layer," Phys. Fluid, Vol. 30, 1987, pp. 706-721.

27. Chorin, A.J., "Numerical study of slightly viscous flow," J. Fluid Mech., Vol. 57, 1973, pp. 785-796.

28. Fritts, M.J., and Boris, J.P., "The Lagrangian solution of transient problems in hydrodynamics using a triangular mesh," J. Comput. Phys., Vol. 31, 1979, pp. 173-215.

29. Zabuski, N.J., Hughes, M.H., and Roberts, K.V., "Contour dynamics for the Euler equations in two-dimensions," J. Comput. Phys., Vol. 30, 1979, pp. 96-106.

30. Chorin, A.J., Hughes, T.J.R., McCracken, M.F., and Marsden, J.E., "Product formulas and numerical algorithms," Comm. Pure Appl. Math, Vol. 31, 1978, pp. 205-256.

31. Hald, O.H. and Del-Prete, V.M. "Convergence of vortex methods for Euler's equations," Math. Comput., Vol. 32, 1978, pp. 791-809

32. Hald, O.H., "Convergence of Vortex Methods for Euler's Equations, III," Ctr. for Pure and Applied Math., PAM-270, University of California, Brekeley, 1985.

33. Beale, J.T. and Majda, A., "Vortex methods. II: Higher order accuracy in two and three dimensions," Math. of Comp., Vol. 39, No. 159, 1982, pp. 29-52.

34. Nakamura, Y., Leonard, A., and Spalart, P., "Vortex simulation of an inviscid shear layer," Proceedings, AIAA/ASME 3rd Joint Thermo-physics, Fluid, Plasma and Heat Transfer Conference, AIAA Paper 82-0948, 1982.

35. Roberts, S., "Accuracy of the random vortex method for a problem with non-smooth initial conditions," J. Comput. Phys., Vol. 58, 1985, pp. 29-43.

36. Perlman, M., "On the Accuracy of Vortex Methods," J. Comput. Phys., Vol. 59, 1985, pp. 200-223.

37. Anderson, C. and Greengard, C.,"On vortex methods," SIAM J. Num. Anal., Vol. 22, 1985, pp. 413-440.

38. Anderson, C.R., " A vortex method for flow with slight density variations," J. Comput. Phys., Vol. 61, 1985, pp. 417-444.

39. Krasny, R., "Desingularization of periodic vortex sheet roll-up," J. Comput. Phys., Vol. 65, 1986, pp. 292-313.

40. Zabuski, N.J. and Overman, E.A., "Regularization of contour dynamical algorithms. I. Tangential regularization," J. Comput. Phys., Vol. 52, 1983, pp. 351-373.

41. Krasny, R., "Computation of vortex sheet roll up in the Treffetz plane," submitted for publication.

42. Ghoniem, A.F., Chorin, A.J., and Oppenheim, A.K., "Numerical modeling of turbulent flow in a combustion tunnel," Phil. Trans. R. Soc. London, A304, 1982, PP. 303-325.

43. Sethian, J.A, "Turbulent combustion in open and closed vessels," J. Comp. Phys., Vol. 54, No. 3, 1984, pp. 425-456.

44. Ashurst, W.T. and Barr, P.K., "Lagrangian-Eulerian calculation of turbulent diffusion flame propagation," Sandia National Laboratories, Livermore, CA, Sandia rept. SAND80-9950, 1982.

45. Lin, P. and Pratt, D.T., "Numerical simulation of a plane mixing layer, with application to isothermal, rapid reactions," AIAA paper 87-0224, Jan. 1988.

46. Ghoniem, A.F. and Givi, P., "Lagrangian simulation of a reacting mixing layer at low heat release,," AIAA Journal Vol. 26, No. 6, 1988, pp. 690-697.

47. Chorin, A.J., in Computing Methods in Applied Sciences and Engineering, edited by R. Glowinski and J.L. Lions, North-Holland, INRIA, Amsterdam, 1980.

48. Ghoniem, A.F. and Oppenhiem, A.K., "Random element method for numerical modeling of diffusional processes," in Proceedings, 8th Int. Conf. Num. Methods Fluid Dynamics, edited by E. Krause (Spring-Verlag, New York, 1982) pp. 224-232.

49. Ghoniem, A.F. and Oppenhiem, A.K., "Numerical solution of the problem of flame propagation by the random element method," AIAA Journal, Vol. 22, No. 10, 1984, pp. 1429-1435.

50. Ghoniem, A.F. and Sherman, F.S., "Grid-free simulation of diffusion using random walk methods," J. Comput. Phys., Vol. 61, No. 1, 1985, pp. 1-37.

51. Anderson, C., "Vortex methods for flows of variable density," Ph.D. thesis, Department of Mathematics, U.C. Berkeley, 1983.

52. Ghoniem, A.F., Heidarinejad, G., Krishnan, A., "Numerical Simulation of a Thermally Stratified Shear Layer Using the Vortex Element Method," J. Comput. Phys., Vol. 79, No. 1, 1988, pp. 135-166.

53. Ghoniem, A.F., Heidarinejad, G., Krishnan, A., "Numerical Simulation of a Reacting Shear Layer Using the Transport Element Method," The AIAA/SAE/ASME/ASEE Joint Propulsion Meeting, June 29-July 1, 1987, La Jolla, California, AIAA-87-1718; also, "Turbulence-combustion interactions in reacting shear layer," Proceeding of the Joint France-U.S.A. Workshop on Turbulent Reactive Flows, Rouen, France, 6-10 July 1987.

54. Ghoniem, A.F., Heidarinejad, G., Krishnan, A., "On Mixing, Baroclinicity and the Effect of Strain in a Chemically Reacting Shear Layer," the 26th AIAA Aerospace Science Meeting, January 11-14, 1988, Reno, Nevada, AIAA-88-0729.

55. Masutani, S.M., Bowman, C.T., "The structure of a chemically reacting plane mixing layer," J. Fluid Mech., Vol. 172, 1986, pp. 93-126.

56. Heidarinejad, G. and Ghoniem, A.F., "Vortex simulation of the reacting shear layer; Effects of Reynolds and Damkohler number," the 27th AIAA Aerospace Science Meeting, January 9-12, 1988, Reno, Nevada, AIAA-88-0573.

57. Ghoniem, A.F. and Krishnan, A., "Origin and manifestation of flow-combustion interaction in a premixed shear layer," for presentation at the 22nd Symposium (International) on Combustion, 8-13 August, 1988, Seatle, Washington.

58. Krishnan, A. and Ghoniem, A.F., "Numerical Simulation of the Structure of a heated Jet in a Cold Environment," the 27th AIAA Aerospace Science Meeting, January 9-12, 1988, Reno, Nevada, AIAA-88-0485.

59. Knio, O.M. and Ghoniem, A.F., "Three dimensional vortex simulation of entrainment augmentation due to streamwise structures," the 27th AIAA Aerospace Sciences Meeting, Reno, Nevada, January 1989, AIAA-89-0574.

60. Brown, G.L. and Roshko, A., "On density effects and large structure in turbulent mixing layers," J. Fluid Mech. Vol. 64, part 4, 1974, pp. 775-816.

61. Batchelor, G.K., An introduction to Fluid Dynamics, Cambridge University Press, London, 1967.

62. Chorin, A.J. and Marsden, J.E., A Mathematical Introduction to Fluid Mechanics, Spring-Verlag, New York, 1979.

63. Milne-Thomson L.M., Theoretical Hydrodynamics, 5th edition, Macmillan press, London, 1968.

64. Teng, Z., "Elliptic-vortex method for incompressible flow at high Reynolds number," J. Comput. Phys., Vol. 46, 1982, pp. 54-68.

65. Betchov, R., and Criminale, N.O., Jr., Stability of parallel flows, Academic Press, New York, 1967.

66. Michalke, A., "On the inviscid instability of the hyperbolic-tangent velocity profile," J. Fluid Mech. Vol. 19, 1964, pp. 543-556.

67. Roberts, F.A. , Dimotakis, P.E. and Roshko, A., Album of Fluid Motion, edited by M. Van Dyke, Parabolic Press, Stanford, CA, 1982, pp. 85.

68. Pozrikidis, C. and Higdon, J.L., "Nonlinear Kelvin-Helmholtz instability of a finite vortex layer," J. Fluid Mech,, Vol. 157, 1985, pp. 225-263.

69. Konrad, J.H., "An experimental investigation of mixing in two-dimensional turbulent shear flows with applications to diffusion-limited chemical reactions," Project SQUID Tech. Rep. CIT-8-PUI, 1976.

70. Ho, C.M. and Huerre, P., "Perturbed free shear layer," Ann. Fluid Mech., 1984, pp. 365-424.

71. Williams, F.A., Combustion Theory, Addison-Welsley publishing company, Reading Mass., First edition, 1965.

72. Mungal, M.G. and Frieler, C.E., "The Effects of Damkohler Number in a Turbulent Shear Layer," Combust. Flame, Vol. 71, 1988, pp. 23-34.

73. Koochesfahani, M.M. and Dimotakis, P.E., "Mixing and chemical reaction in a turbulent liquid mixing layer," J. Fluid Mech., Vol. 170, 1986, pp. 83-112.

Appendix

Computer program for reacting spatial shear layer using vortex and transport element methods.

```
C
C
C
C*************************************************************
C********     WRITTEN BY: GHASSEM HEIDARINEJAD     **********
C********   (LAST REVISION FEBRUARY 22TH, 1989).   **********
C*************************************************************
C
                        PROGRAM S2VAX
C
C       NUMERICAL SIMULATION OF A TWO-STREAM, SPATIALLY-GROWING,
C       CONSTANT DENSITY, NON-PREMIXED REACTING SHEAR LAYER USING
C       TRANSPORT ELEMENT METHOD WITH:
C
C       1. LOW HEAT RELEASE CHEMICAL REACTION
C       2. ARRHENIUS RATE EXPRESSION FOR THE SOURCE TERM
C       3. REDISTRIBUTING THE VORTICITY AND THE SCALAR GRADIENT
C          FIELDS WITH:
C             3.1) INJECTION OF THE NEW ELEMENTS IF THE MAXIMUM
C                  DISTANCE BETWEEN THE NEIGHBORING ELEMENTS
C                  EXCEEDS A PREDETERMINED VALUE "Rmax";
C             3.2) COMBINATION OF THE OLD ELEMENTS ELEMNTS IF
C                  THE MINIMUM DISTANCE BETWEEN THE TWO NEIGHBORING
C                  ELEMENTS  FALLS BELOW A PREDETERMINED VALUE "Rmin";
C             3.3) SMOOTH CHANGE OF "Rmax" AND "Rmin", WITHIN THE DOMAIN.
C       4. ADJUSTABLE EXIT PLANE.
C       5. FOR TURBULENT AND LAMINAR FLAME.
C       6. MOMENTUM DIFFUSION INCLUDED
C          (SORRY NO BOUNDARY LAYER ON THE TOP AND BOTTOM WALLS!!).
C
C-------------------------------------------------------------
C
C
      DIMENSION FZTS1(101,51),ZUSS1(101,51),FZTS2(101,51),ZUSS2(101,51),
     1          ZS11(101,51), ZS12(101,51), ZS(101,51),R11(101,51),
     2          R21(101,51),R12(101,51),R22(101,51)
C
C
      COMMON /NRNVR/ NR,NVR(9)
      COMMON /RCTN/ ARE,RR,QE,TAE,FRAC
      COMMON /NVN/ NV
      COMMON /NXNY/ NX,NY
      COMMON /ZBZB/ ZB(1200,9)
      COMMON /ZUBZ/ ZUB(1200,9)
      COMMON /ZGZG/ ZG(1200,9)
      COMMON /TIMT/ TIM(1200,9)
      COMMON /CAFB/ TPB  200,9),CAB(1200,9),CFB(1200,9)
      COMMON /DCAFB/ DTB(1200,9),DCA(1200,9),DCF(1200,9)
      COMMON /ZSZU1/ ZS1(101,51),ZUS(101,51)
      COMMON /CAFPS/ TPS(101,51),CAS(101,51),CFS(101,51)
      COMMON /PIH2/ PI,PIH,PI2
      COMMON /SOURCE/ S1ST,S2ST,S1ZT,S2ZT
      COMMON /DELDT/ DEL,DT,UAVG,WL,ALPH
      COMMON /DATA1/ HCOL
      COMMON /GAGA1/ GAMA(9),DELT(9),YVOR(9),ERF(9)
      COMMON /LAMSH/ ETA(9),XT0(9)
      COMMON /DATA2/ ALDX,BETDX,X0,ALPHA,BETA,FACT
      COMMON /DATA3/ YMIN,YMAX,YMAX2,XMAX
      COMMON /DATA4/ IDUM(5)
      COMMON /DATA5/ NQTL,NQKA,NQMD
      COMMON /DATA6/ DUM(10,5)
      COMMON /DATA7/ NRCFT
      COMMON /XBDBD/ XBD
```

```
      COMMON /R1R2R/ R1(101,51),R2(101,51)          176
C
C
      COMPLEX FZTS1,FZTS2,S1ZT,S2ZT,ZB,ZUB,ZS,ZS1,ZS11,ZS12,
     1        ZUS,ZUS1,ZUS2,ZUSS1,ZUSS2,ZZ,ZZ1,ZZ2
C
C
C-------------------------------------------------------------
C       SYMBOLS    |     DEFINITION
C-------------------------------------------------------------
C       NR         |     NUMBER OF LAYERS.
C       NVR(J)     |     NUMBER OF ELEMENTS ON "Jth" LAYER.
C
C
C       ELEMENT LOCATED ON "Jth" LAYER IN THE "Z" PLANE.
C
C       ZB(I,J)    |     COMPLEX COORDINATE OF THE CENTER
C       ZG(I,J)    |     CIRCULATION
C       ZUB(I,J)   |     COMPLEX VELOCITY OF THE CENTER
C       TIM(I,J)   |     RESIDENT TIME ASSOCIATED WITH
C       TPB(I,J)   |     TEMPERATURE OF THE CENTER
C       CAB(I,J)   |     AIR CONCENTRATION OF THE CENTER
C       CFB(I,J)   |     FUEL CONCENTRATION OF THE CENTER
C       DTB(I,J)   |     TEMPERATURE VARIATION ASSOCIATED WITH
C       DCA(I,J)   |     AIR CONCENTRATION VARIATION ASSOCIATED WITH
C       DCF(I,J)   |     FUEL CONCENTRATION VARIATION ASSOCIATED WITH
C
C
C       NX * NY GRID POINTS FOR THE FUTURE USE WITH:
C       NX=NX1, NY=NY1, THE COARSE MESH FOR STATISTICAL PURPOSE;
C       NX=NX2, NY=NY2, THE FINE MESH FOR CONTOUR PLOTTING PURPOSE;
C       "Ith" COLUMN "Jth" ROW.
C
C       ZS(I,J)    |     COMPLEX COORDINATE
C       ZUS(I,J)   |     COMPLEX VELOCITY
C       TPS(I,J)   |     TEMPERATURE
C       CAS(I,J)   |     AIR CONCENTRATION
C       CFS(I,J)   |     FUEL CONCENTRATION
C       FZT(I,J)   |     TRANFORM FUNCTION
C                  |
C                  |
C       CONSTANTS NEEDED DURING THE CALCULATION
C                  |
C       HCOL       |     LENGTH OF THE SIDE OF THE INITIAL SQUARE ELEMENT
C       XMAX       |     LENGTH OF THE COMPUTATIONAL DOMAIN
C       DEL        |     CORE RADIUS
C       DT         |     TIME STEP
C       WL         |     WAVELENGTH OF PERTURBATION
C       ALPH       |     MOMMENTUM, TEMPERATURE AND SPECIES DIFFUSIVITY
C       ARE        |     DAMKOHLER NUMBER FOR TEMP-INDEP REACTION
C                  |     OR FREQUENCY FACTOR, Af, FOR TEMP-DEP REACTION
C       QE         |     ENTHALPY OF REACTION
C       TAE        |     ACTIVATION ENERGY
C       NRCFT      |     # OF THE RATIO OF THE FLOW TO CHEM. TIME STEP
C       XBD        |     X COORDINATE OF THE THIRD POINT IN FIXING
C                  |     CONSTANTS OF THE SCALAR SOURCES
C       ALPHA      |     INITIAL Rmax
C       BETA       |     INITIAL Rmin
C                  |
C-------------------------------------------- --------------------
C
C
C       SOME CONSTANTS.
```

```
C
      PI=4.*ATAN(1.)
      PIH=PI/2.0
      PI2=2.0*PI
      FACT=1.0/3.0
      U1=1.0
      YMIN=0.0
      YMAX=1.0
      YMAX2=2.0*YMAX
      XMIN=0.0
      H=YMAX-YMIN
      HH=0.5*H
C
C
C     WAVE LENGTH OF THE MOST UNSTABLE WAVELENGTH BASED ON THE
C     HALF OF THE THICKNESS OF THE SHEAR LAYER AS THE LENGTH SCALE
C     OF PROBLEM.
C
      WL=13.2
C
C
C     ASK FOR LAMINAR OR TURBULENT SHEAR LAYER.
C
 2    TYPE *,' ENTER: TURBULENT/LAMINAR       T/L'
      READ 1005,QTL
      IF( (QTL.EQ.'L'). OR . (QTL.EQ.'l') )THEN
       TYPE *,' P.S. NO COMBIONATION AND INJECTION IS RECOMMENDED !'
       NQTL=0
       NQMD=1
       GO TO 4
      ELSEIF( (QTL.EQ.'T') .OR. (QTL.EQ.'t') )THEN
        NQTL=1
      ELSE
        TYPE *,' ENTER ONLY T/L'
        GO TO 2
      ENDIF
C
C
C     ASK FOR MOMENTUM DIFFUSION INCLUDED OR NOT.
C
 3    TYPE *,' MOMENTUM DIFFUSION IN THE TURBULENT CASE ONLY !'
      TYPE *,' '
      TYPE *,' ENTER: MOMENTUM DIFFUSION      Y/N'
      READ 1005,QMD
      IF( (QMD.EQ.'Y') .OR. (QMD.EQ.'y') )THEN
        NQMD=1
        TYPE *,' MOM. DIFFUSION IN FORM OF VORTEX CORE EXPANSION'
      ELSEIF( (QMD.EQ.'N') .OR. (QMD.EQ.'n') )THEN
        NQMD=0
      ELSE
        TYPE *,' ENTER ONLY Y/N'
        GO TO 3
      ENDIF
C
C
C     ASK FOR CONSTANT/ARRHENIUS RATE EXPRESSION.
C     (TEMPERATURE-INDEPENDENT/TEMPERATURE-DEPENDENT)
C
 4    TYPE *,' ENTER: CONS. RATE/ARRHENIUS    K/A'
      READ 1005,QKA
      IF( (QKA.EQ.'K') .OR. (QKA.EQ.'k') )THEN
        TYPE *,' NO TEMPRATURE DEPENDENCE ON THE REACTION RATE'
        TYPE *,' ENTER CHEMICAL REACTION PARAMETERS'
```

```
        TYPE *,' 1)ALPHA, 2)ARE, 3)RR, 4)FRAC'
        READ *,ALPH,ARE,RR,FRAC
        NQKA=0
      ELSEIF( (QKA.EQ.'A') .OR. (QKA.EQ.'A') )THEN
        TYPE *,' ENTER CHEMICAL REACTION PARAMETERS'
        TYPE *,' 1)ALPHA, 2)ARE, 3)RR, 4)QE,  5)TAE,  6)FRAC'
        READ *,ALPH,ARE,RR,QE,TAE,FRAC
        NQKA=1
      ELSE
        TYPE *,' ENTER ONLY K/A'
        GO TO 4
      ENDIF
C
C
C     READING SOME NECESSARY PARAMETERS
C
      TYPE *,' WHAT ARE THE:'
      TYPE *,' 1) MAXIMUM STEP ......................'
      TYPE *,' 2) MULTIPLE OF "h" for Rmax ..........'
      TYPE *,' 3) MULTIPLE OF "h" for Rmin ..........'
      TYPE *,' 4) TIME AFTER WHICH RESULTS ARE KEPT .'
      TYPE *,' 5) "X" OF EXIT PLANE .................'
      TYPE *,' 6) U2 OF THE LOW SPEED STREAM ........'
      TYPE *,' 7) FILE#9 "YES/NO"  "1/0" ............'
      TYPE *,' 8) FLOW / CHEMISTRY TIME STEP(MAX 10).'
      READ *,ITMAX,ALPHA,BETA,TIME0,XMAX,U2,NOUT,NRCFT
C
C
C     ENTER THE NUMERICAL VALUES FOR REFINED
C     INJECTION AND COMBINATION PROCESS.
C
      TYPE *,' ENTER: DXMAX,DALPHA,DBETA'
      READ *,DXMAX,DALPHA,DBETA
      X0=XMAX-DXMAX
      ALDX=DALPHA/DXMAX
      BETDX=DBETA/DXMAX
      XBD=XMAX-2.0     !TO BE USED TO FIX B.C IN SCALAR SOURCE.
      UAVG = 0.5*(U1+U2)
      DU = U1-U2
      TYPE *,' ENTER:AMPLITUDES OF FUNDAMENTAL AND SUBHARMONIC'
      READ *,AMPF,AMPS
C
C
C     CONVERSION OF THE CONSTANTS IF USING THE CHANNEL HEIGHT "H"
C     AS THE LENGTH SCALE OF THE PROBLEM INSTEAD THE HALF OF
C     THE SHEAR LAYER THICKNESS "0.5*XLT1".
C
      CONV = 1.0/(2.0*WL)      ! CONV OF TEMPORAL/SPATIAL SHEAR LAYER
      SIGMA=1.0*CONV   ! STANDARD DEV OF THE ERF BASE FLOW
      WL=WL*CONV       ! WAVE LENGTH OF PERTURBATION
      AMPF=AMPF*WL     ! AMPLITUDE OF FUNDAMENTAL
      AMPS=AMPS*WL     ! AMPLITUDE OF FIRST SUB-HARMONICS
C
C
C     READ THE INITIAL GAUSSIAN DISTRIBUTION FOR VORTICITY
C     WITHIN THE SHEAR LAYER AT TIME T=0.
C
      READ(3)NR,ICORE,DEL1,XLT1
      TYPE 1001,NR,DEL1,XLT1
      DEL = DEL1*CONV          ! CORE RADIUS IN "Z" PLANE
      XLT = XLT1*CONV          ! THICKNESS OF SPATIAL SHEAR LAYER
      HCOL=XLT/FLOAT(NR-1)     ! ELEMENT'S SIDE "H" IN "Z" PLANE
      GAMTOT=-DU*HCOL.         ! CIRCULATION/COLUMN
```

```
C
C
C       NORMALIZED HEIGHTS AND STRENGTH OF THE
C       COMPUTATIONAL ELEMENTS USING THE CHANNEL HEIGHT
C       AS THE LENGTH SCALE.
C
        DO I = 1,NR
          READ(3)YVOR(I),GAMA1,ERF1
          ERF(I)=UAVG+0.5*DU*ERF1
          YVOR(I)=HH+YVOR(I)*CONV
          GAMA(I)=0.5*GAMA1*GAMTOT/PI2
          DELT(I)=0.5*GAMA1/PI2
          TYPE *,I,YVOR(I),GAMA(I),DELT(I),ERF(I)
        ENDDO
C
C
C       IN THE CASE OF LAMINAR REACTING SHEAR LAYER,
C       ARRANGE FOR VISCOUS EFFECTS IN THE VELOCITY
C       CALCULATIONS.
C
        IF( NQTL.EQ.0 )THEN
          CALL LAM
        ENDIF
C
C
C       CHECK IF TO START THE REACTION OR IT HAS ALREADY STARTED.
C
 26     TYPE *,' START WITH 0/1/2'
        TYPE *,' 0. THE FROM THE ZERO STEP'
        TYPE *,' 1. CONTINUE FROM THE OTHER STEP BUT WITHOUT COMBUSTION'
        TYPE *,' 2. CONTINUE FROM THE OTHER STEP BUT WITH COMBUSTION'
        READ *,IZOS
C
C
C       START WITH A FLAT AND UNPERTURBED SHEAR LAYER TO SAVE
C       COMPUTATIONAL EFFORT DURING THE TRANSIENT PERIOD(BEFORE THE
C       FIRST GENERATION OF ELEMENTS LEAVE THE DOMAIN).
C
        IF( IZOS.EQ.0 )THEN
          INI=1
          TIME=0.0
          NC=XMAX/HCOL
          CALL UNLAER(NC)
C
C
C       ONLY INJECTION & COMBINATION (GO TO MAIN5).
C
        ELSEIF( IZOS.EQ.1 )THEN
          READ(7)ITIME,TIME,NR,(NVR(J),J=1,NR),
     1    ((ZB(I,J),ZUB(I,J),ZG(I,J),TIM(I,J),
     2    I=1,NVR(J)),J=1,NR)
          NV=0
          DO J=1,NR
            DO I=1,NVR(J)
              DCA(I,J)=+RR*DELT(J)
              DCF(I,J)=-DELT(J)
              DTB(I,J)=0.0
            ENDDO
            NV=NV+NVR(J)
          ENDDO
          INI=ITIME+1    ! STARTING STEP
C
C
```

```
C       INJECTION & COMBINATION AND UPDATING                          180
C       (GO TO MAIN4 AND DO A REGULAR CONTINUATION).
C
        ELSEIF( IZOS.EQ.2 )THEN
          READ(7)ITIME,TIME,NR,(NVR(J),J=1,NR),
     1    ((ZB(I,J),ZUB(I,J),ZG(I,J),TIM(I,J),
     2    TPB(I,J),CAB(I,J),CFB(I,J),DTB(I,J),DCA(I,J),DCF(I,J),
     3    I=1,NVR(J)),J=1,NR)
          INI=ITIME+1    ! STARTING STEP
          NV=0
          DO J=1,NR
            NV=NV+NVR(J)
          ENDDO
        ELSE
          TYPE *,' TRY ONLY      0/1/2'
          GO TO 26
        ENDIF
C
C
C       STRENGTH OF FLOW SOURCES AND THEIR LOCATION
C       IN COMPUTATIONAL "ZETA" PLANE.
C
        S1ZT = CMPLX(-1.,0.)
        S2ZT = CMPLX(+1.,0.)
        S1ST = U1/PI2
        S2ST = U2/PI2
C
C
        TYPE *,' ENTER: DT'
        READ *,DT
C
C       DEFINE TWO SET OF FIXED MESH FOR STATISTICAL AND
C       COLOR PLOTTING PURPOSE IN THE FUTURE.
C       FIRTS THE COARSE MESH (USUALLY 11*51) EACH ONE(1) STEP
C       FOR STATISTICAL PURPOSE
C
        TYPE *,' ENTER: COARSE MESH (USUALLY 11*51 AND EACH STEP)    Y/N'
        READ 1005,QN1
        IF( (QN1.EQ.'Y') .OR. (QN1.EQ.'y') )THEN
          NQN1=1
          TYPE *,' ENTER: NX1,NY1'
          READ *,NX1,NY1
          DX1=(XMAX-XMIN)/FLOAT(NX1-1)
          DY1=(YMAX-YMIN)/FLOAT(NY1-1)
          DO J=1,NY1
            YY=DY1*FLOAT(J-1)
            DO I=1,NX1
              IF(I.EQ.1)THEN
                XX=0.025
              ELSE
                XX=DX1*FLOAT(I-1)
              ENDIF
              ZS(I,J)=CMPLX(XX,YY)
              ZZ=CSQRT(CEXP(PI2*ZS(I,J))+1.0)
              IF(YY.GE.0.5) ZZ=-ZZ
              ZS11(I,J)=ZZ
              ZZ1=ZZ-S1ZT
              ZZ2=ZZ-S2ZT
              ZUSS1(I,J)=S1ST/ZZ1+S2ST/ZZ2
              FZTS1(I,J)=PI*(ZZ-1.0/ZZ)
              R11(I,J)=LOG(CABS(ZZ1))
              R21(I,J)=LOG(CABS(ZZ2))
            ENDDO
```

```
          ENDDO
          WRITE(8)NQTL,NQKA,ALPH,ARE,RR,QE,TAE,FRAC,NX1,NY1,
     1    ((ZS(I,J),I=1,NX1),J=1,NY1)
        ENDIF
C
C
C       SECOND THE FINER MESH (USUALLY 101*51) EACH TEN(10) STEP
C       FOR COLOR (AND CONTOURS) PLOTTING PURPOSE.
C
        TYPE *,' ENTER: FINE MESH (USUALLY 101*51 AND TEN STEP)   Y/N'
        READ 1005,QN2
        IF( (QN2.EQ.'Y') .OR. (QN2.EQ.'y') )THEN
          NQN2=1
          TYPE *,' ENTER: NX2,NY2'
          READ *,NX2,NY2
          DX2=(XMAX-XMIN)/FLOAT(NX2-1)
          DY2=(YMAX-YMIN)/FLOAT(NY2-1)
          DO J=1,NY2
            YY=DY2*FLOAT(J-1)
            DO I=1,NX2
              IF(I.EQ.1)THEN
                XX=0.025
              ELSE
                XX=DX2*FLOAT(I-1)
              ENDIF
              ZS(I,J)=CMPLX(XX,YY)
              ZZ=CSQRT(CEXP(PI2*ZS(I,J))+1.0)
              IF(YY.GE.0.5) ZZ=-ZZ
              ZS12(I,J)=ZZ
              ZZ1=ZZ-S1ZT
              ZZ2=ZZ-S2ZT
              ZUSS2(I,J)=S1ST/ZZ1+S2ST/ZZ2
              FZTS2(I,J)=PI*(ZZ-1.0/ZZ)
              R12(I,J)=LOG(CABS(ZZ1))
              R22(I,J)=LOG(CABS(ZZ2))
            ENDDO
          ENDDO
          WRITE(81)NQTL,NQKA,ALPH,ARE,RR,QE,TAE,FRAC,NX2,NY2,
     1    ((ZS(I,J),I=1,NX2),J=1,NY2)
        ENDIF
C
C
        IWRIT=0
        I17=0
C
C------------  THE MAIN DO LOOP OVER THE TIME STEPS -------------
C
        DO 300 ITIMME=INI,ITMAX+1
          ITIME=ITIMME-1
C
C
C       CHECK AT WHAT TIME SHOULD CONTINUE THE CALCULATIONS.
C
          IF(IZOS.EQ.0)GO TO 53
          IF(IZOS.EQ.1)GO TO 59
          IF(IZOS.EQ.2)GO TO 58
C
C
          CALL MAIN1(TIME,AMPF,AMPS)
 53       CONTINUE
          TYPE 1002,ITIME,TIME,NV,(NVR(J),J=1,NR)
C
C
```

```
C       CALCULATE THE VELOCITIES AT THE CENTER OF THE
C       COMPUTATIONAL ELEMENTS IN ORDER TO MOVE THEM TO THE          182
C       NEW LOCATION.
C
          CALL MAIN2
          IF( TIME.LT.TIME0 )GO TO 55
          IF( NOUT.EQ.0 )GO TO 55
          WRITE(9)ITIME,TIME,NR,(NVR(J),J=1,NR),
     1    ((ZB(I,J),ZUB(I,J),ZG(I,J),TIM(I,J),
     2    DCA(I,J),DCF(I,J),CAB(I,J),CFB(I,J),
     3    I=1,NVR(J)),J=1,NR)
          TYPE 1003,ITIME
 55       CONTINUE
C
C
C       CALL FOR THE COARSE MESH CALCULATIONS
C
          IF( NQN1.EQ.1 )THEN
            NX=NX1
            NY=NY1
            DO I=1,NX
              DO J=1,NY
                R1(I,J)=R11(I,J)
                R2(I,J)=R21(I,J)
                ZS1(I,J)=ZS11(I,J)
              ENDDO
            ENDDO
            CALL MAIN3
C
            DO J=1,NY
              DO I=1,NX
                ZUS(I,J)=ZUS(I,J)+ZUSS1(I,J)
                ZUS(I,J)=FZTS1(I,J)*ZUS(I,J)
                ZUS(I,J)=CONJG(ZUS(I,J))
                TPS(I,J)=TPS(I,J)+1.0
                CAS(I,J)=CAS(I,J)+0.5*RR
                CFS(I,J)=CFS(I,J)+0.5
              ENDDO
            ENDDO
            IF( TIME.LT.TIME0 )GO TO 56
            WRITE(8)ITIME,TIME,NR,(NVR(J),J=1,NR),
     1      ((ZUS(I,J),TPS(I,J),CAS(I,J),CFS(I,J),I=1,NX),J=1,NY)
            TYPE 1007,ITIME
C
C
C       PRINT THE RESULTS ON SELECTED POINT OF THE MESH TO MAKE SURE
C       THAT CALCULATIONS ARE CORRECTLY PROCEEDING.
C
 56         CONTINUE
            I1=1
            I2=5
            I3=9
            IF( NQKA.EQ.0 )THEN
              TYPE 1008
            ELSE
              TYPE 1009
            ENDIF
            DO J=1,NY,25
              IF( NQKA.EQ.0 )THEN
                TP1=REAL(ZUS(I1,J))
                TP2=REAL(ZUS(I2,J))
                TP3=REAL(ZUS(I3,J))
              ELSE
```

```
                TP1=TPS(I1,J)
                TP2=TPS(I2,J)
                TP3=TPS(I3,J)
              ENDIF
              CA1=CAS(I1,J)
              CA2=CAS(I2,J)
              CA3=CAS(I3,J)
              CF1=CFS(I1,J)
              CF2=CFS(I2,J)
              CF3=CFS(I3,J)
              TYPE 1010,J,TP1,CA1,CF1,TP2,CA2,CF2,TP3,CA3,CF3
            ENDDO
          ENDIF
C
C
C       CALL FOR THE FINE MSEH CALCULATIONS
C
          IF( NQN2.EQ.1 )THEN
            IF( ITIME/10*10.EQ.ITIME )THEN
              IF( TIME.LT.TIME0 )GO TO 57
              NX=NX2
              NY=NY2
              DO I=1,NX
                DO J=1,NY
                  R1(I,J)=R12(I,J)
                  R2(I,J)=R22(I,J)
                  ZS1(I,J)=ZS12(I,J)
                ENDDO
              ENDDO
              CALL MAIN3
C
              DO J=1,NY
                DO I=1,NX
                  ZUS(I,J)=ZUS(I,J)+ZUSS2(I,J)
                  ZUS(I,J)=FZTS2(I,J)*ZUS(I,J)
                  ZUS(I,J)=CONJG(ZUS(I,J))
                  TPS(I,J)=TPS(I,J)+1.0
                  CAS(I,J)=CAS(I,J)+0.5*RR
                  CFS(I,J)=CFS(I,J)+0.5
                ENDDO
              ENDDO
              WRITE(81)ITIME,TIME,NR,(NVR(J),J=1,NR),
     1        ((ZUS(I,J),TPS(I,J),CAS(I,J),CFS(I,J),I=1,NX),J=1,NY)
              TYPE *,' RESULTS FOR THE FINE MSEH WRITTEN ON FILE #81'
            ELSE
              GO TO 57
            ENDIF
          ENDIF
C
C
 57       CONTINUE
C
C
C       WRITE THE LAST STEP EACH FIVE STEP ON FILE #17
C       FOR THE FUTURE USE.
C
          IF( IWRIT/5*5.EQ.IWRIT )THEN
            IF( I17.EQ.0 )GO TO 61
            READ(17)ID
            REWIND(17)
 61         WRITE(17)ITIME,TIME,NR,(NVR(J),J=1,NR),
     1      ((ZB(I,J),ZUB(I,J),ZG(I,J),TIM(I,J),
     2      TPB(I,J),CAB(I,J),CFB(I,J),DTB(I,J),DCA(I,J),DCF(I,J),
```

```
     3       I=1,NVR(J)),J=1,NR)
             CLOSE(17)
             I17=1
             TYPE 1013,ITIME
           ENDIF
C
C
C       WRITE THE LAST STEP ON FILE #7 FOR THE FUTURE USE.
C
           IWRIT=IWRIT+1
           REWIND(7)
           WRITE(7)ITIME,TIME,NR,(NVR(J),J=1,NR),
     1     ((ZB(I,J),ZUB(I,J),ZG(I,J),TIM(I,J),
     2     TPB(I,J),CAB(I,J),CFB(I,J),DTB(I,J),DCA(I,J),DCF(I,J),
     3     I=1,NVR(J)),J=1,NR)
           TYPE 1004
C
C
C       CHECK FOR THE FINAL STEP, OTHERWISE?
C
           IF(ITIME.GE.ITMAX)GO TO 999
C
C
C       UPDATE THE VALUES OF SCALAR VARIATIONS IN ORDER
C       TO INCLUDE THE EFFECTS OF THE SOURCE TERMS IN THE
C       REACTION PART.
C
 58        CALL MAIN4
           ERTMX=0.0
           ERCAMX=0.0
           ERCFMX=0.0
           DO II=1,NRCFT
             IF(DUM(II,1).GT. ERTMX) ERTMX=DUM(II,1)
             IF(DUM(II,2).GT.ERCAMX)ERCAMX=DUM(II,2)
             IF(DUM(II,3).GT.ERCFMX)ERCFMX=DUM(II,3)
           ENDDO
           TYPE 1011,ERTMX,ERCAMX,ERCFMX
C
C
C       MOVE THE COMPUTATIONAL ELEMENTS TO THE NEW LOCATION,
C       THEN DO THE NECESSARY INJECTION OR COMBINATION.
C
 59        IZOS=3
           CALL MAIN5
C
C
           IF( IDUM(1).EQ.1 )THEN
             TYPE *,' NUMBER OF ELEMENTS EXCEEDED 1200, LET'S STOP ?!!'
             GO TO 999
           ELSE
             IDIF=IDUM(2)-IDUM(3)
             TYPE 1012,IDUM(2),IDUM(3),IDIF
           ENDIF
C
C
 63        CONTINUE
           TIME = TIME + DT
C
 300     CONTINUE
C
C
 1001    FORMAT(/,' NR=',I2,5X,'SIGMA=',F4.2,5X,'THICKNESS=',F4.2)
 1002    FORMAT(//,' STEP=',I3,2X,'TIME=',F5.2,2X,'ELEMENTS=',I5,
```

```
     1          3X,9(1X,I4))
 1003   FORMAT(' WRITING RESULTS OF STEP=',I3,
     1          ' ON FILE #9 FINISHED')
 1004   FORMAT(' WRITING RESULTS OF THE LAST STEP ON FILE #7 FINISHED')
 1005   FORMAT(A1)
 1007   FORMAT(' WRITING RESULTS OF STEP=',I3,
     1          ' ON FILE #8 FINISHED')
 1008   FORMAT(18X,'X=0.1',20X,'X=2.0',20X,'X=4.0',/,
     1         2X,'NODE',6X,'VEL',4X,'C-A',4X,'C-F',
     2                  6X,'VEL',4X,'C-A',4X,'C-F',
     3                  6X,'VEL',4X,'C-A',4X,'C-F')
 1009   FORMAT(18X,'X=0.1',20X,'X=2.0',20X,'X=4.0',/,
     1         2X,'NODE',5X,'TEMP',4X,'C-A',4X,'C-F',
     2                  5X,'TEMP',4X,'C-A',4X,'C-F',
     3                  5X,'TEMP',4X,'C-A',4X,'C-F')
 1010   FORMAT(3X,I2,3(4X,3F7.3))
 1011   FORMAT(' MAX. ERROR IN FRACTIONAL STEP',3X,3E13.4)
 1012   FORMAT(' No.OF INJECTION=',I3,3X,
     1          ' No.OF COMBINATION=',I3,3X,
     2          ' NET No.OF INJECTION=',I4)
 1013   FORMAT(' WRITING RESULTS OF STEP',I3,'   ON FILE #17')
C
C
 999    STOP
        END
C
C*************************************************************
C
C       SUBROUTINE UNLAER(NC)
C
C       FILL IN THE COMPUTATIONAL DOMAIN WITH INITIALLY
C       UNPERTURBED LAYERS, EACH LAYER CONTAIN "NC" ELEMENTS.
C
C-------------------------------------------------------
C
        SUBROUTINE UNLAER(NC)
C
        COMMON /NRNVR/ NR,NVR(9)
        COMMON /RCTN/ ARE,RR,QE,TAE,FRAC
        COMMON /NVN/ NV
        COMMON /ZBZB/ ZB(1200,9)
        COMMON /ZGZG/ ZG(1200,9)
        COMMON /TIMT/ TIM(1200,9)
        COMMON /DCAFB/ DTB(1200,9),DCA(1200,9),DCF(1200,9)
        COMMON /PIH2/ PI,PIH,PI2
        COMMON /DELDT/ DEL,DT,UAVG,WL,ALPH
        COMMON /DATA1/ HCOL
        COMMON /GAGA1/ GAMA(9),DELT(9),YVOR(9),ERF(9)
        COMPLEX ZB
C
C-------------------------------------------------------
C
        NV=0
        XMIN=HCOL*(0.5+FLOAT(NC-1))
        DO J=1,NR
          NVR(J)=0
          DO ICOL=1,NC
            NVR(J)=NVR(J)+1
            XX=XMIN-FLOAT(ICOL-1)*HCOL
            YY=YVOR(J)
             ZB(NVR(J),J)=CMPLX(XX,YY)
             ZG(NVR(J),J)=GAMA(J)
            TIM(NVR(J),J)=0.0
```

```
            DTB(NVR(J),J)=0.0
            DCA(NVR(J),J)=+RR*DELT(J)
            DCF(NVR(J),J)=-DELT(J)
          ENDDO
          NV=NV+NVR(J)
        ENDDO
C
        RETURN
        END
C
C*************************************************************
C
C       SUBROUTINE LAM
C
C       PREPARE THE DATA FOR THE VELOCITY DISTRIBUTION IN TERMS OF
C       THE DIMENSIONLESS PARAMETER AT THE LAYER'S LOCATION
C       USING FIGURE 9.14 FROM BOUNDARY LAYER BY " SCHLICHTING ".
C
C-------------------------------------------------------------
C
        SUBROUTINE LAM
C
        DIMENSION U(100),ET(100)
        COMMON /NRNVR/ NR,NVR(9)
        COMMON /GAGA1/ GAMA(9),DELT(9),YVOR(9),ERF(9)
        COMMON /DELDT/ DEL,DT,UAVG,WL,ALPH
        COMMON /LAMSH/ ETA(9),XT0(9)
C
C-------------------------------------------------------------
C
        READ(2)N,(U(I),ET(I),I=1,N)
        DO J=1,NR
          DO I=1,N
            IF( ERF(J).GT.U(I) ) THEN
              IF(I .EQ. (N-1))THEN
                ETA(J)=0.5*(ET(I)+ET(I+1))
              ELSEIF(I .EQ. N)THEN
                ETA(J)=ET(N)
              ELSE
C       FIRST FIT A QUARATURE(2ND ORDER POLYNOMIAL)
C       TO (u/U1)-(Eta), TO HAVE A MORE ACCURATE READING
C       FOR ETA IF KNOWING u OF LAYER.
C
                U1= U(I)
                ET1=ET(I)
                U2= U(I+1)
                ET2=ET(I+1)
                U3= U(I+2)
                ET3=ET(I+2)
                A11=(ET1-ET2)*(U1-U3)-(ET1-ET3)*(U1-U2)
                A12=(U1-U2)*(U1-U3)*(U3-U2)
                A=A11/A12
                B=(ET1-ET3-A*(U1*U1-U3*U3))/(U1-U3)
                C=ET1-A*U1*U1-B*U1
                ETA(J)=A*ERF(J)*ERF(J)+B*ERF(J)+C
C
C
C       CALCULATE THE ORIGIN OF SHEAR LAYER UPSTREAM
C       OF THE SPLITTER PLATE
C
                IF(ETA(J).EQ.0.0)THEN
                  XT0(J)=0.0
                ELSE
```

```
                XT0(J)=(2.0/(ALPH))*(((YVOR(J)-0.5)/ETA(J))**2)
              ENDIF
            ENDIF
C
              GO TO 18
            ENDIF
 18         CONTINUE
          ENDDO
        ENDDO
C
C
          TYPE 1001
          XT0M=0.0
          TYPE *,'    LAYER'S#    ETA              X0'
          DO J=1,NR
            TYPE *,J,ETA(J),XT0(J)
            XT0M=XT0M+XT0(J)
          ENDDO
          XT0M=XT0M/FLOAT(NR-1)
          TYPE *,' (X0)av',XT0M
          DO J=1,NR
            XT0(J)=XT0M
          ENDDO
C
C
 1001   FORMAT(2X,'VISCOUS EFFECTS ARE AUTOMATICALLY INCLUDED',/,
     1          2X,'IN LAMINAR DIFFUSION REACTING LAYER !!!???')
C
C
        RETURN
        END
C
C*****************************************************************
C
C       SUBROUTINE BOUND(P,Q,ZTS,T)
C
C       CALCULATE THE SCALAR VALUES ON THE THREE POINT
C       ON THE BOUNDARY.  THESE VALUES ARE USED TO FIX
C       THE CONSTATNS OF THE SCALAR SOURCES (T0, C1 AND C2)
C       UPSTREAM OF THE COMPUTATIONAL DOMAIN.
C
C       "P" AND "Q" ARE STRENGTH OF TRANSPORT ELEMENTS BASED
C       ON SCALAR GRADIENTS.
C       "ZTS" ARE COORDINATE IN "ZETA" PLANE
C       "T" IS SCALAR VALUE IN GENERAL
C
C---------------------------------------------------------------
C
        SUBROUTINE BOUND(P,Q,ZTS,T)
C
        DIMENSION P(9500),Q(9500),T(3)
        COMMON /NVN/ NV
        COMMON /PIH2/ PI,PIH,PI2
        COMMON /ZBZB1/ ZB(9500)
        COMMON /BLK24/ DEL2S(9500)
        COMPLEX ZTS(3)
        COMPLEX ZB
C
C---------------------------------------------------------------
C
C       BIOT-SAVART LAW FOR THE THREE POINTS.
C
        DO 40 I=1,3
```

```
            T(I)=0.0
            DO 20 J=1,NV
              DX=REAL(ZTS(I))-REAL(ZB(J))
              DX2=DX*DX
              DY=AIMAG(ZTS(I))-AIMAG(ZB(J))
              DY2=DY*DY
              R2=DX2+DY2
              IF(R2.LT.1.0E-10)THEN
                R2I=0.0
              ELSE
                R2I=1.0/R2
              ENDIF
              COEFJ=1.0-EXP(-R2*DEL2S(J))
              DYM=AIMAG(ZTS(I))+AIMAG(ZB(J))
              DYM2=DYM*DYM
              R2M=DX2+DYM2
              R2MI=1.0/R2M
              COEFJI=1.0-EXP(-R2M*DEL2S(J))
              DXR=DX*R2I
              DYR=DY*R2I
              DXRM=DX*R2MI
              DYRM=DYM*R2MI
              T1=P(J)*(DXR*COEFJ+DXRM*COEFJI)
              T2=Q(J)*(DYR*COEFJ-DYRM*COEFJI)
              T(I)=T(I)+T1+T2
 20         CONTINUE
 40       CONTINUE
C
C
          RETURN
          END
C
C*****************************************************************
C
C         SUBROUTINE DSVARA(DTB0,DCA0,DCF0,DDTB,DDCA,DDCF)
C
C         CALCULATE THE RIGHT HAND SIDE OF THE SCALAR VARIATION
C         EQUATIONS USING ARRHENIUS RATE EXPRESSION.
C         d( Cp )/dt = Da Ca*Cf*Exp(-Ta/T)
C
C         "DTB0", "DCA0" AND "DCF0" ARE THE VARIATIONS OF TEMPERATURE,
C         AIR AND FUEL CONCENTRATION.
C         "DDTB0", "DDCA0" AND "DDCF0" ARE THE RIGHT HAND SIDE OF THE
C         UPDATING EQUATIONS
C
C---------------------------------------------------------------
C
          SUBROUTINE DSVARA(DTB0,DCA0,DCF0,DDTB,DDCA,DDCF)
C
          DIMENSION DTB0(1200,9),DCA0(1200,9),DCF0(1200,9),
     +              DDTB(1200,9),DDCA(1200,9),DDCF(1200,9)
          COMMON /NRNVR/ NR,NVR(9)
          COMMON /RCTN/ DA,RR,QE,TAE,FRAC
          COMMON /CAFB/ TPB0(1200,9),CAB0(1200,9),CFB0(1200,9)
C
C---------------------------------------------------------------
C
          DO 40 J=1,NR
            DO 20 I=1,NVR(J)
              DUM1=EXP(-TAE/TPB0(I,J))
              TP2=TPB0(I,J)*TPB0(I,J)
              TERM1=TAE*DTB0(I,J)/TP2
              TERM2=DCF0(I,J)/CFB0(I,J)
```

```
            TERM3=DCA0(I,J)/CAB0(I,J)
            DUM2=TERM1+TERM2+TERM3
            DUM3=DA*CAB0(I,J)*CFB0(I,J)*DUM1*DUM2
            DDTB(I,J)=FRAC*QE*DUM3
            DDCA(I,J)=-RR*DUM3
            DDCF(I,J)=-DUM3
 20       CONTINUE
 40     CONTINUE
C
C
        RETURN
        END
C
C*****************************************************************
C
C       SUBROUTINE DSVARK(DTB0,DCA0,DCF0,DDTB,DDCA,DDCF)
C
C       CALCULATE THE RIGHT HAND SIDE OF THE SCALAR VARIATION
C       EQUATIONS USING ARRHENIUS RATE EXPRESSION.
C       d( Cp )/dt = Da*Ca*Cf
C
C       "DCA0" AND "DCF0" ARE THE VARIATIONS OF AIR AND FUEL
C       CONCENTRATION.
C       "DDCA0" AND "DDCF0" ARE THE RIGHT HAND SIDE OF THE
C       UPDATING EQUATIONS
C
C---------------------------------------------------------------
C
        SUBROUTINE DSVARK(DTB0,DCA0,DCF0,DDTB,DDCA,DDCF)
C
        DIMENSION DTB0(1200,9),DCA0(1200,9),DCF0(1200,9),
     +            DDTB(1200,9),DDCA(1200,9),DDCF(1200,9)
        COMMON /NRNVR/ NR,NVR(9)
        COMMON /RCTN/ ARE,RR,QE,TAE,FRAC
        COMMON /CAFB/ TPB0(1200,9),CAB0(1200,9),CFB0(1200,9)
C
C---------------------------------------------------------------
C
        DO 40 J=1,NR
          DO 20 I=1,NVR(J)
            TERM=ARE*(DCA0(I,J)*CFB0(I,J)+DCF0(I,J)*CAB0(I,J))
            DDCA(I,J)=-RR*TERM
            DDCF(I,J)=-TERM
 20       CONTINUE
 40     CONTINUE
C
C
        RETURN
        END
C
C*****************************************************************
C
C       SUBROUTINE MAIN1(TIME,AMPF,AMPS)
C
C       INTRODUCE THE NEW ELEMENTS AT THE TIP OF THE
C       SPLITTER PLATE, TO SATISFY THE KUTTA CONDITION.
C       (TO FILL THE GAP GENERATED DURING TIME STEP DT BETWEEN
C        THE INLET SECTION AND THE LEFT END OF EACH LAYER)
C
C---------------------------------------------------------------
C
        SUBROUTINE MAIN1(TIME,AMPF,AMPS)
C
```

```
      COMMON /NRNVR/ NR,NVR(9)
      COMMON /NVN/ NV
      COMMON /RCTN/ ARE,RR,QE,TAE,FRAC
      COMMON /ZBZB/ ZB(1200,9)
      COMMON /ZGZG/ ZG(1200,9)
      COMMON /TIMT/ TIM(1200,9)
      COMMON /DCAFB/ DTB(1200,9),DCA(1200,9),DCF(1200,9)
      COMMON /PIH2/ PI,PIH,PI2
      COMMON /GAGA1/ GAMA(9),DELT(9),YVOR(9),ERF(9)
      COMMON /DELDT/ DEL,DT,UAVG,WL,ALPH
      COMMON /DATA1/ HCOL
      COMPLEX ZB
C
C-----------------------------------------------------------------
C
      WL2=2.0*WL       !WAVELENGTH OF SUB-HARMONIC
      TT=TIME*UAVG
      NCO=TT/WL
      TTF=TT-FLOAT(NCO)*WL
      NCO=TT/WL2
      TTS=TT-FLOAT(NCO)*WL2
      NV=0
      DO 40 J=1,NR
        XMAX=REAL(ZB(NVR(J),J))     ! X OF THE LAST ELEMENT ON LAYER
        NCOL=(XMAX-0.5*HCOL)/HCOL   ! NUMBER OF NEEDED ELEMENT ON LAYER
        DO 20 ICOL=1,NCOL
          NVR(J)=NVR(J)+1
          I=NVR(J)
          XX=XMAX-HCOL*FLOAT(ICOL)
          XXF=XX-TTF
          XXS=XX-TTS
          IF(XXF.LT.0.0)XXF=WL-XXF
          IF(XXS.LT.0.0)XXS=WL2-XXS
C
C       PURTURB THE ELEMNTS BASED ON FUNDAMENTAL AND
C       SUB-HARMONIC WAVES
C
          YY=YVOR(J)+AMPF*SIN(PI2*XXF/WL)+AMPS*SIN(PI2*XXS/WL2)
          ZB(I,J)=CMPLX(XX,YY)
          ZG(I,J)=+GAMA(J)
C
C       ASSIGN TIME AND SCALAR VARIATION TO THE NEWLY GENERATED ELEMENTS
C
          TIM(I,J)=0.0
          DTB(I,J)=0.0
          DCA(I,J)=+RR*DELT(J)
          DCF(I,J)=-DELT(J)
 20     CONTINUE
        NV=NV+NVR(J)
 40   CONTINUE
C
C
      RETURN
      END
C
C*****************************************************************
C
C       SUBROUTINE MAIN2
C
C       PREPROCESSING AND PREPARING THE NECESSARY INFORMATION
C       TO BE USED IN THE VORTEX AND THE SCALAR INTERACRTION
C       CALCULATION ON THE COMPUTATIONAL ELEMENTS NAMELY
C       SUBROUTINES --- "VBSL" AND "VSBSL".
```

```
C
C-----------------------------------------------------------------
C
      SUBROUTINE MAIN2
C
      DIMENSION Z(9500),ZU1(9500),FZT(9500)
      COMMON /NRNVR/ NR,NVR(9)
      COMMON /NVN/ NV
      COMMON /RCTN/ ARE,RR,QE,TAE,FRAC
      COMMON /ZBZB/ ZB(1200,9)
      COMMON /ZBZB1/ ZB1(9500)
      COMMON /ZUBZ/ ZUB(1200,9)
      COMMON /ZGZG/ ZG(1200,9)
      COMMON /ZGZG1/ ZG1(9500)
      COMMON /TIMT/ TIM(1200,9)
      COMMON /TIMT1/ TIM1(9500)
      COMMON /DCAFB/ DTB(1200,9),DCA(1200,9),DCF(1200,9)
      COMMON /CAFB/ TPB(1200,9),CAB(1200,9),CFB(1200,9)
      COMMON /CAFB1/ TPB1(9500),CAB1(9500),CFB1(9500)
      COMMON /PQAF/ PT(1200,9),QT(1200,9),PA(1200,9),QA(1200,9),
     +              PF(1200,9),QF(1200,9)
      COMMON /PQAF1/ PT1(9500),QT1(9500),PA1(9500),QA1(9500),
     +               PF1(9500),QF1(9500)
      COMMON /PIH2/ PI,PIH,PI2
      COMMON /DELDT/ DEL,DT,UAVG,WL,ALPH
      COMMON /GAGA1/ GAMA(9),DELT(9),YVOR(9),ERF(9)
      COMMON /DATA5/ NQTL,NQKA,NQMD
      COMMON /TC1C2/ T0T,C1T,C2T,T0A,C1A,C2A,T0F,C1F,C2F
      COMMON /BLK20/ DEL2(9500)
      COMMON /BLK21/ ZT(9500)
      COMMON /BLK22/ ZU(9500)
      COMMON /BLK24/ DEL2S(9500)
      COMMON /BLK25/ DEL2B(9500)
      COMPLEX CIRC,FZT,Z,ZB,ZB1,ZU,ZU1,ZUB,ZT,ZZ,ZZ1
C
C-----------------------------------------------------------------
C
C       FIRST LET'S FIX THE CONSTANTS OF THE SOURCE TERMS
C       IN THE SCALAR CALCULATIONS.
C
C       --- INITIALLY LET'S CALCULATE :
C
C
C       a) THE STRENGTH IN "Z" PLANE OF AIR CONCENRATION.
C
        CALL PQ(DCA,PA,QA)
C
C
C       b) THE STRENGTH IN "Z" PLANE OF FUEL CONCENTRATION.
C
         CALL PQ(DCF,PF,QF)
C
C
C       c) THE STRENGTH IN "Z" PLANE OF PRODUCT TEMPERATURE.
C
        IF(NQKA.EQ.0)GO TO 15
        CALL PQ(DTB,PT,QT)
 15     CONTINUE
C
C
C       d) TRANSFORM THE COORDINATES AND THE
C          TEMPRATURE GRADIENTS OF THE COMPUTATIONAL
C          ELEMENTS FROM "Z" TO "ZETA" PLANE.
```

```
C          ALSO LET'S PUT THE TWO-DIMENSIONAL ARRAIES
C          INTO THE A ONE DIMENSIONAL FORM
C          (MOSTLY BECAUSE OF THE INTERACTION IN BIOT-SAVART LAW).
C
        IJ=0
        DO 40 J=1,NR
          DO 20 I=1,NVR(J)
            IJ=IJ+1
            ZZ=CSQRT(CEXP(PI2*ZB(I,J))+1.0)
            Y=AIMAG(ZB(I,J))
            IF(Y.GE.0.5) ZZ=-ZZ
            ZB1(IJ)=ZZ
            ZZ=PI*(ZZ-1.0/ZZ)
            AA=CABS(ZZ)
C
C
C       d.1) CORE RADIUS OF VORTEX ELEMENTS IN "ZETA" PLANE
C            (TO BE USED IN MAIN3 IN VELOCITY CALCULATIONS)
C            CHECK FOR MOMENTUM DIFFUSION
C
            IF(NQMD.EQ.1)THEN
              DEL0=ABS(SQRT(DEL*DEL+4.0*ALPH*TIM(I,J)))
            ELSE
              DEL0=DEL
            ENDIF
            DEL1=1.0/(DEL0*AA)
            DEL2B(IJ)=DEL1*DEL1
C
C       d.2) SCALAR GRADIENT CORE RADIUS EXPANDING WITH TIME.
C
            DEL0=ABS(SQRT(DEL*DEL+4.0*ALPH*TIM(I,J)))
            DEL1=1.0/(DEL0*AA)
            DEL2S(IJ)=DEL1*DEL1
C
C
C       d.3) STRENGTH OF SCALAR GRADIENT IN "ZETA" PLANE.
C
            AA2=AA*AA
            ZZ1=CMPLX(PA(I,J),-QA(I,J))
            ZZ1=AA2*ZZ1/ZZ
            PA1(IJ)=REAL(ZZ1)
            QA1(IJ)=-AIMAG(ZZ1)
            ZZ1=CMPLX(PF(I,J),-QF(I,J))
            ZZ1=AA2*ZZ1/ZZ
            PF1(IJ)=REAL(ZZ1)
            QF1(IJ)=-AIMAG(ZZ1)
            ZZ1=CMPLX(PT(I,J),-QT(I,J))
            ZZ1=AA2*ZZ1/ZZ
            PT1(IJ)=REAL(ZZ1)
            QT1(IJ)=-AIMAG(ZZ1)
            Z(IJ)=ZB(I,J)
            ZG1(IJ)=ZG(I,J)
            TIM1(IJ)=TIM(I,J)
 20       CONTINUE
 40     CONTINUE
C
C
C       e) USING THE ABOVE STRENGTH LET'S CALCULATE THE CONSTANTS
C          OF THE TWO SOURCES LOCATED AT THE UPPER-STREAM AND THE
C          LOWER STREAM OF THE IN-COMMING FLOW (i.e. T0, C1, C2 ) IN
C          T = T0 + C1*LOG |ZETA-ZETAsource1| + C2*LOG |ZETA-ZETAsource2|.
C
C
```

```
C       e.1) PRODUCT AS THE FIRST SCALAR.
C
        IF(NQKA.EQ.0)GO TO 25
        RRT=0.0
        CALL SRCS(RRT,PT1,QT1,T0T,C1T,C2T)
 25     CONTINUE
C
C
C       e.2) AIR AS THE FIRST REACTANT.
C
        RRA=0.5*RR
        CALL SRCS(RRA,PA1,QA1,T0A,C1A,C2A)
C
C
C       e.3) FUEL AS THE SECOND REACTANT.
C
        RRF=-0.5
        CALL SRCS(RRF,PF1,QF1,T0F,C1F,C2F)
C
C
C       NOW LET'S DO A SECOND ORDER TIME INTEGRATION.
C
        IORDER=0
 47     IORDER=IORDER+1
        DO 60 IJ=1,NV
          ZZ=CSQRT(CEXP(PI2*Z(IJ))+1.0)
          Y=AIMAG(Z(IJ))
          IF(Y.GE.0.5) ZZ=-ZZ
          ZT(IJ)=ZZ
          FZT(IJ)=PI*(ZZ-1.0/ZZ)
C
C
C       CHECK FOR MOMENTUM DIFFUSION.
C
          IF(NQMD.EQ.1)THEN
            DEL0=ABS(SQRT(DEL*DEL+4.0*ALPH*TIM(I,J)))
          ELSE
            DEL0=DEL
          ENDIF
          DEL1=1.0/(DEL0*CABS(FZT(IJ)))
          DEL2(IJ)=DEL1*DEL1
 60     CONTINUE
C
C
C       FOR THE FIRST ITERATION USE THE ADVANTAGES OF
C       THE SAME GEOMETRY TO CALCULATE THE SCALARS VALUES
C       AT THE CENTER OF ELEMENTS IN THE BIOT-SAVART LAW.
C
        IF( IORDER.EQ.1 )THEN
          CALL VSBSL
          IF(NQTL.EQ.0)THEN
            DO 65 J=1,NR
            DO 65 I=1,NVR(J)
              ZUB(I,J)=CMPLX(ERF(J),0.0)
 65         CONTINUE
            GO TO 175
          ENDIF
C
C
C       IN THE SECOND ITERATION JUST CALCULATE THE VELOCITIES.
C
        ELSE
          CALL VBSL
```

```
      ENDIF
C
C
C     TRANSFORMING THE VELOCITIES FROM ZETA TO Z PLANE
C
      DO 80 IJ=1,NV
        CIRC=CMPLX(0.0,1.0)*ZG1(IJ)
        ZU(IJ)=ZU(IJ)*FZT(IJ)-CIRC*PIH*(1.0+
     +                          1.0/(ZT(IJ)*ZT(IJ)))
        ZU(IJ)=CONJG(ZU(IJ))
 80     CONTINUE
C
C
C     FOR THE SECOND STEP OF THE TIME INTEGRATION CALCULATE
C     THE VELOCITIES ONLY AND CALL VBSL.FTN .
C
      IF( IORDER.EQ.1 )THEN
        DO 100 IJ=1,NV
          Z(IJ)=Z(IJ)+DT*ZU(IJ)
          ZU1(IJ)=ZU(IJ)
 100      CONTINUE
        GO TO 47
      ENDIF
C
C     CALCULATE THE AVERAGE VELOCITY
C
      IJ=0
      DO 140 J=1,NR
        DO 120 I=1,NVR(J)
          IJ=IJ+1
          ZUB(I,J)=0.5*(ZU1(IJ)+ZU(IJ))
 120      CONTINUE
 140    CONTINUE
C
C
 175    CONTINUE
C
C
      RETURN
      END
C
C*************************************************************
C
C     SUBROUTINE MAIN3
C
C     CALCULATE THE VELOCITY AND ALL SCALAR VALUES ON A
C     MESH, WITHIN THE COMPUTATIONAL DOMAIN, FOR THE
C     FUTURE USE.
C     (IT CAN BE CALLED FOR THE FINE AND/OR COARSE MESH)
C
C-------------------------------------------------------------
C
      SUBROUTINE MAIN3
C
      COMMON /NVN/ NV
      COMMON /NXNY/ NX,NY
      COMMON /ZBZB1/ ZB1(2,9500)
      COMMON /ZGZG1/ ZG(9500)
      COMMON /PQAF1/ PT1(9500),QT1(9500),PA1(9500),QA1(9500),
     +               PF1(9500),QF1(9500)
      COMMON /ZSZU1/ ZS(2,101,51),ZUS(2,101,51)
      COMMON /CAFPS/ TPS(101,51),CAS(101,51),CFS(101,51)
      COMMON /PIH2/ PI,PIH,PI2
```

```
      COMMON /SOURCE/ S1ST,S2ST,S1ZT(2),S2ZT(2)
      COMMON /DELDT/ DEL,DT,UAVG,WL,ALPH
      COMMON /TC1C2/ T0T,C1T,C2T,T0A,C1A,C2A,T0F,C1F,C2F
      COMMON /BLK24/ DEL2S(9500)
      COMMON /BLK25/ DEL2(9500)
      COMMON /R1R2R/ RR1(101,51),RR2(101,51)
C
C-----------------------------------------------------------------
C
C     FIRST LET'S CALCULATE THE VELOCITY AND SCALAR VALUES
C     DUE TO THE SOURCES IN "ZETA" PLANE.
      DO 60 J1=1,NY
        DO 40 I1=1,NX
          TPS(I1,J1)=T0T+C1T*RR1(I1,J1)+C2T*RR2(I1,J1)
          CAS(I1,J1)=T0A+C1A*RR1(I1,J1)+C2A*RR2(I1,J1)
          CFS(I1,J1)=T0F+C1F*RR1(I1,J1)+C2F*RR2(I1,J1)
          ZUS(1,I1,J1)=0.0
          ZUS(2,I1,J1)=0.0
          DO 20 J=1,NV
C
C
C     GEOMETRICAL CONSTANTS IN THE BIOT-SAVART LAW.
C
            DX=ZS(1,I1,J1)-ZB1(1,J)
            DX2=DX*DX
            DY=ZS(2,I1,J1)-ZB1(2,J)
            DY2=DY*DY
            R2=DX2+DY2
C
C     CHECK THE GRID POINT NOT TO BE ON THE
C     CENTER OF THE COMPUTATIONAL ELEMENT.
C
            IF( R2.LT.1.0E-10 )THEN
              R2I=0.0
            ELSE
              R2I=1.0/R2
            ENDIF
            COEFJ=1.0-EXP(-R2*DEL2(J))
            COEFJS=1.0-EXP(-R2*DEL2S(J))
            DYM=ZS(2,I1,J1)+ZB1(2,J)
            DYM2=DYM*DYM
            R2M=DX2+DYM2
            R2MI=1.0/R2M
            COFJI=1.0-EXP(-R2M*DEL2(J))
            COFJIS=1.0-EXP(-R2M*DEL2S(J))
            DXR=DX*R2I
            DYR=DY*R2I
            DXRM=DX*R2MI
            DYRM=DYM*R2MI
            CP=DXR*COEFJS+DXRM*COFJIS
            CQ=DYR*COEFJS-DYRM*COFJIS
C
C
C     VELOCITY ON THE MESH.
C
          ZUS(1,I1,J1)=ZUS(1,I1,J1)+ZG(J)*(-DYR*COEFJ+DYRM*COFJI)
          ZUS(2,I1,J1)=ZUS(2,I1,J1)+ZG(J)*(-DXR*COEFJ+DXRM*COFJI)
C
C
C     TEMPERATURE OF THE PRODUCT ON THE MESH.
C
            TPS(I1,J1)=TPS(I1,J1)+PT1(J)*CP+QT1(J)*CQ
C
```

```
C
C       CONCENTRATION OF THE AIR ON THE MESH.
C
              CAS(I1,J1)=CAS(I1,J1)+PA1(J)*CP+QA1(J)*CQ
C
C
C       CONCENTRATION OF THE FUEL ON THE MESH.
C
              CFS(I1,J1)=CFS(I1,J1)+PF1(J)*CP+QF1(J)*CQ
C
 20         CONTINUE
 40       CONTINUE
 60      CONTINUE
C
C
        RETURN
        END
C
C*************************************************************
C
C       SUBROUTINE MAIN4
C
C       UPDATE THE VALUES OF THE SCALAR VARIATION.
C
C       "NRCFT" IS THE RATIO OF THE CHEMISTRY TO THE FLWO
C       TIME STEPS RESPECTIVELY.
C
C-------------------------------------------------------------
C
        SUBROUTINE MAIN4
C
        DIMENSION  DTB0(1200,9), DCA0(1200,9), DCF0(1200,9),
     1               DTB(1200,9),  DCA(1200,9),  DCF(1200,9),
     2            DDTB1(1200,9),DDCA1(1200,9),DDCF1(1200,9),
     3            DDTB2(1200,9),DDCA2(1200,9),DDCF2(1200,9),
     4            DDTB3(1200,9),DDCA3(1200,9),DDCF3(1200,9),
     5            DDTB4(1200,9),DDCA4(1200,9),DDCF4(1200,9),
     6            DDTB5(1200,9),DDCA5(1200,9),DDCF5(1200,9),
     7            DDTB6(1200,9),DDCA6(1200,9),DDCF6(1200,9)
        COMMON /NRNVR/ NR,NVR(9)
        COMMON /DCAFB/ DTB00(1200,9),DCA00(1200,9),DCF00(1200,9)
        COMMON /DELDT/ DEL,DT1,UAVG,WL,ALPH
        COMMON /DATA5/ NQTL,NQKA,NQMD
        COMMON /DATA6/ DUM(10,5)
        COMMON /DATA7/ NRCFT
C
C-------------------------------------------------------------
C
        ICF=0
C
C
C ... FIRST CHECK IF FRACTIONAL STEPS IN CHEMISTRY CALCULATION
C     IS REALLY NEEDED OR NOT ?
C
 8      IF( ICF.EQ.0 )THEN
          DT=DT1
        ELSE
          DT=DT1/FLOAT(NRCFT)
        ENDIF
C
        DO 14 J=1,NR
          DO 12 I=1,NVR(J)
            DTB0(I,J)=DTB00(I,J)
```

```
            DCA0(I,J)=DCA00(I,J)
            DCF0(I,J)=DCF00(I,J)
 12       CONTINUE
 14     CONTINUE
C
C
       IIC=0
 16    IIC=IIC+1
C
C
C      FIRST STEP IN THE FIFTH ORDER RANG-KUTTA TIME INTEGRATION
C
       IF(NQKA.EQ.0)THEN
         CALL DSVARK(DTB0,DCA0,DCF0,DDTB1,DDCA1,DDCF1)
       ELSE
         CALL DSVARA(DTB0,DCA0,DCF0,DDTB1,DDCA1,DDCF1)
       ENDIF
       DO 40 J=1,NR
         DO 20 I=1,NVR(J)
           DTB(I,J)=DTB0(I,J)+0.25*DT*DDTB1(I,J)
           DCA(I,J)=DCA0(I,J)+0.25*DT*DDCA1(I,J)
           DCF(I,J)=DCF0(I,J)+0.25*DT*DDCF1(I,J)
 20        CONTINUE
 40      CONTINUE
C
C
C      SECOND STEP IN THE FIFTH ORDER RANG-KUTTA TIME INTEGRATION
C
       IF( NQKA.EQ.0 )THEN
         CALL DSVARK(DTB,DCA,DCF,DDTB2,DDCA2,DDCF2)
       ELSE
         CALL DSVARA(DTB,DCA,DCF,DDTB2,DDCA2,DDCF2)
       ENDIF
       DO 80 J=1,NR
         DO 60 I=1,NVR(J)
           DTB(I,J)=DTB0(I,J)+DT*(3.0*DDTB1(I,J)+9.0*DDTB2(I,J))/32.0
           DCA(I,J)=DCA0(I,J)+DT*(3.0*DDCA1(I,J)+9.0*DDCA2(I,J))/32.0
           DCF(I,J)=DCF0(I,J)+DT*(3.0*DDCF1(I,J)+9.0*DDCF2(I,J))/32.0
 60        CONTINUE
 80      CONTINUE
C
C
C      THIRD STEP IN THE FIFTH ORDER RANG-KUTTA TIME INTEGRATION
C
       IF( NQKA.EQ.0 )THEN
         CALL DSVARK(DTB,DCA,DCF,DDTB3,DDCA3,DDCF3)
       ELSE
         CALL DSVARA(DTB,DCA,DCF,DDTB3,DDCA3,DDCF3)
       ENDIF
       DO  120 J=1,NR
         DO 100 I=1,NVR(J)
           DTB(I,J)=DTB0(I,J)+DT*(1932.0*DDTB1(I,J)-7200.0*
     +                DDTB2(I,J)+7296.0*DDTB3(I,J))/2197.0
           DCA(I,J)=DCA0(I,J)+DT*(1932.0*DDCA1(I,J)-7200.0*
     +                DDCA2(I,J)+7296.0*DDCA3(I,J))/2197.0
           DCF(I,J)=DCF0(I,J)+DT*(1932.0*DDCF1(I,J)-7200.0*
     +                DDCF2(I,J)+7296.0*DDCF3(I,J))/2197.0
 100       CONTINUE
 120     CONTINUE
C
C
C      FOURTH STEP IN THE FIFTH ORDER RANG-KUTTA TIME INTEGRATION
C
```

```
      IF( NQKA.EQ.0 )THEN
        CALL DSVARK(DTB,DCA,DCF,DDTB4,DDCA4,DDCF4)
      ELSE
        CALL DSVARA(DTB,DCA,DCF,DDTB4,DDCA4,DDCF4)
      ENDIF
      DO 160 J=1,NR
        DO 140  I=1,NVR(J)
          DTB(I,J)=DTB0(I,J)+DT*(439.0*DDTB1(I,J)/216.0-8.0*
     1                DDTB2(I,J)+3680.0*DDTB3(I,J)/513.0-845.0*
     2                DDTB4(I,J)/4104.0)
          DCA(I,J)=DCA0(I,J)+DT*(439.0*DDCA1(I,J)/216.0-8.0*
     1                DDCA2(I,J)+3680.0*DDCA3(I,J)/513.0-845.0*
     2                DDCA4(I,J)/4104.0)
          DCF(I,J)=DCF0(I,J)+DT*(439.0*DDCF1(I,J)/216.0-8.0*
     1                DDCF2(I,J)+3680.0*DDCF3(I,J)/513.0-845.0*
     2                DDCF4(I,J)/4104.0)
 140      CONTINUE
 160    CONTINUE
C
C
C       FIFTH STEP IN THE FIFTH ORDER RANG-KUTTA TIME INTEGRATION
C
      IF( NQKA.EQ.0 )THEN
        CALL DSVARK(DTB,DCA,DCF,DDTB5,DDCA5,DDCF5)
      ELSE
        CALL DSVARA(DTB,DCA,DCF,DDTB5,DDCA5,DDCF5)
      ENDIF
      DO 200 J=1,NR
        DO 180 I=1,NVR(J)
          DTB(I,J)=DTB0(I,J)+DT*(-8.0*DDTB1(I,J)/27.0+2.0*
     1                DDTB2(I,J)-3544.0*DDTB3(I,J)/2565.0+1859.0*
     2                DDTB4(I,J)/4104.0-11.0*DDTB5(I,J)/40.0)
          DCA(I,J)=DCA0(I,J)+DT*(-8.0*DDCA1(I,J)/27.0+2.0*
     1                DDCA2(I,J)-3544.0*DDCA3(I,J)/2565.0+1859.0*
     2                DDCA4(I,J)/4104.0-11.0*DDCA5(I,J)/40.0)
          DCF(I,J)=DCF0(I,J)+DT*(-8.0*DDCF1(I,J)/27.0+2.0*
     1                DDCF2(I,J)-3544.0*DDCF3(I,J)/2565.0+1859.0*
     2                DDCF4(I,J)/4104.0-11.0*DDCF5(I,J)/40.0)
 180      CONTINUE
 200    CONTINUE
C
C
C       UPDATING THE VARIATION OF SCALAR.
C
      IF( NQKA.EQ.0 )THEN
        CALL DSVARK(DTB,DCA,DCF,DDTB6,DDCA6,DDCF6)
      ELSE
        CALL DSVARA(DTB,DCA,DCF,DDTB6,DDCA6,DDCF6)
      ENDIF
      ET=-100.0
      EA=-100.0
      EF=-100.0
      DO 240 J=1,NR
        DO 220 I=1,NVR(J)
          DTB0(I,J)=DTB0(I,J)+DT*(25.0*DDTB1(I,J)/216.0+1408.0*
     1                DDTB3(I,J)/2565.0+2197.0*DDTB4(I,J)/4104.0-
     2                DDTB5(I,J)/5.0)
          DCA0(I,J)=DCA0(I,J)+DT*(25.0*DDCA1(I,J)/216.0+1408.0*
     1                DDCA3(I,J)/2565.0+2197.0*DDCA4(I,J)/4104.0-
     2                DDCA5(I,J)/5.0)
          DCF0(I,J)=DCF0(I,J)+DT*(25.0*DDCF1(I,J)/216.0+1408.0*
     1                DDCF3(I,J)/2565.0+2197.0*DDCF4(I,J)/4104.0-
     2                DDCF5(I,J)/5.0)
```

```
C
C
C       ERROR ESTIMATE
C
            ERDTB=DT*(DDTB1(I,J)/360.0-128.0*DDTB3(I,J)/4275.0-
     1                2197.0*DDTB4(I,J)/75240.0+DDTB5(I,J)/50.0+
     2                2.0*DDTB6(I,J)/55.0)
            IF(ERDTB.GT.ET)ET=ERDTB
            ERDCA=DT*(DDCA1(I,J)/360.0-128.0*DDCA3(I,J)/4275.0-
     1                2197.0*DDCA4(I,J)/75240.0+DDCA5(I,J)/50.0+
     2                2.0*DDCA6(I,J)/55.0)
            IF(ERDCA.GT.EA)EA=ERDCA
            ERDCF=DT*(DDCF1(I,J)/360.0-128.0*DDCF3(I,J)/4275.0-
     1                2197.0*DDCF4(I,J)/75240.0+DDCF5(I,J)/50.0+
     2                2.0*DDCF6(I,J)/55.0)
            IF(ERDCF.GT.EF)EF=ERDCF
 220      CONTINUE
 240    CONTINUE
        DUM(IIC,1)=ET
        DUM(IIC,2)=EA
        DUM(IIC,3)=EF
C
C
C       CHECK FOR THE HIGHEST ERROR
C
        ERMAX=0.0
        IF( ET.GT.ERMAX )ERMAX=ET
        IF( EA.GT.ERMAX )ERMAX=EA
        IF( EF.GT.ERMAX )ERMAX=EF
        IF( ERMAX.GT.1.0E-5 )THEN
          ICF=ICF+1
          GO TO 8
        ELSE
          GO TO 255
        ENDIF
C
C
C       CHECK FOR ADDITIONAL TIME STEP IN CHEMISTRY CALCULATIONS.
C
 255    IF( ICF.EQ.0 )THEN
          GO TO 256
        ELSE
          IF( IIC.LT.NRCFT )GO TO 16
        ENDIF
 256    DO 280 J=1,NR
          DO 260 I=1,NVR(J)
            DTB00(I,J)=DTB0(I,J)
            DCA00(I,J)=DCA0(I,J)
            DCF00(I,J)=DCF0(I,J)
 260      CONTINUE
 280    CONTINUE
C
C
        RETURN
        END
C
C*************************************************************
C
C       SUBROUTINE MAIN5
C
C       TO INJECT OR COMBINE THE COMPUTATIONAL ELEMENTS
C       IF THE DISTANCE BETWEEN THE TWO NEIGHBORING ELEMENT
C       FALLS OUT OF THE RANGE OF TWO PREDTERMINED VALUE
```

```
C       (NAMELY Rmax AND Rmin).          200
C
C-----------------------------------------------------------------
C
        SUBROUTINE MAIN5
C
        DIMENSION ZBDUM(1200,9), ZGDUM(1200,9),TIMDUM(1200,9),
     +            DTBDUM(1200,9),DCADUM(1200,9),DCFDUM(1200,9)
        COMMON /NRNVR/ NR,NVR(9)
        COMMON /NVN/ NV
        COMMON /ZBZB/ ZB(1200,9)
        COMMON /ZUBZ/ ZUB(1200,9)
        COMMON /ZGZG/ ZG(1200,9)
        COMMON /TIMT/ TIM(1200,9)
        COMMON /DCAFB/ DTB(1200,9),DCA(1200,9),DCF(1200,9)
        COMMON /DELDT/ DEL,DT,UAVG,WL,ALPH
        COMMON /DATA2/ ALDX,BETDX,X0,ALPHA,BETA,FACT
        COMMON /DATA3/ YMIN,YMAX,YMAX2,XMAX
        COMMON /DATA1/ HCOL
        COMMON /DATA4/ IDUM(5)
        COMMON /GAGA1/ GAMA(9),DELT(9),YVOR(9),ERF(9)
        COMMON /LAMSH/ ETA(9),XT0(9)
        COMMON /DATA5/ NQTL,NQKA,NQMD
        COMPLEX ZB,ZBDUM,ZUB,VEL
C
C-----------------------------------------------------------------
C
C       MOVE ALL ELEMENTS TO A NEW POSITION.
C
        DO 49 J=1,NR
        DO 49 I=1,NVR(J)
          IF( NQTL.EQ.0 )THEN
            XT=REAL(ZB(I,J))+ERF(J)*DT
            YT=0.5+(YVOR(J)-0.5)*SQRT(1.0+XT/XT0(J))
            ZB(I,J)=CMPLX(XT,YT)
          ELSE
            ZB(I,J)=ZB(I,J)+ZUB(I,J)*DT
          ENDIF
          TIM(I,J)=TIM(I,J)+DT
 49     CONTINUE
C
C
C       REARRANGE THE BLOBS.
C       1. THOSE LEAVING THE COMPUTATIONAL DOMAIN TO BE DELETED.
C       2. THE REST TO BE REFLECTED.
C
        DO 75 J=1,NR
          I=0
 51       I=I+1
 52       XX=REAL(ZB(I,J))
          YY=AIMAG(ZB(I,J))
C
C
C       DELETE ELEMENTS LEAVING THE DOMAIN AND SHIFT ALL VALUES
C       ON EACH LAYER TO MAKE THEM IN ORDER.
C
          IF( XX.GT.XMAX )THEN
            DO 56 II=I+1,NVR(J)
               ZB(II-1,J)= ZB(II,J)
               ZG(II-1,J)= ZG(II,J)
              TIM(II-1,J)=TIM(II,J)
              DTB(II-1,J)=DTB(II,J)
              DCA(II-1,J)=DCA(II,J)
```

```
            DCF(II-1,J)=DCF(II,J)
 56         CONTINUE
            NVR(J)=NVR(J)-1
            GO TO 52
          ENDIF
C
C
C       REFELECT THOSE CROSSING THE SOLID WALL.
C
          IF( YY.GT.YMAX ) YY=YMAX2-YY
          IF( YY.LT.YMIN ) YY=-YY
          ZB(I,J)=CMPLX(XX,YY)
          IF( I.LT.NVR(J) )GO TO 51
 75       CONTINUE
          IDUM(2)=0
          IDUM(3)=0
C
C
C       CHECK FOR INJECTION OF THE NEW ELEMENTS WITHIN THE
C       DIFFERENT ZONE OF THE COMPUTATIONAL DOMAIN
C
          DO 650 J=1,NR
            I=1
 563        RZB=REAL(ZB(I,J))
            DX=RZB-X0
            IF( DX.LT.0.0 )THEN
              AL=ALPHA
            ELSE
              AL=ALPHA+DX*ALDX
            ENDIF
            RMAX=AL*HCOL
            R=CABS(ZB(I,J)-ZB(I+1,J))
            IF( R.GT.RMAX )THEN   !INSERT A NEW ELEMENT IN BETWEEN
               ZB(NVR(J)+1,J)= 0.5*( ZB(I,J)+ ZB(I+1,J))   !AVERAGE
              TIM(NVR(J)+1,J)= 0.5*(TIM(I,J)+TIM(I+1,J))   !"    "
              DTB(NVR(J)+1,J)= 0.5*(DTB(I,J)+DTB(I+1,J))   !"    "
              DCA(NVR(J)+1,J)= 0.5*(DCA(I,J)+DCA(I+1,J))   !"    "
              DCF(NVR(J)+1,J)= 0.5*(DCF(I,J)+DCF(I+1,J))   !"    "
               ZG(NVR(J)+1,J)=FACT*( ZG(I,J)+ ZG(I+1,J))   !SAME GAMA
              ZG(I,J)=ZG(NVR(J)+1,J)
              ZG(I+1,J)=ZG(I,J)
              DO 569 K=I+1,NVR(J) !SHIFT ALL VALUES
                 ZBDUM(K,J)= ZB(K,J)
                 ZGDUM(K,J)= ZG(K,J)
                TIMDUM(K,J)=TIM(K,J)
                DTBDUM(K,J)=DTB(K,J)
                DCADUM(K,J)=DCA(K,J)
                DCFDUM(K,J)=DCF(K,J)
 569          CONTINUE
               ZB(I+1,J)= ZB(NVR(J)+1,J)
               ZG(I+1,J)= ZG(NVR(J)+1,J)
              TIM(I+1,J)=TIM(NVR(J)+1,J)
              DTB(I+1,J)=DTB(NVR(J)+1,J)
              DCA(I+1,J)=DCA(NVR(J)+1,J)
              DCF(I+1,J)=DCF(NVR(J)+1,J)
              DO 574 K=I+1,NVR(J)
                 ZB(K+1,J)= ZBDUM(K,J)
                 ZG(K+1,J)= ZGDUM(K,J)
                TIM(K+1,J)=TIMDUM(K,J)
                DTB(K+1,J)=DTBDUM(K,J)
                DCA(K+1,J)=DCADUM(K,J)
                DCF(K+1,J)=DCFDUM(K,J)
 574          CONTINUE
```

```
            NVR(J)=NVR(J)+1
            IDUM(2)=IDUM(2)+1
            IF( NVR(J).GT.1200 )THEN
              IDUM(1)=1
              RETURN
            ENDIF
            GO TO 563
          ENDIF
          I=I+1
          IF( I.LT.NVR(J) )GO TO 563
 650    CONTINUE
C
C
C       CHECK FOR COMBINATION OF TWO NEIGHBORING ELEMENT
C       WITHIN THE DIFFERENT ZONES OF THE COMPUTATIONAL DOMAIN.
C
       DO 750 J=1,NR
         I=3
 663     RZB=REAL(ZB(I,J))
         DX=RZB-X0
         IF( DX.LT.0.0 )THEN
           BET=BETA
         ELSE
           BET=BETA+DX*BETDX
         ENDIF
         RMIN=BET*HCOL
         R=CABS(ZB(I-1,J)-ZB(I-2,J))
         IF( R.LT.RMIN )THEN   !COMBINE THE TWO NEIGHBORING ELEMENTS
            ZB(I-1,J)=0.5*( ZB(I,J)+ ZB(I-1,J))
           TIM(I-1,J)=0.5*(TIM(I,J)+TIM(I-1,J))
           DTB(I-1,J)=0.5*(DTB(I,J)+DTB(I-1,J))
           DCA(I-1,J)=0.5*(DCA(I,J)+DCA(I-1,J))
           DCF(I-1,J)=0.5*(DCF(I,J)+DCF(I-1,J))
            ZG(I-1,J)=      ZG(I,J)+ ZG(I-1,J)
           DO 671 K=I+1,NVR(J) !SHIFT ALL VALUES
              ZB(K-1,J)= ZB(K,J)
              ZG(K-1,J)= ZG(K,J)
             TIM(K-1,J)=TIM(K,J)
             DTB(K-1,J)=DTB(K,J)
             DCA(K-1,J)=DCA(K,J)
             DCF(K-1,J)=DCF(K,J)
 671       CONTINUE
           NVR(J)=NVR(J)-1
           IDUM(3)=IDUM(3)+1
           IF( I.LE.NVR(J) )GO TO 663
         ENDIF
         I=I+1
         IF( I.LT.NVR(J) )GO TO 663
 750   CONTINUE
       IDUM(1)=0
C
C
 999   RETURN
       END
C
C*********************************************************************
C
C       SUBROUTINE PQ(DELS,P,Q)
C
C       CALCULATE THE GRADIENTS OF SCALAR
C       IN THE PHYSICAL PLANE.
C       "P" AND "Q" ARE SCALAR GRADIENTS IN GENERAL, AND
C       "DELS" IS SCALAR VARIATION ASSOCIATED WITH EACH ELEMENT.
```

```
C
C-----------------------------------------------------------------
C
      SUBROUTINE PQ(DELS,P,Q)
C
      DIMENSION   XL(1200,9),YL(1200,9),DELX(1200,9),
     +           DELY(1200,9),RL(1200,9),P(1200,9),Q(1200,9),
     +           DELS(1200,9)
      COMMON /NRNVR/ NR,NVR(9)
      COMMON /ZBZB/ ZB(2,1200,9)
C
C-----------------------------------------------------------------
C
      DO 60 J=1,NR
        XL(1,J)=ZB(1,1,J)
        YL(1,J)=ZB(2,1,J)
        XL(NVR(J)+1,J)=ZB(1,NVR(J),J)
        YL(NVR(J)+1,J)=ZB(2,NVR(J),J)
        DO 60 I=1,NVR(J)-1
          XL(I+1,J)=0.5*(ZB(1,I+1,J)+ZB(1,I,J))
          YL(I+1,J)=0.5*(ZB(2,I+1,J)+ZB(2,I,J))
 60   CONTINUE
      DO 65 J=1,NR
      DO 65 I=1,NVR(J)
        DELX(I,J)=XL(I+1,J)-XL(I,J)
        DELY(I,J)=YL(I+1,J)-YL(I,J)
        RL(I,J)=SQRT(DELX(I,J)*DELX(I,J)+DELY(I,J)*DELY(I,J))
 65   CONTINUE
      DO 70 J=1,NR
      DO 70 I=1,NVR(J)
      IF(ABS(DELX(I,J)).LT.1.E-07)THEN
        IF(DELY(I,J).GT.0.0)THEN
          P(I,J)=DELS(I,J)*RL(I,J)
        ELSE
          P(I,J)=-DELS(I,J)*RL(I,J)
        ENDIF
        Q(I,J)=0.0
        GO TO 70
      ENDIF
      IF(ABS(DELY(I,J)).LT.1.E-07)THEN
        IF(DELX(I,J).GT.0.0)THEN
          Q(I,J)=-DELS(I,J)*RL(I,J)
        ELSE
          Q(I,J)=DELS(I,J)*RL(I,J)
        ENDIF
        P(I,J)=0.0
        GO TO 70
      ENDIF
      BM=DELY(I,J)/DELX(I,J)
      AM=-1.0/BM
      IF(AM.GT.0.0)THEN
        IF(DELX(I,J).LT.0.0)THEN
          P(I,J)=DELS(I,J)*COS(ATAN(AM))*RL(I,J)
          Q(I,J)=DELS(I,J)*SIN(ATAN(AM))*RL(I,J)
        ELSE
          P(I,J)=-DELS(I,J)*COS(ATAN(AM))*RL(I,J)
          Q(I,J)=-DELS(I,J)*SIN(ATAN(AM))*RL(I,J)
        ENDIF
      ELSE
        IF(DELX(I,J).GT.0.0)THEN
          P(I,J)=DELS(I,J)*COS(ATAN(-AM))*RL(I,J)
          Q(I,J)=-DELS(I,J)*SIN(ATAN(-AM))*RL(I,J)
        ELSE
```

```
            P(I,J)=-DELS(I,J)*COS(ATAN(-AM))*RL(I,J)
            Q(I,J)=DELS(I,J)*SIN(ATAN(-AM))*RL(I,J)
          ENDIF
        ENDIF
 70     CONTINUE
C
C
        RETURN
        END
C
C*****************************************************************
C
C       SUBROUTINE SRCS(RRS,PA,QA,T0,C1,C2)
C
C       CALCULATE THE AVERAGED VALUE OF CONSTANTS OF
C       TWO SOURCES REPRESENTING DENSITY DISTRIBUTION
C       (T0, C1 AND C2).
C
C---------------------------------------------------------------
C
        SUBROUTINE SRCS(RRS,PA,QA,T0,C1,C2)

C
C
C             -RRS
C       ==========================================================
C                 |     #1                        |     #3(FIX TOP)
C                 |     .                         |     .
C  SOURCE #1-->    \    .                          \    .
C  HIGH-SPEED U1    \   .                           \   .
C  REACTANT #1       \  .                            \  .
C                     \ .                             \ .
C      >>>>>>>>>>>>>>>>.-------------------------------.-----------
C                      .                             .\
C                      .                             . \
C  SOURCE #2-->        .                             .  \
C  LOW-SPEED U2        .                             .   \
C  REACTANT #2         .                             .    \
C                      .     |                       .     |
C                      #2    |          (FIX BOTTOM) #3    |
C       ==========================================================
C                          +RRS
C
C---------------------------------------------------------------
C
        DIMENSION PA(9500),QA(9500),ZPS(3),ZTS(3),T(3)
        COMMON /PIH2/ PI,PIH,PI2
        COMMON /SOURCE/ S1ST,S2ST,S1ZT,S2ZT
        COMMON /XBDBD/ XBD
        COMPLEX ZPS,ZTS,ZZ,S1ZT,S2ZT
C
C---------------------------------------------------------------
C
        NY=3
        ZPS(1)=CMPLX(0.0,0.999)
        ZPS(2)=CMPLX(0.0,0.001)
C
C
C       a) FIX THE THIRD POINT ON THE HIGH-VELOCITY SIDE.
C
        ZPS(3)=CMPLX(XBD,0.999)
        DO 20 J=1,NY
```

```
            ZZ=CSQRT(CEXP(PI2*ZPS(J))+1.0)
            IF(AIMAG(ZPS(J)).GE.0.5)ZZ=-ZZ
            ZTS(J)=ZZ
 20       CONTINUE
          CALL BOUND(PA,QA,ZTS,T)
          A11=LOG(CABS(ZTS(1)-S1ZT))
          A21=LOG(CABS(ZTS(2)-S1ZT))
          A31=LOG(CABS(ZTS(3)-S1ZT))
          A12=LOG(CABS(ZTS(1)-S2ZT))
          A22=LOG(CABS(ZTS(2)-S2ZT))
          A32=LOG(CABS(ZTS(3)-S2ZT))
          AA=2.0*RRS*(A11-A31)-(T(1)-T(2))*(A11-A31)+
     +       (T(1)-T(3))*(A11-A21)
          BB=(A11-A31)*(A12-A22)-(A11-A21)*(A12-A32)
          C2T=AA/BB
          C1T=(2.0*RRS-(T(1)-T(2))-C2T*(A12-A22))/(A11-A21)
          T0T=RRS-T(1)-C1T*A11-C2T*A12
C
C
C         b) FIX THE THIRD POINT ON THE LOW-VELOCITY SIDE.
C
          ZPS(3)=CMPLX(XBD,0.001)
          DO 40 J=1,NY
            ZZ=CSQRT(CEXP(PI2*ZPS(J))+1.0)
            IF(AIMAG(ZPS(J)).GE.0.5) ZZ=-ZZ
            ZTS(J)=ZZ
 40       CONTINUE
          CALL BOUND(PA,QA,ZTS,T)
          A11=LOG(CABS(ZTS(1)-S1ZT))
          A21=LOG(CABS(ZTS(2)-S1ZT))
          A31=LOG(CABS(ZTS(3)-S1ZT))
          A12=LOG(CABS(ZTS(1)-S2ZT))
          A22=LOG(CABS(ZTS(2)-S2ZT))
          A32=LOG(CABS(ZTS(3)-S2ZT))
          AA=2.0*RRS*(A21-A31)-(T(1)-T(2))*(A11-A31)+
     +       (T(1)-T(3))*(A11-A21)
          BB=(A11-A31)*(A12-A22)-(A11-A21)*(A12-A32)
          C2B=AA/BB
          C1B=(2.0*RRS-(T(1)-T(2))-C2B*(A12-A22))/(A11-A21)
          T0B=RRS-T(1)-C1B*A11-C2B*A12
C
C
C         c)AVERAGE THE CONSTANTS OF THE TWO SET OF SOURCES.
C
          T0=0.5*(T0T+T0B)
          C1=0.5*(C1T+C1B)
          C2=0.5*(C2T+C2B)
C
C
          RETURN
          END
C
C*************************************************************
C
C         SUBROUTINE VBSL
C
C         VORTEX INTERACTION USING THE DIRECT BIOT-SAVART LAW
C         IN CALCULATING THE VELOCITY AT THE CENTER OF THE
C         COMPUTATIONAL ELEMENTS.
C
C-------------------------------------------------------------
C
          SUBROUTINE VBSL
```

```
C
      COMMON /NVN/ NV
      COMMON /SOURCE/ S1ST,S2ST,S1ZT(2),S2ZT(2)
      COMMON /BLK20/ DEL2(9500)
      COMMON /BLK21/ ZT(2,9500)
      COMMON /BLK22/ ZU(2,9500)
      COMMON /ZGZG1/ ZG(9500)
C
C-----------------------------------------------------------
C
C     a) VELOCITY DUE TO THE MASS SORCES.
C
      DO 20 I=1,NV
        AR=ZT(1,I)-S1ZT(1)
        AI=S1ZT(2)-ZT(2,I)
        BR=ZT(1,I)-S2ZT(1)
        BI=S2ZT(2)-ZT(2,I)
        AN=S1ST/((AR*AR)+(AI*AI))
        BN=S2ST/((BR*BR)+(BI*BI))
        ZU(1,I)=(AR*AN)+(BR*BN)
        ZU(2,I)=(AI*AN)+(BI*BN)
 20   CONTINUE
C
C
C     VELOCITY DUE TO THE VORTEX INTERACTION AND IMAGES.
C
      DO 50 I=1,NV-1
C
C     b) CONTRIBUTION OF IMAGE OF ELEMENT "I" ON ITSELF.
C
        DY=ZT(2,I)+ZT(2,I)
        R2=DY*DY
        COEF=1.0-EXP(-R2*DEL2(I))
        ZU(1,I)=ZU(1,I)+COEF*ZG(I)/DY
C
C
        DO 50 J=I+1,NV
C
C     c) CONTRIBUTION OF ELEMENT "J" ON ELEMENT "I".
C
        DX=ZT(1,I)-ZT(1,J)
        DX2=DX*DX
        DY=ZT(2,I)-ZT(2,J)
        DY2=DY*DY
        R2=DX2+DY2
        R2I=1.0/R2
        COEFJ=1.0-EXP(-R2*DEL2(J))
        COEFI=1.0-EXP(-R2*DEL2(I))
C
C
C     d) CONTRIBUTION OF IMAGE OF ELEMENT "J" ON ELEMENT "I"
C       AND IMAGE OF ELEMENT "I" ON ELEMENT "J".
C
        DYM=ZT(2,I)+ZT(2,J)
        DYM2=DYM*DYM
        R2M=DX2+DYM2
        R2MI=1.0/R2M
        COEFJI=1.0-EXP(-R2M*DEL2(J))
        COEFIJ=1.0-EXP(-R2M*DEL2(I))
        DXR=DX*R2I
        DYR=DY*R2I
        DXRM=DX*R2MI
        DYRM=DYM*R2MI
```

```
          ZU(1,I)=ZU(1,I)+ZG(J)*(-DYR*COEFJ+DYRM*COEFJI)
          ZU(2,I)=ZU(2,I)+ZG(J)*(-DXR*COEFJ+DXRM*COEFJI)
          ZU(1,J)=ZU(1,J)+ZG(I)*( DYR*COEFI+DYRM*COEFIJ)
          ZU(2,J)=ZU(2,J)+ZG(I)*( DXR*COEFI-DXRM*COEFIJ)
 50     CONTINUE
C
C
C       e) CONTRIBUTION OF THE LAST ELEMENT ON ITSELF.
C
        DY=ZT(2,NV)+ZT(2,NV)
        R2=DY*DY
        COEF=1.0-EXP(-R2*DEL2(NV))
        ZU(1,NV)=ZU(1,NV)+COEF*ZG(NV)/DY
C
C
        RETURN
        END
C
C*************************************************************
C
C       SUBROUTINE VSBSL
C
C       VORTEX INTERACTION USING THE DIRECT BIOT-SAVART LAW
C       IN CALCULATING THE VELOCITY AND THE SCALAR VALUES AT
C       THE CENTER OF THE COMPUTATIONAL ELEMENTS.
C
C-------------------------------------------------------------
C
        SUBROUTINE VSBSL
C
        COMMON /NRNVR/ NR,NVR(9)
        COMMON /NVN/ NV
        COMMON /RCTN/ ARE,RR,QE,TAE,FRAC
        COMMON /CAFB/ TPB(1200,9),CAB(1200,9),CFB(1200,9)
        COMMON /CAFB1/ TPB1(9500),CAB1(9500),CFB1(9500)
        COMMON /PQAF1/ PT1(9500),QT1(9500),PA1(9500),QA1(9500),
     +                 PF1(9500),QF1(9500)
        COMMON /TC1C2/ T0T,C1T,C2T,T0A,C1A,C2A,T0F,C1F,C2F
        COMMON /SOURCE/ S1ST,S2ST,S1ZT(2),S2ZT(2)
        COMMON /BLK20/ DEL2(9500)
        COMMON /BLK21/ ZT(2,9500)
        COMMON /BLK22/ ZU(2,9500)
        COMMON /ZGZG1/ ZG(9500)
        COMMON /BLK24/ DEL2S(9500)
C
C-------------------------------------------------------------
C
C       a) CONTRIBUTION OF THE MASS AND SCALAR SOURCES.
C
        DO 20 I=1,NV
          AR=ZT(1,I)-S1ZT(1)
          AI=S1ZT(2)-ZT(2,I)
          BR=ZT(1,I)-S2ZT(1)
          BI=S2ZT(2)-ZT(2,I)
          R1=AR*AR+AI*AI
          R2=BR*BR+BI*BI
C
C
C       a.1) SOURCE TERMS FOR VELOCITY.
C
          AN=S1ST/R1
          BN=S2ST/R2
          ZU(1,I)=(AR*AN)+(BR*BN)
```

```
            ZU(2,I)=(AI*AN)+(BI*BN)
C
C
C       a.2) SOURCE TERMS FOR SCALARS.
C
            R1=SQRT(R1)
            R2=SQRT(R2)
            TPB1(I)=T0T+C1T*LOG(R1)+C2T*LOG(R2)
            CAB1(I)=T0A+C1A*LOG(R1)+C2A*LOG(R2)
            CFB1(I)=T0F+C1F*LOG(R1)+C2F*LOG(R2)
 20       CONTINUE
C
C
C       INTERACTION BETWEEN ELEMENTS AND THEIR IMAGES.
C       (REDUCING "N**2" CALCULATION TO "(N**2)/2")
C
C       ----- FIRST DO LOOP OVER ELEMNTS IN THE BIOT-SAVART LAW.
C
          DO 50 I=1,NV-1
C
C
C       b) CONTRIBUTION OF IMAGE OF ELEMENT "i" ON ITSELF.
C
            DY=ZT(2,I)+ZT(2,I)
            R2=DY*DY
            COEF=1.0-EXP(-R2*DEL2(I))
            COEFS=1.0-EXP(-R2*DEL2S(I))
C
C
C       b.1) ... VELOCITY
C
            ZU(1,I)=ZU(1,I)+COEF*ZG(I)/DY
C
C
C       b.2) ... SCALAR
C
            TPB1(I)=TPB1(I)+QT1(I)*(-COEFS/DY)
            CAB1(I)=CAB1(I)+QA1(I)*(-COEFS/DY)
            CFB1(I)=CFB1(I)+QF1(I)*(-COEFS/DY)
C
C
C       --- SECOND DO LOOP OVER NUMBER OF ELEMENTS IN BIOT-SAVART LAW.
C
          DO 50 J=I+1,NV
              DX=ZT(1,I)-ZT(1,J)
              DX2=DX*DX
              DY=ZT(2,I)-ZT(2,J)
              DY2=DY*DY
C
C
C       CALCULATION OF SOME NECESSARY GEOMETRICAL PARAMETERS.
C
              R2=DX2+DY2
              R2I=1.0/R2
              COEFJ=1.0-EXP(-R2*DEL2(J))
              COEFI=1.0-EXP(-R2*DEL2(I))
              COEFJS=1.0-EXP(-R2*DEL2S(J))
              COEFIS=1.0-EXP(-R2*DEL2S(I))
              DYM=ZT(2,I)+ZT(2,J)
              DYM2=DYM*DYM
              R2M=DX2+DYM2
              R2MI=1.0/R2M
              COFJI=1.0-EXP(-R2M*DEL2(J))
```

```
            COFIJ=1.0-EXP(-R2M*DEL2(I))
            COFJIS=1.0-EXP(-R2M*DEL2S(J))
            COFIJS=1.0-EXP(-R2M*DEL2S(I))
            DXR=DX*R2I
            DYR=DY*R2I
            DXRM=DX*R2MI
            DYRM=DYM*R2MI
            CPJI=+DXR*COEFJS+DXRM*COFJIS
            CQJI=+DYR*COEFJS-DYRM*COFJIS
            CPIJ=-DXR*COEFIS-DXRM*COFIJS
            CQIJ=-DYR*COEFIS-DYRM*COFIJS
C
C
C       c) CONTRIBUTION OF ELEMENT "j" AND ITS IMAGE ON ELEMENT "i"
C       c.1) VELOCITY
C
            ZU(1,I)=ZU(1,I)+ZG(J)*(-DYR*COEFJ+DYRM*COFJI)
            ZU(2,I)=ZU(2,I)+ZG(J)*(-DXR*COEFJ+DXRM*COFJI)
C
C
C       c.2) SCALAR
C
            TPB1(I)=TPB1(I)+PT1(J)*CPJI+QT1(J)*CQJI
            CAB1(I)=CAB1(I)+PA1(J)*CPJI+QA1(J)*CQJI
            CFB1(I)=CFB1(I)+PF1(J)*CPJI+QF1(J)*CQJI
C
C
C       d) CONTRIBUTION OF ELEMENT "i" AND ITS IMAGE ON ELEMENT "j".
C
C
C       d.1) VELOCITY
C
            ZU(1,J)=ZU(1,J)+ZG(I)*( DYR*COEFI+DYRM*COFIJ)
            ZU(2,J)=ZU(2,J)+ZG(I)*( DXR*COEFI-DXRM*COFIJ)
C
C
C       d.2) SCALAR
C
            TPB1(J)=TPB1(J)+PT1(I)*CPIJ+QT1(I)*CQIJ
            CAB1(J)=CAB1(J)+PA1(I)*CPIJ+QA1(I)*CQIJ
            CFB1(J)=CFB1(J)+PF1(I)*CPIJ+QF1(I)*CQIJ
 50     CONTINUE
C
C
C       e) CONTRIBUTION OF THE IMAGE OF THE LAST ELEMENT ON ITSELF.
C
       DY=ZT(2,NV)+ZT(2,NV)
       R2=DY*DY
       COEF=1.0-EXP(-R2*DEL2(NV))
       COEFS=1.0-EXP(-R2*DEL2S(NV))
C
C
C       e.1) VELOCITY.
C
       ZU(1,NV)=ZU(1,NV)+COEF*ZG(NV)/DY
C
C
C       e.2) SCALAR.
C
       TPB1(NV)=TPB1(NV)-COEFS*QT1(NV)/DY
       CAB1(NV)=CAB1(NV)-COEFS*QA1(NV)/DY
       CFB1(NV)=CFB1(NV)-COEFS*QF1(NV)/DY
C
```

```
C
C       SHIFT THE SCALAR VALUES AND PUT THEM IN A 2-D ARRAY.          210
C
        IJ=0
        DO 80 J=1,NR
          DO 60 I=1,NVR(J)
            IJ=IJ+1
            TPB(I,J)=1.0+TPB1(IJ)
            CAB(I,J)=0.5*RR+CAB1(IJ)
            CFB(I,J)=0.5+CFB1(IJ)
 60       CONTINUE
 80     CONTINUE
C
C
        RETURN
        END
```